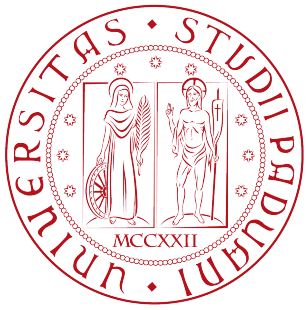

UNIVERSITÀ DEGLI STUDI DI PADOVA

Dipartimento di Fisica e Astronomia "G. Galilei"

CORSO DI DOTTORATO DI RICERCA IN FISICA

Ciclo XXIX

Study of Isospin Symmetry Breaking effects in the A=23 and A=46 multiplets

Tesi redatta con il contributo finanziario della Fondazione Cariparo

COORDINATORE: Ch.mo Prof. Gianguido Dall'Agata
SUPERVISORE: Ch.ma Prof. Silvia Monica Lenzi
CO-SUPERVISORE: Dr. Francesco Recchia

DOTTORANDO: Alberto Boso

Il sole della mattina brillò sulla spada di bronzo.
Non restava più traccia di sangue.
"Lo crederesti, Arianna?" disse Teseo.
"Il Minotauro non s'è quasi difeso."

Jorge Luis Borges, La casa di Asterione, L'Aleph

E adesso aspetterò domani
Per avere nostalgia
Signora libertà, signorina fantasia
Così preziosa come il vino
Così gratis come la tristezza
Con la tua nuvola di dubbi e di bellezza

F. De Andrè, Se ti tagliassero a pezzetti

Abstract

Isospin formalism, which describes the neutron and the proton as two states of the same particle, the nucleon, is one of the essential descriptive tools of a broad range of nuclear phenomena. The success of the isospin symmetry concept belies its broken nature. Not only the symmetry is broken by the proton-neutron mass difference and the Coulomb interaction, but also by the nucleon-nucleon interaction itself. The investigation of isospin symmetry conservation and breaking effects has revealed a wealth of nuclear structure information. Two of the main consequences of the isospin symmetry breaking (ISB) are the differences in the level schemes of mirror nuclei and the possible mixing of states with different values of isospin quantum number. In this thesis, two experiments performed to study these phenomena are presented.

The first experiment was performed at the GANIL laboratory, France. It aimed at the study of the excitation energy differences between analogue states in the mirror nuclei ^{23}Mg-^{23}Na. These differences, called MED, should in principle be only of electromagnetic origin and allow to extract detailed nuclear structure information such as the nature of particle angular-momentum re-coupling along yrast structures (e.g. backbending), the evolution of the nuclear radius or deformation and the identification of pure single-particle configurations. Moreover, systematic studies in the $f_{7/2}$ shell have shown that electromagnetic ISB terms are insufficient to reproduce the experimental MED values, and an additional isospin non-conserving term of non-Coulomb origin has to be introduced. While this phenomenon has been extensively studied in the $f_{7/2}$ shell, the information in the lower *sd* space is still scarce and more experimental information is needed. High spin states were populated with the ^{16}O+^{12}C fusion evaporation reaction and evaporated particles and γ rays, emitted in the de-excitation of the reaction products, were detected with the DIAMANT-NEUTRON WALL-EXOGAM setup. New transitions and levels have been identified in the ^{23}Mg nucleus and

the measured MED have been extended up to $J = 15/2^+$. The experimental data have been compared with shell model calculations. A new approach, which takes into account the isovectorial effect of the neutron skin on the MED, has been successfully adopted.

The second experiment described in this thesis took place in the GSI laboratory, Germany. The scope of the measurement was the study of the degree of isospin mixing in the 2^+ states of the ^{46}Cr-^{46}V-^{46}Ti, T=1 isospin triplet. If the isospin symmetry holds, no mixing would occur and the Coulomb matrix elements, (proportional to $\sqrt{B(E2; 0^+ \rightarrow 2^+)}$), would vary linearly with the third component of the isospin, T_z, along the triplet. Therefore, a precise measurement of the $2^+ \rightarrow 0^+$ transition probability allows to extract information on the degree of isospin mixing in the $N = Z$ member of the triplet, where T=0 and T=1 states coexist. The experimental setup was composed of the γ-ray tracking array AGATA, the FRS fragment separator and the LYCCA calorimeter. Radioactive beams of the nuclei of interest were produced via the fragmentation of a ^{58}Ni primary beam. The B(E2; $0^+ \rightarrow 2^+$) value for the proton rich ^{46}Cr nucleus was deduced from the Coulomb excitation cross section on a gold target. The ^{46}V value was measured using a differential plunger as target, consisting of a triple stack of gold foils. The Doppler shift of the emitted γ rays after each target is different, resulting in a triple-peak structure, whose shape depends on the lifetime of the state. The B(E2; $0^+ \rightarrow 2^+$) value can then be obtained from the measured lifetime. The ^{46}Ti nucleus was studied with both techniques in order to have a common reference point.

In the first part of this thesis the basic concepts of the isospin formalism are introduced. In the second and third chapter, the data analysis, the results, and the interpretation of the data regarding the two experiments are presented. Finally, in the last section, a summary of the work is given and the future perspectives are discussed.

Riassunto

La simmetria di isospin, che permette di descrivere il neutrone e il protone come due stati diversi di un'unica particella, il nucleone, è uno degli strumenti più potenti a nostra disposizione per descrivere una vasta gamma di fenomeni di struttura nucleare. Nonostante la sua utilità, la simmetria di isospin è però rotta non solo dalla differenza in massa tra protone e neutrone e dalla forza Coulombiana, ma anche dall'interazione nucleone-nucleone stessa. Lo studio della simmetria di isospin e della sua rottura permette di estrarre una notevole quantità di informazioni sulla struttura dei nuclei in gioco. Due delle conseguenze principali della rottura di simmetria di isospin sono le differenze negli schemi dei livelli di nuclei speculari e il possibile mixing di stati caratterizzati da numero quantico di isospin differente. In questo lavoro di tesi sono presentati due esperimenti volti allo studio di questi fenomeni.

Il primo esperimento è stato realizzato presso i laboratori di GANIL, in Francia. Lo scopo della misura è lo studio delle differenze nell'energia di eccitazione negli stati analoghi dei nuclei ^{23}Mg-^{23}Na. Tali differenze, note come Mirror Energy Differences (MED), dovrebbero in linea di principio essere interamente attribuibili all'interazione elettromagnetica e permettono di dedurre interessanti informazioni sulla struttura dei nuclei in gioco, come l'allineamento di particelle lungo la linea *yrast*, la variazione del raggio nucleare al variare del momento angolare, la deformazione e lo studio di particolari configurazioni di particella singola. D'altro canto, dettagliati studi svolti nella shell $f_{7/2}$ hanno dimostrato come l'interazione elettromagnetica non sia sufficiente per riprodurre i dati sperimentali e un ulteriore termine di rottura della simmetria di isospin, di origine non nucleare, debba essere introdotto. Questo fenomeno è stato largamente studiato nella shell $f_{7/2}$, mentre l'informazione nell shell *sd* è ancora scarsa e ulteriori misure sperimentali sono senza dubbio necessarie. Gli stati ad alto spin nei nuclei di interesse sono stati popolati con la reazione di fusione evaporazione ^{16}O+^{12}C

e le particelle e i raggi γ emessi nella diseccitazione dei prodotti di reazione sono stati rivelati tramite l'apparato sperimentale composto dai rivelatori DIAMANT, NEUTRON WALL e EXOGAM. Sono stati identificati nuovi livelli energetici e transizioni nel nucleo ^{23}Mg e le MED sperimentali sono state estese fino allo stato $J = 15/2^+$. I dati sperimentali sono stati poi confrontati con calcoli teorici di modello a shell, dove un nuovo approccio, che tiene in conto dell'effetto della neutron skin sulle MED, è stato utilizzato con successo.

Il secondo esperimento descritto in questa tesi è stato realizzato nel laboratorio GSI, in Germania. L'obiettivo della misura è lo studio del grado di mixing del numero quantico di isospin nello stato eccitato 2^+ nel tripletto di isospin a T=1 ^{46}Cr-^{46}V-^{46}Ti. Se l'isospin fosse un buon numero quantico non ci sarebbe mixing e gli elementi di matrice Coulombiani (proporzionali a $\sqrt{B(E2; 0^+ \rightarrow 2^+)}$) avrebbero un andamento lineare con la terza componente dell'isospin, T_z. Pertanto una misura precisa della probabilità di transizione $2^+ \rightarrow 0^+$ permette di testare il grado di mixing nel membro del tripletto con $N = Z$, dove stati con T=0 e T=1 coesistono. L'apparato sperimentale utilizzato è composto dallo spettrometro a tracciamento γ AGATA, dal separatore FRS e dal calorimetro LYCCA. I fasci radioattivi di interesse sono stati prodotti nella frammentazione di un fascio primario di ^{58}Ni. Il valore della B(E2; $0^+ \rightarrow 2^+$) per il nucleo ^{46}Cr è stato dedotto dalla sezione d'urto di eccitazione Coulombiana su un bersaglio di oro. Per il nucleo ^{46}V è stato invece utilizzato un nuovo dispositivo composto da tre fogli di oro disposti in successione. Lo spostamento Doppler the raggi γ emessi dopo ognuno dei tre bersagli è differente, creando cosi una struttura caratterizzata da tre picchi, la cui forma di riga dipende unicamente dalla vita media dello stato in esame. Da questa può quindi essere estratto il valore della probabilità di transizione, B(E2; $0^+ \rightarrow 2^+$).

Nella prima parte di questa tesi i concetti base del formalismo di isospin sono presentati. Nel secondo e nel terzo capitolo l'analisi dati, i risultati e l'interpretazione dei dati riguardanti i due esperimenti sono descritti. Infine, nell'ultima sezione, sono riportati il sommario del lavoro svolto e sono discusse le prospettive future di questo lavoro.

Contents

Contents vii

1 Isospin Symmetry 1
- 1.1 Isospin Formalism . . . 1
- 1.2 Physics of Mirror Nuclei . . . 4
  - 1.2.1 Energy Differences between excited IAS . . . 6
  - 1.2.2 Contributions to the MED . . . 7
    - 1.2.2.1 The Coulomb multipole term . . . 8
    - 1.2.2.2 The Coulomb monopole term . . . 9
    - 1.2.2.3 Isospin Symmetry Breaking Nuclear Term . . . 12
- 1.3 Isospin Mixing . . . 14
  - 1.3.1 Electromagnetic transitions selection rules . . . 15

2 MED in mirror nuclei ^{23}Mg $-^{23}$ Na 21
- 2.1 Previous studies on ^{23}Mg-^{23}Na . . . 22
- 2.2 Fusion Evaporation reactions . . . 24
- 2.3 The experiment . . . 26
- 2.4 The Experimental Setup . . . 27
  - 2.4.1 EXOGAM . . . 29
  - 2.4.2 DIAMANT . . . 31
  - 2.4.3 Neutron Wall . . . 33
- 2.5 Data Analysis . . . 37
  - 2.5.1 Structure of the data . . . 37
  - 2.5.2 Trigger Condition . . . 37
  - 2.5.3 EXOGAM analysis . . . 38

2.5.4 DIAMANT analysis . . . 46
2.5.5 Neutron Wall analysis . . . 51
2.6 Channel Selection . . . 55
2.7 Experimental results . . . 56
2.7.1 Identification of new transitions in ^{23}Mg-^{23}Na . . . 56
2.7.2 Determination of γ-ray intensity . . . 60
2.7.2.1 Angular Distributions . . . 62
2.8 Level schemes . . . 67
2.9 Theoretical interpretation . . . 69

3 Isospin Mixing in T=1 Isospin triplet ^{46}Cr $-^{46}$ V $-^{46}$ Ti 87
3.1 Previous studies . . . 89
3.2 Coulomb excitation . . . 90
3.3 Triple target measurement . . . 93
3.4 Experimental Setup . . . 97
3.4.1 Beam production . . . 98
3.4.2 The FRagment Separator (FRS) . . . 98
3.4.2.1 Detectors along FRS beam line . . . 103
3.4.3 The Lund-York-Cologne CAlorimeter (LYCCA) . . . 106
3.4.4 Advanced GAmma Tracking Array (AGATA) . . . 110
3.5 Data Analysis . . . 115
3.5.1 Fragment Separator FRS . . . 116
3.5.1.1 Time Projection Chamber (TPC) Calibrations . . . 118
3.5.1.2 MUSIC Calibrations . . . 119
3.5.1.3 FRS Scintillators Calibrations . . . 119
3.5.1.4 Particle Identification . . . 123
3.5.2 LYCCA Analysis . . . 125
3.5.2.1 Plastic ToF scintillator calibrations . . . 125
3.5.2.2 DSSSD calibrations . . . 127
3.5.2.3 CsI detectors calibrations . . . 128
3.5.2.4 Particle Identification . . . 128
3.5.3 AGATA Analysis . . . 129
3.5.3.1 Energy calibrations . . . 130

3.5.3.2 Efficiency calibrations 130
3.5.3.3 Doppler Correction Optimization 141
3.5.3.4 Background reduction 143
3.6 Results 144
3.6.1 Coulomb excitation cross section 146
3.6.1.1 Dead Time estimate 151
3.6.1.2 Scattering Angle reconstruction 152
3.6.1.3 Background considerations 153
3.6.1.4 Error Analysis 155
3.6.1.5 Cross section and B(E2) results 156
3.6.2 Lifetime measurements 162
3.6.3 B(E2) in the T=1, A=46 triplet 173

Conclusions and Perspectives **177**

References **181**

List of Figures **187**

List of Tables **199**

Chapter 1

Isospin Symmetry

After the discovery of the proton in 1919, Ernest Rutherford suggested the existence of neutrally-charged particles inside the atomic nucleus in 1920. This assumption was verified in 1932, when James Chadwick discovered the neutron. The mass of the neutron is very close to the mass of the proton and the nuclear interaction affects the two particles in a nearly identical way. These properties naturally lead to the description of the proton and the neutron as two different quantum states of the same particle, the nucleon. This can be formally achieved, following Werner Heisenberg's idea, with the introduction of a new quantum number, the isobaric spin or isospin.

1.1 Isospin Formalism

Two fundamental assumptions of nuclear structure are the *charge-symmetry* and the *charge-independence* of the nuclear interaction. The former requires that the proton-proton interaction V_{pp} is identical to the neutron-neutron interaction V_{nn}, while the latter can be formally expressed as $(V_{pp} + V_{nn}) = 2V_{pn}$ [1]. Nucleon-nucleon scattering experiments have shown a slight charge asymmetry in the scattering lengths for the *nn* and *pp* systems [2]. This however refers to free-nucleon interactions; the concepts of *charge-symmetry* and *charge-independence* are to a good approximation valid for the effective nucleon-nucleon interaction inside the nuclear medium.

Neglecting the Coulomb interaction, *charge-symmetry* and *charge-independence* imply an identical behavior in isobaric nuclei provided that the possible configurations of these isobaric multiplets are constrained by the Pauli principle, which guarantees the antysimmetrization of the total nuclear wavefunction.

The isospin quantum number couples together the concepts of *charge-symmetry* and *charge-independence* of the nuclear interaction and the Pauli principle.

The nucleon is characterized by the isospin value $t = \frac{1}{2}$, while the projection t_z on the z axis in the abstract isospin space is different for the proton and the neutron:

$$t_z = +\frac{1}{2} \quad \text{for} \quad \text{the neutron} \tag{1.1}$$

$$t_z = -\frac{1}{2} \quad \text{for} \quad \text{the proton} \tag{1.2}$$

The isospin quantum number follows the usual angular momentum algebra, therefore a nucleus composed of $A = N+Z$ nucleons has a total isospin projection value of:

$$T_z = \sum_{i=1}^{A} t_z = \frac{N-Z}{2}$$

The total isospin T is the sum vector of the individual isospin vectors of all the A nucleons:

$$\mathbf{T} = \mathbf{t_1} \oplus \mathbf{t_2} \oplus ... \oplus \mathbf{t_A}$$

which limits the possible T values to:

$$\frac{|N-Z|}{2} \leq T \leq \frac{N+Z}{2}$$

In Fig. 1.1 the possible couplings of the two-nucleon system are reported.

In such a system the total isospin T can be either 1 or 0. We have therefore an *isospin triplet* composed by the $T = 1$, $T_z = -1, 0, 1$ states, and a $T = 0$, $T_z = 0$ *isospin singlet*. Due to the isospin algebra described above, the like-

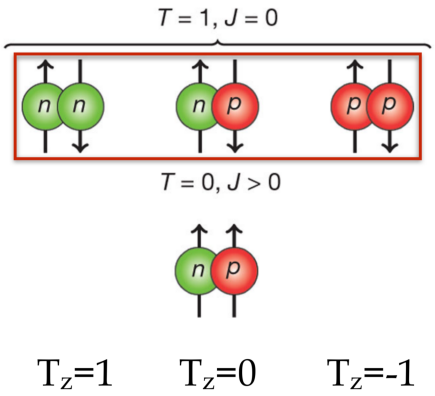

Figure 1.1: Possible couplings of a pair of nucleons.

particle systems, p-p and n-n, can exist only in the $T = 1$ state, since the isospin projection T_z is, respectively, -1 and 1. On the other hand the p-n system can exist in both $T = 1$ and $T = 0$ states. It is important to notice that the $T = 1$ state requires that the proton and the neutron have antiparallel spins, while in the $T = 0$ state the spins must be parallel as a consequence of the Pauli principle: since protons and neutrons are fermions, the total wavefunction must be antisymmetric on exchange of space, spin and isospin coordinates of two particles: $P_{12}\Psi = -\Psi$, where $P_{12} = P^r P^\sigma P^\tau$ is the exchange operator. This imposes the selection rule, for the nucleon-nucleon system, $(-1)^{L+S+T} = -1$. The $T = 0$ and $T = 1$ states represent two completely different configurations for the p-n system. The *deuteron*, the only bound two-nucleon system, corresponds to the $T = 0$ state, while the $T = 1$ state is unbound.

This feature can be easily extended to heavier systems, where, in general, the ground state of a nucleus is characterized by the lowest possible value of the isospin T: $T = |T_z|$ [1]. If we consider an isobaric quadruplet composed of nuclei with $T_z = \pm\frac{3}{2}, \pm\frac{1}{2}$, we have $T = \frac{3}{2}$ states in all the four nuclei, which constitute an isospin quadruplet. These states will be the ground states for the $T_z = \pm\frac{3}{2}$ members of the multiplet, while the $T_z = \pm\frac{1}{2}$ nuclei will have $T = \frac{1}{2}$ ground state.

States characterized by the same quantum numbers J and T, which differ only

[1] Noticeable exceptions are the N=Z odd–odd nuclei in the $f_{7/2}$ shell and ^{34}Cl, where the ground state has $T = 1$.

in T_z along an isospin multiplet, are called *Isobaric Analogue States (IAS)*[1].

The isospin symmetry can be tested in several ways and has many consequences in Nuclear Structure [3]. For example Fermi matrix elements in beta decay are different from zero only along isobaric multiplets. Moreover, $E\lambda$ and $M\lambda$ electromagnetic transitions are allowed only between states with $\Delta T = 0, \pm 1$, and $E1$ transitions between $\Delta T = 0$ states in $N = Z$ nuclei are forbidden and must have equal strength in mirror nuclei.

In this work we will present the results of two experiments aimed to test two different consequences of the Isospin Symmetry [3]:

- Mirror nuclei should have identical level schemes, except for small differences due to the electromagnetic interaction
- $E2$ transition matrix elements should have a linear dependence on T_z in an isobaric multiplet

These concepts and the way to study them are described in the following sections.

1.2 Physics of Mirror Nuclei

The binding energy of the ground states of nuclei can be expressed by the Bethe-Von Weizsäcker mass equation. Along an isobaric chain the binding energy assumes the well known parabolic form with respect to Z.

The ground states along an isobaric multiplet do not have, in general, the same isospin T. In other words, the ground states are not Isobaric Analogue States. The isospin symmetry implies that IAS should have the same binding energy. On the other hand the Coulomb interaction splits the degeneracy of these states, lowering the binding energy of a state in one nucleus with respect to the isobaric analogue state of a higher-Z member of the multiplet [1]. This binding energy difference between IAS along an isobaric multiplet is called *Coulomb Displacement Energy* (CDE). In Fig. 1.2 the binding energies of the ground states and the $T = \frac{3}{2}$ IAS along the A=21, $T = \frac{3}{2}$ isospin quadruplet are reported.

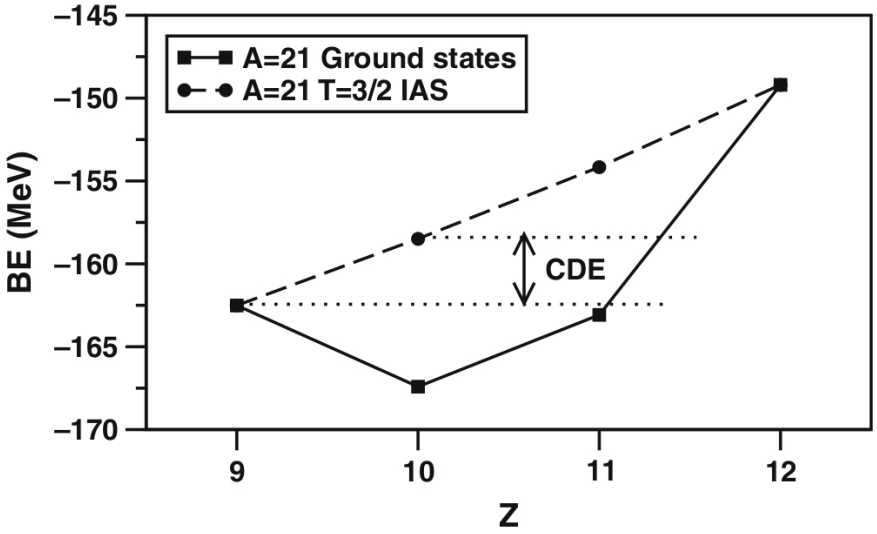

Figure 1.2: Ground state binding energies and CDE between $T = \frac{3}{2}$ states vs. proton number Z along the A=21, $T = \frac{3}{2}$ isospin quadruplet. Picture taken from [1].

The dependence of the binding energy of a set of IAS from the the proton number Z (or the third component of the isospin T_z) is given by the Isobaric Multiplet Mass Equation (IMME) proposed by E.P. Wigner in 1957 [4]. It can be expressed, considering only two-body interactions, as:

$$BE(\alpha, T, T_z) = a + bT_z + cT_z^2 \tag{1.3}$$

where α refers to the quantum numbers needed to fully define the state. It can be shown that the coefficients a, b and c depend only on T and not on T_z and, in particular, they are strictly related to the three tensor components of the interaction [1, 5]:

- the a coefficient depends on the isoscalar part of the interaction
- the b coefficient is related to the isovector contribution ($V_{pp} \neq V_{nn}$)
- the c coefficient takes into account the isotensor term ($2V_{pn} \neq (V_{nn} + V_{pp})$)

It is clear that the b and c coefficients can give information about the charge-symmetry and charge-independence of the nucleon-nucleon interaction.

The Coulomb Displacement Energy (CDE) between two members of a multiplet obtained by the exchange of p protons with neutrons is defined as:

$$CDE(T, T_z) = M_{T,T_z} - M_{T,T_z+p} + p\Delta_{nH} \tag{1.4}$$

with M the atomic mass, Δ_{nH} the neutron-hydrogen atomic mass difference and T_z the isospin projection for the larger-Z isobar.

The CDE can be immediately related to the coefficients of the IMME:

$$CDE(T, T_z) = -p(b + c[2T_z + p] - \Delta_{nH}) \tag{1.5}$$

Many theoretical works have been performed in the attempt to reproduce the CDE in a wide range of IAS. Nolen and Schiffer assumed that the charge-asymmetry comes only from the Coulomb interaction. An exchange term to take into account the Pauli principle and an electromagnetic spin-orbit term were included as well. However, the calculated CDE underestimate the experimental ones by 7%, corresponding to several hundreds of keV. This is the so called "Nolen-Schiffer anomaly"[6].

Many interpretations have been proposed, such as charge-asymmetric components in the nucleon-nucleon interaction [7, 8], or neutron skin effects [9]. However the full origin of the Coulomb Displacement Energy is not yet completely understood.

1.2.1 Energy Differences between excited IAS

By detecting the γ rays in the de-excitation of a nucleus we get information about the energy of the states with respect to the ground-state binding energy. Therefore, if we compare excitation energies between IAS, the bulk contribution of the CDE is by definition canceled out. This contribution comes from the bulk Coulomb energy and it is of the order of tens of MeV.

The differences in the excitation energies between excited IAS are called *Coulomb Energy Differences* (CED):

$$CED_{J,T} = E^*_{J,T,T_z} - E^*_{J,T,T_z+p} \tag{1.6}$$

The CED allow the study of the variation of the Coulomb and, more generally, all the charge-dependent contributions to the excitation energy of the states as a function of the angular momentum J and the excitation energy E. The measured CED are of the order of ∼100 keV or less and are very sensitive to several nuclear structure properties, as it will be discussed in the following sections [1].

Experimentally, the most accessible isospin multiplets are the $T = 1$ triplets and the $T = \frac{1}{2}$ doublets. The latter, composed of a pair of nuclei with interchanged numbers of protons and neutrons, are called *mirror nuclei*. In these particular cases the CED are called, respectively, Triplet Energy Differences (TED) and Mirror Energy Differences (MED):

$$TED_{J,T} = E^*_{J,T,T_z=-1} + E^*_{J,T,T_z=+1} - 2E^*_{J,T,T_z=0} = 2\Delta c_J \quad (1.7)$$

$$MED_{J,T} = E^*_{J,T,T_z=-T} - E^*_{J,T,T_z=T} = -\Delta b_J \quad (1.8)$$

where Δb_J and Δc_J are the variations of the IMME coefficients with increasing J with respect to the ground state. It is therefore clear that the MED give information about the charge-symmetry of the interaction (which is related to the isovector component) while the TED are sensitive to the charge-independence (and so to the isotensor term). In this work we will focus on the study of MED.

Under the assumption of charge-symmetry and charge-independence of the nuclear interaction, the MED should be only of electromagnetic origin. If such symmetries hold, it should be possible to fully describe the MED as effects of the different contributions of the Coulomb interaction, which we will describe in the following section.

1.2.2 Contributions to the MED

The electromagnetic force is the main isospin symmetry breaking interaction in nuclear matter, since it acts only between the charged protons and not between neutrons. Therefore, it is the main responsible for differences in excitation energy between analogue states in isobaric nuclei. Its contribution to the MED is usually divided in two parts: a multipole term, sensitive to the nucleon recoupling with

increasing angular momentum J, and a monopole term, which takes into account the variation of the radius with J and single-particle corrections [1, 10, 11].

1.2.2.1 The Coulomb multipole term

In Fig. 1.3 the average overlap of the wavefunctions of two like-particles in the $f_{\frac{7}{2}}$ shell as a function of the angular momentum J is reported.

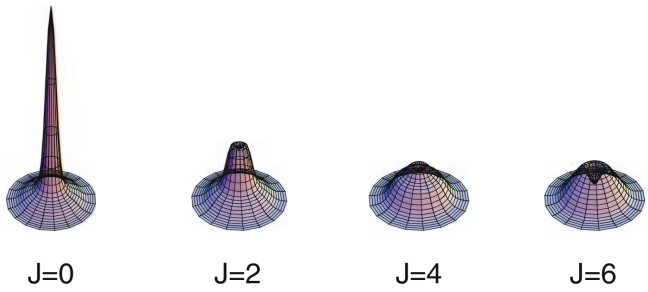

Figure 1.3: Average overlap of the wavefunctions of two like-particles in the $f_{\frac{7}{2}}$ shell as a function of the angular momentum J. Calculations from [12].

It is clear how, with increasing J, the average separation between the two particles increases and thus the spatial overlap between them decreases [12].

The alignment of nucleons has well known effects in the energy sequence along a rotational band; in particular, for a nucleus it can be energetically favorable to increase the angular momentum by recoupling a pair of nucleons to higher J values rather than increasing the rotational frequency. This causes a net deviation from the usual smooth trend in the spin vs. transition energy plot, a phenomenon called *backbending*. However, under the assumption of isospin symmetry, this energy deviation will be exactly the same in both mirror nuclei, and thus will not affect the MED.

On the other hand the Coulomb interaction acts only between protons; since it is repulsive, the decrease in the spatial overlap between two protons will cause a decrease in the excitation energy of the state. On the contrary, the alignment of a pair of neutrons occurs in the mirror partner without any Coulomb effect. Therefore the alignment of a neutron pair in the proton-rich nucleus will cause an increase in the MED, and viceversa.

As an example we report in Fig. 1.4 the experimental MED of the mirror nuclei ^{51}Fe $-^{51}$ Mn [13]. The configuration of these nuclei can be thought as an inert core of ^{40}Ca with 11 valence nucleons (6 protons and 5 neutrons in ^{51}Fe and viceversa in ^{51}Mn) which are located in the $f_{\frac{7}{2}}$ shell. The band termination is therefore reached at $J = \frac{27}{2}$.

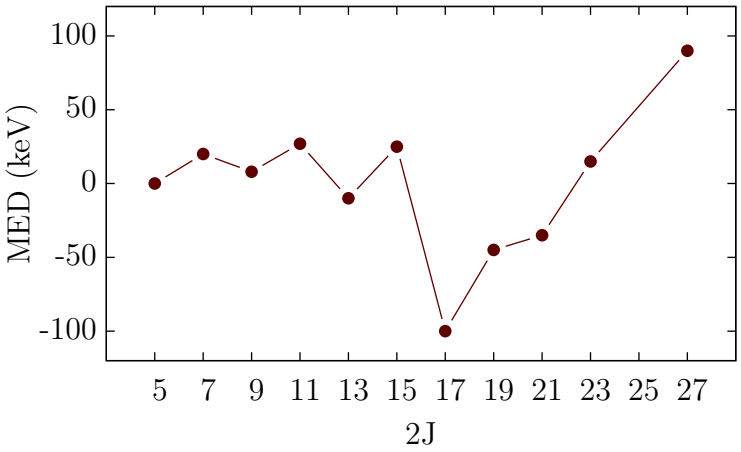

Figure 1.4: MED in mirror nuclei of A=51, ^{51}Fe $-^{51}$ Mn [13].

In ^{51}Fe, due to the blocking effect of the odd neutron, the first alignment will occur between a pair of protons to the highest possible value of angular momentum, $J = 6$. In the same way, in ^{51}Mn the alignment of a pair of neutrons occurs. This is reflected in the MED by the net decrease at $J = \frac{17}{2}$.

Since at $J = \frac{17}{2}$ the protons (neutrons) in ^{51}Fe (^{51}Mn) are fully aligned, larger spins can be reached only with a recoupling in the other fluid. The MED therefore increase towards the band termination at $J = \frac{27}{2}$.

The study of MED allows therefore to extract information about the change in the way the nucleus generates its angular momentum, from a collective rotational motion to a full (non collective) alignment of the angular momentum vectors of the valence nucleons.

1.2.2.2 The Coulomb monopole term

The monopole term is responsible to three different contributions to the mirror energy differences. In the following sections we will describe each of these

contributions.

Radial term

The monopole term takes into account the central component of the electromagnetic field in nuclei. Its contributions to the total energy can be described as the Coulomb energy of a uniformly charged sphere [11, 14]:

$$E_{C_m} = \frac{3}{5}\frac{Z(Z+1)e^2}{R}$$

Due to the difference in Z between the mirror nuclei we have:

$$\Delta E_{C_m} \approx \frac{3}{5}\frac{(2Z-1)e^2}{R}$$

This effect on the total binding energy amounts to tens of MeV, but if the radius R is the same for all the analog mirror states its contribution to the MED is null, since they are referred to the ground state.

The wavefunction configuration is however very dependent on the angular momentum J and the occupation numbers of different orbitals change dramatically with increasing spin and excitation energy. Since different orbitals have different radii, the overall nuclear radius varies as a function of J.

As an example we consider nuclei located in the middle of the $f_{\frac{7}{2}}$ shell, which are well deformed and manifest collective behavior at low spin. The quadrupole collectivity is due to the coupling between the $f_{\frac{7}{2}}$ and the $p_{\frac{3}{2}}$ orbits, which give therefore an important contribution to the wavefunction configuration. At higher spins the angular momentum is generated by aligning nucleons in the $f_{\frac{7}{2}}$ orbit, decreasing therefore the occupation of the $p_{\frac{3}{2}}$ orbit.

In this mass region p orbitals have larger radius than f orbitals, thus with increasing spin the radius of the nucleus decreases and the Coulomb energy increases. This happens in both mirror nuclei, but due to the different number of protons it will have a larger impact on the proton-rich member, affecting the MED [15].

The nuclear radius R is therefore a function of J and we can write the radial

contribution to the MED as:

$$\Delta V_{C_m}(J) = -\frac{3}{5}(2Z-1)e^2\frac{\Delta R(J)}{R^2(J=0)} \tag{1.9}$$

Single particle energy corrections

The quantitative description of the Coulomb term can be improved by introducing single particle energy corrections [6, 11]. The first one of them, called E_{ll}, modifies the energy of the proton orbits proportionally to the square of the orbital momentum l in the harmonic-oscillator representation and it is due to the truncation of the valence space adopted. It is expressed as:

$$E_{ll} = \frac{-4.5Z_{cs}^{13/12}[2l(l+1)-N(N+3)]}{A^{1/3}(N+\frac{3}{2})}\ \text{keV} \tag{1.10}$$

where Z_{cs} is the proton number in the underlying closed shell and N is the principal quantum number of the given shell.

Another important single particle energy correction is related to the electromagnetic spin-orbit force (EMSO) [6, 16], which results from the Larmor precession of the nucleons in the nuclear electric field due to their intrinsic magnetic moments and to the Thomas precession experienced by the protons because of their charge.[1] Its general expression is [6, 16]:

$$E_{ls} = (g_s - g_l)\frac{1}{2m_N^2c^2}\left(-\frac{Ze^2}{R_C^3}\right)\langle \mathbf{l}\cdot\mathbf{s}\rangle \tag{1.11}$$

where g_s and g_l are the gyromagnetic factors.

It is thus clear that the EMSO interaction acts differently on protons and neutrons and on configurations where the orbital angular momentum l and the spin quantum number s are parallel or antiparallel. Its contribution to the MED can be therefore relevant in particular configurations where a proton in one nucleus and a neutron in its mirror partner are excited from an orbit where l and s are anti-aligned to an orbit where they are aligned.

[1] The EMSO effect is nearly two orders of magnitude smaller than the nuclear spin orbit effect.

This is the case, for example, in the upper *sd* shell where, at high spin, excitations of nuclei from the $d_{\frac{3}{2}}$ to the $f_{\frac{7}{2}}$ orbital are important.

1.2.2.3 Isospin Symmetry Breaking Nuclear Term

If the only isospin symmetry-breaking interaction at play in the nuclear matter was the electromagnetic one, the experimental MED should be fully reproduced by the Coulomb terms described so far. A significant test can be done by considering the $J = 0, 2, 4, 6; T = 1$ states in the isobaric nuclei ^{42}Ti, ^{42}Sc, ^{42}Ca as outlined in [11, 1]. Since these nuclei present two particles above the double magic ^{40}Ca nucleus, it can be assumed that their configuration is $f^2_{7/2}$ and a two body effective interaction in this shell can be obtained. As we saw in Eq. (1.7) the TED and the MED account for the isotensor and isovector components of the effective interaction, respectively. We can therefore write the following expressions:

$$MED_J(A = 42, T = 1) = V^{(1)}_{CM,f_{\frac{7}{2}}}(J) + V^{(1)}_{B,f_{\frac{7}{2}}}(J) \quad (1.12)$$

$$TED_J(A = 42, T = 1) = V^{(2)}_{CM,f_{\frac{7}{2}}}(J) + V^{(2)}_{B,f_{\frac{7}{2}}}(J) \quad (1.13)$$

where $V^{(1,2)}_{CM,f_{\frac{7}{2}}}(J)$ denotes the Coulomb contribution and $V^{(1,2)}_{B,f_{\frac{7}{2}}}(J)$ describes a possible additional isospin non conserving term. Deformation and single particle effects can be safely neglected for these states and the V_{CM} terms can therefore be expressed only by the multipole term calculated for two protons in the $f^2_{7/2}$ shell in the harmonic oscillator basis. The contribution of the isospin symmetry breaking term V_B can be obtained from the difference between the experimental MED and the V_{CM} terms, and is reported in Tab. 1.1.

The ISB terms V_B are not negligible as should be expected from isospin symmetry. On the contrary, they result to be of the same order of magnitude of the Coulomb terms and therefore can not be neglected in the calculations of the MED. The main contribution is obtained at $J = 0$ for the isotensor term and at $J = 2$ for the isovector component. The origin of this term is still unknown, and it was considered to be of nuclear nature in [11]. In order to include it in shell model calculations, an extension to the whole fp shell has to be found. The

	J=0	J=2	J=4	J=6
$V_{CM,f_{\frac{7}{2}}}$	83	25	-6	-12
$V^{(1)}_{B,f_{\frac{7}{2}}} = MED_{exp} - V_{CM,f_{\frac{7}{2}}}$	5	**93**	17	-48
$V^{(2)}_{B,f_{\frac{7}{2}}} = TED_{exp} - V_{CM,f_{\frac{7}{2}}}$	**117**	81	3	-43

Table 1.1: $f_{7/2}$ Coulomb and isospin non conserving matrix elements deduced from experimental data in A=42. Taken from [1].

prescription described in [11] consists in the use of a schematic ISB interaction where all the matrix elements are null except those relative to two nucleons in the $f_{\frac{7}{2}}$ shell. The strength of these matrix elements is determined by the findings of Tab. 1.1 and therefore nucleons coupled to $J = 0$ and $J = 2$ are considered for the isotensor and isovector contribution respectively. The V_B terms can be expressed as:

$$V^{(1)}_{B,fp} = \beta_1 V_{B,f_{\frac{7}{2}}}(J = 2) \tag{1.14}$$

$$V^{(2)}_{B,fp} = \beta_1 V_{B,f_{\frac{7}{2}}}(J = 0) \tag{1.15}$$

where the scaling constant β_1 and β_2 are of the order of ~ 100 keV. This procedure has proven to be very successful in the description of MED and TED in the whole $f_{\frac{7}{2}}$ shell; a review can be found in [1]. On the other hand, it has been suggested in a recent work by Bentley et al. [17] that the experimental data on the MED can be reproduced either by a positive value of β_1 for two nucleons coupled to $J = 2$ or by a similar negative value for a $J = 0$ coupling, suggesting that the MED are sensitive to the relative contributions at different J and not to absolute values. These studies must be extended to other mass regions, such as the *sd* shell, where the $J = 2$ coupling is obviously restricted to the $d_{3/2}$ and $d_{5/2}$ shells, while the $J = 0$ one can occur also in the $s_{1/2}$ orbit. The experimental information in this region is however scarce, and a systematic study of MED and TED is not yet possible. This is indeed one of the reasons which motivated this work.

1.3 Isospin Mixing

As reported in Sec. 1.1, excited states of nuclei with $T_z = N - Z$ can have only $T > T_z$. This general feature of nuclear systems is schematically drawn in Fig. 1.5 where the allowed and forbidden states are illustrated.

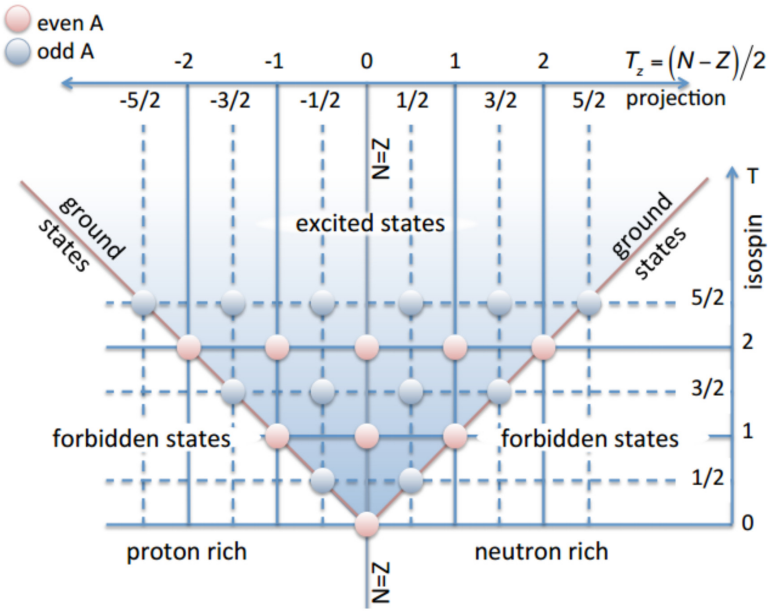

Figure 1.5: Forbidden and allowed isospin states for nuclei along the $N \sim Z$ line [18].

Generally the ground state of a nucleus has the lowest possible value of isospin $T = T_z$, while higher T states are much higher in energy. One exception to this general trend are a number of odd-odd nuclei, where isovector correlations are so strong that $T = 1$ states are much lower in energy, eventually becoming the ground states. Due to the small difference in excitation energy, mixing between $T = 0$ and $T = 1$ states with same spin and parity is expected to be sizeable in these nuclei. This mixing is caused by any isospin non-conserving (INC) interaction, such as the Coulomb force or any INC nuclear term, and is of the order of few percent. Being a hint of isospin symmetry breaking, the degree of isospin mixing can be experimentally studied by measuring the violation of the selection rules imposed by the isospin symmetry. In the next section we will focus

on the consequences of pure isospin symmetry on the electromagnetic transitions selection rules.

1.3.1 Electromagnetic transitions selection rules

The Hamiltonian of the electromagnetic interaction can be divided in two terms [19, 20]:

$$\hat{H} = \sum_k \hat{H}^{(k)} = \hat{H}^{(0)} + \hat{H}^{(1)} \tag{1.16}$$

where $\hat{H}^{(0)}$ refers to the isoscalar component while $\hat{H}^{(1)}$ is the isovector term, which acts on the third component of the isospin, T_z. Assuming isospin symmetry, an eigenstate of the system can be described as $|\alpha; T, T_z\rangle$, where T and T_z are the isospin quantum number and its third projection and α takes into account any other quantum number needed to fully characterize the state. The application of the Wigner-Eckhart theorem allows to express the matrix element as [19, 20]:

$$\begin{aligned}
&\langle \alpha; T^f, T_z^f | \sum_k \hat{H}^{(k)} | \alpha'; T^i, T_z^i \rangle = \\
&= \langle \alpha; T^f, T_z^f | \hat{H}^{(0)} + \hat{H}^{(1)} | \alpha'; T^i, T_z^i \rangle = \\
&= (-1)^{T^f - T_z^f} \begin{pmatrix} T^f & 0 & T^i \\ -T_z^f & 0 & T_z^i \end{pmatrix} \langle \alpha; T^f || \hat{H}^{(0)} || \alpha'; T^i \rangle + \qquad (1.17) \\
&+ (-1)^{T^f - T_z^f} \begin{pmatrix} T^f & 1 & T^i \\ -T_z^f & 0 & T_z^i \end{pmatrix} \langle \alpha; T^f || \hat{H}^{(1)} || \alpha'; T^i \rangle \qquad (1.18)
\end{aligned}$$

where the dependence on T_z is taken into account by the Wigner 3j-coefficients, while the reduced matrix elements are independent from it. In a electromagnetic transition inside a nucleus, the third component of the isospin T_z is obviously conserved, implying $T_Z^i = T_Z^f = T_z$.

Focusing on the isoscalar term (1.17) we can write the 3j-coefficients as [19, 20]:

$$(-1)^{T^f - T_z} \begin{pmatrix} T^f & 0 & T^i \\ -T_z & 0 & T_z \end{pmatrix} = \frac{1}{\sqrt{2T^i + 1}} \delta_{T^i T^f} \tag{1.19}$$

which translates in the following expression for the matrix elements:

$$\langle \alpha; T^f || \hat{H}^{(0)} || \alpha'; T^i \rangle = (\sqrt{2T^i + 1}) \langle \alpha; T^f, T_z | \hat{H}^{(0)} | \alpha'; T^i, T_z \rangle \delta_{T^i T^f} \tag{1.20}$$

thus isoscalar matrix elements vanish except for $T \to T$ transitions.
For the isovector term the 3j-coefficients give:

$$(-1)^{T^f - T_z} \begin{pmatrix} T^f & 1 & T^i \\ -T_z & 0 & T_z \end{pmatrix} = (-1)^{T^f - T_i} \sqrt{\frac{T_>^2 - T_z^2}{T_>(2T_> - 1)(2T_> + 1)}} \tag{1.21}$$

where $T_>$=max(T^i, T^f). This expression is simplified, for $T^i = T^f = T$, to:

$$\begin{pmatrix} T & 1 & T \\ -T_z & 0 & T_z \end{pmatrix} = (-1)^{T - T_z} \frac{T_z}{\sqrt{T(T+1)(2T+1)}} \tag{1.22}$$

As a consequence, analogue transitions with $\Delta T = \pm 1$ have the same strength in mirror nuclei. This is not the case in $\Delta T = 0$ transitions due to the non-vanishing isoscalar contribution. This approach can be applied, in particular, to electric transitions. In a shell model framework, the dipole and quadrupole operators can be divided in their isoscalar and isovector components as [21]:

$$\hat{T}_\mu(E1) = \sum_{k=1}^{A} e_k r_\mu(k) = \frac{e}{2} \left(\sum_{k=1}^{A} r_\mu(k) + 2 \sum_{k=1}^{A} \hat{t}_z(k) r_\mu(k) \right) \tag{1.23}$$

$$\hat{T}_\mu(E2) = \sum_{k=1}^{A} e_k r_\mu^2(k) = \frac{e_\nu + e_\pi}{2} \hat{T}_\mu^{\,(0)}(E2) + \frac{e_\nu - e_\pi}{2} \hat{T}_\mu^{\,(1)}(E2) \tag{1.24}$$

where e_ν and e_π are the neutron and proton effective charges, respectively. It is possible to demonstrate [19, 20] that, in the long wavelength limit, the E1 operator has a purely isovector character. This leads naturally to two important selection rules:

- Analogue E1 transitions in mirror nuclei must have the same strength
- $\Delta T = 0$ E1 transitions in self-conjugate nuclei are forbidden

On the other hand the quadrupole electric operator has both the isoscalar and isovector terms. Therefore, for $\Delta T = 0$ transitions, it follows from 1.19 and 1.22

$$\begin{aligned}
&\langle \alpha; T, T_z | \hat{T}_\mu^{(0)}(E2) + \hat{T}_\mu^{(1)}(E2) | \alpha'; T, T_z \rangle = \\
&= \frac{1}{\sqrt{2T+1}} \langle \alpha; T || \hat{T}_\mu^{(0)}(E2) || \alpha'; T \rangle + \\
&+ \frac{T_z}{\sqrt{T(T+1)(2T+1)}} \langle \alpha; T || \hat{T}_\mu^{(1)}(E2) || \alpha'; T \rangle
\end{aligned} \tag{1.25}$$

which immediately brings to the relation we aim to test in this work:

- Electric quadrupole matrix elements between $\Delta T = 0$ states are linear in T_z within an isobaric multiplet

The selection rules derived in this Chapter are exactly valid only under the assumption of isospin symmetry. The Coulomb interaction obviously brakes this symmetry and can induce mixing between states with different isospin quantum number. The electromagnetic interaction can be considered as a small perturbation with respect to the dominant nuclear force and, therefore, the selection rules are still approximately valid. However the small isospin admixtures that it causes can allow transitions otherwise forbidden or induce violations to the relations previously derived.

Let us consider a $T = 1$ state mixed with a $T = 0$ state described by:

$$|\psi\rangle = \delta |\psi; T = 1\rangle + \gamma |\psi; T = 0\rangle \tag{1.26}$$

where ψ comprises all the quantum numbers which fully describe the state and γ and δ are the amplitudes of the different components, which satisfy $\gamma^2 + \delta^2 = 1$. Introducing the raising and lowering operators:

$$T_+ = T_1 + iT_2 \tag{1.27}$$

$$T_- = T_1 - iT_2 \tag{1.28}$$

the mixing probability is given by:

$$\gamma^2 = \frac{1}{2}\langle\psi|T_- T_+|\psi\rangle \tag{1.29}$$

Therefore, for example:

- Electric dipole transitions between two states $|\phi\rangle$ and $|\psi\rangle$ are allowed between the $T = 0$ component of $|\phi\rangle$ and the $T = 1$ component of $|\psi\rangle$, and vice versa.
- Isospin mixing between T and $T + 1$ states can add additional isovector terms to the quadrupole electromagnetic operator, resulting in a deviation from the linear trend.

From 1.21 and 1.22 we have the following relations:

$$\begin{aligned}&\langle\alpha; T+1, T_z|\hat{T}_\mu^{(1)}(E2)|\alpha'; T, T_z\rangle = \\ &= \sqrt{\frac{(T+T_z+1)(T-T_z+1)}{(2T+3)(T+1)(2T+1)}}\langle\alpha; T+1||\hat{T}_\mu^{(1)}(E2)||\alpha'; T\rangle\end{aligned} \tag{1.30}$$

$$\begin{aligned}&\langle\alpha; T, T_z|\hat{T}_\mu^{(1)}(E2)|\alpha'; T+1, T_z\rangle = \\ &= \sqrt{\frac{(T+T_z+1)(T-T_z+1)}{(2T+3)(T+1)(2T+1)}}\langle\alpha; T||\hat{T}_\mu^{(1)}(E2)||\alpha'; T+1\rangle\end{aligned} \tag{1.31}$$

Since the Coulomb interaction is a small perturbation of the nuclear force, $\gamma \ll \delta$ and the possible mixing amounts to few %. Thus the overall matrix element will be given by a combination of (1.25), (1.30) and (1.31) and the deviation from the linear trend (1.25) gives information on the degree of mixing.

It is important to stress that isospin mixing can occur only in the $T_z = 0$, $N = Z$ member of a isobaric multiplet, where $T = 0$ and $T = 1$ states can coexist at similar excitation energy.

As already stated, the two experiments described in this thesis intend to test the consequences of the Isospin Symmetry Breaking presented in this Section:

Mirror Energy Differences and Isospin Mixing. We will present the experiments in the following chapters.

Chapter 2

MED in mirror nuclei ^{23}Mg $-^{23}$ Na

As already pointed out in Chapter 1, the study of mirror energy differences (MED) has allowed to obtain very important results in the $f_{7/2}$ shell, where mirror nuclei have been extensively studied, both from the experimental and the theoretical side. Nuclei near the middle of the shell present rotational bands and the energy differences between isobaric states in mirror nuclei constitute a very delicate probe of the nuclear structure. As already shown, the MED are sensitive to the way the nucleons align in order to increase the nuclear angular momentum and to the evolution of the nuclear radius along the *yrast* band. Moreover, the role of any other isospin non conserving force can be tested via the analysis of the MED. The extension of these investigations to other mass regions is therefore very important to check the limits of validity of the isospin symmetry for different masses, to look for possible INC contributions, such as those identified in the $f_{7/2}$ shell, and to search for other isospin breaking effects.

The important information contained in the MED can be extracted if a proper theoretical description of the data is achieved. What we have learned from the systematic studies in the $f_{7/2}$ shell relies on the good amount of experimental data and the excellent shell model description of the structure of these nuclei [1]. A mass region where the shell model reproduces with good accuracy the experimental data is the lower *sd* shell. Here, rotational bands have been observed in

nuclei in the mass region A=20-24. In particular, ^{20}Ne and ^{24}Mg present rotational ground-state bands. This mass region was studied extensively in the 70's and has been revisited in the last decades by means of fusion-evaporation reactions using large γ arrays. The mirror pair A=21 was studied at Legnaro with the GASP array up to the $11/2^+$ state [22]. The heavier A=23, T=1/2 mirror pair, presents a ground state band and excited rotational bands. Pioneer studies conducted via transfer reactions in the 70's proposed the presence of high spin states up to 14 MeV in ^{23}Mg but most of the spins of the high lying states were not firmly assigned. On the other hand, in the neutron-rich partner ^{23}Na, states above $11/2^+$ were uncertain. The aim of the experiment presented in this thesis is therefore to combine the large population at high spin given by fusion evaporation reactions with the high capabilities of large γ array coupled to charged-particle and neutron detectors to extend the level schemes of the A=23, T=1/2 mirror pair up to high spin states, allowing a detailed study of the MED as a function of the angular momentum J.

In the first part of this chapter the experimental information available at the time of the present experiment is presented. In the following sections the basic concepts of fusion evaporation reactions and the details of the experiment are described. Afterwards, in sections 2.5 and 2.7, the steps of the data analysis and the experimental results are shown. Finally, the data are interpreted and compared to shell model calculations in 2.9.

2.1 Previous studies on ^{23}Mg-^{23}Na

The structure of ^{23}Mg and ^{23}Na nuclei has been studied with different reactions and techniques in the past years. Most of the experiments were performed with the ^{12}C+^{12}C fusion evaporation reaction [23, 24, 25, 26, 27] and measuring proton-γ and neutron-γ coincidences. Particle spectroscopy studies in ^{23}Na were also conducted using the ^{19}F(^{6}Li,d)^{23}Na [28], ^{12}C(^{15}N,α)^{23}Na [29, 30, 27] and ^{11}B(^{16}O,α)^{23}Na [31].

Prior to the experiment described in this work, the available spectroscopic information was limited to states of low spin, since the fusion evaporation measurements were performed mainly in the 70's when the selectivity of the available

setups did not allow the observation of states populated with such small cross sections, while the transfer mechanism does not favour the population of high spin states. In the proton-rich partner, ^{23}Mg, high spin states were resonantly populated up to 14 MeV excitation energy [23] but most of the spins of the high lying states had not been firmly assigned. On the other hand, the neutron-rich partner, ^{23}Na, was well known at low spin but states above $11/2^+$ were assigned only tentatively. We report in Fig. 2.1 the proposed rotational bands in ^{23}Na known at the time of this experiment from the work of Gomez del Campo *et al.* [31].

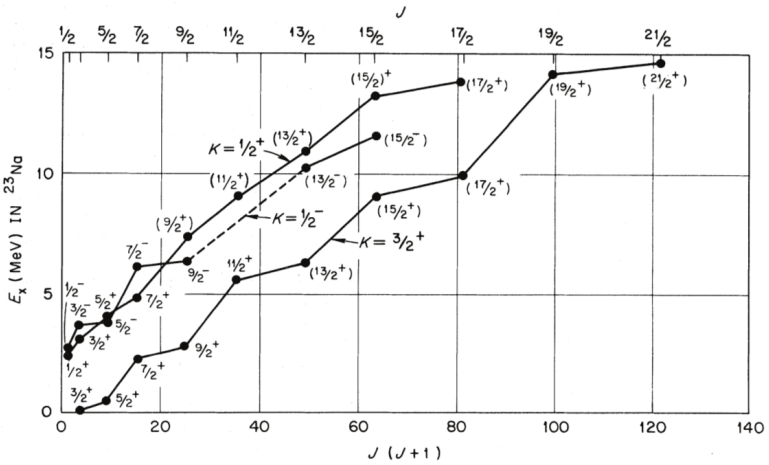

Figure 2.1: Proposed rotational bands in ^{23}Na from Ref. [31].

The extension of the scarce information available at high spin at the time was the main motivation of the experiment subject of this work.

After performing this experiment, the results of another experiment on the A=23 mirror nuclei were published by Jenkins *et al.* [32]. The ^{12}C+^{12}C fusion evaporation reaction was studied at the Argonne National Laboratory with the Gammasphere array [33]. The level schemes of ^{23}Na and ^{23}Mg were extended up to $J = 17/2^+$ and $J = 13/2^+$ respectively.

Although it is not related to the main topic of this thesis, it is important to notice that the study of light mirror nuclei is particularly interesting from an astrophysical point of view, since it helps to constrain the rates for proton capture reactions in the *rp* process. Information on states relevant for these reactions in

unstable nuclei can be inferred from fusion evaporation reactions studied with large γ arrays. In particular, rates for the ^{22}Na(p,γ)^{23}Mg reaction were obtained by studying relevant states in ^{23}Mg populated in the ^{12}C(^{12}C,n) reaction [34]. The comparison with the analogue states in ^{23}Na was crucial.

The astrophysical proton capture reactions populate mainly low spin, non *yrast* states. The relevant levels are therefore in general weakly populated in symmetric fusion evaporation reactions where the de-excitation of the nucleus proceeds mostly along the *yrast* line. In the experiment subject of this thesis the nuclei of interest were populated via the evaporation of an α particle and a proton or a neutron, as we will see in the next sections. This favors the population of the residual nuclei at high spin.

2.2 Fusion Evaporation reactions

Fusion evaporation reactions are the ideal tool to populate nuclei at high spin and high excitation energy. In this kind of reaction a projectile and a target nuclei fuse together, forming an intermediate highly excited system, named *compound nucleus*. Calling E_p and m_p the energy and the mass of the projectile, and m_t and M_{CN} the masses of the target and compound nuclei, the excitation energy of the compound is given by:

$$E^*_{CN} = Q + E_p \left(1 - \frac{m_p}{m_p + m_t}\right)$$

where Q is the reaction Q-value defined as the difference between the initial and final masses:

$$Q = \left(\sum_i m_i - \sum_f m_f\right) = (m_b + m_t - m_{CN})\, c^2$$

A scheme of the fusion evaporation reaction process is reported in Fig. 2.2.

The compound nucleus is a highly excited rotating object which acts to reduce its energy. This happens in two steps:

- *Light Particle emission*: in the first step of the de-excitation the compound nucleus evaporates light particles, like alphas, protons and neutrons, with

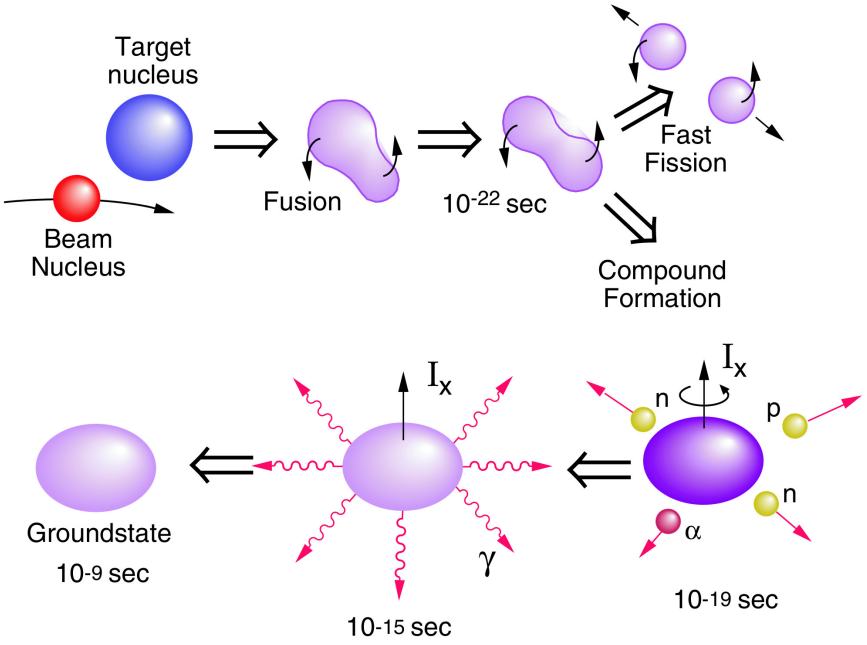

Figure 2.2: Fusion Evaporation reaction mechanism. Taken from [35].

an isotropic distribution in the center of mass frame and with a thermal energy spectrum[1]. The neutron emission is generally faster than the charged particles one, since it is not affected by the Coulomb barrier. Each evaporated particle lowers the excitation energy of the compound nucleus by about $\sim 5-8$ MeV, carrying away only few units of angular momentum. This process generally continues until the excitation energy of the compound becomes comparable or lower than the particle separation energy. In this situation the γ-ray emission becomes favorable with respect to particle emission, and the de-excitation proceeds through a second step.

- *γ-ray emission*: after the particle emission, the residual nucleus is in an high angular momentum J state, while its excitation energy is comparable to the particle separation energy. At this stage the de-excitation continues via γ-ray emission. At high excitation energy the density level is high, thus

[1]The emitted particles angular distribution will obviously not be isotropic in the laboratory frame. Due to the motion of the compound nucleus it will be peaked at forward angles, following the center-of-mass velocity: $v_{cm} = \frac{m_b}{(m_b+m_t)}\sqrt{\frac{2E_b}{m_b}}$

many decay paths are possible. When the nucleus de-excites to lower energy values, the spacing between levels becomes wider and the decay proceeds via discrete transitions between *yrast* states.

The moment of inertia $\mathscr{I}$ of two masses m_1 and m_2 rotating around the center of mass is given by

$$\mathscr{I} = \frac{m_1 m_2 d^2}{m_1 + m_2}$$

where d is the distance between the centers of the bodies; therefore a mass-symmetric beam-target combination will give a higher moment of inertia $\mathscr{I}$ for the compound nucleus which translates in a stronger population of high spin *yrast* states. Viceversa a strongly asymmetric beam-target combination favors the population of *non-yrast* states.

2.3 The experiment

The present experiment was performed at GANIL (Grand Accélérateur National d'Ions Lourds), France. The symmetric fusion evaporation reaction ^{16}O + ^{12}C was used. The oxygen beam was delivered by the CIME (Cyclotron pour Ions de Moyenne Energie, or Cyclotron for Ions of Medium Energy) accelerator, which provided a pulsed beam with a radio frequency of 11.257 MHz, which translates in a period $T = 88.8$ ns. This gives a time reference for the whole system, which is particularly important for the n-γ discrimination in the neutron detector array Neutron Wall, as we will describe in detail in Sec. 2.5.5.

In the first part of the experiment, an energy of 60 MeV has been used for the oxygen beam, while in the second part the energy was increased to 70 MeV to favor the population of high spin states. Data were recorded to disk for a total amount of ∼24 hours for each energy. The beam current was kept between 2 and 5 pnA during the experiment.

Two ^{12}C targets have been used, the thickness of which was 170 and 300 μg/cm^2, implying that the γ rays emitted in the de-excitation of the recoil nuclei were emitted in flight. The chosen target thickness assured a optimal compromise between a high integrated cross section and a sufficiently small Doppler

broadening due to the slowing down of the recoils inside the target material.

The reaction chosen for this experiment allows to populate different nuclei in the lower *sd* shell; in Fig. 3.10 we report the most intense reaction channels, with the relative population cross section given by the code HIVAP [36].

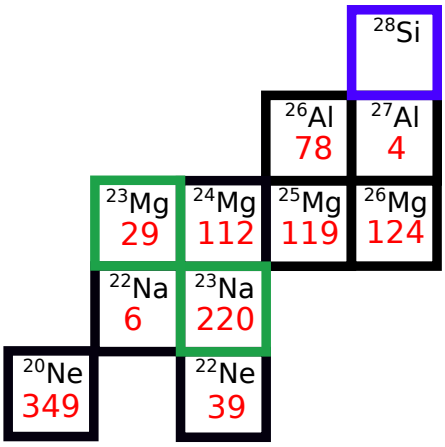

Figure 2.3: Predicted cross sections for the reaction ^{16}O + ^{12}C at 60 MeV (red numbers, in mb) for the different channels produced after particle evaporation, obtained with the HIVAP code [36]. Only the most intense channels are reported. The nuclei of interest are highlighted in green.

2.4 The Experimental Setup

The experimental study of high spin states in nuclei located along the $N \sim Z$ line in the *sd* shell is particularly challenging due to the low production cross sections at high angular momentum and to the great number of competing channels produced in the reaction. In order to cleanly select the reaction channel and to identify the γ rays emitted in the de-excitation of the nuclei of interest, we need a detection system with the following properties:

- *Large γ efficiency*: high spin states are weakly populated in fusion evaporation reactions and $\gamma - \gamma$ coincidences are needed in order to firmly reconstruct the level schemes up to high values of angular momentum.

- *Good energy resolution*: nuclei which lie in the same mass region are often characterized by similar structure properties, which translate in similar level schemes and transition energies; this is particularly true in mirror nuclei, where the analogue transitions can differ by only few keV. A good resolving power is therefore needed to disentangle between different transitions and to cleanly separate peaks relative to different nuclei and levels. This condition is greatly fulfilled by using HPGe detectors.

- *Charged particle discrimination*: in the lower part of the *sd* shell the Coulomb barrier is rather low and nuclei evaporate charged particles with high probability. It is therefore absolutely essential to discriminate between α particles and protons.

- *Sensitivity to charged particle emission direction*: momentum conservation implies that, when a charged particle is evaporated, the residual nucleus deviates from the beam direction affecting the Doppler broadening of the peaks since the angle between the recoil ion and the γ ray is unknown. This effect is more significative in light nuclei where the mass of the residual nucleus is comparable with the one of the evaporated particles. A kinematical reconstruction of the ion trajectory can be performed if the charged particle emission direction is determined.

- *Large neutron detection efficiency*: proton rich nuclei along the $N \sim Z$ line are populated in fusion evaporation reactions by the emission of neutrons. Since this process moves the residual nucleus farther from the valley of stability, its cross section is much lower than the one relative to the evaporation of protons. This implies that the tagging on charged particles is not sufficient to cleanly select reaction channels which populate proton rich nuclei, since the γ spectrum will be dominated by other more intense channels. The possibility of tagging on neutrons is therefore crucial to firmly assign a given transition to a proton-rich nucleus.

The requirements reported above were greatly fulfilled by the experimental setup available in GANIL, composed of the γ-ray spectrometer EXOGAM [37, 38], the charged-particle detector array DIAMANT [39, 40] and the neutron detector

array Neutron Wall [41]. In the next sections we will describe in detail this detection system.

2.4.1 EXOGAM

The γ rays emitted in the reaction were detected using the γ-ray spectrometer EXOGAM [37, 38] which consists of an array of segmented HPGe detectors. Four co-axial n-type Ge crystals are arranged in the configuration of a four leaf clover and placed in the same cryostat. The individual crystals for each EXOGAM Clover are 60 mm diameter and 90 mm long before shaping. The detection efficiency can be significantly increased by adding together the signals corresponding to scattered events between adjacent crystals (the so called addback procedure). As depicted in Fig. 2.4, each of the individual crystals of a Clover is electronically segmented into four parts; this reduces the opening angle by a factor of two with respect to the full detector allowing a better determination of the interaction point of the γ ray within the crystal. Since the uncertainty on the interaction position is one of the major contributions to the Doppler broadening of the photopeak, the use of segmented crystals allows to improve significantly the Doppler correction for γ rays emitted in flight. Each detector has 5 outputs, 4 from the different segments and 1 from the central contact. The energy resolution obtainable from the segment signals is worse than the core one, therefore the former are used for the determination of the first interaction point, while the latter for the energy measurement.

Anti Compton shields

Each EXOGAM clover is surrounded by a Compton-suppression shield. These shields are composed of a back catcher, a rear side element and a side shield, as sketched in Fig. 2.5. To maximize the solid angle coverage with Ge material, the side elements have to be as thin as possible. To obtain a high detection efficiency it is therefore necessary to use high Z material; BGO is the natural choice. The back catcher prevents forward scattered γ rays from escaping through the large solid angle situated behind the Clover. At this forward direction the Compton scattered γ rays have the highest possible energy so a larger thickness of material

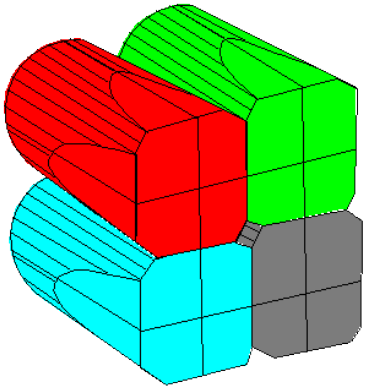

Figure 2.4: The segmented Clover germanium detector crystals. Taken from [42].

is required to obtain a good detection efficiency. Behind the crystals the available space is enough to use larger Compton suppression shields with lower stopping power, which give the same suppression at a much lower cost. The back catcher is therefore made by CsI(Tl) scintillators.

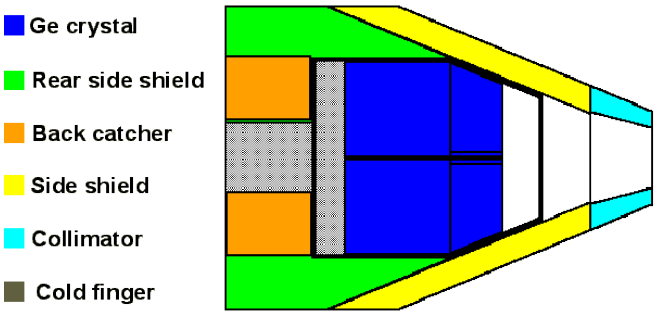

Figure 2.5: The different elements of the Compton suppression shield for the segmented CLOVER Ge detectors (not to scale) [37, 42].

Each part of the Compton suppression shield comprises several BGO / CsI(Tl) crystals. The outputs from the PMTs are coupled together such that 4 signals are sent to the electronics. A heavy metal collimator is needed for each clover to avoid that direct radiation coming from the target reaches the suppression shield. Two types of time information are available for the Compton suppression. In the

first one the start is given by any of the 4 HPGe detectors in the Clover, and the stop by any of the elements of the anti Compton shield. In the second one the information is restricted to each single germanium detector: the crystal gives the start, the adjacent Compton-suppression shield gives the stop. In the offline analysis the second type of information is used.

In the present experiment 10 EXOGAM Clovers were present; 7 were placed at 90° and 3 at 135° with respect to the beam direction. The distance from the target to the front of each Clover was 14.7 cm.

2.4.2 DIAMANT

The detection and the identification of the particles evaporated in the reaction are needed to cleanly select the channel of interest. Moreover, this allows to reduce the Doppler broadening of the peaks in γ-ray spectra performing a kinematical reconstruction of the trajectory of the residual nuclei. The required properties of a charged particle detector can be summarized as:

- good detection efficiency, which is strictly related to geometrical coverage as close as possible to 4π.
- good discrimination between different types of particles (in particular protons and α particles);
- high granularity, in order to minimize the probability of pile up and to limit the counting rate in the individual detectors, in particular in the forward direction where the kinematics of the reaction focuses the majority of the evaporated particles. This allows also to reduce the uncertainty on the angle of emission of the charged particles, improving the kinematical reconstruction.
- transparency to γ rays.

In the present experiment we used the charged particle detector DIAMANT [39, 40], a 4π array consisting of 80 CsI(Tl) 3 mm scintillators coupled to PIN-photodiodes. CsI(Tl) scintillation crystals are widely used for charged particle discrimination since their scintillation light is characterized by a fast and a slow

components, the amplitude ratio of which, as well as the decay time constant of the fast component, depends on the type of incident particle. Therefore the shape of the signal is different for α particles and protons, allowing a clear discrimination between them. The detectors are arranged in a polyhedron compact geometry consisting of square and triangular shaped detectors which allows to cover $\sim 90\%$ of the 4π solid angle. The detectors are placed at a distance of 3 cm from the target, inside the reaction chamber. The nominal detection efficiency amounts to 70% for protons and 50% for α particles, while the energy resolution at 5.5 MeV is $\sim$2%. The electronics is based on VXI cards [40], which provide as output three variables: energy, time and a particle identification parameter (PID). The PID is obtained from the pulse shape analysis by means of the ballistic deficit method [43, 44]. The CsI detectors are shielded from elastically scattered beam ions and δ electrons produced when the beam hits the target by means of tantalum absorber foils, the thickness of which was optimized for each angle. A schematic view of the DIAMANT detector is reported in Fig. 2.6.

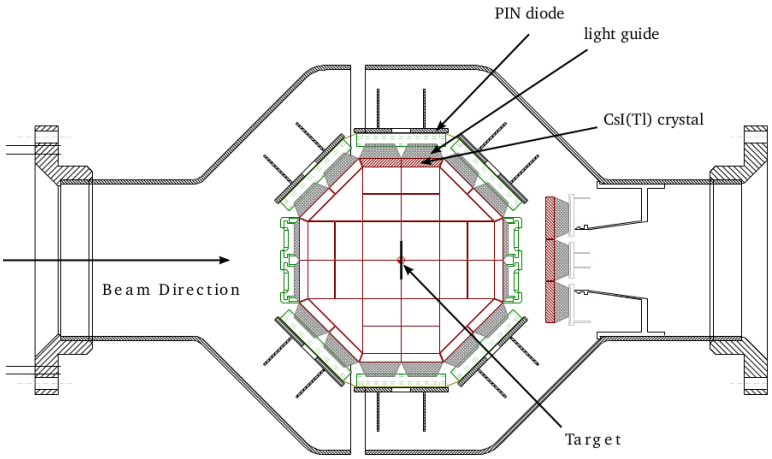

Figure 2.6: Schematic view of the light charged particle detector DIAMANT. Taken from [45].

We summarized in Tab. 2.1 the main properties of the DIAMANT light charged-particle detector.

Number of CsI detectors	80
Solid Angle Coverage	90%
Energy resolution at 5.5 MeV	2%
Nominal α detection efficiency	50%
Nominal proton detection efficiency	70%

Table 2.1: Main properties of DIAMANT.

2.4.3 Neutron Wall

The detection of the neutrons evaporated by the compound nucleus is crucial in the spectroscopy of the proton-rich nuclei along the $N \sim Z$ line, which are populated in reaction channels with extremely low cross sections. In the present experiment the neutrons were detected by the Neutron Wall array [41], composed of 50 BC501A liquid scintillators arranged in 16 detector modules in hexagonal and pentagonal geometrical configurations. The solid angle coverage is $\sim 1\pi$, placed in the forward direction, where the majority of the evaporated neutrons are focused by the kinematics of the reaction. The detectors thickness is 15 cm and the distance from the target amounts to 50 cm. A schematic drawing of the array is reported in Fig. 2.7.

The neutron detection technique based on liquid scintillators exploits the scattering of neutrons by light nuclei such as hydrogen. When a neutron scatters on a H ion the energy of the recoiling proton is absorbed by the molecules of the scintillator. In the subsequent de-excitation, the molecules of the liquid scintillator emit light characterized by two components, a fast one due to fluorescence (with a characteristic decay time of $\tau \sim 1$ ns) and a slower one due to delayed fluorescence (with $\tau \sim 100$ ns). The resulting pulse shape is different according to the type and the energy of the incident particle. This allows the discrimination between neutrons and γ rays. The light output is collected by a photo-multiplier (PMT) which converts it into an electric signal. The front-end electronics has two inputs for each detector: the PMT anode and an external time-reference signal. The measured variables for each individual detector are the zero-cross over time (ZCO) [46], the time of flight (TOF) and the collected charge (QVC) which is proportional to the detected energy.

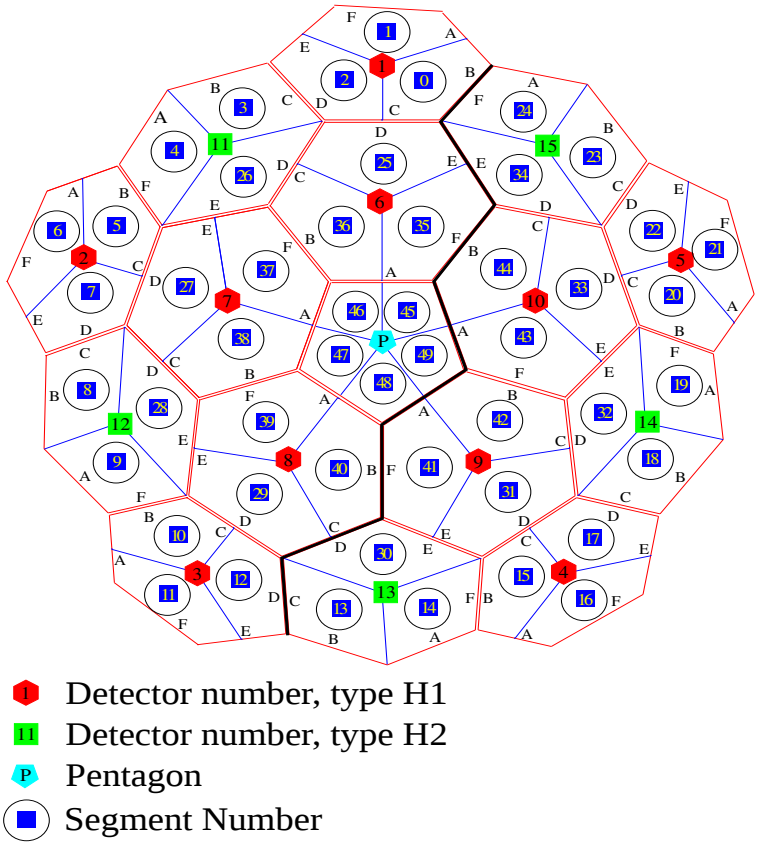

Figure 2.7: Schematic view of the neutron detector Neutron Wall viewed from outside of the array downstream of the target position. Picture taken from [45].

The zero-cross over time [46] is obtained from a pulse shape discriminator (PSD) which converts the anode input pulse into a bipolar signal and from a zero crossing discriminator which gives a logic pulse when the bipolar signal from the PSD crosses the baseline. Due to the different pulse shape, the zero crossing time is different for neutrons and γ rays, allowing a rather clean discrimination between them.

To extract the time information, the pulse from each detector is sent to a Constant Fraction Discriminator (CFD) module. This allows to avoid the dependence of the triggering time from the signal peak height, and therefore from the energy (time walk effect).

In addition to the detectors described above, four TACs (Time to Amplitude Converter) were used in the experimental setup in order to properly correlate the neutron detection with the pulsed beam structure. The timing diagrams are reported in Fig. 2.8. The available TACs are:

- *Fast Trigger vs Neutron Wall CFD-OR:* when the trigger condition is satisfied, a fast signal is created. This TAC has as start this signal and as stop the OR of the individual Neutron Wall time signals.
- *Neutron Wall CFD-OR vs RFQ:* the OR of the individual Neutron Wall time signals gives the start while the time reference of the radio frequency coming from the cyclotron serves as stop.
- *Fast Trigger vs RFQ:* the Fast Trigger signal serves as start and the radio frequency gives the stop.
- *BaF_2 vs RFQ:* the start is given by the time signal of a BaF_2 detector placed close to the reaction chamber while the stop comes from the radio frequency. This TAC is used to monitor the beam structure.

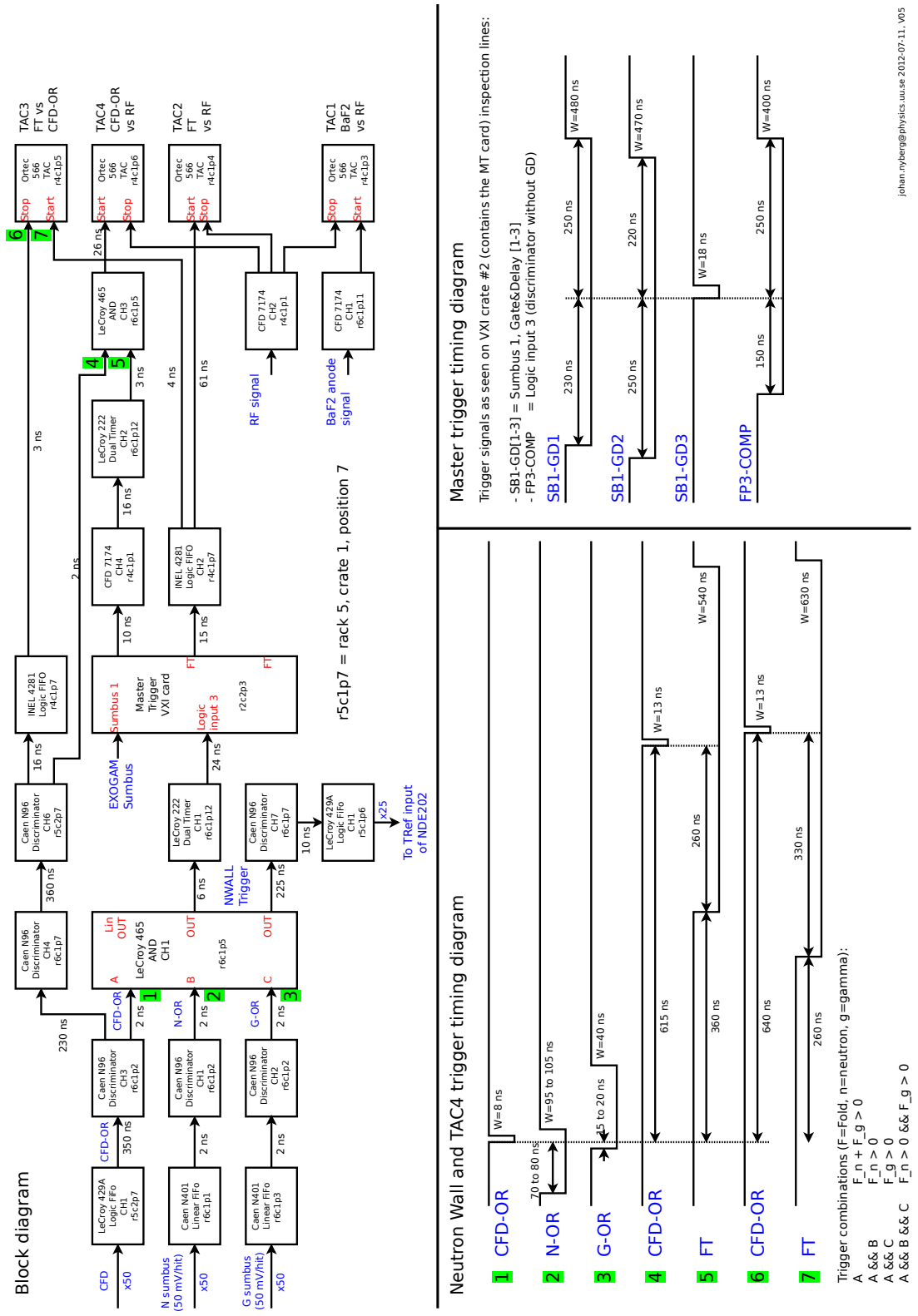

Figure 2.8: Trigger block and timing diagrams for Neutron Wall and TACs.

2.5 Data Analysis

In this section we present the different steps of the data analysis. In the first paragraph we will describe the structure of the raw data written to disk during the experiment and the software used in the offline sorting, while in the next paragraphs we will describe step by step the analysis of the data coming from the different detectors and the coincidences treatment.

2.5.1 Structure of the data

Raw data were recorded on disk, event-by-event, in data blocks with the same fixed length. When the trigger condition is fulfilled, the event is recorded as a collection of 16 bit words. In Tab. 2.2 we report the observables written to disk for EXOGAM, DIAMANT and the Neutron Wall. The data are sorted offline using specific C++ routines in the ROOT data analysis framework. The GRU (Ganil Root Utilities) package, developed for the analysis of experiments performed in GANIL, has been used in this analysis. User-written subroutines can be implemented in the code to perform special operations. This software allows to perform calibrations for each detectors, to put specific gates on particles and neutron matrices, to build particle-gated spectra and to look for γ-γ coincidences. After the offline sorting, ROOT files and trees are created.

2.5.2 Trigger Condition

In the present experiment, data were recorded when at least three γ rays or two γ rays and a neutron were detected in coincidence. The main trigger was created in the Master Trigger VXI card which receives as inputs a Sumbus signal from EXOGAM and a logic signal from the Neutron Wall as reported in Fig. 2.8. The amplitude of the Sumbus signal is proportional to the multiplicity of γ rays detected in EXOGAM. To obtain the logic pulse from the neutron detectors, a hardware gate on the ZCO signals was set in order to reduce as much as possible the γ contribution, avoiding any loss in neutrons. The OR (N-OR in Fig. 2.8) of this ZCO-gated signals is sent to the Master Trigger card. When the trigger condition is satisfied the Master Trigger card generates a Fast Trigger (FT) signal

EXOGAM			
Crystals		Segments	
Energy	Clover ID Crystal ID Energy	Energy	Clover ID Crystal ID Segment ID Energy
Time	Clover ID Crystal ID Time	Time	Clover ID Crystal ID Segment ID Time
Anti Compton			
Energy		Clover ID Crystal ID Energy	
Clover Time		Clover ID Time	
Crystal Time		Clover ID Crystal ID Time	

DIAMANT		Neutron Wall		TACs
CsI Detectors		Scintillators		
Energy	Detector ID Energy	Energy	Detector ID Energy	FT vs CFD-OR
Time	Detector ID Time	Time	Detector ID Time	CFD-OR vs RFQ FT vs RFQ
PI	Detector ID PI	ZCO	Detector ID ZCO	BaF_2 vs RFQ

Table 2.2: Parameters acquired in the present experiment.

and later a validation signal which starts the data readout.

2.5.3 EXOGAM analysis

The analysis of the EXOGAM data required energy and efficiency calibrations, time alignment, addback and Compton suppression. These procedures are de-

scribed in the following sections.

Energy calibrations

The energy information in EXOGAM is given by the central contact of each individual detector since the resolution of the segments is worse; for this reason particular care has been taken in the calibrations of the core spectra. Standard ^{60}Co and ^{152}Eu sources have been used to determine the calibration coefficients. In Fig. 2.9 we report the residuals for each detector, defined as the difference between the true energy and the energy measured after linear calibrations: $Res = E_{true} - E_{measured}$, obtained with the ^{152}Eu source.

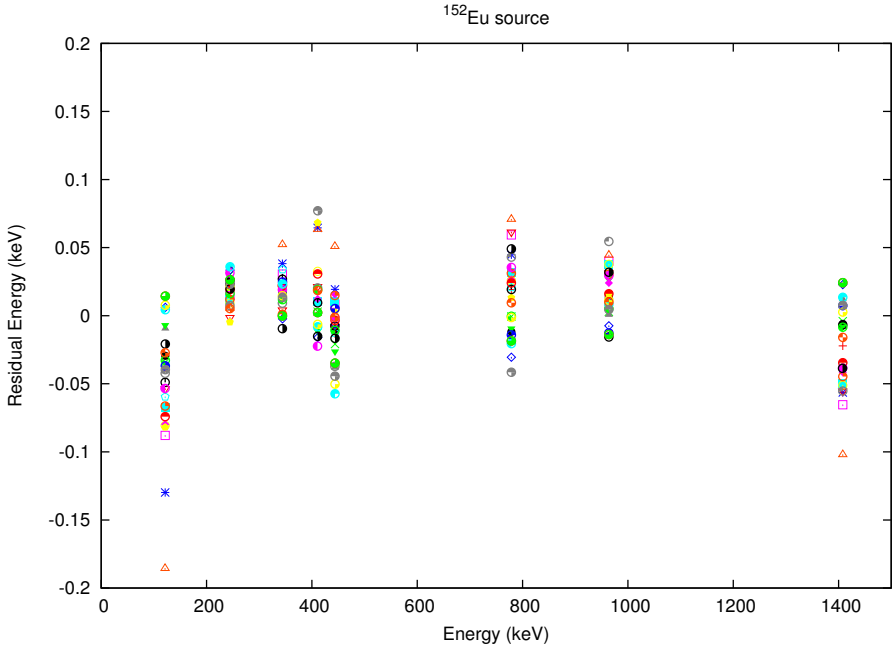

Figure 2.9: Energy residuals for each detector obtained with the^{152}Eu source.

All the residuals are within ±0.2 keV, which confirms the quality of the calibrations. The gain of a single detector may change in time due to instabilities of the electronics. For this reason, calibration data with radioactive sources were taken both before and after the experiment. No significant changes have been noticed.

Although the segments energy information is not used, it is nevertheless important to properly calibrate them. When multiple hits are detected in adjacent segments the center of the segment where the largest deposit of energy is measured is assumed as first interaction point. The same radioactive sources ^{60}Co and ^{152}Eu have been used for segments calibrations.

Efficiency calibrations

In order to extract the intensity of the transitions, it is necessary to measure the γ-efficiency curve of the experimental setup. The standard procedure is to calculate the area of peaks relative to well known transitions in calibration sources. In the present experiment a ^{152}Eu source has been used, complemented with a previously measured efficiency curve obtained with a ^{152}Eu source and the ^{35}Cl(n, γ) reaction, which extends up to $\sim$8.5 MeV. The two data sets have then been normalized to get a single curve which covers the full range. This curve was subsequently fitted with the semi-empirical expression:

$$\epsilon(E) = \frac{A_0 + A_1 \ln(E) + A_2 \ln(E)^2 + A_3 \ln(E)^3 + A_4 \ln(E)^4}{E}$$

where ϵ is the efficiency and E the energy, expressed in keV. The experimental data and the fitted curve are reported in Fig. 2.10 while the fitted curve parameters can be found in Tab. 2.3.

A_0	A_1	A_2	A_3	A_4
-17358.1	11325.0	-2802.34	309.918	-12.544

Table 2.3: Coefficients of the measured efficiency curve.

With the previously measured data set the efficiency follows a simple exponential decay curve (dashed red line in Fig. 2.10) while in the points relative to the present experiment a strong absorption of the low-energy γ rays is evident. This is due to the presence of DIAMANT, which was not present in the previous measurement.

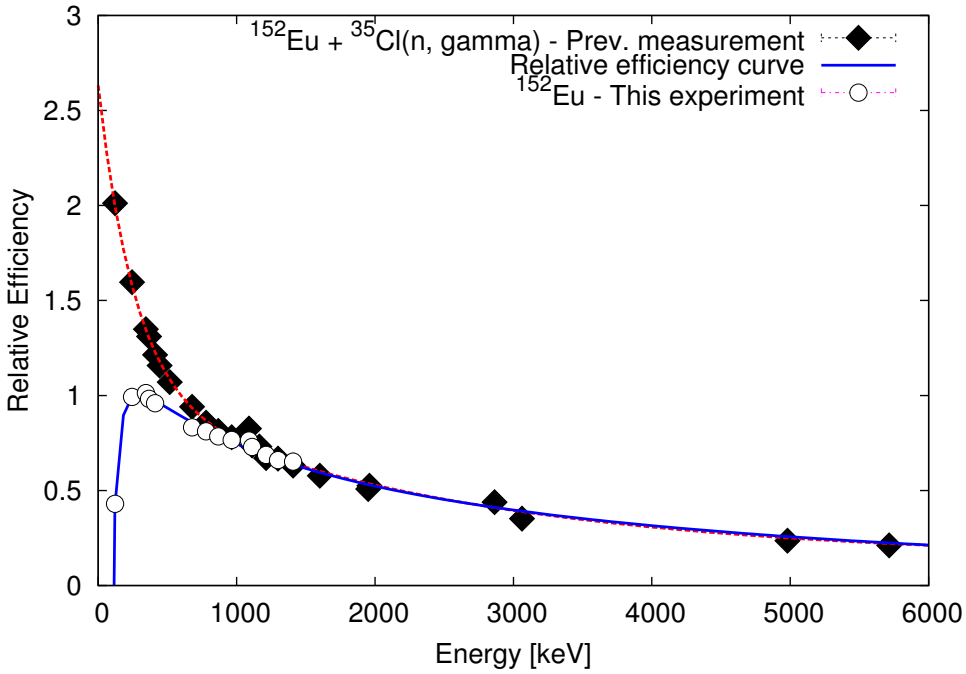

Figure 2.10: Experimental data and relative efficiency curve of the EXOGAM array. The white circles correspond to the present experiment while the black squares come from a previous data set. The blue curve is the one used in the present analysis. The different shape at energies below 500 keV is due to the absorption of the reaction chamber and of DIAMANT, which were not present in the ^{35}Cl(n, γ) measurement.

Absolute Efficiency estimate Although a relative efficiency curve is sufficient for the aim of the experiment described here, it is possible to obtain an estimate of the absolute efficiency of the setup from the ^{60}Co source run with the *sum peak method*. ^{60}Co β-decays to excited states in ^{60}Ni. The $4^+ \rightarrow 2^+ \rightarrow 0^+$ cascade results in the emission of a 1173- and a 1332-keV γ rays in coincidence. The probabilities to detect in one clover, after the Addback procedure, the first, the second, or both γ rays are given by:

$$P_1 = \epsilon_1(1-\epsilon_2) \quad (2.1)$$
$$P_2 = (1-\epsilon_1)\epsilon_2 \quad (2.2)$$
$$P_{12} = \epsilon_1\epsilon_2 \quad (2.3)$$

where P represents the probability and ϵ is the γ efficiency of each Clover at the given energy. The effects of the angular correlations are neglected and estimated to be of the order of $\sim 5\%$. Therefore, from the number of counts in the 1173-keV, 1332-keV and in the 2505-keV sum peak, it is possible to obtain the absolute efficiency at 1173 and 1332 keV as:

$$\epsilon_{1173} = \frac{N_{2505}}{N_{1132}+N_{2505}} \quad (2.4)$$
$$\epsilon_{1132} = \frac{N_{2505}}{N_{1173}+N_{2505}} \quad (2.5)$$

The values obtained in the present experiment for each Clover are reported in Tab. 2.4.

Clover ID	$\epsilon_{1173}(\%)$	$\epsilon_{1332}(\%)$
1	0.50	0.48
2	0.63	0.60
3	0.55	0.53
4	0.43	0.40
5	0.53	0.50
6	0.53	0.50
7	0.46	0.43
8	0.61	0.58
9	0.51	0.48
10	0.43	0.41
Total	5.19	4.91

Table 2.4: Absolute efficiency determined with the *sum peak method* for each EXOGAM Clover in the present setup.

Time Alignment

When the trigger condition is fulfilled a Fast Trigger (FT) signal is generated and a time window for the event builder of 500 ns is opened. Every hit detected within this interval is recorded in the same event. Since the period of the beam pulsing is $\sim$ 90 ns, more than one bunch is contained in the time window. It is therefore important to put a software time condition offline to restrict the particle and γ coincidences to one single bunch. Moreover it is crucial to align the time signals of each individual HPGe detector to put a common narrow gate.

In the EXOGAM detectors, the start of the recorded time interval is given by the signal of the individual crystal, processed by a Constant Fraction Discriminator to minimize the walk effect, while the stop is given by the FT signal, properly delayed of $\sim$ 600 ns. The time spectra of all the HPGe detectors have been aligned in order to have the prompt peak at channel 20000 and the second bunch peak at channel 18000.

Addback

The Clover configuration of EXOGAM allows to recover the total energy of γ rays which Compton scatter between different crystals by adding together the deposits of energy measured in the various detectors. The γ-ray energies detected in prompt coincidence in adjacent crystals of the same Clover are therefore summed together. This allows to reduce the background, increase the detection efficiency and improve the peak-to-total ratio. In Fig. 2.11 the comparison between spectra obtained with a ^{60}Co source with and without applying the addback procedure is reported.

Compton Suppression

The peak-to-total can be further improved and the background reduced by rejecting the events in which a γ ray deposits only part of its energy in a HPGe detector due to Compton scattering. The anti Compton shield of EXOGAM has been described in section 2.4.1. In the offline analysis we discarded events in which a germanium detector and the adjacent anti Compton shield fired in coincidence. The effect of the addback and the Compton suppression is clearly visible

in Fig. 2.11.

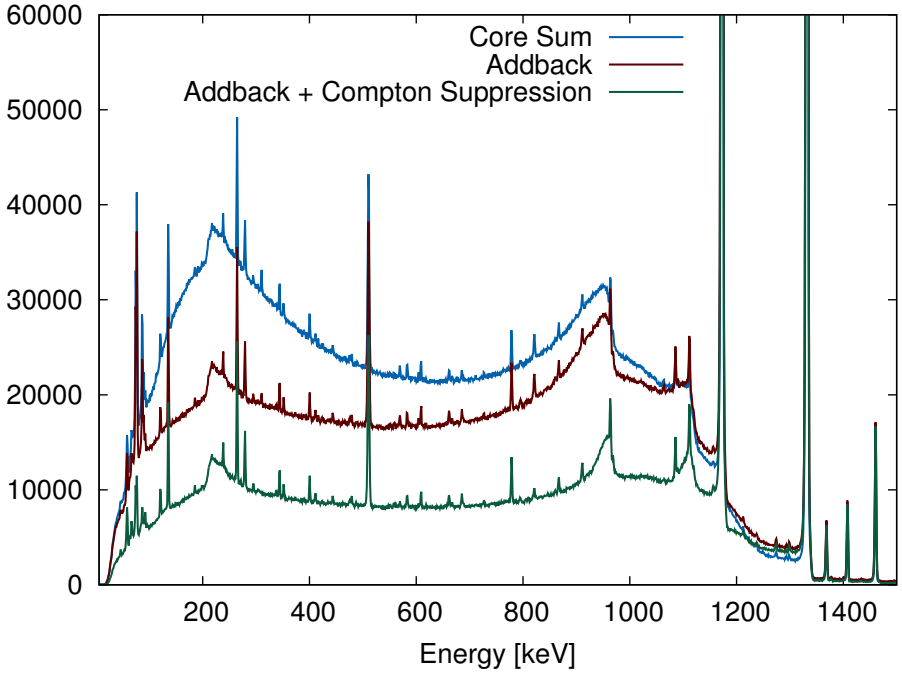

Figure 2.11: EXOGAM spectra obtained with a ^{60}Co source. The sum of the crystals, the addback and the addback + Compton suppression spectra are reported.

Doppler Correction

In fusion evaporation reactions where a thin target is used, the reaction products escape from the target material and therefore the γ rays coming from their de-excitation are emitted in flight. The resulting peaks are therefore broadened and shifted by the Doppler effect. The detected energy is given by the well known formula:

$$E^{\gamma} = E_0^{\gamma} \frac{\sqrt{1-\beta^2}}{1-\beta\cos(\theta)} \approx E_0^{\gamma}(1+\beta\cos(\theta)) \tag{2.6}$$

The velocity β of the recoiling nuclei changes on an event-by-event basis and it is dependent on the energy and angle of emission of the evaporated particles.

To determine the best average β value, we corrected the γ spectra for each value of β from 0 to 10 % and we fitted the peak corresponding to the well known $\frac{9}{2}^+ \rightarrow \frac{7}{2}^+$, 627-keV transition in ^{23}Na. We took as the optimal β value the one which maximizes the energy resolution. In Fig. 2.12 we reported a 2D histogram where the x axis represents the Doppler corrected energy and the y axis the corresponding β value.

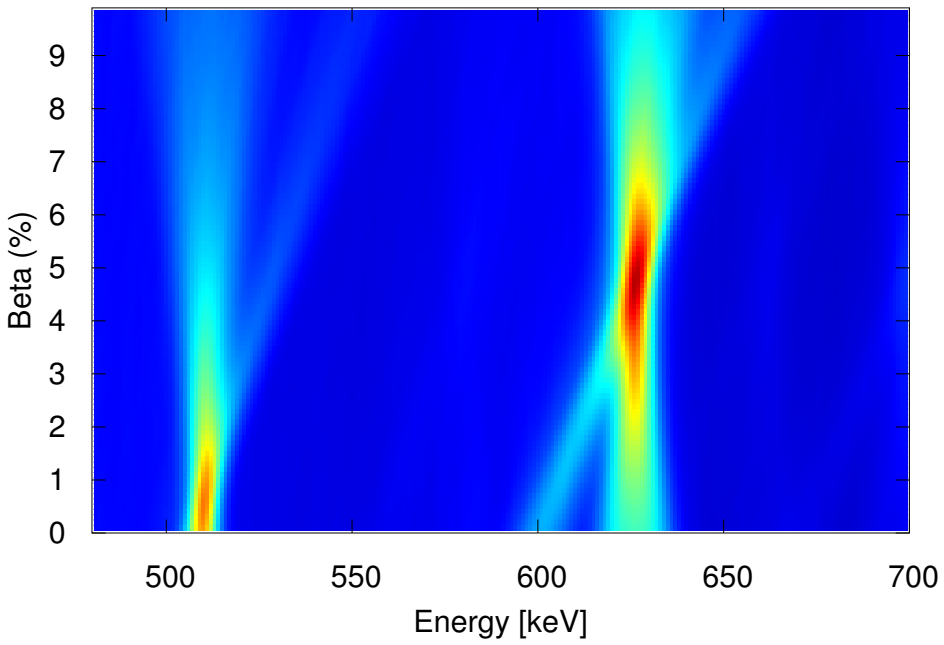

Figure 2.12: 2D histograms of the Doppler-corrected energy vs. the relative β value.

The different behavior between the 511-keV peak, emitted at rest, and the 627-keV peak emitted in flight is clearly visible. The 627-keV peak shows also the dependence of the measured energy from the γ-ray angle: the photons detected at 90° show only Doppler broadening while the ones detected at 135° present both Doppler shift and broadening.

$\gamma - \gamma$ coincidences

The structure of nuclear systems is characterized by the presence of different levels with well defined angular momentum and parity quantum numbers. The de-excitation from one level to another proceeds via the emission of a γ ray with a given multipolarity and energy. When a nucleus is populated at high spin, a high γ-ray multiplicity occurs. To properly fix the excitation energy of nuclear levels, to track their decay paths and to determine their spin and parity it is essential to study the coincidences between the γ rays emitted in their de-excitation. This is a standard procedure in γ spectroscopy and it consists in considering only events in which two or more γ rays are detected within a prompt coincidence window in different detectors and subsequently filling a 2D histogram with the energies measured by the different detectors. The use of the addback procedure in the present experiment implies that the γ multiplicity of the event is determined by the number of Clover detectors which fire. The gate on a given transition in the 2D spectrum allows to obtain extremely clean spectra, enhancing the selectivity offered by the coincidences with charged particles and neutrons.

2.5.4 DIAMANT analysis

In this section we will present the analysis of the charged particle detector DIAMANT. As we already saw in Sec. 2.4.2 each detector has three outputs: time, energy and particle ID parameter. The different steps of the analysis consist in the time alignment of the different detectors and the creation of 2D matrices which allow to discriminate between the different type of particles.

Time alignment

As already stated, more than one bunch of the beam is contained inside the event builder window. To look for particle coincidences with DIAMANT it is therefore necessary to align the peaks of the different detectors and to put a prompt gate in the time spectrum. The time output of each detector is given by the interval between the signal of the individual crystal and the Fast Trigger signal, delayed of ~ 600 ns. In the present analysis we aligned the time spectra in order to have

the peak of the α particle at channel 2200 and the proton peak at 2000. A time condition has then been put in order to select only prompt peaks, discarding events coming from other bunches.

Particle identification

As described in Sec. 2.4.2 different types of particles will have different amplitude ratio between the fast and the slow components of the scintillation light as well as different decay time constant of the fast component. This allows to obtain the so-called particle ID parameter, which is exploited to discriminate between different particles. 2D matrices have been created for each detector where the particle ID parameter is plotted against the energy. A typical example is reported in Fig. 2.13.

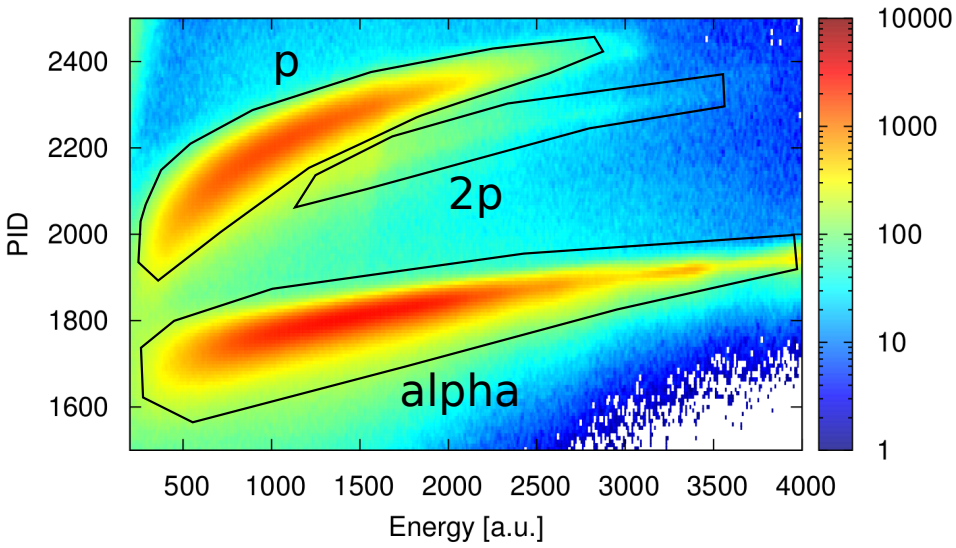

Figure 2.13: DIAMANT PID vs energy matrix. Protons, α and two proton gates are visible.

Proper gates allow to select the type of particle and to identify the reaction channel. The time gates previously described assure that the coincidence is prompt.

Detection efficiency

Since the detection efficiency is lower than 100%, the gates on different particles are not totally clean. A reaction channel populated via the emission of N identical particles will be observed also in coincidence with $N-1, N-2, ...1, 0$ particles. This provides a way to determine experimentally the efficiency of the detector. The probability $P(k, N)$ of detecting k identical particles out of N emitted is:

$$P(k, N) = \binom{N}{k} \epsilon^k (1-\epsilon)^{N-k}$$

The ratio between the area of a peak observed in coincidence with k_1 particles and the area in the spectrum relative to k_2 particles will therefore be:

$$R = \frac{I_{\gamma,k_1}}{I_{\gamma,k_2}} = \frac{k_2!}{k_1!} \cdot \frac{(N-k_2)!}{(N-k_1)!} \cdot \frac{\epsilon^{k_1-k_2}}{(1-\epsilon)^{k_1-k_2}}$$

Which for $k_2 = k_1 - 1 \equiv k$ reduces to:

$$R = \frac{N-k+1}{k} \frac{\epsilon}{(1-\epsilon)}$$

Therefore from the ratio between the area of the two peaks we can estimate the detection efficiency. In Tab. 2.5 we report the measured efficiency for α and protons. The measured efficiencies are lower than the nominal ones; this is due to the absorbers needed to shield the detectors from the scattered beam. Since the range of the ^{16}O scattered beam is comparable with the one of light charged particles such as α the thickness of the material required to stop the scattered projectiles will absorb also the less energetic charged particles, decreasing the detection efficiency.

^{23}Na - αp channel				
γ energy	$I_{\alpha p}/I_p$	ϵ_α	$I_{\alpha p}/I_\alpha$	ϵ_p
440	0.32	24 %	0.63	39 %
627	0.29	22 %	0.60	38 %

Table 2.5: Measured detection efficiencies for α and protons.

Kinematical Correction

The Doppler shift of a γ ray emitted in flight is given by Eq. (2.6) and depends on the velocity β of the recoil and on the angle θ between the direction of the γ ray and the one of the recoiling nucleus. Differentiating Eq. (2.6) we obtain a first order estimate of the peak broadening:

$$\left|\frac{\Delta E_\gamma}{E_\gamma}\right| = \cos^2\theta(\Delta\beta)^2 + (\beta\sin\theta)^2(\Delta\theta)^2$$

The major contribution to the uncertainty in the angle θ is the opening angle of the EXOGAM detectors. The use of electronically segmented crystals allows to reduce the error in the interaction position inside the germanium material, as we have already seen. In addition, due to momentum conservation, the evaporation of particles from the compound nucleus induces a spread in the velocity and direction of the residual nuclei. This effect is particularly important for light nuclei, since the evaporation of, i.e., an α particle from the compound nucleus ^{28}Si carries away $\sim$15% of the mass.

However, the good granularity of DIAMANT allows to measure the angle of emission of the evaporated particles and therefore to reconstruct the trajectory of the residual nucleus. The conservation of the angular momentum can be expressed as:

$$\vec{p}_R = \vec{p}_{CN} - \sum_{i=1}^{n}\vec{p}_i \tag{2.7}$$

where R is the residual nucleus, CN the compound and n the number of evaporated particles. The Doppler shift is given by

$$E^\gamma = E_0^\gamma\left(1 + \frac{\vec{v}_R}{c}\cdot\vec{d}_\gamma\right)$$

where $\vec{d}_\gamma$ is the versor in the direction of the emitted γ ray. Taking into account Eq. (2.7) we have:

$$E^\gamma = E_0^\gamma\left(1 + \frac{m_{CN}}{m_R}\frac{\vec{v}_{CN}\cdot\vec{d}_\gamma}{c} - \sum_{i=1}^{n}\frac{m_i}{m_R}\frac{\vec{v}_i}{c}\cdot\vec{d}_\gamma\right)$$

Therefore it is possible to apply an event-by-event kinematical correction by measuring the angle of emission and the energy of the emitted particles. This improves both the energy resolution and the peak-to-total ratio, resulting in an increase in the resolving power of the detector.

In the present experiment we are interested in the (αp) and (αn) reaction channels; since the major effect on the velocity and trajectory of the compound nucleus is given by the heaviest masses, we performed a kinematical correction considering only the evaporated α particles. The energy resolution of DIAMANT is not sufficient to determine event-by-event the energy of the α. Since in the evaporation process the particles are emitted isotropically in the center of mass frame, we decided to assume an average energy for the emitted α in the center of mass and then transform it in the laboratory frame taking into account the velocity of the compound nucleus and the angle of emission of the particle.

To optimize the Doppler and kinematical correction we need to adjust two parameters, the velocity of the compound nucleus β_{CN} and the average energy of α particles in the center of mass frame, E^*_α. An optimal Doppler correction will maximize the energy resolution and give the correct centroid. To do so we performed a 2D scan on β_{CN} and E^*_α and we created matrices where in the z axis we put either the energy resolution or the difference between the measured and the real centroid of the well known $\frac{9}{2}^+ \rightarrow \frac{5}{2}^+$, 2263-keV transition in ^{23}Na, obtained via an automatic fit. An example of these matrices are reported in Fig. 2.14 and 2.15 for the beam energy 60 MeV. The same procedure has been applied to the runs with a beam energy of 70 MeV.

The optimal parameters obtained are reported in Tab. 2.6 for both the beam energies. The kinematical correction allows to improve significantly the Doppler correction and to obtain a better energy resolution, as can be seen in Fig. 2.16, where a portion of the spectrum in coincidence with one α is reported. The simple average Doppler correction described in Sec. 2.5.3 and the kinematical correction are compared. The FWHM of, for example, the 627-keV peak in ^{23}Na decreases from 11.5 to 6.9 keV when the kinematical correction is applied.

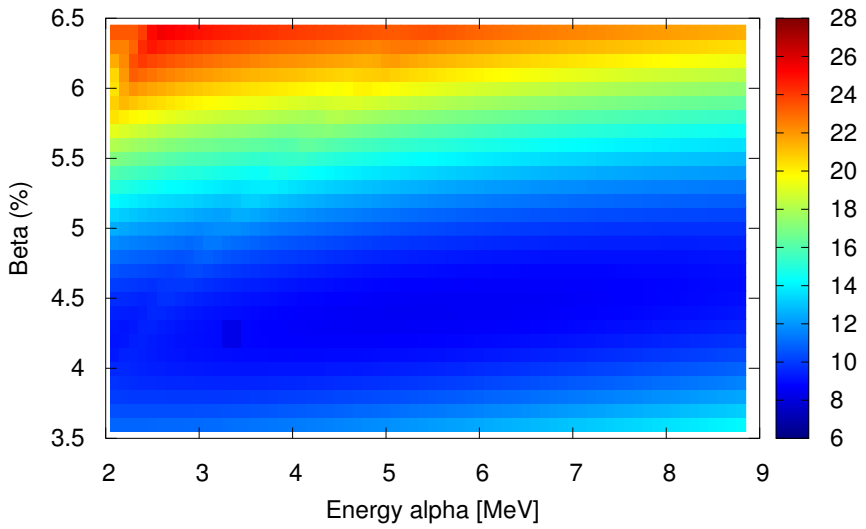

Figure 2.14: Energy resolution as a function of β_{CN} and E^*_α for the $\frac{9}{2}^+ \rightarrow \frac{5}{2}^+$, 2263 keV transition in ^{23}Na.

Beam Energy	β_{CN}	E^*_α
60 MeV	0.047%	6 MeV
70 MeV	0.050%	8 MeV

Table 2.6: Optimized values for β_{CN} and E^*_α.

2.5.5 Neutron Wall analysis

As already seen, the outputs of the Neutron Wall detectors are three: the collected charge (QVC) proportional to the energy, the zero crossing time (ZCO) and the time of flight (TOF). Since the Neutron Wall has a good efficiency for the detection of γ rays, it is crucial to achieve a good neutron-γ discrimination to obtain the cleanest possible spectra. This is done by putting individual 2D gates in the ZCO vs time matrices of each detector. The ZCO parameter exploits the different shape generated by the recoil of a proton or of an electron in the (n, p) or (γ, e^-) processes, as described in Sec. 2.4.3. The time information for each detector is given by the difference between its CFD signal and the OR of all

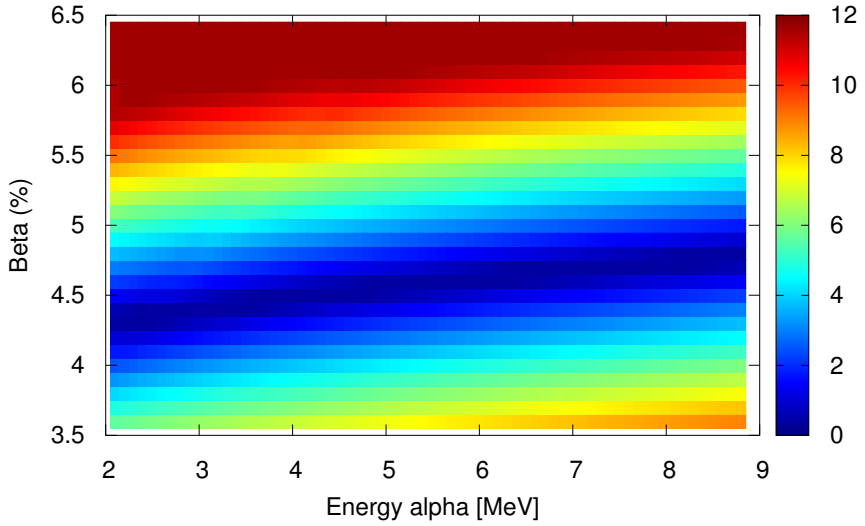

Figure 2.15: Difference between the measured and the known energy values as a function of β_{CN} and E^*_α for the $\frac{9}{2}^+ \rightarrow \frac{5}{2}^+$, 2263-keV transition in ^{23}Na.

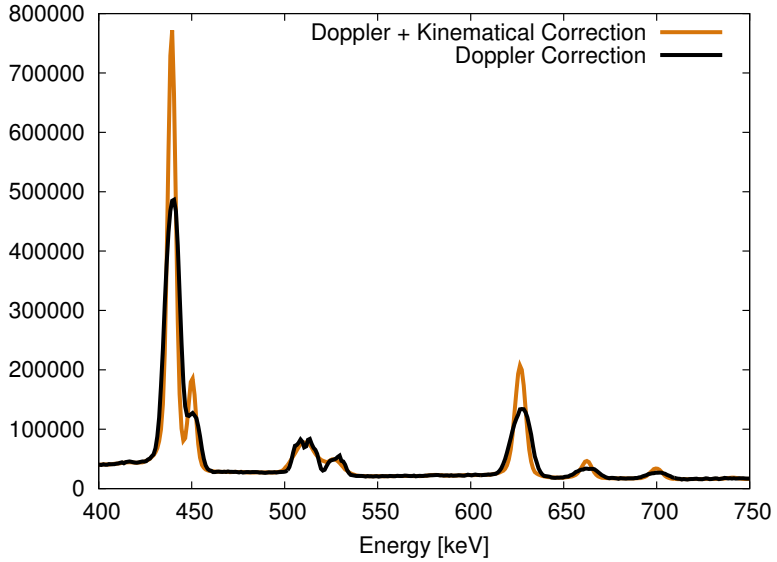

Figure 2.16: Portion of the γ spectrum in coincidence with one α particle. The average Doppler and full kinematic corrections are compared.

the Neutron Wall detectors, properly delayed. Since γ rays travel faster than neutrons and are emitted in a great amount in fusion evaporation reactions, the OR is usually given by the interaction of a photon with one of the scintillators. If this is the case the time spectrum will present a sharp peak coming from γ rays and a large bump due to neutrons, as seen in Fig. 2.17.

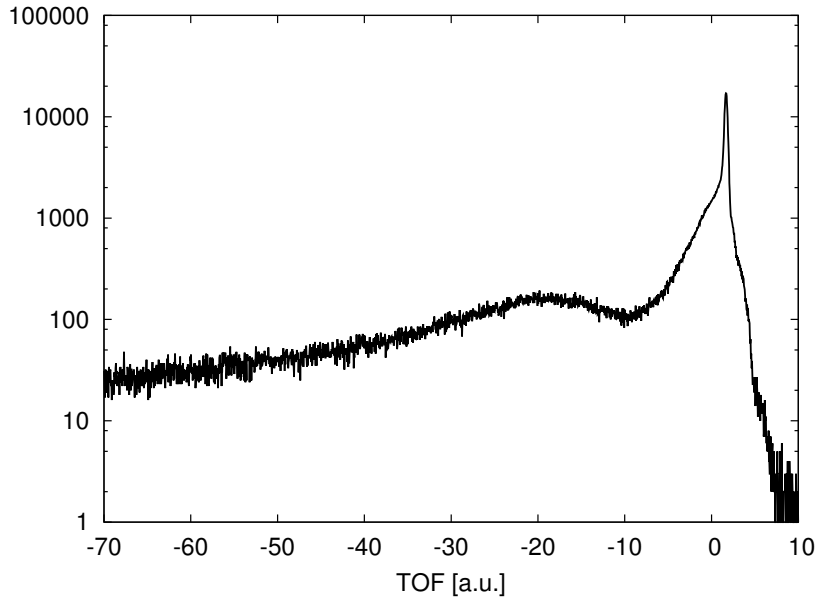

Figure 2.17: TOF spectrum of one NWall detector. The sharp peak of γ rays as well as the large neutron bump are visible.

However, if only one hit is recorded in the Neutron Wall, it will serve both as start and as CFD-OR, therefore all the multiplicity one events will have the same TOF. This does not allow to discriminate between neutrons and γ. To overcome this limitation the information coming from the Neutron Wall CFD-OR vs RFQ TAC is used. This TAC measures the time interval between the OR of all the Neutron Wall detectors and the radio frequency of the cyclotron, properly delayed; the output will be therefore different if the OR is given by a neutron or by a γ ray. By adding this time interval to the TOF parameter of the individual detector (the so called TRF variable) it is possible to recover also the events with multiplicity one. By setting proper gates in the 2D matrices TRF vs ZCO we obtain clean gates on the neutrons, as can be seen in Fig. 2.18.

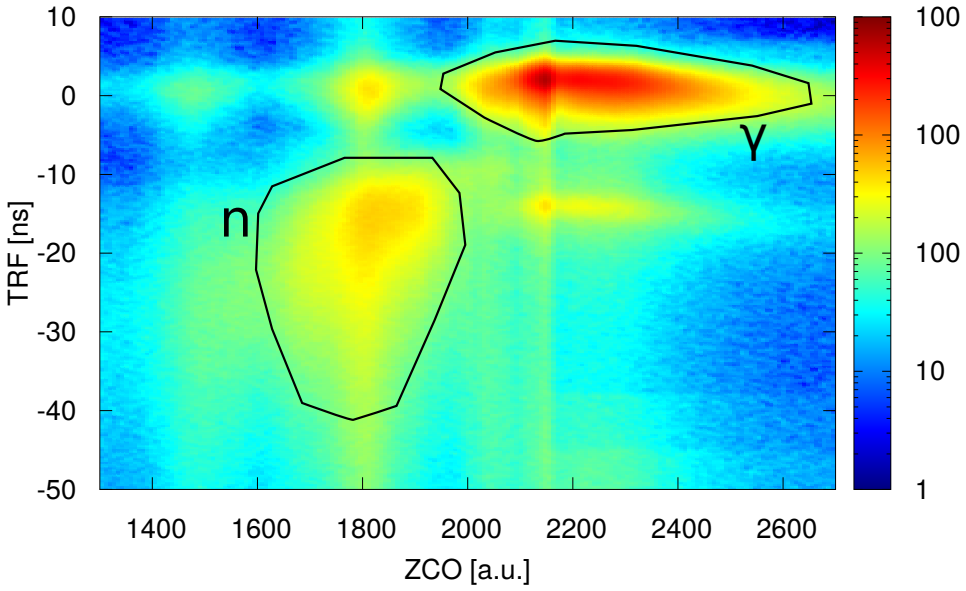

Figure 2.18: TRF vs ZCO matrix of one Neutron Wall detector. The neutron and γ loci are clearly visible.

Since the time window of the event builder contains more than one bunch, it is impossible to know which bunch gave the CFD-OR simply from the TRF information. Therefore it may happen that γ rays of one bunch are considered in coincidence with neutrons of a different bunch. To avoid this we exploit the time information coming from the Fast Trigger vs CFD-OR TAC selecting only the events in which the CFD-OR is in prompt coincidence with the trigger.

The effect of the gating on neutrons is visible in Fig. 2.19, where the γ spectra in coincidence with 1 α and 1 α - 1 neutron are compared.

By requiring prompt coincidences with neutrons, the transitions coming from the αn channels are strongly enhanced and new peaks which were previously hidden by the background become clearly visible. Peaks originating in reaction channels which do not involve the evaporation of neutrons (which are generally much strongly populated) are highly suppressed, but the most intense are still visible. This is due to the leakage of γ rays inside the neutron gates. To estimate

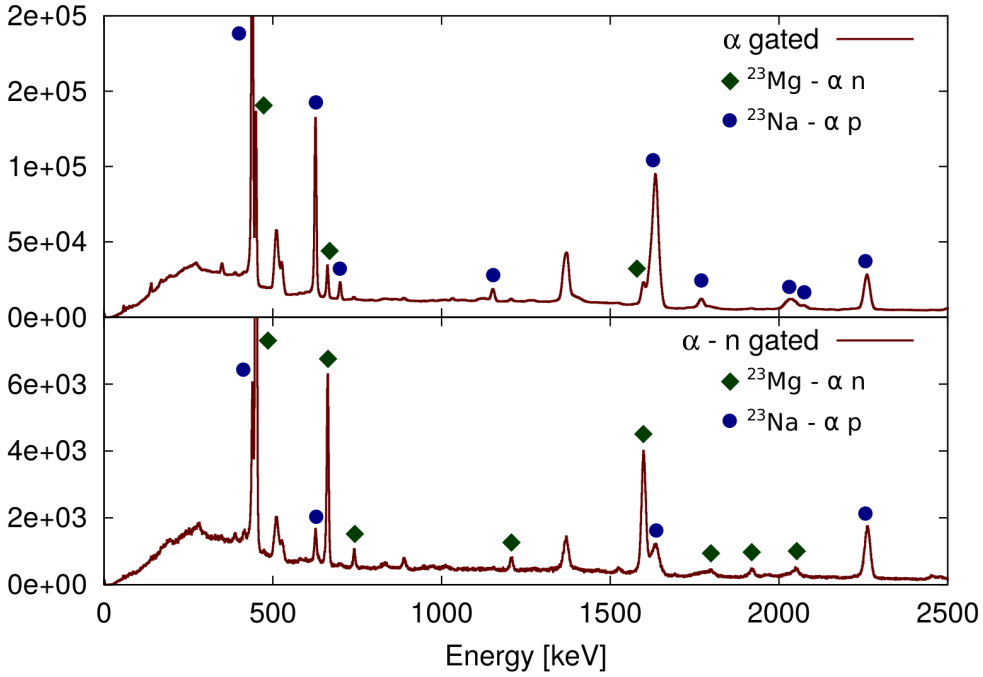

Figure 2.19: γ spectrum in coincidence with 1 α (upper panel) and 1 α and 1 α + 1 neutron (lower panel). The blue dots indicate peaks coming from ^{23}Na (αp) channel while the green squares highlight transitions from ^{23}Mg (αn) channel

the amount of this γ leakage we considered the $\frac{9}{2}^+ \rightarrow \frac{7}{2}^+$ analogue transitions in the mirror nuclei ^{23}Na-^{23}Mg (αp and αn channel) with and without the gate on neutrons. These transitions lie respectively at 627 and 663 keV. The ratio between the number of counts changes from to 5.6 to 0.16 when the neutron condition is required. This suggests a γ leakage of the order of $\sim$2.8%

Following the same procedure described in Sec. 2.5.4 we estimate the 1 neutron detection efficiency to be 21%.

2.6 Channel Selection

In the previous sections we described the procedures to identify neutrons and charged particles. Time conditions are put on each detector in order to select only particles and γ rays in prompt coincidence with the trigger. In such a way a new parameter PID, which defines the reaction channel of interest, is defined as:

$$\text{PID} = 1 \times N_\nu + 4 \times N_\alpha + 16 \times N_\pi$$

where N_i is the number of i particles.

2.7 Experimental results

In this section the results of the experiment will be described. We firstly show the γ-ray spectra of the nuclei of interest, highlighting the newly identified transitions. We then describe the procedure we adopted to construct the new level schemes for ^{23}Na and ^{23}Mg.

2.7.1 Identification of new transitions in ^{23}Mg-^{23}Na

Requiring coincidences with the proper combination of charged particles and neutrons it is possible to obtain the γ spectra of the nuclei of interest. The ^{23}Na nucleus is populated in the α-p channel. In Fig. 2.20 the relative γ-ray spectrum is presented.

The spectrum is extremely clean and the contamination from other reaction channels is negligible, proving the high selectivity of DIAMANT. Moreover this confirms the proper optimization of the beam energy for the present experiment, since the evaporation of more than two particles is clearly suppressed with respect to the evaporation of two. The highest spin state previously reported is the $J = 17/2^+$ at 11072 keV [32]. This level is populated with rather good statistics as can be evaluated from the particle gated γ-ray spectrum showing the 2034 keV transition.

The ^{23}Mg nucleus is populated in the α-n channel and its spectrum is shown in Fig. 2.21.

The spectrum is rather clean and allows the identification of γ rays belonging to ^{23}Mg. However few contaminant transitions are clearly observable. This is due to γ leakage into the neutron gates, as discussed in Sec. 2.5.5. This leakage has been estimated to be of the order of few percent. The cross section of the contaminating channels is much larger than the one of the channel of interest, resulting in clearly visible peaks. The strongest contaminations are due to ^{23}Na

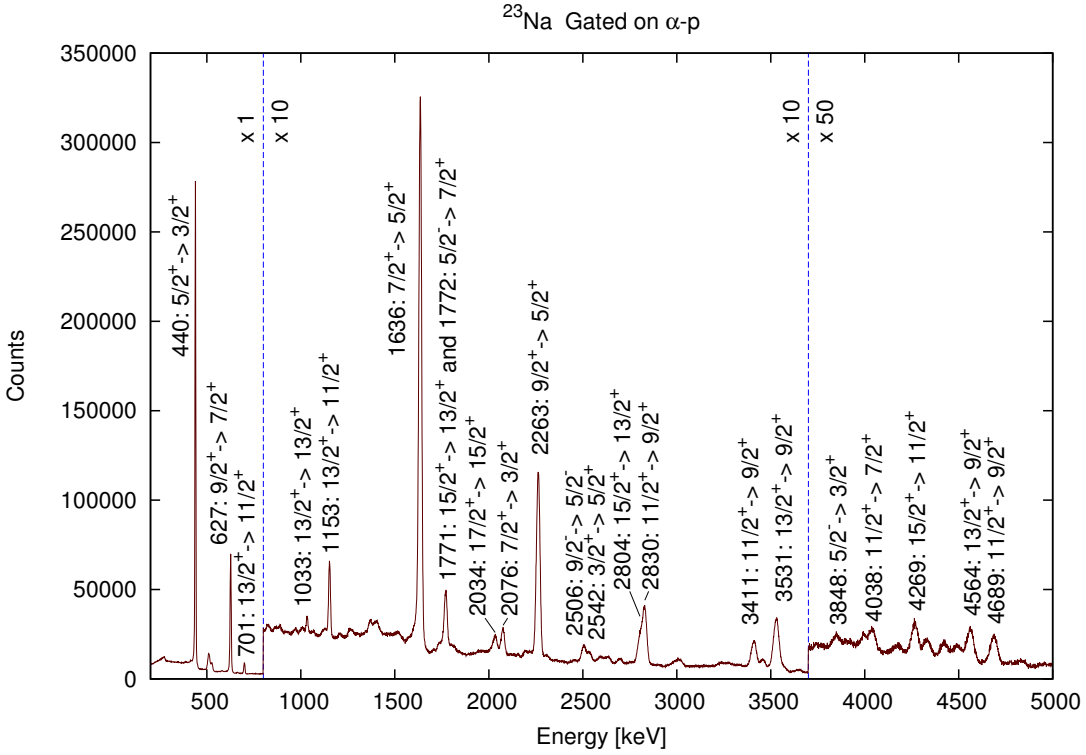

Figure 2.20: Spectrum of γ rays detected in coincidence with one α particle and one proton, corresponding to ^{23}Na. The most intense transitions are marked with their energy.

and ^{24}Mg, populated in α-p and α channels, respectively. The highest spin previously reported is $J = 13/2^+$, assigned to levels at 6192 and 7143 keV. Both levels are populated in the present experiment, de-excited respectively by γ transitions of 3480 and 1207 keV, observable in the spectrum. To further clean the spectra and to establish coincidence relationships between different transitions, gated projection of $\gamma - \gamma$ matrices have been studied. In Fig. 2.22 we report the particle gated $\gamma - \gamma$ projection relative to the mirror nuclei of mass A=23. A sum of gates on two of the most intense transitions has been requested.

The γ spectra of the nuclei of interest are very similar as expected for mirror nuclei. Analogue transitions are usually within few keV difference. We can exploit this mirror symmetry to search unknown states in ^{23}Mg which are the analogue of already observed levels in ^{23}Na. Since the aim of this experiment is to extend our

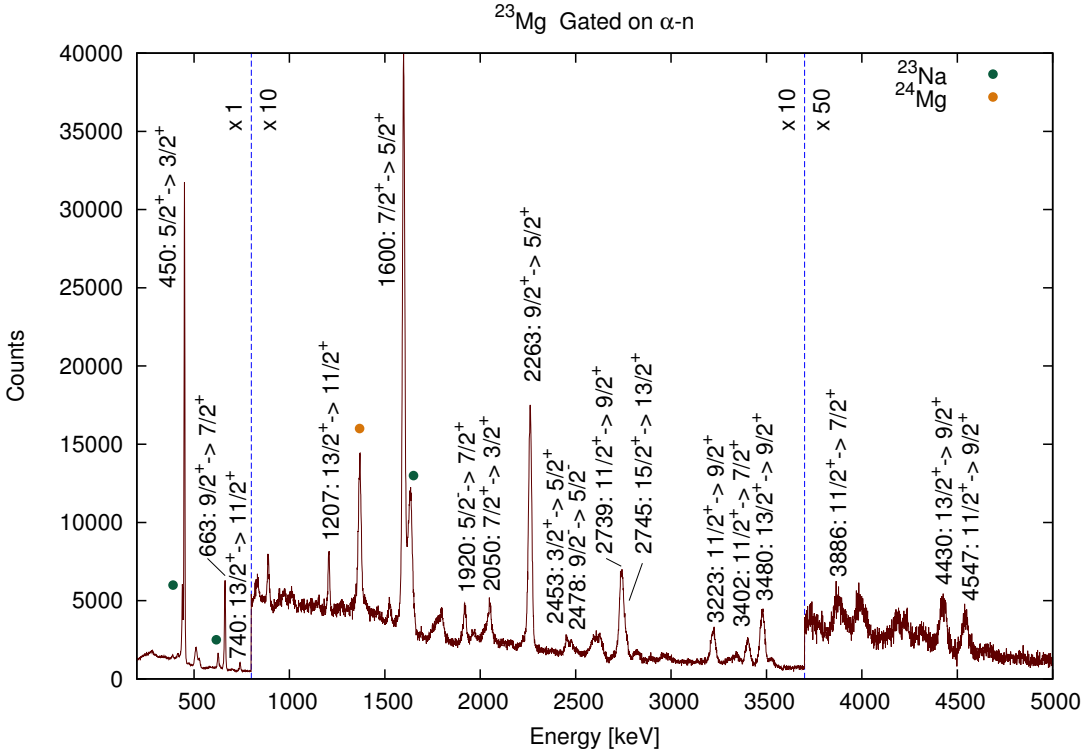

Figure 2.21: Spectrum of γ rays detected in coincidence with one α particle and one neutron, corresponding to ^{23}Mg. The most intense transitions are marked with their energy. Contaminant peaks are marked with orange (^{24}Mg) and green (^{23}Na) circles.

experimental knowledge of mirror energy differences we look for the analogue state of the *yrast* $15/2^+$ state in ^{23}Na at 9038 keV excitation energy. The strongest decay branching of this state is via a 2804-keV transition to the $J = 13/2^+$, 6235-keV level, which subsequently decays mainly via a 3531-keV γ ray. The analogue of the latter transition in ^{23}Mg is the 3480-keV, $13/2^+ \rightarrow 9/2^+$ transition. In order to be selective toward the highest spin states we therefore projected the $\gamma - \gamma$ αp and αn matrices gated on the 3531 and 3480 keV transitions, respectively. The resulting spectra are reported in Fig. 2.23.

The similarity between the two spectra is striking and strongly suggests to consider the newly observed 2745- and 3402-keV transitions in ^{23}Mg as the analogue of the 2804- and 3568-keV transitions in ^{23}Na. This allows to place two

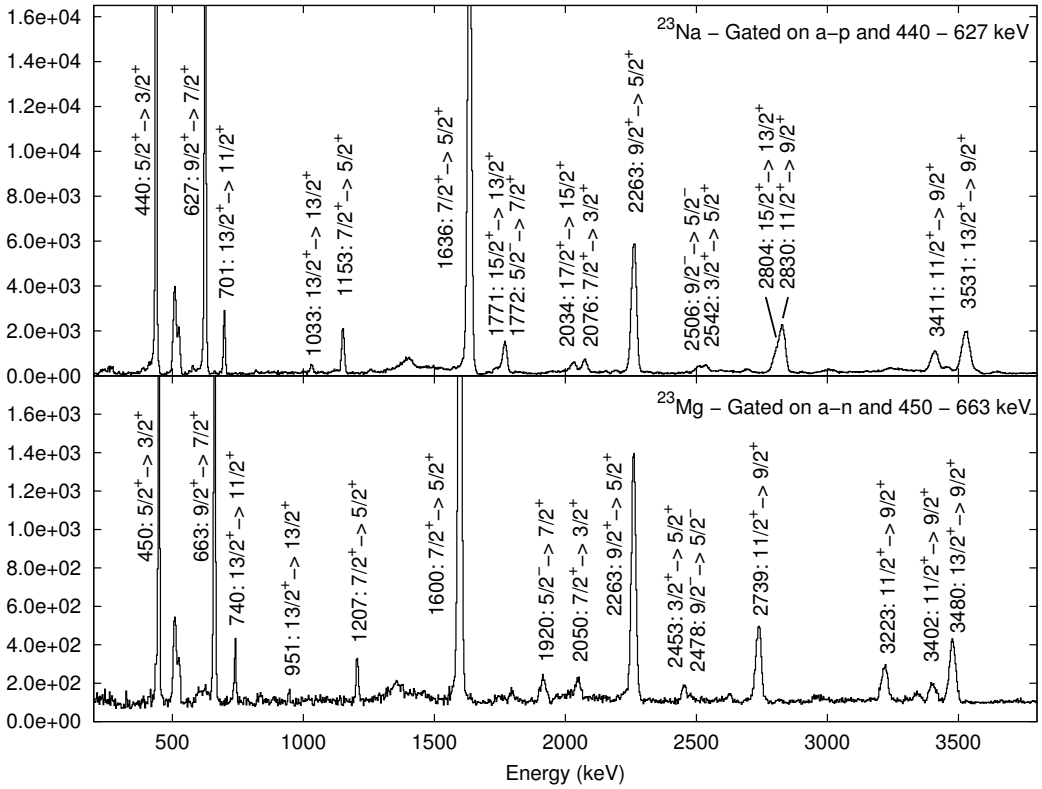

Figure 2.22: Projection of particle gated $\gamma - \gamma$ matrices. A sum of gates on two of the most intense transitions, reported in the picture, has been applied.

new states in the ^{23}Mg level scheme at excitation energy 8937 keV and 9594 keV, respectively. From systematic and mirror-symmetry arguments we assign to both of them spin parity $J = 15/2^+$. To further confirm the existence of these two new levels we look for the other branching already observed in ^{23}Na, i.e. the analogue of the 1771-keV $15/2^+ \rightarrow 13/2^+$ and 2450-keV $15/2^+ \rightarrow 13/2^+$ transitions, which de-excite the 9038- and 9802-keV levels and both feed the $J = 15/2^+$ 7268-keV state, analogue of the $J = 15/2^+$ 7143-keV state in ^{23}Mg. Therefore we project the particle gated $\gamma - \gamma$ matrices with gates on the most intense transitions de-exciting this level, i.e. the 1153- and 4564-keV in ^{23}Na, and the 1207 and 4430 keV in ^{23}Mg. The resulting spectra are reported in Fig. 2.24.

The transitions we are looking for at 1794 keV and 2451 keV are clearly visible, proving the observation of the two $J = 15/2^+$ states in ^{23}Mg. This allows

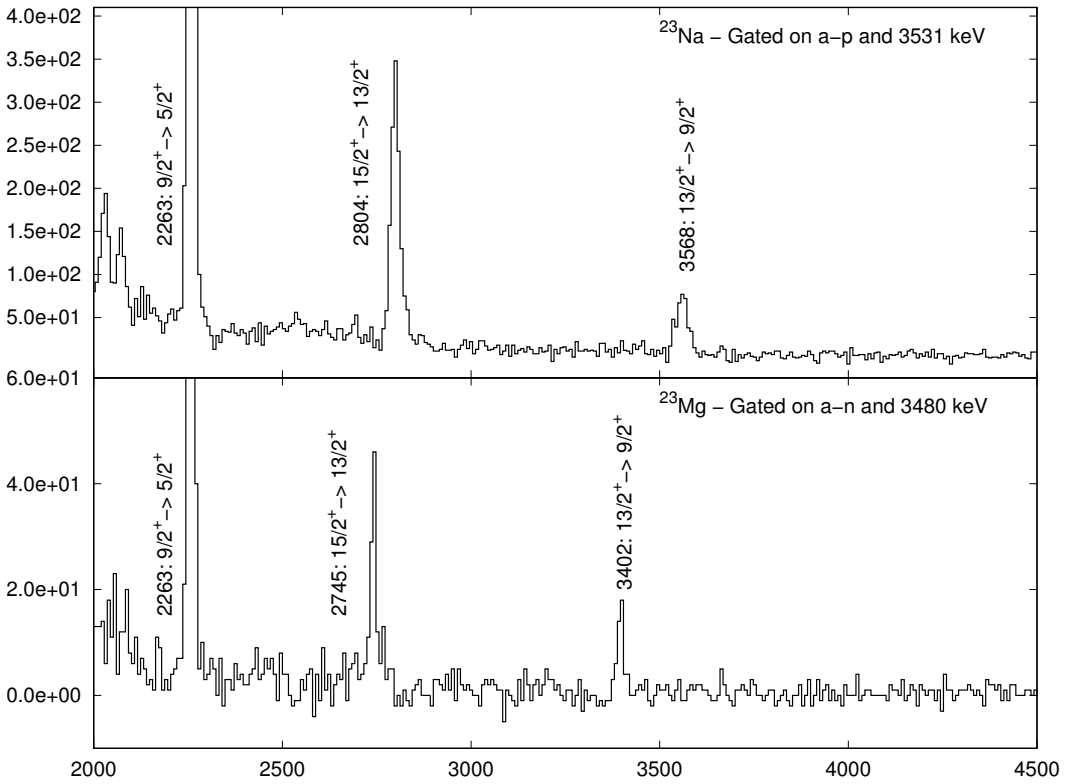

Figure 2.23: Projection of particle gated $\gamma - \gamma$ matrices for ^{23}Na and ^{23}Mg gated on the $13/2^+ \rightarrow 9/2^+$ transition at 3531 and 3480 keV energy, respectively.

to extend the mirror energy differences to spin $J = 15/2^+$ for both *yrast* and *yrar* bands.

2.7.2 Determination of γ-ray intensity

Particle-γ-γ coincidences allow to determine the excitation energy of a given state and to reconstruct the level scheme of the nuclei of interest. A key point in this procedure is the determination of the intensity of a given transition, which allows to properly place it in the level scheme and to measure the branching ratios of the different decay paths of the de-exciting state. γ-ray intensities are usually extracted from singles spectra correcting the number of counts in the peak for the efficiency of the apparatus at that energy. However high-lying transitions

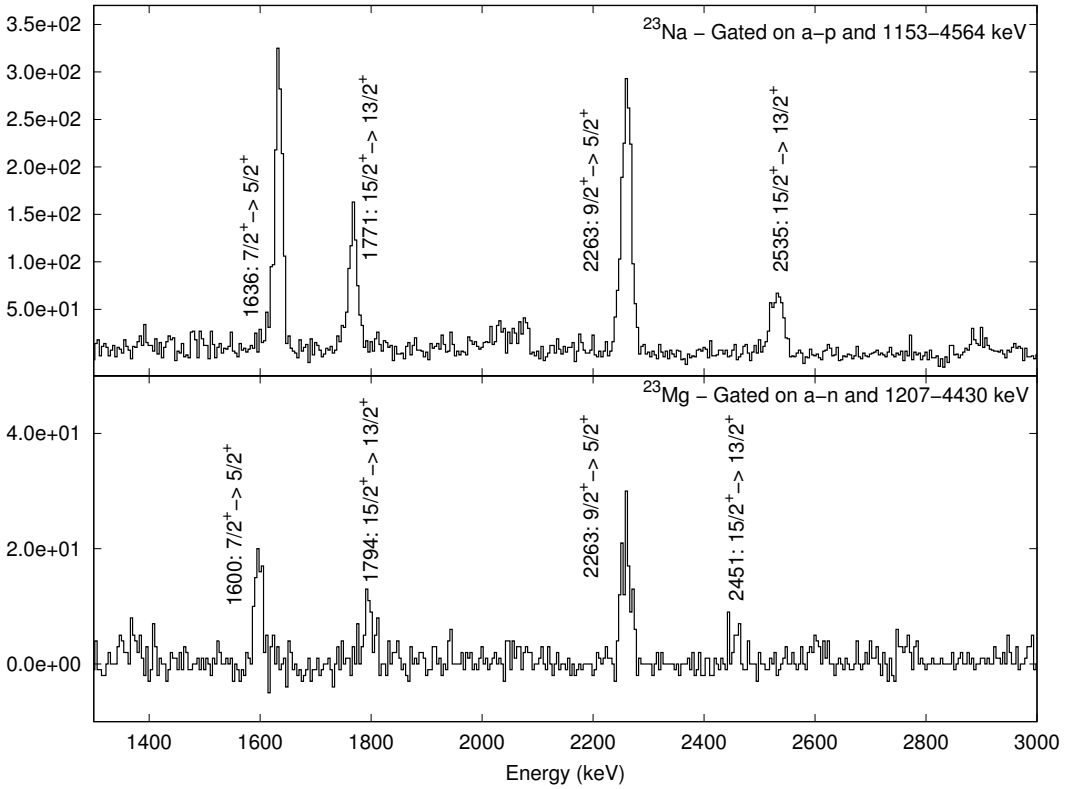

Figure 2.24: Projection of particle gated $\gamma - \gamma$ matrices for ^{23}Na and ^{23}Mg gated on 1153- OR 4564-keV and 1207- OR 4430-keV transitions, respectively.

are usually visible only exploiting the selectivity of $\gamma - \gamma$ correlations. In this case the intensity has to be determined by considering the $\gamma - \gamma$ efficiency and all the possible decays of the final state. While this procedure is trivial for symmetric 4π arrays, careful attention has to be paid when asymmetric arrays, such as EXOGAM, are used, since the angular distributions of the γ rays affect the observed intensity. In the following section we briefly describe the basic notions on angular distributions and the way they are taken into account in the present analysis.

2.7.2.1 Angular Distributions

In a fusion evaporation reaction the direction of the angular momentum vector $\mathbf{l} = \mathbf{r} \times \mathbf{p}$ of the residual nucleus after particle evaporation is to a good approximation perpendicular to the beam direction. This alignment is slightly attenuated by the emission of evaporated particles (neutrons, protons and α-particles) and by the emission of γ rays. The effect will be to provide a distribution of m states peaked symmetrically around the $m = 0$ value corresponding to the reaction plane. In this situation the angular distribution of a γ ray depends on the multipolarity L of the transition and can be parameterized as:

$$W(\theta) = \sum_k A_k P_k(\cos(\theta)) + \sum_k \rho_k(J_i) A_k(J_i L L' J_f) P_k(\cos(\theta)) \qquad (2.8)$$

where $W(\theta)$ is the γ-ray intensity at angle θ with respect to the beam direction used as quantization axis and ρ_k are the statistical tensors describing the initial state population. For parity-conserving decays, such as γ-ray emissions, k is restricted to even values lower or equal to $2l$ where l is the angular momentum of the emitted photon; $P_k(\cos(\theta))$ are the Legendre polynomials and A_k is the angular distribution coefficient. The A_k value depends on the magnetic-substates population distribution, the multipolarity of the transition and the values of the initial and final state spins. Generally, in fusion evaporation reactions, transition multipolarities are mostly restricted to angular momentum values of 2 or less (i.e. usually only E2, M1 or E1 decays are observed). Therefore only A_2 and A_4 coefficients are needed. The angular distributions for different values of A_2 and A_4 are reported in Fig. 2.25, where the violet and the blue dashed lines represent typical dipole and quadrupole transitions, respectively.

At 0°, 90° and 180° strong differences in intensity are observed, while at 45° and 135° transitions of different multipolarity exhibit the same character.

By measuring the intensity of a γ-ray transition as a function of the detection angle it is possible to distinguish between transitions of different multipolarity and therefore to extract information about the spin and parity of the de-exciting state.

In the present setup EXOGAM was composed of 7 Clovers placed at 90 de-

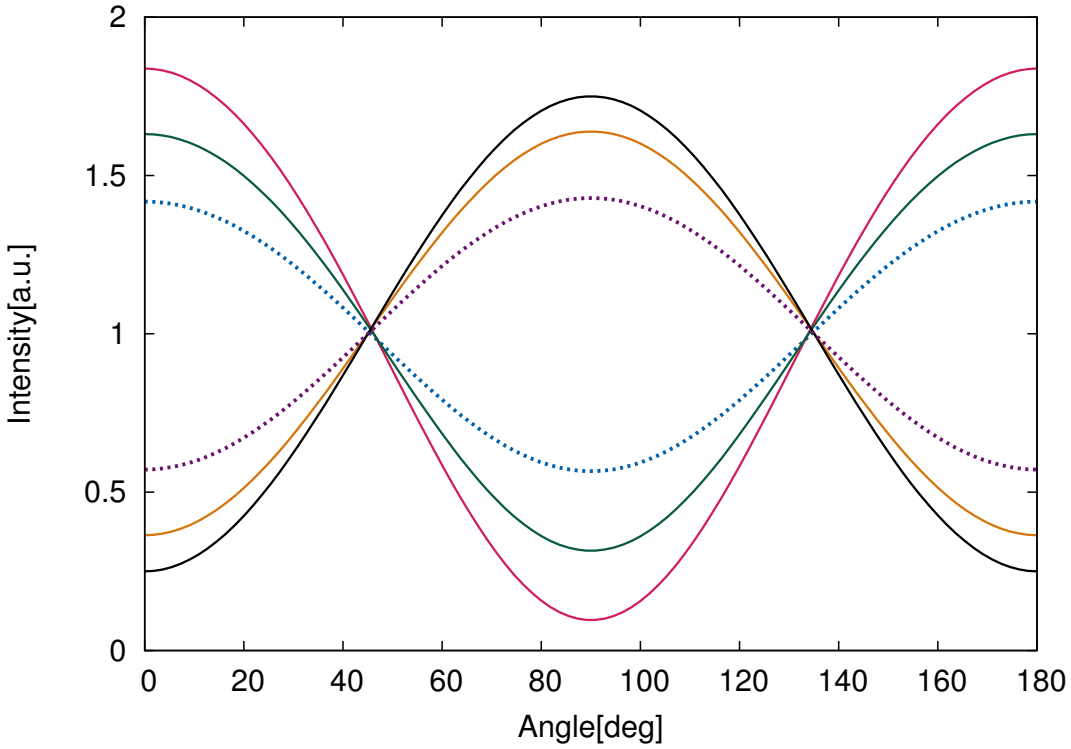

Figure 2.25: Angular distribution for the following values of A_2 and A_4. $A_2 = -0.7; A_2 = 0.0$ (orange); $A_2 = 0.2; A_2 = -0.2$ (red); $A_2 = 0.1; A_2 = -0.1$ (green); $A_2 = -0.8; A_2 = 0.0$ (black); $A_2 = -0.5; A_2 = 0.0$ (dashed violet); $A_2 = 0.4; A_2 = -0.02$ (dashed blue).

grees and 3 Clovers at 135 degrees. Therefore the γ-detection efficiency is a factor $\sim$2.2 larger at 90 with respect to 135 degrees. This implies that dipole transitions are more likely observed than quadrupole transitions, affecting the intensity determination.

Pure dipole transitions between states of the same parity are quite rare. Usually $\Delta j = 1$ parity-conserving transitions present a mixed $E2 + M1$ character. On the other hand, pure stretched $E2$, $\Delta j = 2$ transitions occur frequently, which show strong intensity anisotropies at different angles.

We measured the anisotropy of emission by comparing the efficiency corrected number of γ rays detected at 90° and 135°. This was done in singles spectra for the strongest transitions. Weak transitions are usually visible only in gated

projection of $\gamma - \gamma$ matrices. In this case two asymmetric matrices were created putting on one axis the counts observed from the Clovers placed at 90° (or 135°) and on the other axis the counts from any detector. By gating on the "all" axis we can compare the efficiency corrected number of counts of the γ ray of interest detected at 90° (or 135°) and therefore extract the ratio of the two: $R_{ADO} = \frac{I_{90°}}{I_{135°}}$. The results and the inferred character for the strongest transitions between positive-parity states are reported in Fig. 2.26 and Tab. 2.7, 2.8. The R_{ADO} values obtained from well known E2 transitions in the even-even nuclei ^{24}Mg and ^{20}Ne are reported as well for comparison. The average value is $R_{ADO}(E2) = 0.78$.

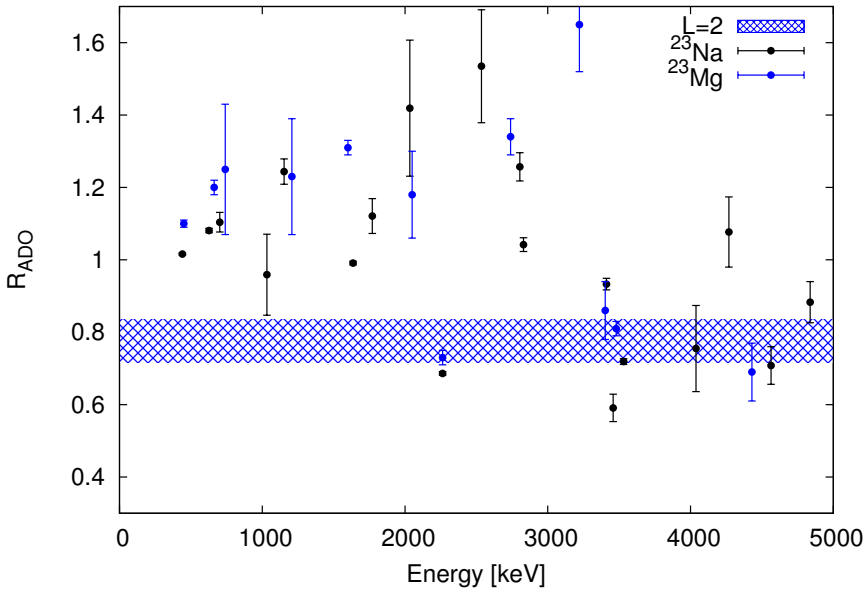

Figure 2.26: R_{ADO} for ^{23}Na and ^{23}Mg measured in the present experiment. Typical values for L=2 stretched quadrupole transitions, obtained by the measured R_{ADO} for known E2 transitions in ^{24}Mg and ^{20}Ne, are highlighted by the blue area.

As shown in Fig. 2.25 the effect of the angular distributions on the detected intensity at 135° is negligible. Therefore to take into account their effect and to determine the real intensity of the γ-ray transitions we considered in our analysis only γ rays detected at 135°. This was done in singles spectra for the strong transitions and in $\gamma - \gamma$ projections gated on the "all" axis for the weak ones.

E_γ (keV)	E_i	E_f	J_i	J_f	$R_{90/135}$	Mult	I
440	440	0	$5/2^+$	$3/2^+$	1.016(3)	M1+E2	1708(6)
1636	2076	440	$7/2^+$	$5/2^+$	0.991(5)	M1+E2	≡1000
2263	2703	440	$9/2^+$	$5/2^+$	0.686(5)	E2	645(5)
627	2703	2076	$9/2^+$	$7/2^+$	1.081(6)	M1+E2	554(3)
2830	5533	2703	$11/2^+$	$9/2^+$	1.042(19)	M1+E2	210(3)
3458	5533	2076	$11/2^+$	$7/2^+$	0.591(38)	E2	56(3)
4038	6115	2076	$11/2^+$	$7/2^+$	0.755(119)	E2	32(5)
3411	6115	2703	$11/2^+$	$9/2^+$	0.933(16)	M1+E2	149(2)
3531	6235	2703	$13/2^+$	$9/2^+$	0.719(8)	E2	368(4)
702	6235	5533	$13/2^+$	$11/2^+$	1.104(27)	M1+E2	54(1)
1033	7268	6235	$13/2^+$	$13/2^+$	0.959(112)	M1+E2	9(2)
1153	7268	6115	$13/2^+$	$11/2^+$	1.244(35)	M1+E2	61(1)
4564	7268	2703	$13/2^+$	$9/2^+$	0.708(52)	E2	67(6)
1771	9038	7268	$15/2^+$	$13/2^+$	1.121(48)	M1+E2	15(4)
3505	9038	5533	$15/2^+$	$11/2^+$			12(4)
2804	9038	6235	$15/2^+$	$13/2^+$	1.257(39)	M1+E2	67(5)
2535	9802	7268	$15/2^+$	$13/2^+$	1.535(156)	M1+E2	12(4)
3568	9802	6235	$15/2^+$	$13/2^+$			22(4)
4269	9802	5533	$15/2^+$	$11/2^+$	1.077(97)	M1+E2	5(3)
2034	11072	9038	$17/2^+$	$15/2^+$	1.419(188)	M1+E2	37(4)
4838	11072	6235	$17/2^+$	$13/2^+$	0.883(57)	E2	16(2)

Table 2.7: Angular distribution, multipolarity and intensity of the transitions between positive parity states in ^{23}Na.

Since the number of counts detected at 135° is obviously lower than the total, a larger error on the number of counts, and therefore on the measured intensity, is obtained.

In Tab. 2.7 and 2.8 we report the ratio between the intensity observed at 90° and 135° for the strongest transitions between positive parity states observed in ^{23}Na and ^{23}Mg in the present experiment, together with the inferred character and the intensity of the transitions.

E_γ (keV)	E_i	E_f	J_i	J_f	$R_{90/135}$	Mult	I
450	450	0	$5/2^+$	$3/2^+$	1.10(1)	M1+E2	1867(38)
1599	2050	450	$7/2^+$	$5/2^+$	1.31(2)	M1+E2	≡1000
2263	2713	450	$9/2^+$	$5/2^+$	0.73(2)	E2	782(22)
663	2713	2050	$9/2^+$	$7/2^+$	1.20(2)	M1+E2	487(4)
2739	5452	2713	$11/2^+$	$9/2^+$	1.34(5)	M1+E2	227(28)
3402	5452	2050	$11/2^+$	$7/2^+$	0.86(8)	E2	101(10)
3223	6115	2713	$11/2^+$	$9/2^+$	1.65(13)	M1+E2	136(10)
3886	6115	2050	$11/2^+$	$7/2^+$			31(4)
3480	6192	2713	$13/2^+$	$9/2^+$	0.81(2)	E2	388(10)
740	6192	5452	$13/2^+$	$11/2^+$	1.25(18)	M1+E2	53(7)
951	7143	6192	$13/2^+$	$13/2^+$			12(7)
1207	7143	6115	$13/2^+$	$11/2^+$	1.23(16)	M1+E2	62(5)
4430	7143	2713	$13/2^+$	$9/2^+$	0.69(8)	E2	126(11)
1794	8937	7143	$15/2^+$	$13/2^+$			23(10)
2745	8937	6192	$15/2^+$	$13/2^+$			56(9)
2451	9594	7143	$15/2^+$	$13/2^+$			18(10)
3402	9594	6192	$15/2^+$	$13/2^+$			27(11)

Table 2.8: Angular distribution, multipolarity and intensity of the transitions between positive parity states in ^{23}Mg.

2.8 Level schemes

The $\gamma - \gamma$ coincidence analysis described in the previous sections, together with the estimated transition intensities allow us to construct the level schemes of the nuclei of interest ^{23}Na and ^{23}Mg which are shown in Fig. 2.27 and 2.28, where the width of the arrows indicates the relative intensity of the transitions. It is important to underline that several other transitions, linking states of both positive and negative parity, were observed in this work. They had been previously reported in [32] and can be confirmed by the present measurement. These transitions correspond to non-*yrast* states, which are weakly populated by the reaction adopted here. We therefore report only the positive parity states relevant for the study of the mirror energy differences.

The level schemes look very similar, as expected for mirror nuclei. We confirm the previously known level schemes and we add two new levels and four new transitions in the case of ^{23}Mg, which are reported in Tab. 2.9. The experimentally known MED can therefore be extended up to $J = 15/2^+$ and are reported in Tab. 2.9.

E_i (keV)	J_i	E_γ(keV)	E_f (keV)	J_f
8937	$15/2^+$	**1794**	7143	$13/2^+$
8937	$15/2^+$	**2745**	6192	$13/2^+$
9594	$15/2^+$	**2451**	7143	$13/2^+$
9594	$15/2^+$	**3402**	6192	$13/2^+$

J	$E_{^{23}Mg}$(keV)	$E_{^{23}Na}$ (keV)	MED (keV))
3	0	0	0
5	450	440	10
7	2050	2076	-26
9	2713	2703	10
11	5452	5533	-81
13	6192	6234	-42
15	8937	9038	-101

Table 2.9: Top: new levels and transitions identified in this work in ^{23}Mg. Bottom: mirror energy differences in the mirror pair ^{23}Mg-^{23}Na.

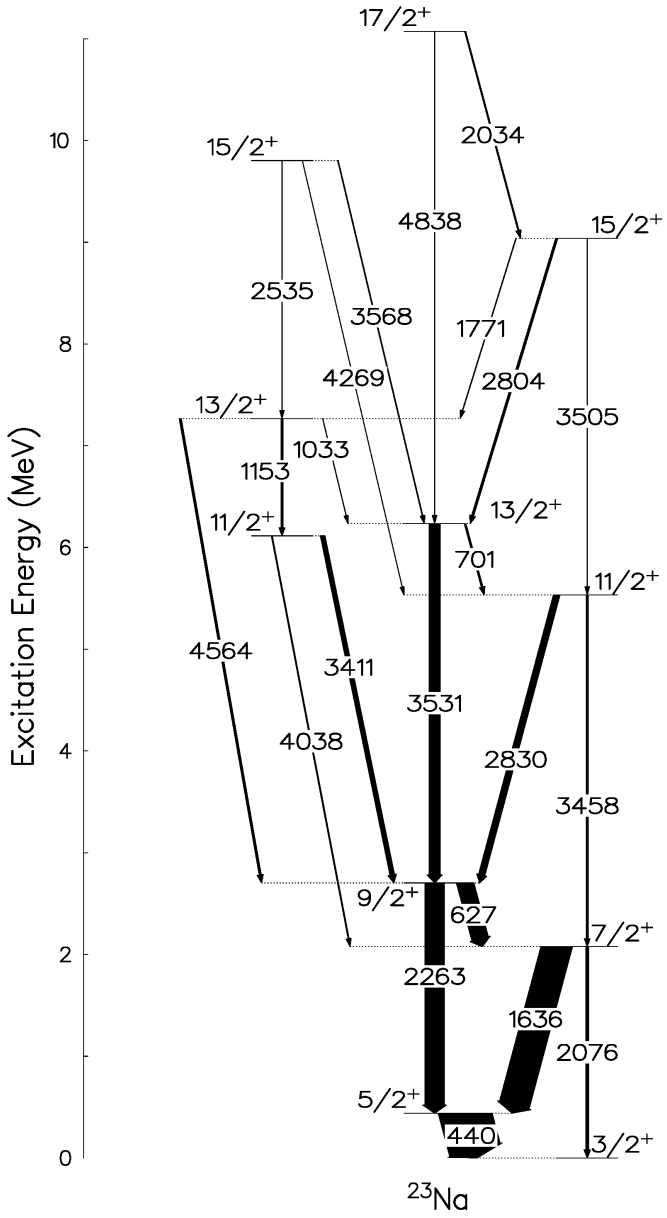

Figure 2.27: Level scheme of positive parity states in ^{23}Na obtained in this work. The width of the arrows indicates the relative intensity of the transitions.

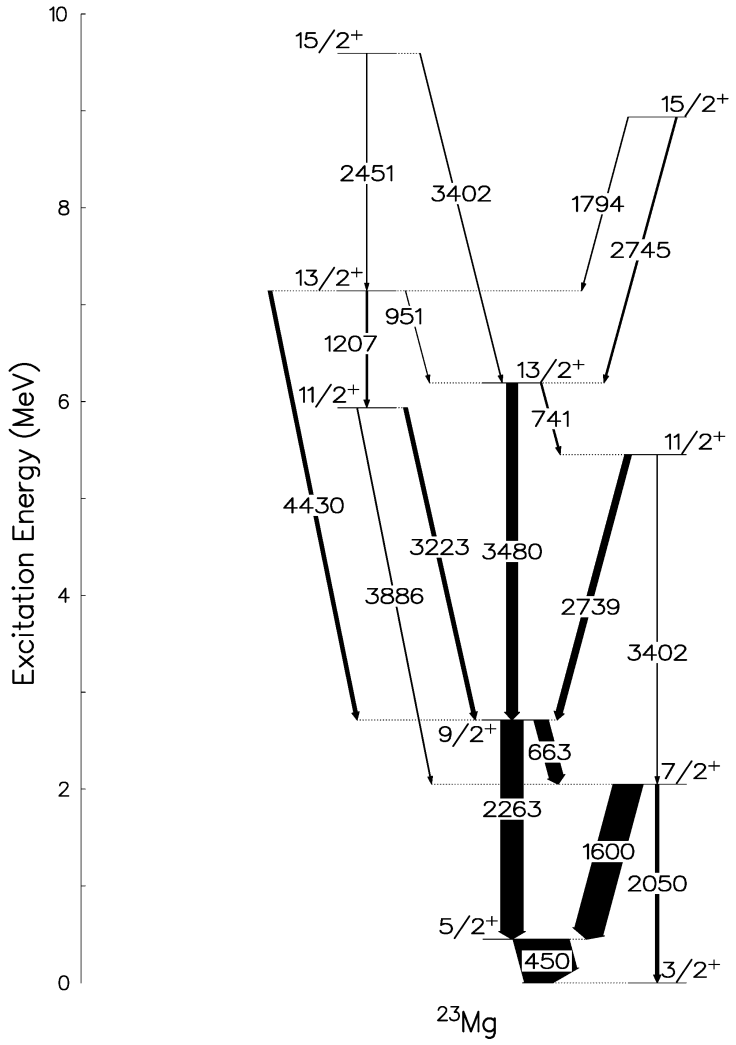

Figure 2.28: Level scheme of positive parity states in ^{23}Mg obtained in this work. The width of the arrows indicates the relative intensity of the transitions.

2.9 Theoretical interpretation

With the measurement described here the experimental MED have been extended up to $J = 15/2^+$. In order to extract information on the nuclear structure of these nuclei and on its evolution with increasing angular momentum, the experimental values have been compared with shell model calculations, performed with the

ANTOINE code [47]. The effective interaction adopted is the USD [48]. This interaction has been deduced for the model space span by the $d_{5/2}$-$s_{1/2}$-$d_{3/2}$ orbits. The comparison between the calculated and the experimental level schemes for ^{23}Na and ^{23}Mg is reported in Fig. 2.29.

The agreement between the calculations and the experimental points is good, confirming the quality of the USD interaction in this mass region. A further test for shell model interactions is represented by their capability to reproduce experimental branching ratios. B(E2) and B(M1) transition probabilities have been calculated and the theoretical branching ratios have been deduced by making use of the experimental transition energies. The comparison with the experimental data is reported in Fig. 2.30, where the measured intensities have been normalized in order to have the same total intensity for the decay from each state.

The experimental branching ratios are reproduced very well by the USD interaction. It is interesting to notice that the values obtained in the present experiment confirm the previously measured ones with the only exception of the decay from the 2703-keV, $J^\pi = 9/2^+$ state. This level decays via a 2263-keV, E2 transition and a 627-keV, E2+M1 γ ray. The branching ratios values reported by Jenkins *et al.* [32] are 63% and 37%, respectively, while in the present work we obtained 54% and 46%, which compare better with the shell model values of 57% and 43%.

The USD interaction allows to obtain a good agreement with the experimental data for both level schemes and branching ratios. However, it is from the study of the mirror energy differences that the most insightful nuclear structure information can be obtained. The first approach we followed is the one reported in Chapter 1 of this thesis and described in detail in [1]. The USD interaction conserves the isospin symmetry and therefore does not contribute to the MED. On the other hand, it determines the wavefunction configuration and the occupation numbers of the different orbitals for each J value. The contribution of the multipole Coulomb interaction V_{CM} has been included using Coulomb matrix elements obtained in the harmonic oscillator basis. In this model space, s orbits have radii larger than the d orbits [15] and therefore the effect of the changes in the nuclear radius as a function of the angular momentum has been estimated from the variation of the occupation numbers of the $s_{1/2}$ orbital with increasing

Figure 2.29: Experimental (black) and calculated (red) level schemes for the mirror pair A=23. The USD interaction [48], without electromagnetic terms, has been used.

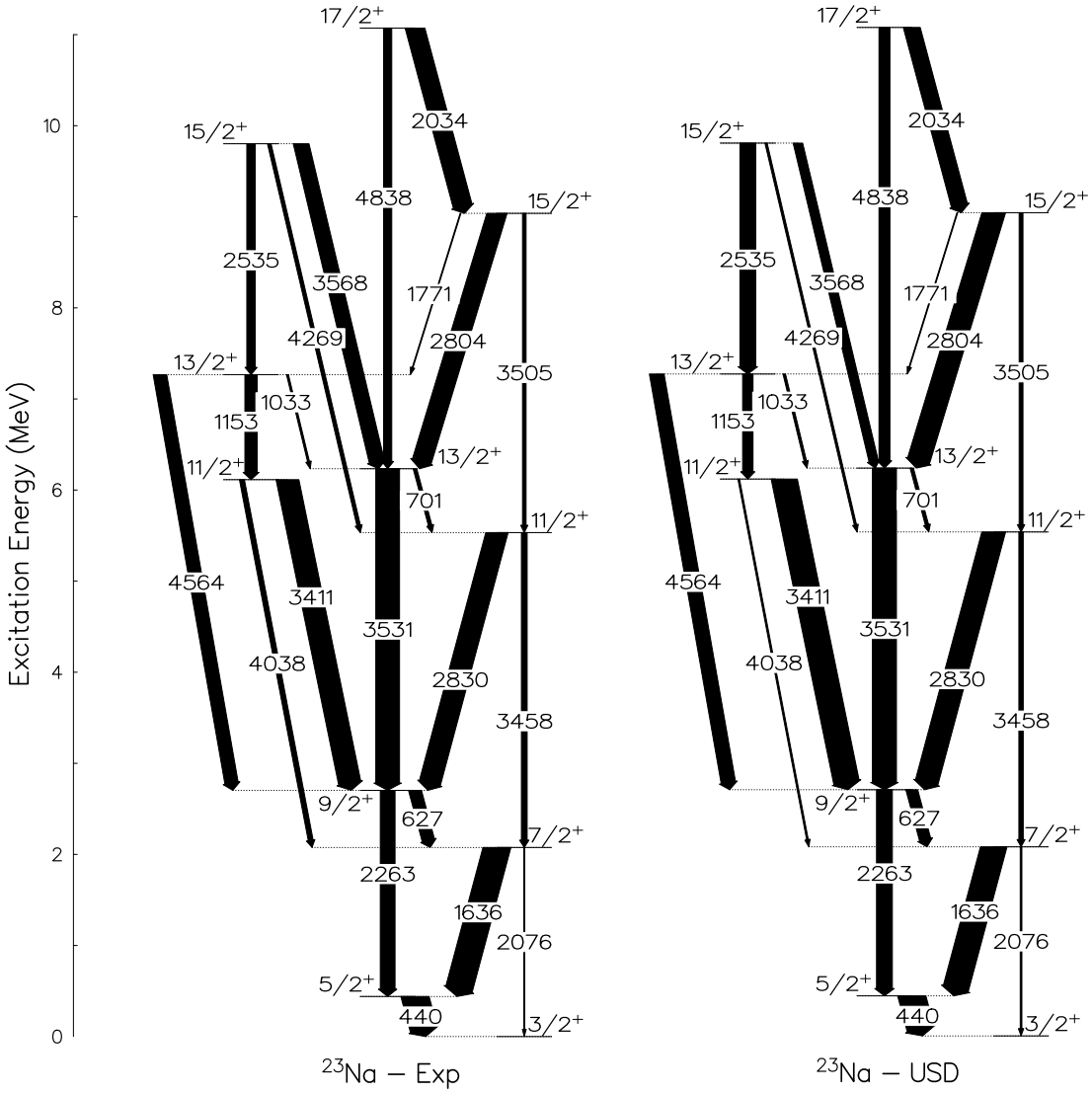

Figure 2.30: Experimental (left) and calculated (right) branching ratios for the mirror pair A=23. The USD interaction [48], without electromagnetic terms, has been used.

J as:

$$\Delta V_{Cm}(J) = \alpha(n_{\pi,s1/2}(0) + n_{\nu,s1/2}(0) - (n_{\pi,s1/2}(J) + n_{\nu,s1/2}(J))$$

where α is the strength of the interaction, set at 100 keV. Corrections to the single-particle energies of protons and neutrons induced by the electromagnetic spin-orbit interaction E_{ls} and the E_{ll} term, described in Sec. 1.2.2.2, have been taken into account as well. Moreover, as we saw in Sec. 1.2.2.3, systematic studies in the $f_{7/2}$ shell have shown that electromagnetic ISB terms are insufficient to reproduce the experimental MED values, and an additional isospin non-conserving term of, apparently, non-Coulomb origin V_B has to be introduced. In the $f_{7/2}$ shell this effect, usually referred as the *J=2 Anomaly*, can be successfully taken into account by using an effective isovector interaction where all the matrix elements are set to zero except the ones relative to two nucleons coupled to $J = 2$ in the $f_{7/2}$ shell. This procedure works particularly well in the $f_{7/2}$ shell, where the wavefunction is dominated by one single orbit. Moving to the *sd* shell the situation changes, since the occupation numbers of the $d_{5/2}$, $s_{1/2}$ and $d_{3/2}$ orbitals can, in principle, be comparable. The contribution to the V_B term relative to two nucleons coupled to $J = 2$ in both the $d_{5/2}$ and $d_{3/2}$ orbits has thus to be considered[1]. An isospin non-conserving isovector interaction was therefore implemented considering as the only two non-null matrix elements the ones corresponding to two nucleons coupled to $J = 2$ in the $d_{5/2}$ and in the $d_{3/2}$ orbits. The strength of these matrix elements was set to 100 keV, in analogy with the value used in the $f_{7/2}$ shell. The effect of these interactions on the MED is reported in Fig. 2.31 together with the contribution of the single orbits.

It is clear how the effect of the $d_{3/2}$ orbital is totally negligible and the $V_B^{J=2}$ term comes entirely from the $d_{5/2}$ shell. In a recent work, Bentley *et al.* examined the J dependence of the isospin non conserving term V_B throughout the whole $f_{7/2}$ shell [17]. They obtained the experimental non-Coulomb isospin-symmetry-breaking term $V_{B,exp}$ for all the known mirror pairs in the shell by subtracting to the measured MED the contribution of the multipole and monopole electromagnetic terms described in Sec. 1.2.2.1 and 1.2.2.2. Subsequently, they fitted the

[1]The $s_{1/2}$ orbit is obviously not considered in this case since the Pauli principle restricts the coupling of two protons in this shell only to $J = 0$.

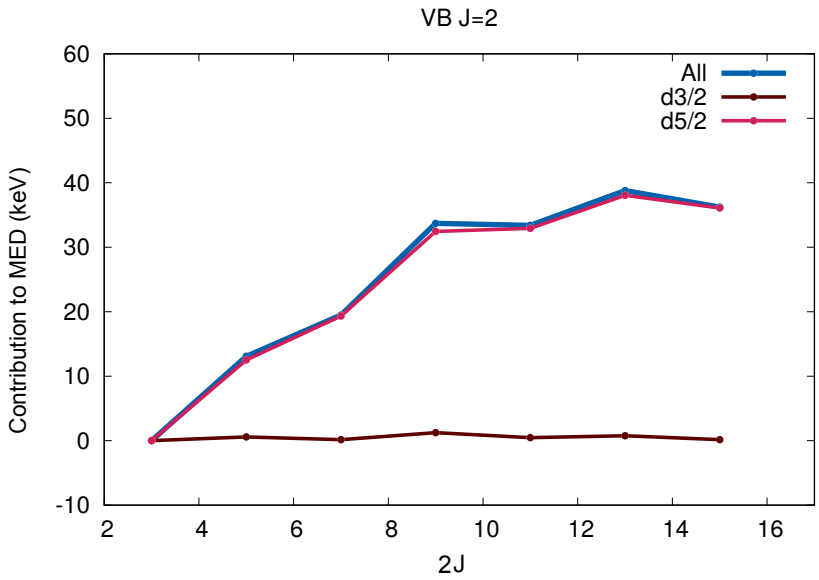

Figure 2.31: Contribution to the isospin non conserving term $V_B^{J=2}$ of the $d_{5/2}$ and $d_{3/2}$ orbits. The overall effect, obtained summing the two, is reported as well.

$V_{B,exp}$ values with the expression:

$$\Delta V_{B,th}(\alpha) = \sum_{J=0,2,4,6} \Delta c_B^J(\alpha) V_B^J$$

where $\Delta c_B^J(\alpha)$ is the difference between the two mirror nuclei of the expectation value of an operator which counts the pairs of protons coupled to angular momentum J in the $f_{7/2}$ shell and α refers to the nuclear excited state. In such a way, they tested the importance of the coupling of two protons to a given J value in the ISB V_B term. The key finding in their work was that either a large positive $J = 2$ or a large negative $J = 0$ term allow to obtain a precise agreement with the experimental data. This suggests that the MED are not sensitive to the absolute values of the ISB isovector matrix elements, and the overall effect depends only on the relative importance of the contributions at different J values. This behavior has been tested in the $f_{7/2}$ shell, where the experimental information available is large. In order to study the analog effect in the *sd* shell we calculated the V_B term relative to two nucleons coupled to $J = 0$ and we compared it with

the $J = 2$ term in the $d_{5/2}$ shell. The results of the comparison are reported in Fig. 2.32.

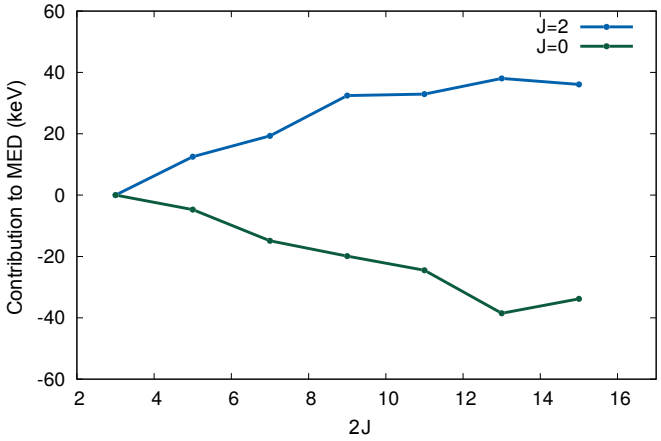

Figure 2.32: Contribution to the isospin non conserving term V_B of the the matrix elements relative to two nucleons coupled to $J = 0$ and $J = 2$ in the $d_{5/2}$ shell.

The contribution of the $J = 0$ term has the same trend and opposite sign with respect to the one of the $J = 2$ one, confirming the results of [17] also for the *sd* shell. As already done in Fig. 2.31 for the $J = 2$ term, we compared the contribution of the different orbits to the $V_B^{J=0}$ term. In this case also the $s_{1/2}$ shell comes into play. The results are reported in Fig. 2.33.

As it was the case for the $J = 2$ term, the major contribution to the $V_B^{J=0}$ term comes from the $d_{5/2}$ orbit, but the effect of the $s_{1/2}$ shell is not negligible and has to be taken into account. It is interesting, at this point, to plot the occupation numbers of the different shells as a function of the angular momentum J. The results are reported in Fig. 2.34.

From the occupation number analysis it is clear how the wavefunction is dominated by particles in the $d_{5/2}$ shell. On the other hand the average number of particles in the $s_{1/2}$ and $d_{3/2}$ orbitals is lower than 2, which explains why the contribution of these shells to the V_B term is smaller.

In the present analysis we considered a V_B term obtained from an effective isovector interaction in which the only non-null matrix elements are the one relative to two nucleons coupled to $J = 0$. The contributions of all the orbits of the *sd* shell have been taken into account. This is almost equivalent to consider the

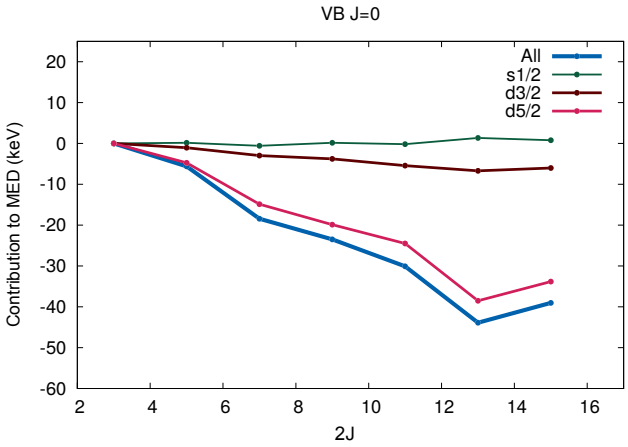

Figure 2.33: Contribution to the isospin non conserving term $V_B^{J=0}$ of the $s_{1/2}$, $d_{5/2}$ and $d_{3/2}$ orbits. The overall effect, obtained summing the two, is reported as well.

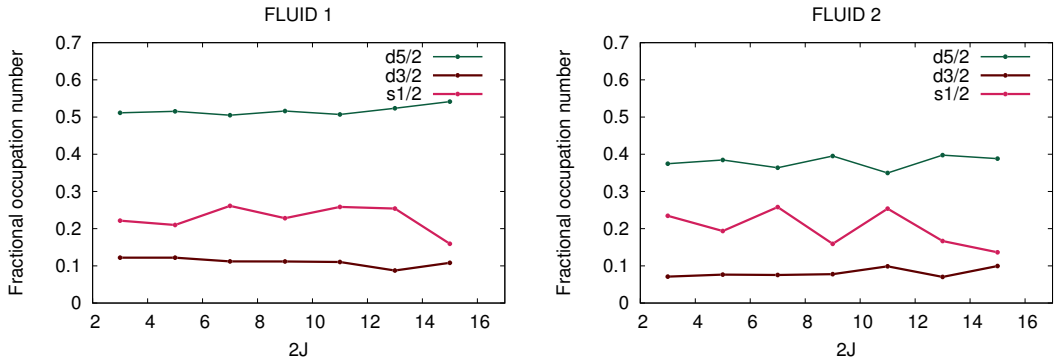

Figure 2.34: Fractional occupation numbers, defined as $\frac{n}{2j+1}$, for the $d_{5/2}$, $s_{1/2}$ and $d_{3/2}$ orbitals for the *yrast* states in the mirror nuclei of mass 23. Fluid 1 corresponds to neutrons for ^{23}Na and protons for ^{23}Mg. The opposite holds for Fluid 2.

term relative to $J = 2$ with an opposite sign, as we saw in Fig. 2.32. The comparison between shell model calculations and the experimental data is reported in Fig. 2.35, where the single contribution of the different terms is shown. The theoretical value MED_{theo} is defined as $MED_{theo} = \Delta V_{CM} + \Delta V_{Cm} + \Delta V_B$, where the strength of the ISB term V_B and the radial term V_{Cm} are set to -60 and 100

keV, respectively.

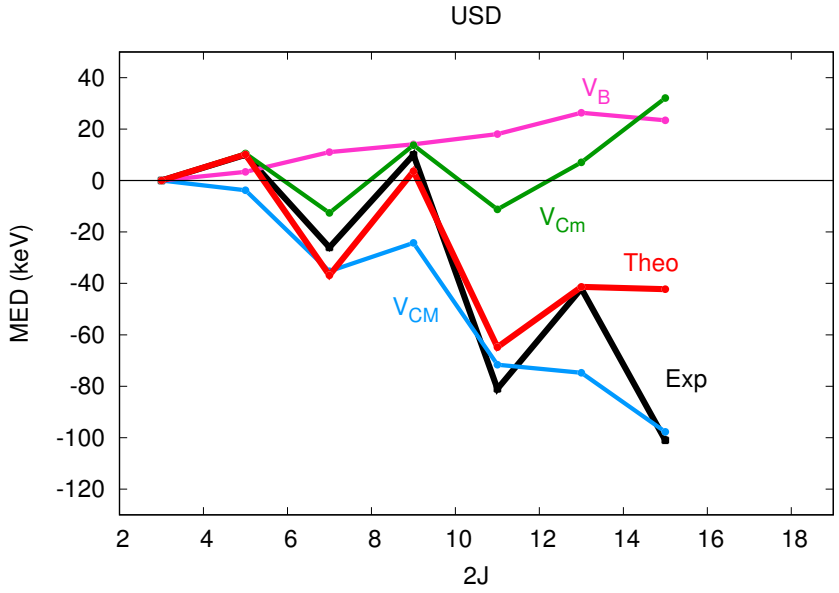

Figure 2.35: Experimental and theoretical MED in mirror nuclei ^{23}Mg $-^{23}$ Na obtained with the USD interaction. The ISB part V_B, the radial contribution V_{Cm} and the multipole term V_{CM} are enlightened.

The trend of the experimental MED is well reproduced by the Coulomb multipole term V_{CM} which is sensitive to the alignment of valence protons: as we saw in Sec. 1.2.2.1 the recoupling of a pair of particles to higher values of angular momentum implies a reduction of the overlap between their wavefunctions, causing a decrease in the Coulomb energy. Since isospin symmetry implies that, when a nucleus aligns protons its mirror aligns neutrons, this affects the MED. On the other hand, it is clear that the radial term V_{Cm} is needed to improve the agreement with the experimental data. This confirms the crucial role played by the $s_{1/2}$ orbit in this mass region. It has been recently argued that the $s_{1/2}$ orbit extends $\sim$ 1.5 fm more than the d orbitals [15], which implies a sizeable effect on the nuclear radius and on the MED when nucleons move from the former to the latter orbit and vice versa. The contribution of the nuclear ISB term V_B is small and never exceeds $\sim$ 30 keV. On the other hand, it clearly improves the agreement with the experimental data. Systematic studies in the *sd* shell depict

a different situation with respect to the one in the $f_{7/2}$, where the V_B term is generally needed: this contribution is essential in mass A=21, where it gives the only negative term crucial to reproduce the experimental data, while its importance is less clear in the other mirror pairs studied so far. Any interpretation of this term is therefore far from being conclusive.

To further investigate this issue an alternative approach has been adopted. The monopole corrected MCI interaction [49] has been used in a no-core approach. This interaction is derived from the realistic nucleon - nucleon N3LO potential [50] so that the Coulomb multipole term, the corrections to the single-particle energies and the nuclear ISB contribution are naturally taken into account. The isospin non conserving part of the nuclear interaction is therefore derived from first principles and not added *ad hoc* as it is the case with the V_B term considered so far. Moreover, different potential wells have been used for protons and neutrons, following ref. [15]: isospin symmetry implies that the proton radius $\rho_{\pi>} = \sqrt{\langle r_\pi^2 \rangle}$ of the proton-rich nucleus of the mirror pair is equal to the neutron radius of the neutron-rich one, $\rho_{\nu<}$. Therefore, considering a Coulomb interaction which depends only on Z and ρ_π, $C_{Z\pi(\nu)} = Z(Z-1)e^2/\rho_\pi$ and neglecting other ISB terms, we can express the difference in binding energy between the two mirror nuclei (the so called Mirror Displacement Energy (MDE)) as:

$$MDE = C_{Z+1\pi>} - C_{Z\pi<} = C_{Z+1\nu<} - C_{Z\pi<} \tag{2.9}$$

The straightforward implication of this relation is that, by knowing the MDE and the proton radius ρ_π of one of the two mirror nuclei, the neutron radius ρ_ν of the same nucleus can be determined as well. Then, the isospin symmetry fixes the proton and neutron radii of the mirror nucleus. This is the basic idea behind the work of Duflo and Zuker [51] who fitted the experimentally known mean square proton radii with the formula:

$$\sqrt{\langle r_\pi^2 \rangle} = \rho_\pi = A^{1/3}\left(\rho_0 - \frac{\zeta}{2}\frac{t}{A^{4/3}} - \frac{v}{2}\left(\frac{t}{2}\right)\right)^2 e^{g/A} \tag{2.10}$$

$$+ \lambda[z(D_\pi - z)/D_\pi^2 \times n(D_\nu - n)/D_\nu^2]A^{-1/3} \tag{2.11}$$

where $t = N - Z$. The term 2.10 is derived by noting that r_π is an isospin vector. Therefore, its square is composed by a scalar, a vector and a tensor component, associated with coefficients ρ_0 , ζ, and ν, respectively [52]. The $\exp(g/A)$ factor corrects for the larger radii observed in light nuclei. The second term 2.11 takes into account the shell effects which depends on the orbital occupancies of the extruder-intruder (EI) valence spaces, delimited by N, Z = 6, 14, 28, 50, ... The degeneracy of each valence shell is then given by $D_{\pi,\nu}$ = 8, 14, 22, ... and the number of active particles is indicated by n, z [53, 54]. The parameter ζ is strictly related to the neutron skin by the relation:

$$\Delta r_{\nu\pi} = \rho_\nu - \rho_\pi = \frac{\zeta t}{A} e^{g/A} \tag{2.12}$$

The quality of the fit of all charge radii of nuclei with mass A<60 turns out to be independent from the value of ζ as far as it is within a reasonable range of 0.3-1.2. This offers the possibility to optimize the value of the neutron skin and, therefore, of the neutron radius ρ_ν in order to reproduce the mirror displacement energy.

The nuclear radius is related to the potential well by the relation:

$$\hbar\omega_\pi = \frac{41.47}{\langle r_\pi^2 \rangle} \sum_i m_i (N_i + 3/2)/A \tag{2.13}$$

where m_i and N_i are the total occupancy and principal quantum number of the main shell i. By fixing the proton and neutron radii to the values that allow to reproduce the mirror displacement energies, the potential wells of the two fluids are determined as well and are, in general, different. In other words the proton radius of the neutron rich nucleus is obtained from the fit of the experimentally known charge radii. From this value the $\hbar\omega_{\pi<}$ and $\hbar\omega_{\nu>}$ can be obtained. The neutron radius of the neutron-rich nucleus (and therefore the proton radius of the proton-rich), is fixed in order to reproduce the MDE. From these, $\hbar\omega_{\pi>}$ and $\hbar\omega_{\nu<}$ are determined as well.

In the standard shell-model calculations on MED one single potential well is used for both protons and neutrons; the use of a different $\hbar\omega$ for each fluid is attempted *for the first time* here. It is important to notice that this implies the use of different matrix elements for each nucleus, since they are adjusted to

the radius of each single isotope. This procedure therefore takes into account the difference in the proton radius between the two nuclei. However, the contribution of the radial term is given by the *variation* of the radius as a function of J. This is the only effect which is not included in this approach and its contribution is therefore taken into account separately, as described in Sec. 1.2.2.2, by computing the variation of the occupation number of the $s_{1/2}$ orbital with increasing angular momentum.

Before calculating the MED, we report in Fig. 2.36 the comparison of the excitation energies calculated with the MCI interaction with the experimental data.

Although the reproduction of the experimental data is slightly worse than the one given by the USD interaction the result is remarkable. It is crucial to keep in mind that, while the effective USD interaction is fitted to the data, the MCI interaction is obtained from first principles. The good agreement obtained represents therefore an encouraging signature of the applicability of these fundamental calculations.

A crucial test bench for shell model interactions is the reproduction of the experimental MED, since they emphasize subtle differences between the mirror nuclei and are by definition extremely sensitive to the isovector isospin non conserving terms of the interaction. We therefore calculated the expected MED for the A=23 mirror pair. The results of the calculations are reported in Fig. 2.37 together with the experimental data.

From Fig. 2.37 it is evident how the shell model calculations performed with the MCI interaction follow very well the trend of the experimental data. This remarkable result shows the possibility to reproduce also the MED data using a realistic no-core interaction which already includes all the relevant ISB terms. It is noteworthy that the agreement with the experimental data seems even better that the one given by the USD interaction, confirming the improvement in the understanding of the origin of the nuclear ISB term. On the other hand it is still clear how the inclusion of the radial term V_{Cm} is crucial to improve the theoretical description, further confirming the fundamental role of the $s_{1/2}$ shell in the evolution of radii in this mass region [55]. This term follows the qualitative trend of the experimental MED for all J values except for $J = 15/2^+$, where the

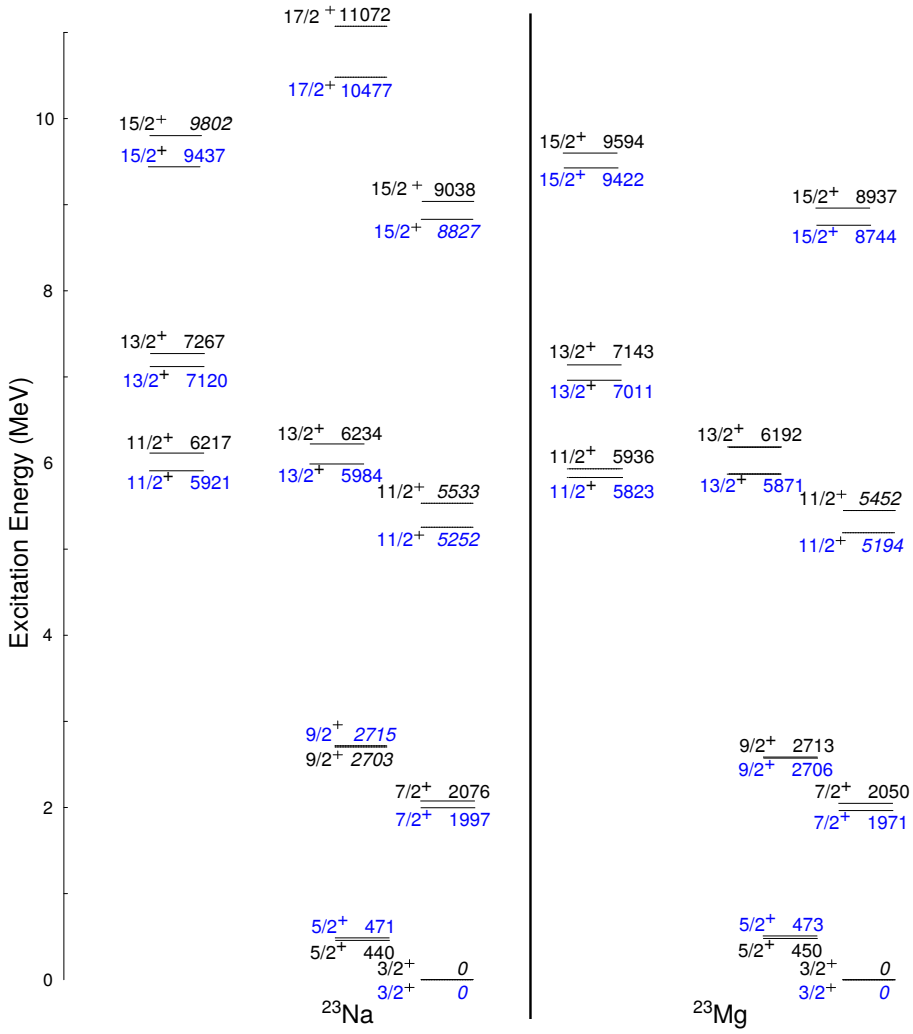

Figure 2.36: Experimental (black) and calculated (blue) level schemes for the nucleus ^{23}Na. The MCI interaction has been used.

predicted sizeable decrease in the number of nucleons in the $s_{1/2}$ orbital should entail a reduction of the radii of the two nuclei and, consequently, an increase in the MED. This effect is however not reflected in the experimental data, where the MED decrease at $J = 15/2^+$.

In order to address this issue we further refined our approach. As already seen, the parameter ζ in relation (2.10) is sensitive to the neutron skin thickness and determines therefore the difference between the proton and neutron radii

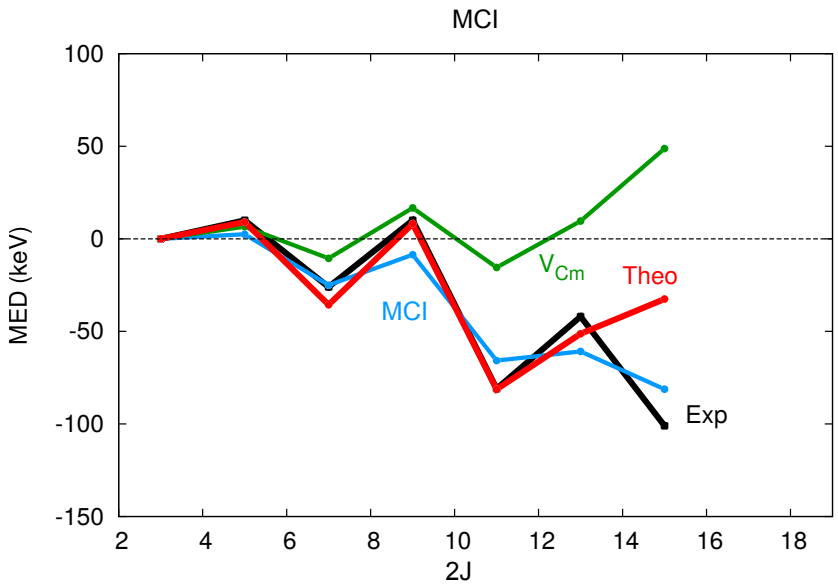

Figure 2.37: Experimental and theoretical MED in mirror nuclei ^{23}Mg $-^{23}$ Na obtained with the MCI interaction. The radial term V_{Cm} and the MCI contribution are enlightened.

in both mirror nuclei. The same procedure described above to find the optimal value of ζ needed to reproduce the MDE in the ground state can in principle be followed also for the excited states. For each value of angular momentum the ideal ζ value which allows to reproduce the differences in excitation energy between the respective analog states can be determined. This requires the fit of the proton radii with the formulas (2.10) and (2.11). The experimental information is however limited to the ground state charge radii. We therefore keep this value fixed to the ground state one and vary the neutron skin ζ in order to reproduce the MED. The procedure is repeated for *each excited state* and therefore the matrix elements are obtained for each excited state varying the size parameter of the harmonic oscillator well in agreement with ζ.

It is interesting to analyze the behavior of the calculated MED when the ζ parameter varies. The case of mass A=23 is reported in Fig. 2.38.

Noticeably, the variation of ζ implies a shift in all the MED but does not change the relative values for the different J states. The trend of the theoretical MED is essentially linear and monotonically decreases as ζ increases. This behav-

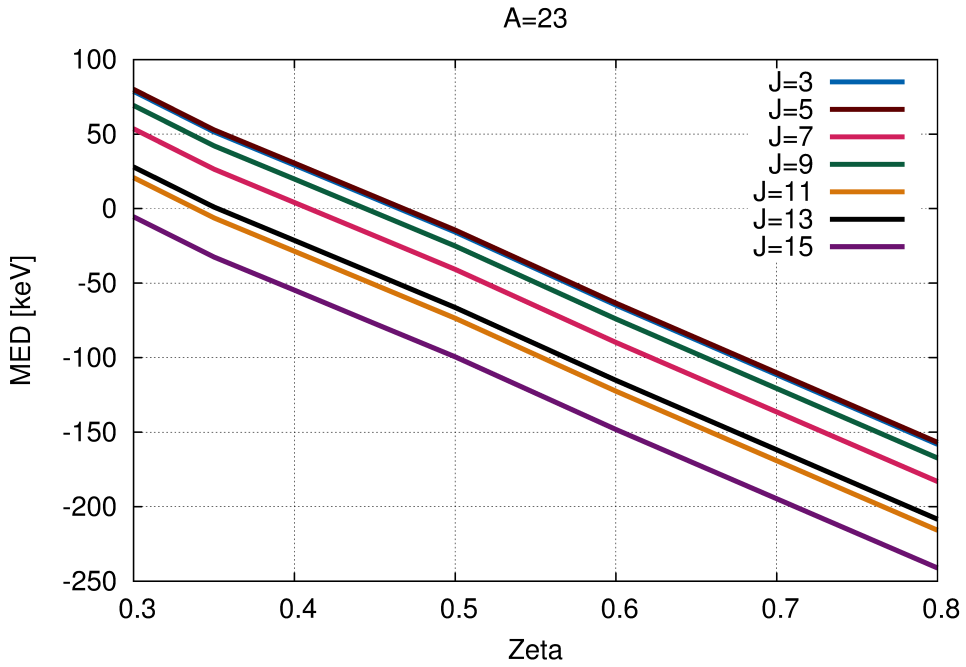

Figure 2.38: Calculated MED for the A=23 mirror pair as a function of the ζ parameter.

ior can be naively explained in the following way: a larger neutron skin implies an increase of the neutron radius in the $N > Z$ member of the mirror pair and therefore of the proton radius of the $N < Z$ nucleus. In the proton rich nucleus the protons will therefore lie farther apart causing a reduction of the Coulomb energy. Since the proton radius of the neutron-rich nucleus is kept fixed, the overall effect will be a net decrease in the MED. It can be shown that this is the case in all the *sd* shell.

The linear trend can be exploited to determine the optimal value of ζ (and therefore of the neutron skin) needed to reproduce the experimental MED value for each level. These ζ values allow, by definition, to reproduce the experimental data. However, in order to have predictive power and to shed light on the nuclear structure effects involved, the origin of the changes in ζ must be investigated. Keeping in mind the link between ζ and the neutron skin, the most straightforward way to proceed is to look for a correlation between ζ and the difference in proton and neutron radii. As already seen the latter are strictly related to the

variation of the occupation numbers of the $s_{1/2}$ orbital. In Fig. 2.39 we report the variation as a function of the angular momentum J of ζ and of the difference between the occupation number of the $s_{1/2}$ orbital for neutrons and protons in the neutron rich member of the mirror pair.

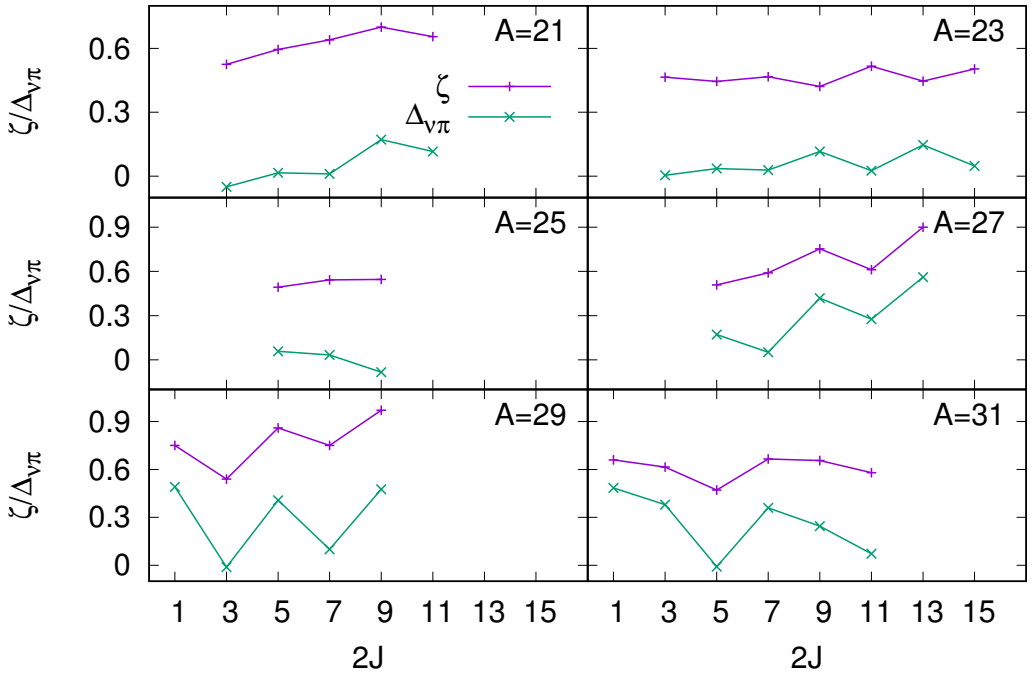

Figure 2.39: ζ and difference in the occupation number of the $s_{1/2}$ orbital for neutrons and protons for the known mirror nuclei in the *sd* shell.

The correlation between the difference in the number of neutrons and protons in the $s_{1/2}$ orbital and the optimal value of ζ is striking, further confirming the crucial role played by this shell in the radius determination. This result is of great importance since it shows the possibility to determine the neutron skin needed to reproduce the experimental MED starting from the calculated occupation numbers. In other words, it offers a way to naturally include the radial term in the interaction. Since all the other isospin non conserving terms known so far are already included in the MCI interaction used here, this represents, in principle, the last step towards a full description of the MED with a unique, complete,

interaction.

It worth considering the physical meaning of this result. In the "usual" approach adopted in the systematic studies in the $f_{7/2}$ shell the radial term is related to the total number of *nucleons* in one specific shell. It gives therefore an *isoscalar* contribution, which does not distinguish between the two fluids and is due to the difference in the proton number Z of the two mirror nuclei. On the other hand, in the new approach presented here, it is the difference between neutron and proton radii, the neutron skin, which gives rise to a sizeable contribution to the MED. In other words, it is an *isovector* contribution. The origin of this effect can be qualitatively understood by keeping in mind that the isospin symmetry implies the equality between the π radius of one nucleus and the ν radius of its mirror. A variation in the neutron skin reflects therefore in a variation between the π radii of the two members of the mirror pair, which naturally affects the MED.

It is clear from Fig. 2.39 how the trend of the difference between neutron and proton occupation numbers with respect to the angular momentum J is always in phase with ζ except for the case of mirror nuclei of mass A=23. Further investigations are ongoing to understand this effect, which will certainly give crucial information on the evolution of the structure of these nuclei with increasing angular momentum J.

The next goal is to find the quantitative relation between the difference in the occupation numbers of neutrons and protons and the skin value needed to reproduce the experimental MED. This would allow to deduce the latter from the former and to include therefore also the radial term in the interaction used in shell model calculations. The resulting predictive capability of this kind of approach would thus be particularly powerful, allowing to clearly identify the contribution of the different ISB terms on the MED and to extract therefore several insightful nuclear structure information from the comparison of the level schemes of mirror nuclei.

Chapter 3

Isospin Mixing in T=1 Isospin triplet ^{46}Cr $-^{46}$ V $-^{46}$ Ti

In this Chapter we report on an experiment performed at GSI (Helmholtzzentrum für Schwerionenforschung), which aimed to study the degree of Isospin Mixing in the T=1, A=46, ^{46}Cr$-^{46}$V$-^{46}$Ti isospin triplet. A theoretical overview of Isospin Mixing along isobaric multiplets has been reported in Sec. 1.2.2.3. In particular it has been shown that, in absence of mixing, the electromagnetic quadrupole matrix elements $\mathcal{M}(E2) \propto \sqrt{B(E2)}$ are linear with respect to the third component of the isospin quantum number, T_z, along a T=1 isospin triplet. To test this relationship, precise measurements of $B(E2 : 0^+_{g.s.} \rightarrow 2^+_1)$ are needed. Experimental values about these reduced transition probabilities can be obtained via either lifetime or Coulomb excitation measurements. The original idea regarding the present experiment was to extract the $B(E2 : 0^+_{g.s.} \rightarrow 2^+_1)$ for ^{46}Cr $-^{46}$ V $-^{46}$ Ti nuclei via precise lifetime measurements of the T=1, 2^+ state in each nucleus. A new technique, based on the use of a triple gold target, was to be adopted to extract lifetimes via a Recoil Distance Doppler Shift method, as we will explain in detail in Sec. 3.3. The use of the same technique, together with identical experimental conditions and the use of the same "analogue" mechanism for the population of the 2^+ states would allow to keep under control the systematic errors and to push forward the precision on the relative measurement.

However the achievable beam intensity during the real experiment was much

lower than the one estimated in the original proposal. This was particularly evident in the case of the ^{46}Cr secondary beam, where the available rate was up to one order of magnitude lower than the expected one. As a result, the predicted statistics was too small to be able to extract valuable information from a lifetime measurement for the 2^+ state in this nucleus. The experiment was therefore split in two parts: the original idea of the Recoil Doppler Distance Shift technique has been used for the less exotic ^{46}V and ^{46}Ti nuclei, while a Coulomb excitation measurement was performed for ^{46}Ti and the challenging ^{46}Cr. The well known stable nucleus ^{46}Ti was studied with both methods to have a reliable reference point. The study of the $B(E2 : 0^+_{g.s.} \rightarrow 2^+_1)$ via Coulomb excitation requires a lower amount of statistics since the total number of counts will be concentrated in a single peak instead of being split in a multiple structure, as it is the case in the RDDS technique. This allows to obtain the quadrupole matrix elements also for the ^{46}Cr nucleus. On the other hand the use of the Coulomb excitation reaction implies that the $B(E2)$ can not be obtained in a model independent way.

This Chapter is divided in several sections. In the first one we present the previous studies and the experimental information available for the nuclei of interest. In Sec. 3.2 and 3.3 we give an outlook on the experimental methods adopted: Coulomb excitation reactions and Recoil Distance Doppler Shift method with a triple gold target. In Sec. 3.4 we describe the experimental setup used in this experiment. Afterwards the different steps of the analysis and the experimental results will be presented.

The analysis of the experiment described here was performed in collaboration with Scott Alexander Milne from the University of York. His focus was mainly related to the triple stack measurement while mine regarded in particular the Coulomb excitation experiment. On the other hand, most of the analysis was in common between the two parts of the experiment and it was therefore developed and optimized in strict collaboration.

3.1 Previous studies

The aim of this work is the measurement of the $B(E2)$ of the $J^\pi : 2^+ \rightarrow 0^+_{g.s.}$ transitions in the T=1 isospin triplet ^{46}Cr $-^{46}$ V $-^{46}$ Ti. The energy of these transitions has been measured many times with different techniques and setups [56, 57, 58, 59, 60, 61]. The adopted values are reported in Fig. 3.1.

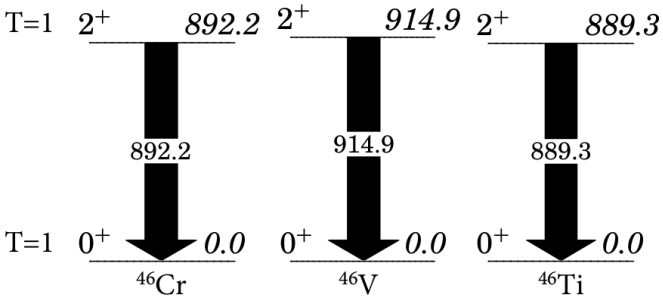

Figure 3.1: Adopted energies for the $J^\pi : 2^+ \rightarrow 0^+_{g.s.}$ transitions in the T=1 Isospin triplet ^{46}Cr $-^{46}$ V $-^{46}$ Ti [56, 57, 58, 59, 60, 61].

On the other hand the $B(E2)$ values and so the transition matrix elements, M_p , are less precisely known. The best experimental information available for ^{46}V and ^{46}Ti comes from a Recoil Distance Doppler Shift experiment performed by O. Möller *et al.* at the University of Cologne [59]. They used the fusion evaporation reaction ^{16}O+^{32}S and the experimental setup was composed of one EUROBALL cluster and five large volume HPGe detectors. The most precise measurement regarding the exotic ^{46}Cr nucleus comes instead from a intermediate-energy Coulomb excitation experiment conducted by K. Yamada *et al.* at RIKEN with the DALI2 scintillator array [62]. The M_p values for all the triplet are reported in Fig. 3.2.

It is clear how any conclusion about the linearity of the matrix elements is impossible to draw due to the large error bars for ^{46}Cr and ^{46}V. A new measurement, aimed at the reduction of the uncertainties, is therefore needed. This is the main goal of the experiment presented here. The choice of this particular triplet was motivated by the study from S.M. Lenzi *et al.* [57] and later shell model calculations, which predict a $2^+_{T=0}$ state within 100-200 keV of the $2^+_{T=1}$ state. This state is currently unobserved. The close energy predicted for the two $J = 2^+$

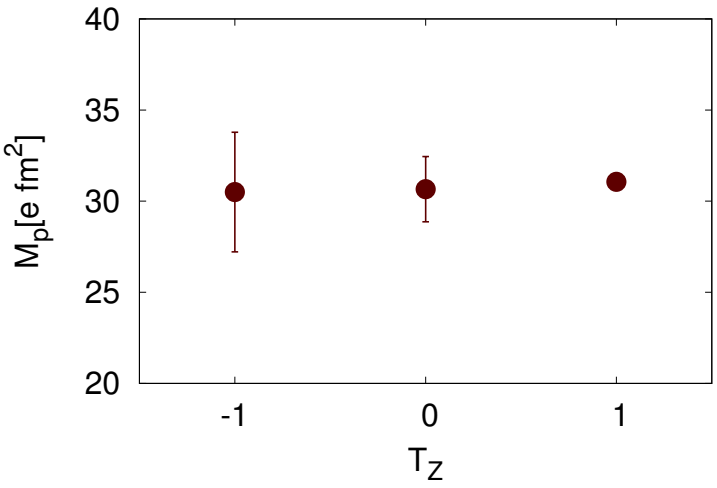

Figure 3.2: Known M_p values for the $J^\pi : 2^+ \rightarrow 0^+_{g.s.}$ transitions in the T=1 Isospin triplet ^{46}Cr $-^{46}$ V $-^{46}$ Ti.

states can induce a sizeable isospin mixing between these levels in ^{46}V, resulting in a deviation from the linear trend of the matrix elements M_p as a function of the third component of the isospin T_Z. Moreover, no other 0^+ or 2^+ states have been observed or predicted at energies close to the ones of the states of interest. Any isospin mixing effect could therefore be unambiguously attributed to the mixing between the $2^+_{T=0}$ and the $2^+_{T=1}$ states in ^{46}V. The A=46, T=1 triplet represents thus an ideal case to look for isospin mixing effects on the quadrupole matrix elements.

3.2 Coulomb excitation

As stated in the introduction to this Chapter, the quadrupole matrix elements for the ^{46}Cr nucleus have been obtained through a Coulomb excitation measurement. Within this technique the $B(E2)$ is estimated from the cross section of the process. In a Coulomb excitation reaction the projectile and/or the target nuclei are excited through the exchange of virtual photons in the Coulomb field of one another. In order to extract the physical information on the electromag-

netic transition probabilities it is of extreme importance to disentangle between the electromagnetic and the nuclear contributions to the excitation of the nuclei. In such a condition the excitation cross section can be expressed using the same electromagnetic multipole matrix element that are used to characterize electromagnetic decays of nuclear levels. A "safe" condition can be obtained by keeping the beam energy below the Coulomb barrier between target and projectile. In this way the distance between two nuclei is always large enough to ensure that the short-range nuclear interaction does not contribute to the excitation. This low energy regime is however impossible for radioactive beams produced by fragmentation with the in-flight technique, where relativistic energies are reached. In this kind of experiments the beam energy is usually above ∼50 MeV/nucleon, i.e. at least an order of magnitude above the maximum energy needed to keep the the center the mass energy of the system below the Coulomb barrier. This limitation is overcome by rejecting events with large scattering angles, which correspond to small impact parameters.

Following the semi-classical approach to relativistic Coulomb excitation reactions proposed by Alder and Winther [63], we can assume that the excitation cross section can be described as the product of the inelastic scattering Rutherford cross section and the Coulomb excitation probability:

$$\left(\frac{d\omega}{d\Omega}\right)_{i\to f} = \left(\frac{d\omega}{d\Omega}\right)_{Rutherford} P_{i\to f} \tag{3.1}$$

where the Coulomb excitation probability $P_{i\to f}$ is given by the square of the excitation amplitude

$$a_{i\to f} = \frac{1}{i\hbar}\int_{-\infty}^{\infty} dt e^{i\omega_{fi}t}\langle f|V(\mathbf{r})|i\rangle \tag{3.2}$$

where $\omega_{fi} = (E_f - E_i)/\hbar = \Delta E/\hbar$ and $V(\mathbf{r})$ is the Coulomb potential, which can be rewritten in a multipole expansion as:

$$V(\mathbf{r}) = \sum_{LM} V_{LM}(\mathbf{r}) = \sum_{LM} \frac{4\pi}{2L+1}\frac{1}{r^{L+1}} Y^*_{LM}(\mathbf{n})\mathbf{M}(EL, M) \tag{3.3}$$

The electric multipole moment $\mathbf{M}(EL, M)$ can be expressed as:

$$\mathbf{M}(EL, M) = \int d^3 r \rho(\mathbf{r}) r^L Y_{LM}(\mathbf{n}) \tag{3.4}$$

This is related to the reduced transition probability by the expression:

$$B(EL; i \to f) = \sum_{M_i M_f} |(\mathbf{M}(EL, M))_{fi}|^2 = \frac{1}{2J_i + 1} |\langle f || \mathbf{M}(EL, M) || i \rangle|^2 \tag{3.5}$$

where the second equation makes use of the reduced matrix element, which eliminates the dependence from the projections on M_i. The reduced transition probability for the inverse transition $f \to i$ is simply given by

$$B(EL; f \to i) = \frac{2J_i + 1}{2J_f + 1} B(EL; i \to f) \tag{3.6}$$

The multipole expansion given by Eq. (3.3) allows to rewrite Eq. (3.2) as:

$$a_{i \to f} = i \sum_{\lambda} \chi^{\lambda}_{i \to f} f_{\lambda}(\xi) \tag{3.7}$$

χ is the strength parameter expressed as:

$$\chi^{(\pi\lambda)}_{i \to f} \approx \frac{Z_t e \langle f | M(\pi\lambda\mu) | i \rangle}{\hbar c b^{\lambda}} \tag{3.8}$$

where b is the distance of closest approach between the two nuclei.

The factor $f_{\lambda}(\xi)$ is a measure of the adiabaticity of the collision. The parameter ξ is related to the time the projectile spends in proximity of the target and to the timescale of the internal motion of the excited nucleus and can be expressed as:

$$\xi = \frac{\tau_{collision}}{\tau_{nuclear}} = \frac{b}{\gamma v} \frac{\Delta E}{\hbar} \tag{3.9}$$

For large values of ξ the collision will be adiabatic, $f_{\lambda}(\xi) \propto e^{-\pi\xi}$ and the excitation probability is small. This condition is fulfilled for large impact parameter, low velocity or large excitation energy. On the other hand, if ξ is small, $f_{\lambda}(\xi) \to 1$, a more violent reaction occurs and the excitation probability is larger.

In low energy Coulomb excitation reactions, due to the small velocity of the projectile, the adiabatic condition is avoided only for excitation energy up to 1-2 MeV, while in the relativistic regime ξ is generally an order of magnitude smaller and states of energy 10-20 MeV can be reached.

The total cross section for exciting a state by pure Coulomb excitation is obtained by integrating $|\chi|^2$ over impact parameter b_{min} and b_{max}

$$\sigma_\lambda = 2\pi \int_{b_{min}}^{b_{max}} bdb|\chi^{(\pi\lambda)}(b)|^2 \tag{3.10}$$

In relativistic reactions the analysis is restricted to very forward scattering and therefore to large impact parameters b below which nuclear interactions can also occur. A lower limit for b can be set as the sum of the radii of the interacting nuclei plus 5 fm: $R = R_T + R_P$ +5 fm.

$$\sigma_{\pi\lambda} \approx \left(\frac{Z_t e^2}{\hbar c}\right)^2 \frac{\pi B(\pi\lambda; 0 \to \lambda)}{e^2 R^{2\lambda-2}} (\lambda - 1)^{-1} \tag{3.11}$$

The sum over π and λ give the total cross section:

$$\sigma_{i\to f} = \sum_{\pi\lambda} \sigma_{\pi\lambda} \tag{3.12}$$

Eq. (3.11) express the relation between the Coulomb excitation cross section and the B(E2) value.

3.3 Triple target measurement

The Recoil Distance Doppler Shift (RDDS) method is a well established experimental technique to measure lifetimes of nuclear states in a range $1 - 100$ ps. It exploits the different energy shifts exhibited by γ rays emitted at different velocities by the recoiling nucleus due to the Doppler effect. The energy measured in the laboratory frame is given by:

$$E^\gamma = E_0^\gamma \frac{\sqrt{1-\beta^2}}{1 - \beta\cos(\theta)}$$

Different velocities β will therefore cause different observed energies in the

laboratory frame. In the most conventional configuration a target-degrader system is used to vary the value of β. The target foil is used to populate the state of interest while the degrader either slows or stops the recoiling nucleus. The velocity of the nucleus is therefore different before and after the degrader resulting in different Doppler shifts depending on where the γ ray emission takes place. The distribution of counts in the two peaks is strictly related to the lifetime of the state under analysis. If we call I_u and I_s the number of counts relative to γ rays emitted, respectively, after and before the degrader we have the following relations:

$$\begin{aligned} I_u(t) &= N_0 e^{-\frac{d}{v\tau}} \\ I_s(t) &= N_0 - N_0 e^{-\frac{d}{v\tau}} \\ R &= \frac{I_u}{I_u + I_s} = e^{-\frac{d}{v\tau}} = e^{-\frac{d}{\beta c\tau}} \end{aligned} \tag{3.13}$$

where d is the distance between target and degrader, N_0 is the total number of the nuclei of interest, and τ is the lifetime of the nuclear state, which can be therefore determined by the ratio R of the areas of the two peaks.

In the present experiment a similar technique for high-precision in-beam lifetime measurements, developed at the University of York, has been used. The underlying idea is the same as the one described for the conventional RDDS method but instead of a target-degrader combination a new-developed device, known as Stretched Gold Target (SGT), has been used. It consists of three gold foils, separated by a fixed distance, resulting in a triple structure for the transition of interest. In such a way each of the three targets acts both as target and as degrader, enhancing the excitation probability, as schematically reported in Fig. 3.3. To properly extract the lifetime of the state of interest, detailed lineshape simulations have to be performed. The excitation probability in each gold foil, the decays which occur inside one of the targets, the absorption of γ rays in the gold material and the angular distributions of the de-exciting transitions affect the lineshape of the triple-peak structure and therefore have to be taken into account.

To increase the sensitivity of the measurement and to get the best possible results a number of SGT properties have to be optimized.The most crucial point is the thickness of each gold foil as it affects the excitation yield, the energy loss and

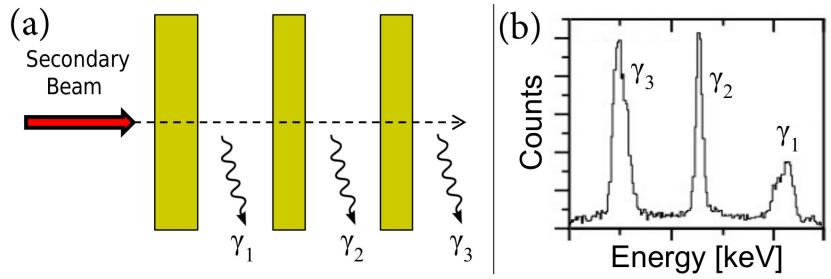

Figure 3.3: (a) Schematic view of the Stretched Gold Target (SGT) developed at the University of York. The three gold foils act both as targets and as degraders. (b) Simulated triple peak structure resulting from the use of the SGT device. The Doppler correction is optimized for the second peak. As a consequence, the first and third peaks show a larger broadening. Picture taken from [64].

the portion of ions which decay inside the target. A thicker target ensures a larger amount of statistics but, on the other hand, a larger number of ions will decay inside it, reducing the resolvability of the triple structure. Moreover the thickness needs to be sufficient to induce a sizeable slowing down of the recoiling nuclei, improving the separation of the peaks. In order to find the optimal thickness, detailed simulations (performed by S.A. Milne from the University of York [64]) have resulted in the choice of 0.375-0.25-0.25 mm for the three targets.

The distance between the gold foils affects the distribution of counts in the three peaks and it is therefore strictly related to the sensitivity of the measurement to different values of lifetimes. To determine the optimal distances detailed simulations have been performed in the region of interest for the estimated lifetimes, ~ 5 ps. Following this procedure a separation of 1.0 mm between both the first and the second, and the second and the third target, have been chosen. The design of the Stretched Gold Target used in the present experiment is reported in Fig. 3.4.

The beam energy has to be tuned since it affects both the excitation cross section and the recoiling ions velocity, i.e. the separation of the peaks. Moreover shell model estimates predict two 2^+ states, one with $T = 0$ and the other with $T = 1$ in ^{46}V within 100 keV in excitation energy and a 1^+ state within 80 keV. Therefore the beam energy has been chosen in order to avoid any overlap between the γ-ray structures corresponding to different transitions. Detailed simulations

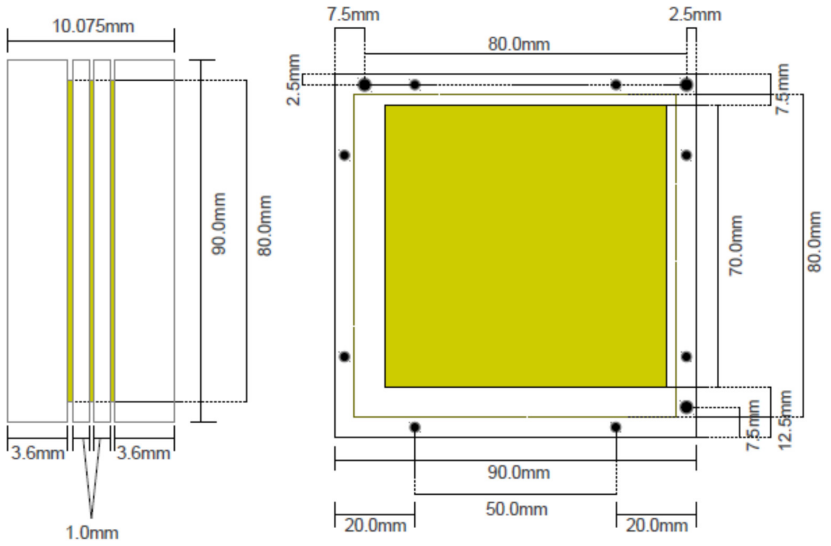

Figure 3.4: Stretched Gold Target used in the present experiment. Aluminum frames are placed around the gold foils [64].

considering the energy loss in each gold foil, the ion velocity after each target and the consequent separation of the peaks have been performed, resulting in a ideal secondary beam energy of 175 MeV/u.

3.4 Experimental Setup

The experiment presented here was performed in the framework of the PreSPEC-AGATA campaign (2012-2014), which took place at the GSI (Helmholtzzentrum für Schwerionenforschung) in Darmstadt, Germany. The PreSPEC collaboration is a part of the NUclear-STructure, Astrophysics and Reactions (NUSTAR) collaboration, which has the goal of coordinating and promoting the nuclear physics program conducted at GSI and planned for FAIR.

In the PreSPEC-AGATA campaign, radioactive beams were produced via the in-flight fragmentation technique at relativistic energies. The secondary beams of interest were separated and selected by the FRagment Separator (FRS) system and then impinged on a reaction target, surrounded downstream by the Advanced GAmma Tracking Array (AGATA) γ-ray array. The reaction products were then identified by the LYCCA calorimeter. A sketch of the experimental setup is reported in Fig. 3.5. In this section we will briefly describe the different parts of the apparatus.

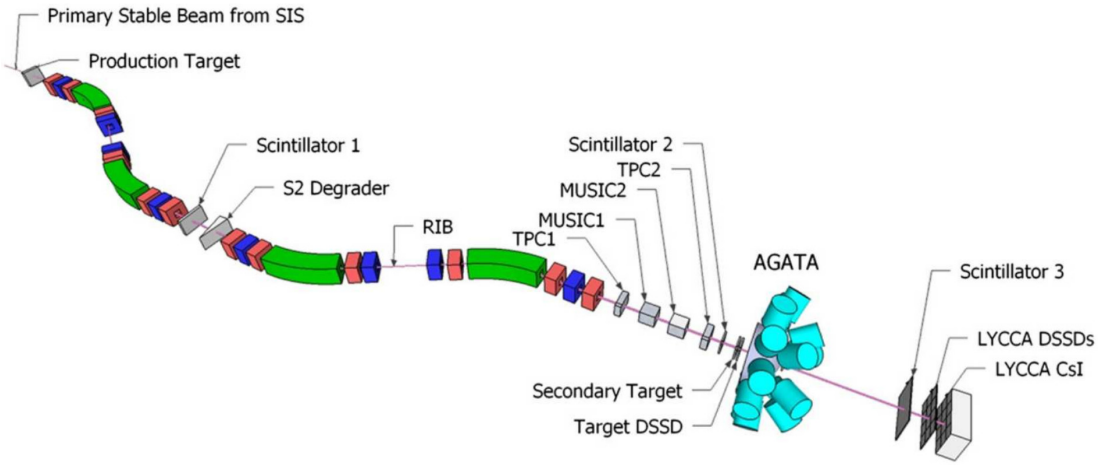

Figure 3.5: Schematic view of the experimental setup used in the PreSPEC-AGATA campaign at GSI [65].

3.4.1 Beam production

The production of radioactive beams at the FRS-GSI facility is obtained through the in-flight fragmentation technique. The Electron Cyclotron Resonance (ECR) ion source provides a beam of stable ions which are subsequently accelerated by the UNiversal LINear ACcelerator (UNILAC) up to 20 MeV/u energy. The pre-accelerated beam is then injected in the SchwerIonenSynchroton (SIS-18) which has a radius of 34.5 m and can provide a maximal bending power of 18 Tm. The accelerating potential is achieved through two radiofrequency cavities at 16 kV, which allows to reach beam energies up to 2 GeV/u [66]. The extraction of the beam from the SIS-18 requires at least one second. The extracted beam has therefore a time structure in spills characterized by a typical one second extraction and three seconds ramping time. Beam intensity up to $\sim 3 \cdot 10^9$ ions/spill can be achieved. The primary beam is then sent to a light production target (usually beryllium), where it undergoes a fragmentation reaction. In such a way, a cocktail of reaction fragments with lower mass is produced. In the present experiment a primary beam of ^{58}Ni and a thick 2.5 g/cm^2 ^{9}Be production target have been used.

After the fragmentation reaction, the secondary beams are sent to the FRagment Separator (FRS), described in the next section, where they are selected and separated.

3.4.2 The FRagment Separator (FRS)

The FRagment Separator (FRS) [67] is a double-achromatic magnetic spectrometer designed to separate the relativistic ions produced in the fragmentation of the SIS beams. It is divided in four sections, each of which comprises a magnetic dipole. The FRS exploits the $B\rho - \Delta E - B\rho$ method, combining the mass spectroscopy through magnetic fields with the analysis of the energy loss ΔE of ions in matter. This procedure allows to select the fragments both in A and Z. A particle of mass A and charge q inside a magnetic field B is subjected to the Lorentz force:

$$B\rho = \beta\gamma\frac{A}{q} \tag{3.14}$$

where ρ is the particle trajectory, and β and γ are the relativistic parameters. For fully stripped ions $q = Z$. The quantity $B\rho$ is called *magnetic rigidity* and determines the trajectory of the ions inside the bending magnets. The first two dipoles separate the relativistic fragments according to the A/q ratio. Therefore ions with the same $B\rho$ are focused at the same point in the second focal plane S2. The other two dipoles act in the opposite way, counterbalancing the dispersion in momentum. This implies that the position on the last focal plane S4 depends only from the A/q ratio and not from the initial ion velocity β, i.e. the FRS system is achromatic. The FRS optics is sketched in Fig. 3.6.

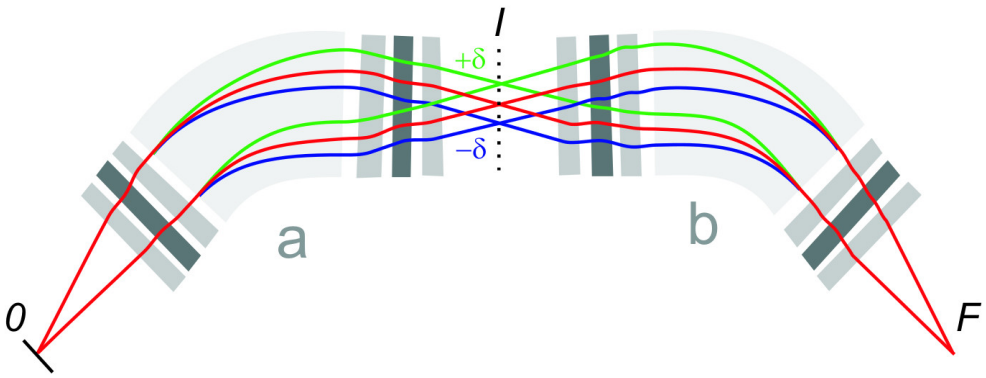

Figure 3.6: Schematic view of the FRS achromatic optics. a) and b) label the first two and second two dipoles of FRS, respectively. In the second focal plane S2, placed in position I in the figure, ions with the same A/q are dispersed due to the different initial momentum. This effect is counterbalanced in the last two dipoles, giving an overall achromatic transmission. Picture taken from [68].

Each of the four FRS sections is also equipped with a series of quadrupoles and hexapoles. Magnetic quadrupoles defocus the beam along one direction and focus it along the perpendicular one. A proper combination of quadrupoles has therefore the overall effect of focusing the beam both in X and Y axis. Magnetic hexapoles are placed along the beam path to correct higher order aberrations. To further improve the selection capabilities of the FRS, a wedge degrader is placed in S2. The energy loss of an atomic specie in the matter is proportional to Z^2

according to the well-known Bethe-Bloch relation:

$$-\left\langle \frac{dE}{dx} \right\rangle = \frac{4\pi n Z^2}{m_e c^2 \beta^2} \left(\frac{e^2}{4\pi e_0} \right)^2 \left[\ln \left(\frac{2 m_e c^2 \beta^2}{I(1-\beta^2)} \right) - \beta^2 \right] \tag{3.15}$$

where n is the electron density of the material, m_e and e are the electron mass and charge and I is the excitation potential of the material. The energy loss inside the degrader implies a variation in the $B\rho$ of the fragment. Since different atomic species will loose a different amount of energy, this causes a separation also in Z. Fig. 3.7 helps to understand the isotope selection in the FRS. The first two dipoles separate the ions in A/q and therefore select the areas of the nuclide chart identified by the full lines. The energy loss in the degrader varies the $B\rho$ depending on the proton number Z. Finally, the last two dipoles separate the fragments according to the new value of $B\rho$ resulting in a selection also in Z illustrated by the dotted lines. A complete scheme of the $B\rho - \Delta E - B\rho$ method within the FRagment Separator is reported in Fig. 3.8.

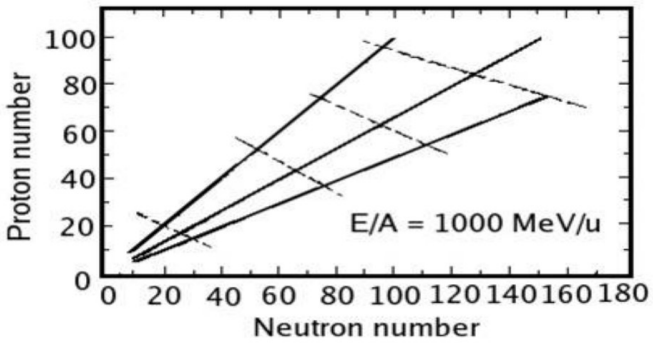

Figure 3.7: Schematic view of the FRS isotope selection. Picture taken from [67].

Five sets of thick copper slits (reported in Fig. 3.9) are placed along the beam path in FRS. The first one is situated after the reaction target, and the other four after each focal plane. The aim of the slits is to cut the acceptance of the spectrometer in X and Y direction, in order to eliminate contaminant fragments. The magnetic field of the dipoles is tuned in such a way to transmit the desired secondary beam along the central trajectory. Since different isotopes will have different trajectories, the slits can be adjusted in order to stop most of the undesired ions.

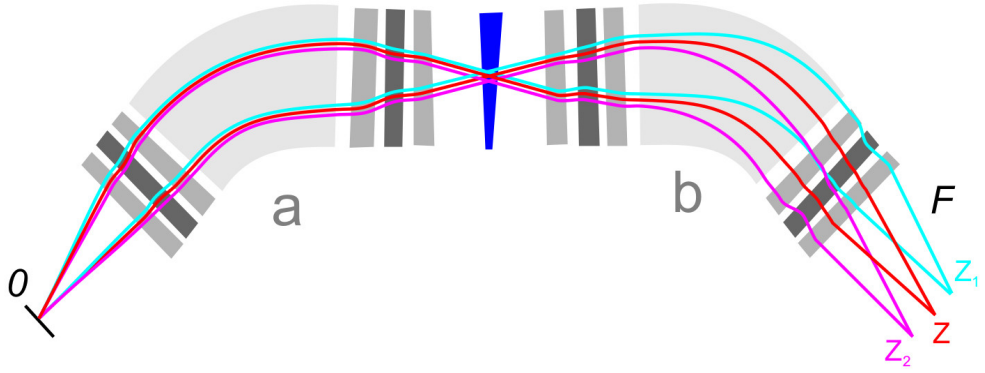

Figure 3.8: Schematic view of the $B\rho - \Delta E - B\rho$ method within the FRS. The blue degrader varies the $B\rho$ depending on the proton number Z. Picture taken from [68].

The optical properties of the FRS are determined by two quantities: the dispersion parameter D and the magnification M. The dispersion parameter is defined as:

$$D = \frac{\Delta x}{\Delta B\rho / B\rho} \tag{3.16}$$

where Δx is the distance in the horizontal direction. The dispersion parameter D is sufficient to determine the magnetic rigidity of an ion after the first two dipoles in FRS. Calling $(B\rho_0)_2$ the magnetic rigidity of the central trajectory we can obtain the $B\rho$ of a fragment which pass at position x_2 in S2 from the relation:

$$B\rho_2 = (B\rho_0)_2 \left(1 + \frac{x_2}{D_2}\right) \tag{3.17}$$

In a similar way the magnetic rigidity in the final focal plane $S4$ can be determined from the position x_4 in the horizontal dispersive plane, the dispersion parameter D_4 and the magnification M, following:

$$B\rho_4 = (B\rho_0)_4 \left(1 + \frac{x_4 - Mx_4}{D_4}\right) \tag{3.18}$$

By adjusting the shape of the degrader in S2 and the magnetic settings, the FRS can be run either in monochromatic or achromatic mode. The monochro-

Figure 3.9: Thick copper slits placed along FRS beam line.

matic setting is used when a mono-energetic secondary beam is needed. For a given A/q the position of the fragments in S2 depends from the ion velocity. By using a shaped degrader, the energy loss of the ions in the material compensates this momentum spread, resulting in a well defined fixed energy for all the ions of the same specie after the degrader, as reported in Fig. 3.10. On the other hand this kind of setting induces a broad spatial distribution at the final focal plane.

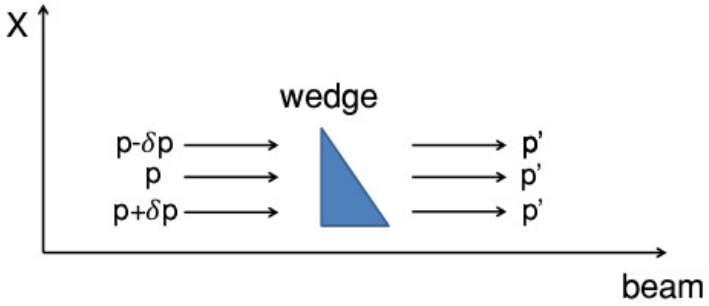

Figure 3.10: The energy loss of the ions in the shaped degrader counterbalances the momentum dispersion of ions with the same A/q.

In the present experiment FRS was used in the achromatic mode, which focuses fragments with the same A/q at the same x position in S4, independently

from the initial momentum p_0. For a fixed value of A/q, the dispersion on the focal plane due to the momentum spread is

$$\Delta x = D\Delta p/p_0 = D\Delta B\rho/B\rho \tag{3.19}$$

If no material is put in S2 the achromaticity condition can be obtained from Eq. (3.17) and (3.18): $D_4 = -D_2 M_4$. If a shaped wedge is placed in S2 the energy loss in it depends from the position x_2 and therefore from the initial momentum difference, according to $\Delta x_2 = D_2(\Delta p/p_0)$. Calling p_1 and p_2 the momenta of two different fragments, the achromaticity condition can be satisfied if the degrader shape is chosen in such a way that $\Delta p_1/p_1 = \Delta p_2/p_2$. This mode reduces the spatial distribution of a given isotope at the final focal plane, so that contaminants arriving at different positions in S4 can be removed by using slits in S3 and S4. The choice of the achromatic mode in the present experiment was motivated by the higher estimates for secondary beam rates. Three main settings were used to produce the secondary beams of interest: ^{46}Cr, ^{46}V, ^{46}Ti. In order to have a energy of $\sim$ 170 MeV/u at the secondary target for all the beams, different degraders were put in S1 and S2, as summarized in Tab. 3.1.

Beam	^{46}Cr	^{46}V	^{46}Ti
Secondary Target	2.5 g/cm^2 ^{9}Be	2.5 g/cm^2 ^{9}Be	2.5 g/cm^2 ^{9}Be
S1 degrader	2.0 g/cm^2 ^{27}Al	2.0 g/cm^2 ^{27}Al	2.0 g/cm^2 ^{27}Al
S2 degrader	8.0 g/cm^2 ^{27}Al	6.8 g/cm^2 ^{27}Al	5.7 g/cm^2 ^{27}Al

Table 3.1: Targets and degraders used in FRS for the different settings.

To uniquely identify a isotope, its position, velocity and atomic number have to be measured. This is possible thanks to a series of detectors which are placed along the FRS beam line, which will be described in the next sections.

3.4.2.1 Detectors along FRS beam line

Time Projection Chambers Time Projection Chambers (TPCs) are detectors used to measure x and y positions along the beam line [69]. Two TPCs are placed in the second focal plane S2 and two in last focal plane S4. The availability

of two (x_1, y_1) and (x_2, y_2) measurements at different positions z_1 and z_2 along the beam axis allows to extrapolate the (x_3, y_3) position at any other z_3 position, tracking the particle trajectory. The volume of each TPC is filled with a mixture of 10% methane and 90 % argon. A charged incident particle ionizes the gas, producing electron-ion pairs. A uniform electric field is generated by applying a high voltage between a cathode and four anodes wires, placed into C-shaped cathodes, as illustrated in Fig. 3.11.

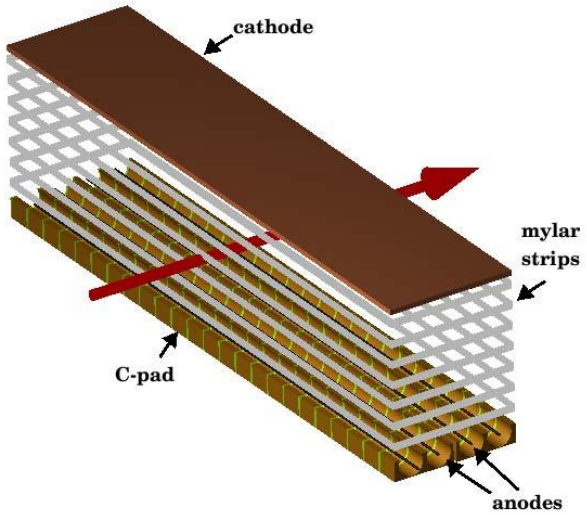

Figure 3.11: Drawing of a Time Projection Chamber in the FRS [69].

Electrons drift towards the anode wires, inducing a positive charge on the C-pads. Each C-pad is connected to one of two delay lines, with a time difference of 15 ns between neighboring pads. The position of the ion in the y direction is given by the electrons drift time, while the x position is determined from the time interval between the signals induced on the right and left sides of the delay lines. In this way each TPC gives 4 y and 2 x independent position estimates. Commissioning experiments using ^{40}Ar and ^{80}Kr beams have shown internal position resolutions of $\sigma_x = 88\mu$m and $\sigma_y = 200\mu$m, while detection efficiency $> 99\%$ and $> 90\%$ have been obtained for counting rates of 40 and 250 kHz respectively with a 1 GeV/u ^{238}U beam [69].

Scintillator Detectors To determine the A/q of the ions, the velocity β has to be measured. To this purpose two plastic scintillators, SC_2 and SC_4 are situated in the second and fourth focal planes, respectively. The plastic material is BC420, which has a decay constant $\tau \sim 1.5$ ns that ensures a fast time response. The active area is 200 mm in the X plane and 80 mm in the Y plane and the active thickness is 3 mm for SC_2 and 5 mm for SC_4. The scintillation light generated by the incident particle is collected by two Photo Multiplier Tubes (PMTs) placed on the left and right side of each detector. The time difference between the signals registered in the PMTs measures the Time of Flight of the particle between the two detectors. Two independent ToF measurements, one from the left and one from the right side, are therefore available. The time resolution obtainable is ~ 40 ps. The best ToF estimate is given by the average of the two:

$$ToF = \frac{(T_{L4} - T_{L2}) + (T_{R4} - T_{R2})}{2} \tag{3.20}$$

The velocity β is then naturally determined by:

$$\beta = \frac{d}{ToF \cdot c} \tag{3.21}$$

where d is the distance between the two scintillators ($\sim$34 m). Moreover, the difference between the left and right readouts of the same scintillators allows to measure the interaction position of the ion in the dispersive X plane. The position resolution, measured to be ~ 4 mm, is much worse than the TPCs one. However, in particular experimental conditions, where the secondary beam rate is quite high, the TPCs tracking efficiency drops dramatically, and scintillators position information has to be used, in order to recover the majority of the statistics. Finally, the light output collected in the PMTs is proportional to the energy released by the ions in the plastic material, allowing a energy loss measurement. However, due to the low resolution offered by the scintillators, the atomic number of the ions was determined from the MUSIC detectors, which will be described in the next paragraph.

Multiple Sampling Ionization Chamber (MUSIC) The proton number Z of the fragment is precisely determined by means of two Multiple Sampling

Ionization Chambers (MUSIC) [70], placed between the TPCs in the fourth focal plane. They have an active area of 200 mm × 200 mm and an active thickness of 400 mm. Each detector is filled with CF_4 gas at atmospheric pressure and the anode plate is divided in 8 sections along the Z direction. The gas ionization induced by the ion produces electron-ion pairs. A -8 kV voltage is applied to the cathode, making the electrons drift to the anode strips. Each anode section registers an independent signal, which is proportional to the energy released by the ion in the gas. The energy loss of each event is then determined by means of the average of the 8 different values. The energy loss is proportional to Z^2 according to the Bethe-Bloch relation (3.15). A correction to the velocity dependence is applied via a specific function $f(\beta)$ which gives:

$$Z = \frac{\Delta E}{f(\beta)}$$

3.4.3 The Lund-York-Cologne CAlorimeter (LYCCA)

Nuclear structure experiments with relativistic beams require the detection of the outgoing particle after the secondary target in order to select the reaction channel, track the ion trajectory and determine its velocity event-by-event. In the PreSPEC setup this task is accomplished by the Lund-York-Cologne CAlorimeter (LYCCA), which combines the use of plastic scintillators, Double-Side Silicon Strip Detectors (DSSSD) and CsI counters to measure the ion atomic number Z, Time of Flight (ToF) and (x,y) positions downstream with respect to the secondary target. A schematic drawing of the apparatus is reported in Fig. 3.12.

Plastic Scintillators The time information is obtained event by event from two plastic scintillators placed before and after the secondary target, as reported in Fig. 3.12. A picture of the detector is reported in Fig. 3.13. The difference between the signals registered in them provide the Time of Flight (ToF) of the ion along its trajectory. Each scintillator consists in a 2 mm thick plastic membrane with a diameter of 27 cm.

The light generated by the interaction of the ion with the plastic material is collected by 32 PhotoMultipliers, which therefore allow 32 independent measure-

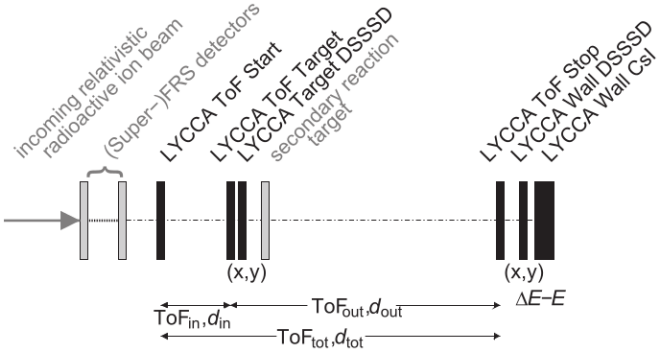

Figure 3.12: Schematic drawing of the LYCCA detectors used in the PreSPEC setup at GSI [71]. The ToF target scintillators was not available in the present experiment.

ments. By taking the average of the different values it is therefore possible to improve the time resolution of a factor $\frac{1}{\sqrt{32}}$ [71]. In a previous commissioning experiment it has been shown that time resolutions below 10 ps can be reached [72] with this configuration. By comparing the signals recorded in the different PMTs it is possible, in addition, to extract information about the (x,y) position of the incident particle [73]. This is of great importance in experiments where the beam rate is sufficiently high to imply dead time in the FRS TPCs: it has been shown that the efficiency of these detectors decreases rapidly with the increase of the counting rate [69]. On the other hand, however, the position resolution of these detectors is worse than the one given by the TPCs. By comparing the positions tracked from the TPCs and the ones measured by the scintillators a position resolution of 6.7 mm and 5.1 mm has been obtained in the X an Y direction, respectively [73].

Target DSSSD Double-Side Silicon Strip Detectors (DSSSD) allow to measure both the position and the energy loss of the incident particle. Each of the LYCCA DSSSDs consists in an ion implanted silicon wafer, silicondioxide (SiO_2) passivated, and operated totally depleted with floating guard rings [71]. The nominal thickness is 300-320 μm. The active area of 58.5×58.5 mm^2 is divided in 32 strips on both front (junction) p-side and rear (ohmic) n-side in orthogonal directions. The interstrip distance is 30 μm on the p-side while it is 200 μm on the n-side,

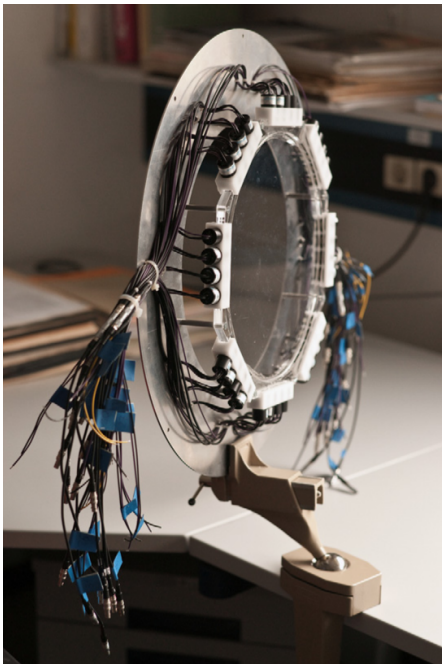

Figure 3.13: Picture of the ToF scintillator used in the PreSPEC-AGATA campaign [71].

resulting in 1024 1.83×1.83 mm^2 pixels. The hit position is determined by the strip with the highest energy deposition on both sides of the DSSSD. A picture of the detector is reported in Fig. 3.14.

LYCCA Wall The LYCCA wall is placed ∼3.7 m downstream with respect to the secondary target. It is composed of 16 modules for $E-\Delta E$ and (x,y) position measurement, and its hit pattern, together with the labeling of each module, is reported in Fig 3.15.

The ΔE and position information are obtained from DSSSD detectors like the one described in Sec. 3.4.3. An array of 9 CsI(Tl) crystals is placed 10 mm behind each wall DSSSD, allowing the measurement of the energy E of the incident particle. The area of each crystal is 19.4×19.4 mm^2. All detectors except the ones in positions 1, 2, 23 and 24 have a depth of 33 mm and are followed by a 7 mm light guide and a PhotoDiode(PD). The remaining detectors have a depth of 10 mm and a light guide of 5 mm [71]. The incident ion releases its

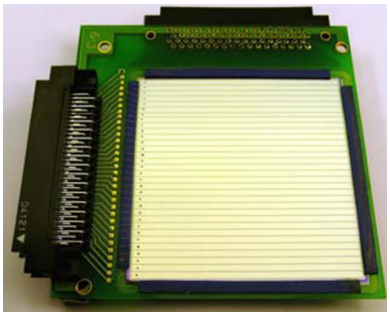

Figure 3.14: Picture of the target DSSSD detector used in the PreSPEC-AGATA campaign [71].

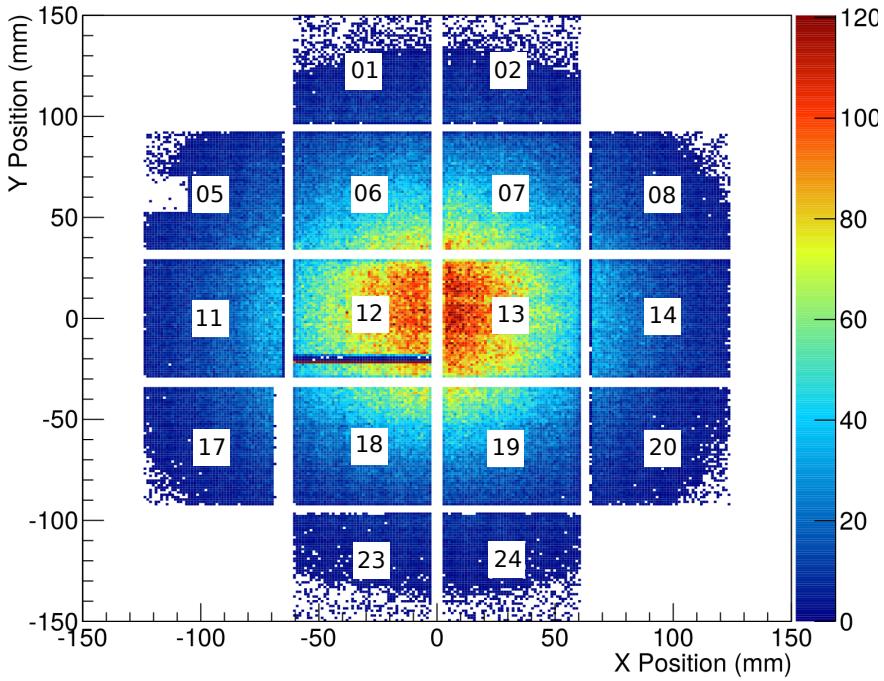

Figure 3.15: Lycca Wall hit pattern observed in the present work. The convention used to label each module is reported. The white lines represent the spacing between the modules or broken strips.

energy in the CsI material, generating photons via the scintillation process which are then collected by the PhotoDiodes placed at the back of the detector. The CsI material, doped with thallium, ensures high stopping power combined with high light output, peaked at $\lambda = 550$ nm.

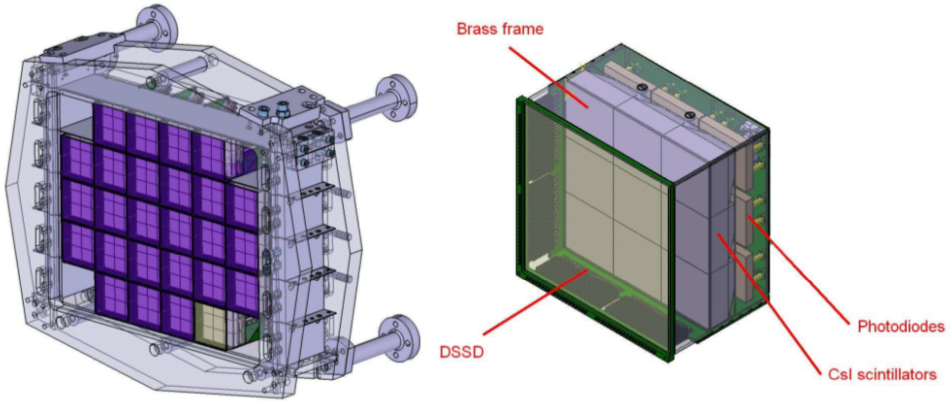

Figure 3.16: Schematic drawing of the full LYCCA Wall (sx) and of a single module (dx) [71].

The (x,y) position measurements in the Target and Wall DSSSD, together with the information tracked from the TPCs or obtained from the ToF scintillators allows to fully determine the ion trajectory both before and after the secondary target. This gives an estimate of the angle of scattering of the interacting particle and, combined with the ToF measurements given by the plastic scintillators, allow to obtain an event-by-event value for the ion velocity β, which is essential for the Doppler correction. The atomic number is selected from the $E - \Delta E$ measurement in the LYCCA WALL.

3.4.4 Advanced GAmma Tracking Array (AGATA)

In the present experiment the γ-ray Advanced GAmma Tracking Array (AGATA) spectrometer was used [74]. It represents part of the new generation of γ-tracking arrays composed of highly segmented High-Purity Germanium (HPGe) detectors. The goal of this new kind of spectrometers is to exploit the high electrical segmentation of the crystals to track the γ-ray trajectory inside the detector material, to reconstruct its energy, to reduce the background by discarding events which do not correspond to realistic Compton scattering sequences and to determine precisely the interaction position. The possibility to avoid the use of anticompton shields increases the solid angle covered by the HPGe material resulting in a

detection efficiency far greater than its predecessors.

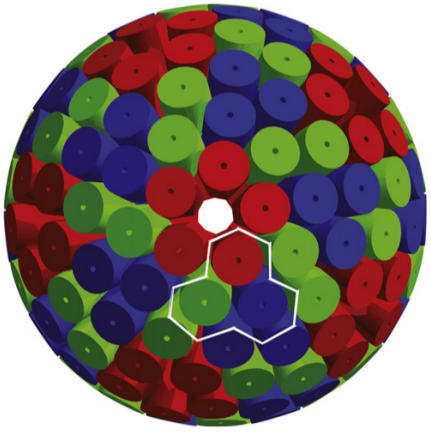

Figure 3.17: Schematic view of the final configuration of the AGATA γ ray spectrometer [74].

In its final configuration AGATA will be a 4π sphere composed of 180 HPGe detectors grouped in triple clusters, as reported in Fig. 3.17. Each AGATA triple cluster [75] is composed of three differently shaped hexagonal tapered coaxial HPGe detectors, encapsulated in a sealed thin aluminum case. Each crystal has a length of 90 mm and a diameter at the rear of 80 mm and is electrically divided in 36 segments. Each crystal is labeled A,B or C according to its shape, while each segments is identified by the convention reported in Fig. 3.18.

AGATA runs on fully digital electronics. The 37 preamplifier signals from each crystal (36 from the segments and 1 from the central core electrode) are digitized at 100 MHz by high-resolution (14 bits) fast ADCs.

In the 2014 PreSPEC-AGATA campaign, 22 HPGe detectors were available. The standard configuration based on triple cryostats had to be revised due to the large beam spot size typical of RIB at GSI ($\mathrm{FWHM}_X \sim 6$ cm). In order to avoid crystal damage due to scattered particles or neutrons, the inner detectors were grouped in double clusters. The detectors were placed at the nominal distance of 23.5 cm from the reaction target. The configuration of the AGATA crystals in the present experiment, based on 6 triple clusters (with two missing detectors) and 3 double clusters is depicted in Fig. 3.19, while a picture of the setup is shown in Fig. 3.20.

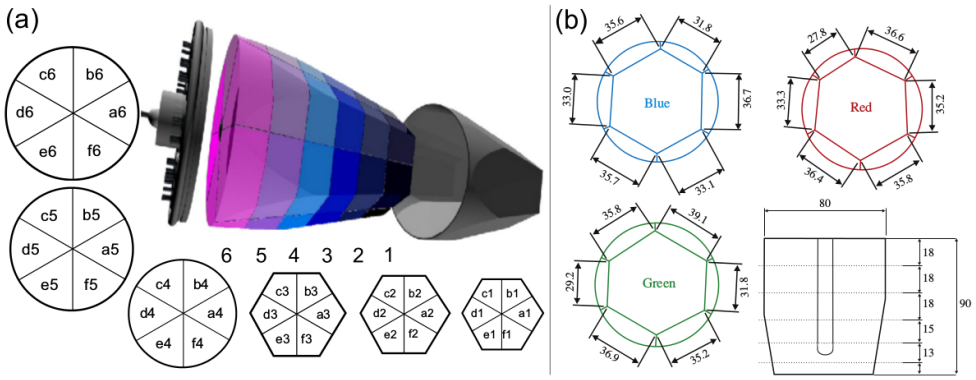

Figure 3.18: (a) Labeling scheme for the standard AGATA crystal. (b) Scheme of the three different crystal shapes in a AGATA triple cluster. Dimensions are reported in mm. Taken from [64], adapted from [74].

Pulse Shape Analysis In beam γ-ray spectroscopy experiments require good Doppler correction in order to properly determine the energy of the observed γ rays and to improve the energy resolution. A key point in this procedure is the estimate of the angle between the emitting particle and the photon. It is therefore essential to determine the interaction position of the γ ray with the crystals. The use of segmented detectors allows to improve the angle measurement by considering as the first interaction point the center of the segments which records the largest signal. However to track the photon path in the detector a sub-segment resolution is required. This can be achieved in the new generation of γ-ray spectrometers via Pulse Shape Analysis. The electron produced by the photo-electric or Compton effect produces electron-hole pairs in the HPGe crystal resulting in a net charge collected from the electrodes, while the neighboring segments see an alternate current resulting in a null charge collection. The shape of the measured signals depend on the position of the interaction. In Fig. 3.21 the signal shape of the six segments and the core of a detector for an interaction occurring in the fourth segment are reported.

To determine the interaction position of the γ ray it is necessary to compare the measured signals with reference ones. References database of signal shapes called "bases" can be obtained by scanning each detector with a collimated source. On the other hand the references basis can be simulated using electric field sim-

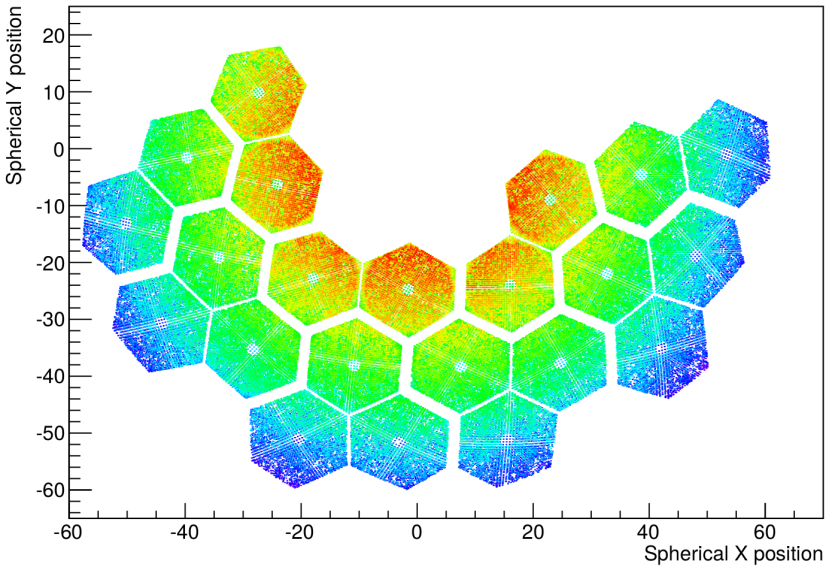

Figure 3.19: AGATA clusters configuration in the PreSPEC-AGATA campaign at GSI in 2014.

ulation codes stored in the AGATA Data Library (ADL) [77, 78]. A comparison between the simulated and the experimental signal is reported in Fig. 3.22. The good agreement justifies the use of simulated basis as a reference, as it is done in this work.

AGATA electronics records 100 ADC samples (1μs) for each pulse trace. The adaptive grid search algorithm [79] is used to determine the reference signal which is closest to the measured one. The typical position resolution that can be obtained with an AGATA crystal is $\sim$5 mm FWHM [80, 81].

γ-ray Tracking The information given by the Pulse Shape Analysis is used by tracking algorithms to reconstruct the photon path in the HPGe volume. This allows to disentangle between different γ rays and to discriminate and suppress the background. Currently, there are two different tracking algorithms available for AGATA: Orsay Forward Tracking (OFT) [82] and Mars Gamma Tracking (MGT) [83], both using the forward tracking principles. The MGT code has been used in this work. Forward tracking algorithms start from the identification of clusters of interactions that could belong a single γ ray, exploiting the

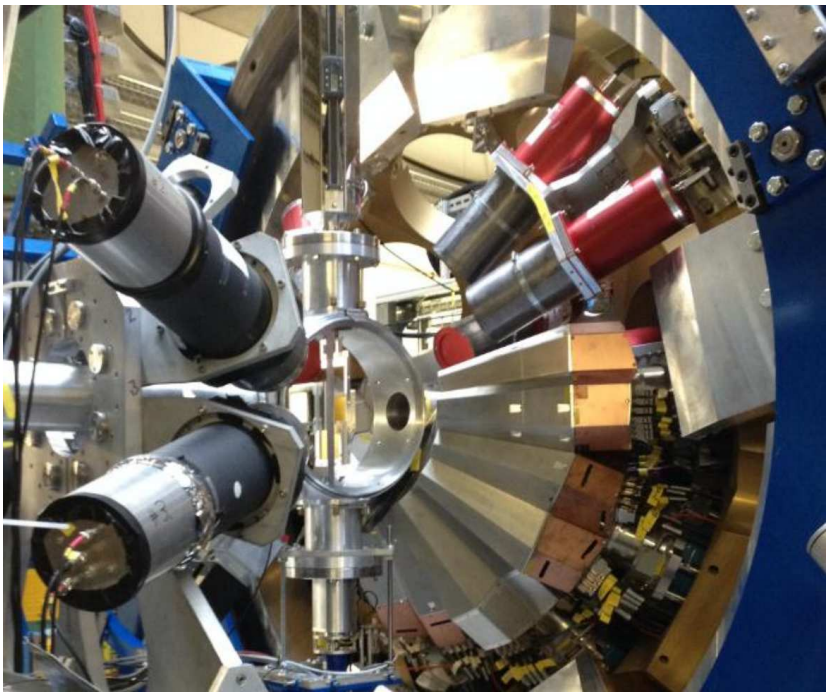

Figure 3.20: The AGATA γ-ray spectrometer in the PreSPEC-AGATA campaign at GSI in 2014.

angular dependence of the Compton cross section described by the Klein-Nishina relation. These clusters are composed of hits with an angular distance lower than a threshold value. For each cluster and each permutation of the interaction points a Figure of Merit (FoM) is calculated based on the distance between the interaction points, the interaction probability of the γ ray, the Compton and the photo-electric cross sections, and a compliance of the deposited energy and the scattering angle in Compton scattered events. The sequence of interactions with the best Figure of Merit is chosen as the γ-ray track and, if the FoM is above a given threshold, it is accepted, otherwise the event is discarded. The algorithm tries to recover initially discarded clusters, combining them in new clusters and evaluating the relative FoM. If the obtained value is acceptable, the cluster is recognized as a good event, otherwise the cluster is definitively discarded as an incomplete scattering of the incident γ rays. With such procedure a Compton background suppression is obtainable, without loosing angular coverage or ef-

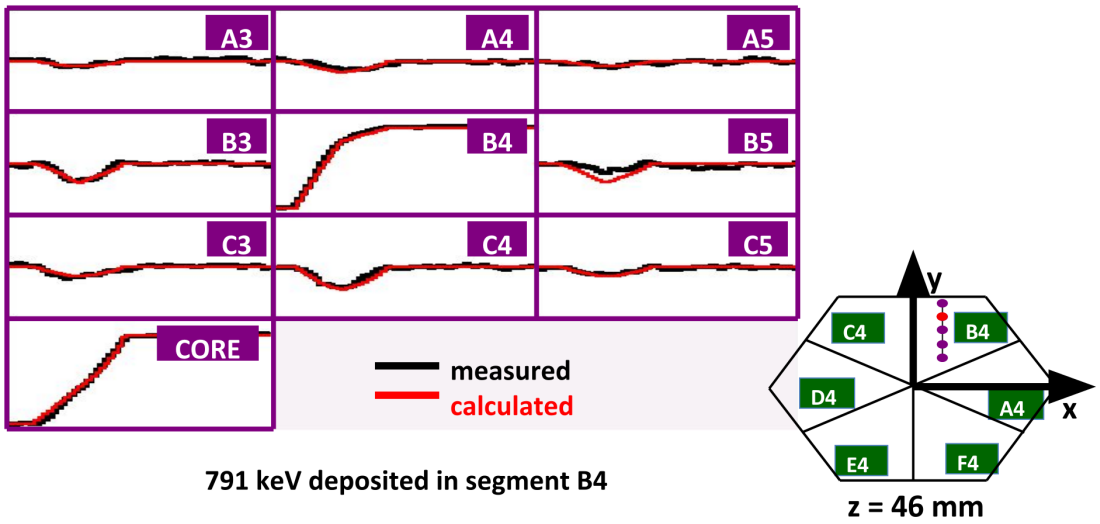

Figure 3.21: Signal shape in the different segments of a detector for an interaction in the segment B4. The signals induced in the other segments can be used to deduce the position of the interaction. Figure taken from [76].

ficiency due to anticompton shields. The tracking allows to achieve an higher photopeak efficiency and a better Peak to Total (P/T) ratio. In Fig. 3.23 an example of clusterization of interaction points in an ideal 4π HPGe shell is reported.

3.5 Data Analysis

As shown in the previous Chapter, the experimental setup used in the present work is rather complex. An accurate data analysis is needed in order to properly select good events and obtain γ-ray spectra from the signals of the different detectors. In this Chapter the calibrations, the processing and the conditions applied to the data will be described. In particular, the procedure to identify the ions of interest, the selection of "safe" Coulomb excitation events and the gates and conditions applied to reduce the background in γ-ray energy spectra will be explained.

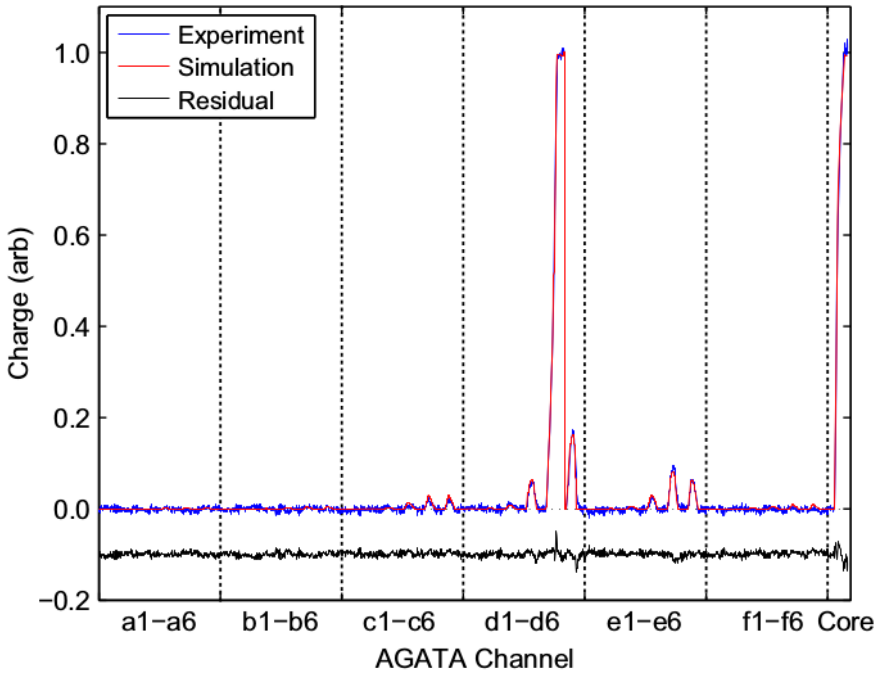

Figure 3.22: Comparison between the simulated (red) and experimentally measured (blue) pulse shapes induced by a hit in the segment d5 [74]. The good agreement justifies the use of simulated basis as a reference.

3.5.1 Fragment Separator FRS

Prior to the experiment, different unreacted beam runs were performed in order to calibrate the different detectors along FRS and LYCCA. The ^{58}Ni stable beam, with a primary energy of 599.65 MeV/u, was transported through the FRS along the beam line and no reaction target was put in the chamber. This procedure was repeated for different amounts of degrader material in the second focal plane S2, implying different energy and velocity for the ^{58}Ni beam in each run. The energy of the ions can be estimated from calculations, allowing scintillators and MUSIC calibrations to be performed. In Tab. 3.2 the different variables of the unreacted calibration runs are reported.

The FRS settings have to be adjusted in order to transport to the final focal plane the nuclei of interest with the maximum possible intensity. However ^{46}Cr, ^{46}V and ^{46}Ti lie many nucleons far from the primary beam ^{58}Ni in the nuclide

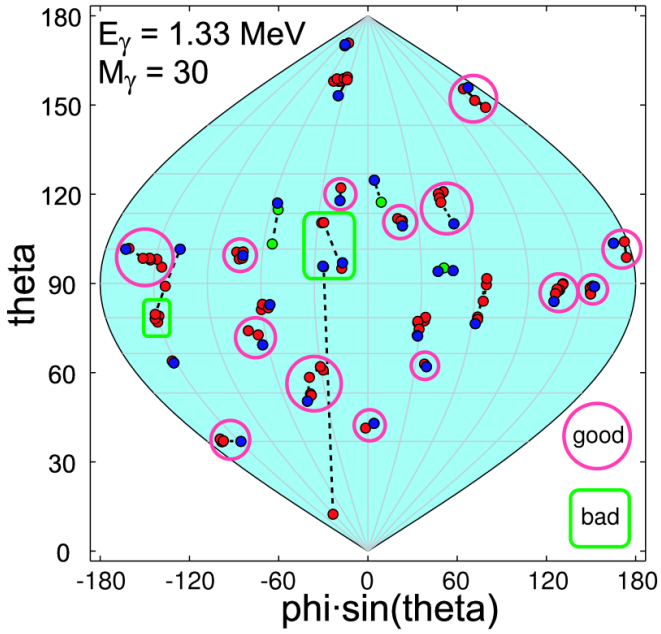

Figure 3.23: Representation of a $E_\gamma = 1.33$ MeV, $M_\gamma = 30$ event detected in a full 4π Ge shell reconstructed with a cluster tracking algorithm.

chart. For this reason the procedure of finding the correct FRS settings for the nuclei of interest by scanning down from ^{58}Ni would be difficult and long. An alternative way is given by the isomer tagging technique. It consists in setting approximately correct values for the FRS magnets and then in finding in the resulting particle ID plot a nucleus with a well-known isomeric state. This is done by implanting all the nuclei in a thick plastic target placed in the reaction chamber. Then correlating the PID of the ions with the γ-ray spectrum recorded in AGATA it is possible to identify the nuclei implanted in coincidence with the observation of the γ emitted from the isomeric state. The half-life of the isomer has to be longer than the flight path through the FRS ($\sim$200 ns) to be observed. In this experiment the $J^\pi = (19/2^-)$, $T_{1/2} = 556(6)$ ns isomer in ^{43}Ti [85] has been used for this purpose. Once the ^{43}Ti nucleus is identified, the FRS settings can easily be adjusted for each of the nuclei of interest.

The central trajectory along FRS has been estimated from LISE [84] simulations and then corrected for the experimental measured magnetic fields for each dipole magnet.

Run	^{58}Ni - 1	^{58}Ni - 2	^{58}Ni - 3	^{58}Ni - 4
S2 Degrader		5.7 g/cm^2	6.8 g/cm^2	8.0 g/cm^2
FRS ToF [ns]	159.675	175.116	180.227	187.478
FRS β	0.78505	0.71583	0.69553	0.66863

Table 3.2: Properties of the ^{58}Ni calibration runs performed prior to the experiment. The ToF and β values have been obtained by LISE simulations [84].

3.5.1.1 Time Projection Chamber (TPC) Calibrations

Time Projection Chambers (TPC) are used to determine the (x,y) position of the ion in the S2 and S4 focal planes. In order to calibrate them, fiber mask runs were performed: an active grid, composed of vertical and horizontal scintillator fibers, was put in front of each TPC. The distance between vertical fibers was 12 mm while between horizontal fibers 6 mm. Each time an ion hits the grid, scintillation light is produced, which is then collected by PMTs. In a such a way the raw hit pattern is obtained. By plotting the resulting values against the known fibers positions it is possible to obtain proper calibrations for each TPC. In Fig. 3.24 the calibrated hit pattern is reported.

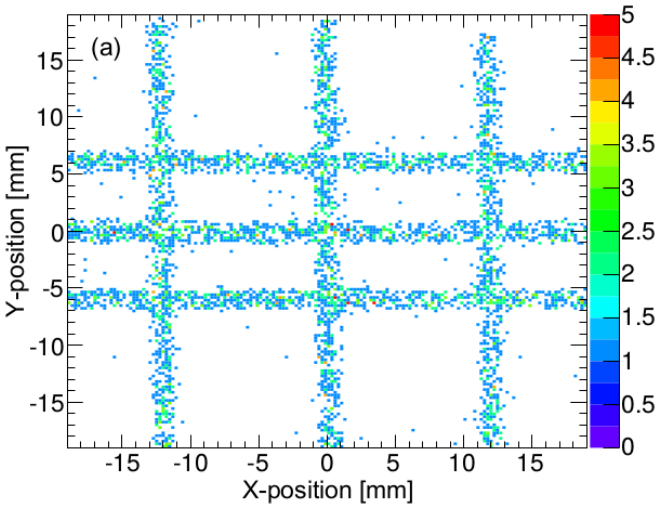

Figure 3.24: Calibrated hit pattern of the first TPC placed in S2.

3.5.1.2 MUSIC Calibrations

The atomic number Z of the ion is determined from the energy it releases in the Multi Sampling Ionisation Chamber (MUSIC) detectors. The energy loss follows the Bethe-Bloch relation (3.15) and depends, in particular, from Z^2 and a quadratic function of β, $f(\beta)$. In order to calibrate them we used the unreacted ^{58}Ni runs, which allow to find the relation between β and the energy loss dE, keeping the atomic number Z fixed to a well known value. The MUSIC calibrations proceeded in two steps. Firstly, we aligned the raw dE energy loss value of each of the 8 anode segments to an arbitrary value. In second place, we plotted the aligned dE value of each run against the relative LISE FRS β value. A quadratic trend was observed, as it is shown in Fig. 3.25, which allowed to fit the experimental points with a parabola, determining in this way the function $f(\beta)$. The atomic number Z of an unknown ion can therefore be found scaling the energy loss recorded in the MUSIC detectors to the energy loss of a ^{58}Ni nucleus at the same velocity β_{FRS}:

$$Z_{ion} = Z_{Ni}\sqrt{\frac{dE_{ion}}{dE_{Ni}(\beta)}}$$

where Z_{Ni} is the atomic number of nickel, i.e. 28. The same procedure is applied to both MUSIC detectors and the adopted Z is the average between the obtained estimates.

3.5.1.3 FRS Scintillators Calibrations

The main task of the FRS plastic scintillators is to measure the Time of Flight (ToF) between the second and the fourth focal planes of the Fragment Separator. This allows to obtain the velocity β of the ion, which is essential to determine its A/q ratio. Beside this, combining the information from the left and right PMT of both scintillators, it is possible to measure the X position of the ion. As we saw in Sec. 3.4.2.1 this is particularly important when the secondary beam rate is sufficiently high to cause sizeable dead time in the TPCs detectors.

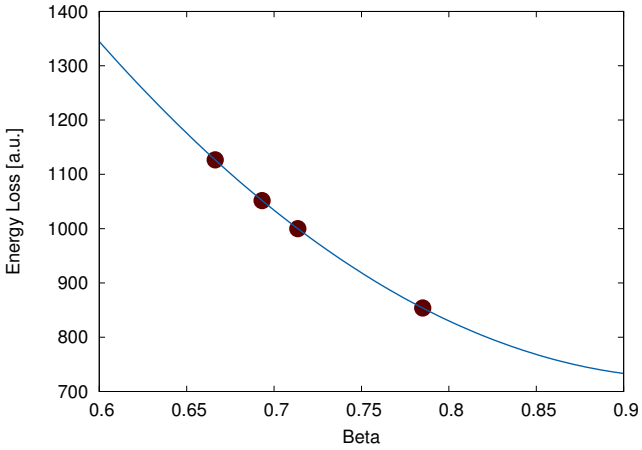

Figure 3.25: Experimental energy loss for the different ^{58}Ni runs as a function of the velocity β for the first of the MUSIC detectors. The blue line represents the quadratic function $f(\beta)$ fitted to the data.

Time of Flight calibrations Two independent measurements of the Time of Flight between S2 and S4 are given by the difference between the signals of the left and the right PMTs of the two scintillator detectors, respectively. In order to calibrate them, we plotted the raw time interval measured by the scintillators for each ^{58}Ni run against the correct value simulated with LISE [84]. The choice of the unreacted stable beam runs ensured small velocity spread for the ions, allowing a more precise calibration to be performed. In such a way gains and offsets were obtained for both left and right ToF measurements. The adopted ToF and β values are then given by Eq. (3.20) and (3.21). The ToF spectra present a sharp cut around ∼207 ns as can be seen in Fig. 3.26.

This effect is clearly not physical and comes from a saturation of the Time to Digital Converter (TDC) modules: when the recorded value is out of the range it is added to the last channel of the TDC scale. To overcome this issue we considered the signals coming from the Multi-Hit TDC (MhTDC) modules. The calibration had therefore to be performed separately. It was however noticed that the gains and offsets obtained from the ^{58}Ni runs were not compatible with the experimental beam runs. The reasons for this are unclear. The most probable explanation is a variation in either the cabling or the delay times in the MhTDC from calibration

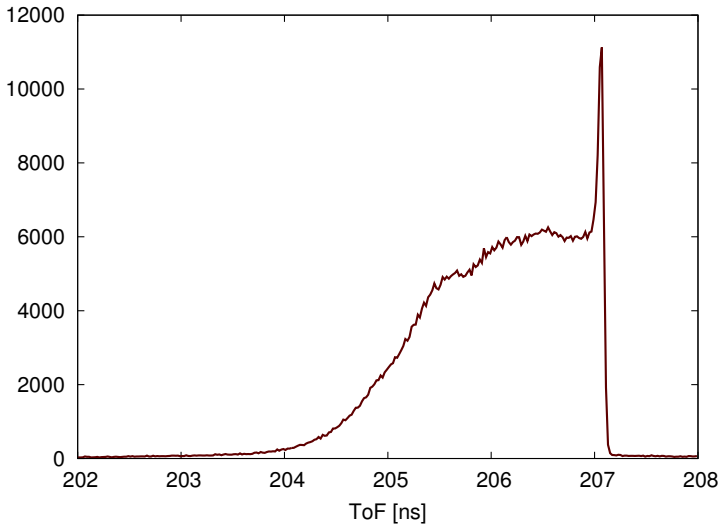

Figure 3.26: Calibrated ToF spectrum for the ^{46}Ti experimental run obtained with the TDC modules. A sharp cut off due to the saturation of the TDC is visible at ∼207 ns.

to experimental runs. The latter were therefore used to calibrate the ToF value. The resulting spectra for ToF_{LL} and ToF_{RR} are reported in Fig. 3.27.

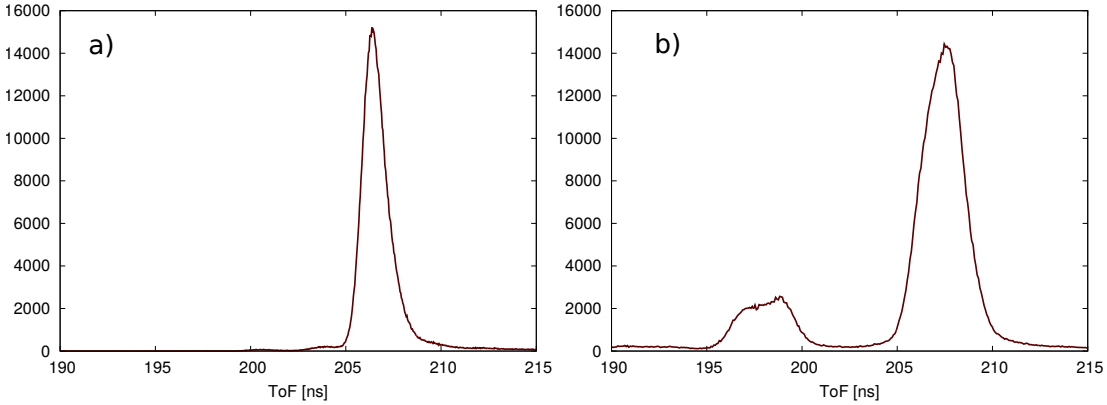

Figure 3.27: Calibrated ToF spectrum for the ^{46}Ti experimental run obtained with the Multi-Hit TDC modules using a) the right PMTs and b) the left PMTs. A double structure is visible in the ToF_{LL} spectrum which is due to the bad behavior of the left PMT in S2.

The ToF_{LL} spectrum presents a double structure which is not visible in the

ToF_{RR} one, which leads to two different and not consistent estimates of the ToF. This results in a biased A/q determination which causes a double blob in the PID plot for each nucleus. Further investigations on this issue have shown that it is due to an anomalous behavior of the left PMT in S2. This anomaly has been observed in limited time intervals during the data taking and its origin is unclear. A way to overcome this issue is using only the information coming from the right PMT.

Position Calibrations As already pointed out the efficiency of the TPC detectors drops very rapidly with the increase of the beam rate [69]. During the experimental beam runs regarding ^{46}Ti and ^{46}V counting rates of approximately $3-4\times10^6$ ions per spill were reached in the second focal plane. At these rates the measured efficiency was $\sim$ 20%, consistent with estimates obtained in a previous commissioning experiment [69]. The use of TPCs in the present work would imply therefore a loss in statistics of a factor $\sim$4, which is unacceptable. The X position in both focal planes is needed to obtain the A/q of the ion, therefore positions obtained from the scintillators have to be used. These are estimated from the time difference between the two PMTs of each scintillator, dt_{LR}. In order to calibrate them we plotted the dt_{LR} value against the X position obtained from the TPCs and tracked to the Z position of the scintillators. A linear trend was observed, which allowed to extract gains and offsets for the calibrations, as shown in Fig. 3.28.

It is important to notice that the information from both left and right PMTs are needed to measure the X positions. The bad behavior of the left PMT in S2 will therefore results in a double blob in the PID. This effect can not be avoided, and the events related to the two different blobs have therefore to be treated separately in the analysis. In order to measure the total number of incoming particles of a given specie, the sum of the number of counts inside both blobs has to be considered. Luckily, this anomalous behavior was observed over fixed periods of time during the beam runs. This allows to group events with the correct and incorrect position determinations and put different gates upon them.

In the next section we combine the information coming from the MUSIC, TPCs and scintillator detectors to present the Particle Identification plot obtained

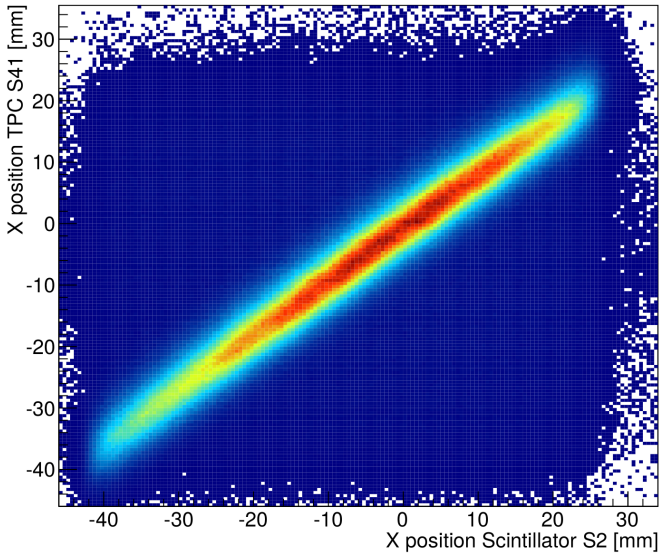

Figure 3.28: Correlation between the X position in the fourth focal plane S4 measured by the TPCs and from the time difference between the two PMTs of the plastic scintillator.

for this experiment.

3.5.1.4 Particle Identification

In Fig. 3.29 we report the Particle Identification plot for the ^{46}Ti setting. In the left panel the X position from the TPCs has been adopted, while in the right panel scintillator detectors have been used in the position determination. It is immediately clear how the use of scintillators position worsen the overall spectrum and produces a double blob, as we saw in the previous section. However due to the beam rate in S2 the tracking efficiency of TPCs in the second focal plane is $\sim$ 20 %, resulting in a factor $\sim$4 of loss in statistics. For this reason TPCs were not used in this analysis.

The Particle Identification plot for ^{46}Cr is presented in Fig. 3.30.

Due to the smaller beam intensity the gain factor in statistics is $\sim$1.8 from TPCs to scintillators position measurements. The scintillator positions have been used in this case as well, in order to maximize the statistics.

The Z identification has been performed with the MUSIC detectors. In

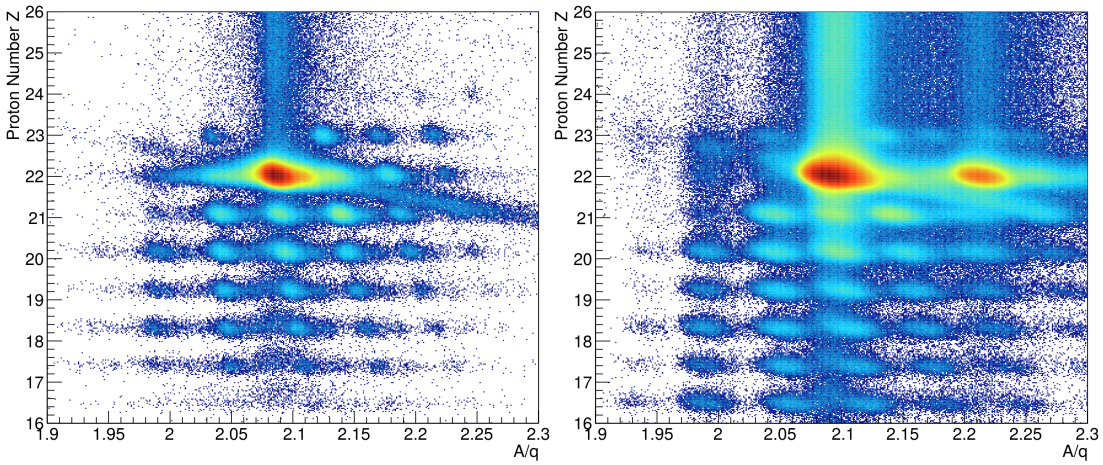

Figure 3.29: Particle Identification plot relative to the ^{46}Ti setting. Left Panel: X position from TPCs in S2 and S4. Right Panel: X position from scintillators in S2 and S4.

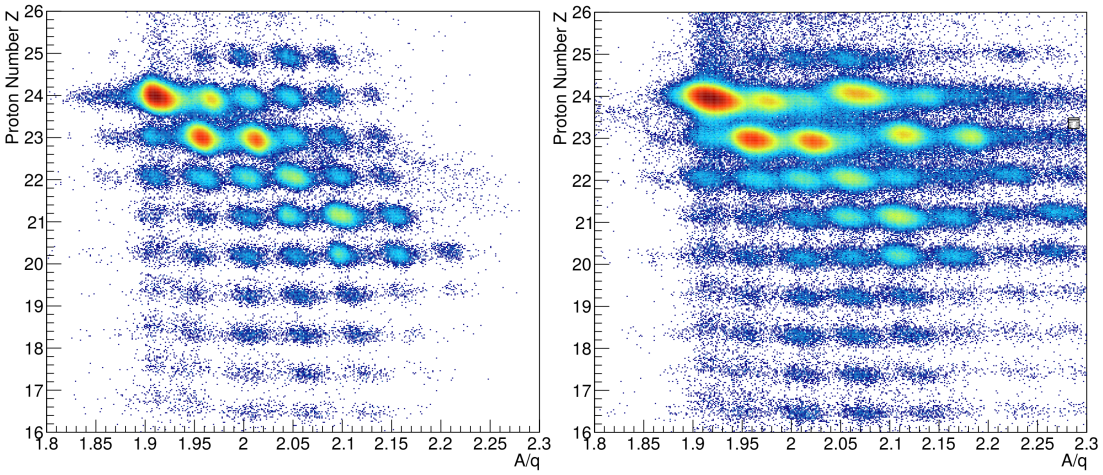

Figure 3.30: Particle Identification plot relative to the ^{46}Cr setting. Left Panel: X position from TPCs in S2 and S4. Right Panel: X position from scintillators in S2 and S4.

Fig. 3.29 a not negligible number of events is characterized by the same A/q but larger Z with respect to the ^{46}Ti nucleus. These events have a correct A/q but wrong Z value. This effect is produced by pile-up in the MUSIC detectors. These events were simply discarded in the present analysis. Since pile-up is rate

dependent it is not observed in the ^{46}Cr spectrum, due to the much lower intensity.

The incoming PID matrices allow to estimate the different ions present in the secondary beams, which are reported in Tab. 3.3, for the three main settings adopted in the experiment: ^{46}Ti, ^{46}Cr and ^{46}V.

Setting	^{46}Ti	^{46}Cr	^{46}V
Ions	^{46}Ti (82%) ^{47}Ti (2%) ^{45}Sc (1%) ^{42}Ca (1%)	^{46}Cr (53%) ^{45}V (16%) ^{46}V (11%) ^{47}Cr (4%)	^{46}V (69%) ^{45}Ti (9%) ^{47}V (4%) ^{46}Ti (2%)

Table 3.3: Composition of the secondary beams for the settings used in the present experiment.

3.5.2 LYCCA Analysis

In the PreSPEC setup the outgoing ions are identified and tracked by the Lund-York-Cologne Calorimeter (LYCCA), described in Sec. 3.4.3. The identification of the atomic number of the ions is based on the $E - dE$ technique. Moreover, the possibility to determine the Time of Flight and the trajectory of the outgoing nuclei allows a precise event-by-event Doppler correction to be performed. The calibrations and optimization of the DSSSD and scintillator detectors are described in the following paragraphs.

3.5.2.1 Plastic ToF scintillator calibrations

The plastic scintillators placed before and after the secondary target are used to measure the Time of Flight of the ion and therefore to extract the velocity β. As pointed out in Sec. 3.4.3, the time of the interaction with the plastic material is determined by the average of the signals coming from the 32 PMTs which surround the circular membrane. However, the signal recorded by each individual PMT depends from the point of interaction of the particle with the detector, since the scintillation light produced has to travel through the plastic material before reaching the PMT. To correct this effect we plotted the distance

from the hit position to the PMT, dx, against the time delay between the hit and the PMT signal, dt. In such a way it is possible to extract gains and offsets for each PMT and to obtain a time information which is independent from the position of the interaction. The (x,y) hit position is determined by tracking the position given by the TPCs in S4, the target DSSSD and the Wall DSSSD at the Z position of the scintillator. In Fig. 3.31 the dependence of the measured time against the distance from the hit position is reported for a single PMT.

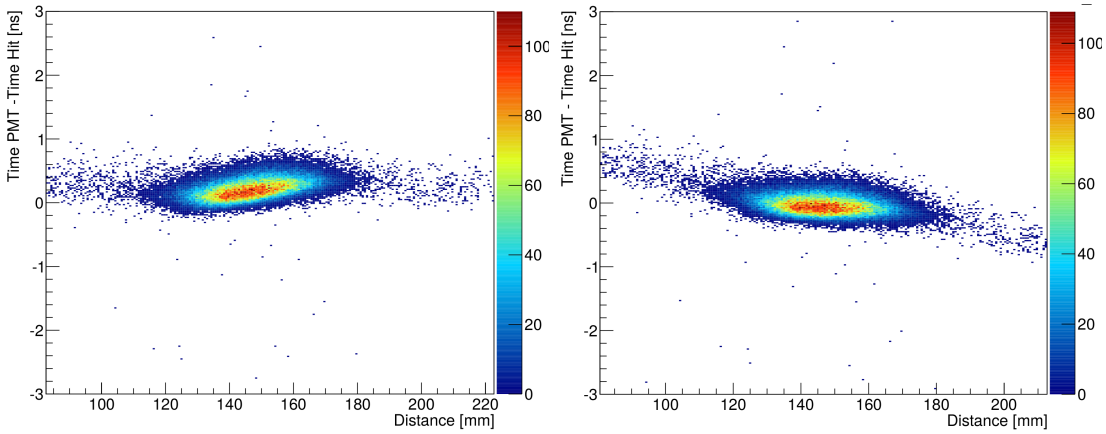

Figure 3.31: Correlation between the PMT recorded time and the distance from the hit position to the PMT for PMT number 5 of the LYCCA ToF Start detector. Left Panel: before position correction. Right Panel: after position correction.

Beside the ToF measurement, the Start and Stop plastic scintillators can also be used to extract information on the (x,y) interaction position. As already pointed out, this possibility becomes of particular interest when the beam rate is sufficiently high that the dead time in the TPCs detectors is sizeable. The FRS scintillators allow to estimate the X position, but give no information on the Y coordinate. However both informations are needed. The path of the ion has to be completely tracked in order to determine the scattering angle after the reaction target, which is essential to discard the contribution of the nuclear interaction on the measured cross section. The ToF scintillators become therefore the ideal tool to determine (x,y) coordinates of the particle before the secondary target. Combining this information with the (x,y) positions measured in the target and Wall DSSSD it is possible to fully determine the scattering angle.

The position measurement in the LYCCA scintillators is obtained from the time delay between the signals in the different PMTs. A minimization routine is used, where scintillator (x,y)-positions are scanned to find the minimum variance in the position-corrected time signal.

3.5.2.2 DSSSD calibrations

The (x,y) positions in the DSSSD detectors are determined by the strips which records the largest signal on both p and n sides, while the total energy loss (ΔE) is given by the average between the total energy loss measured in the p-side and in the n-side. Therefore the crucial point in the calibration of DSSSD is the alignment of the signals of all the strips on both sides of each detector to a fixed value. The calibration ^{58}Ni runs were used to this purpose. An example of this gain-matching procedure is reported in Fig. 3.32 for the Wall module number 7.

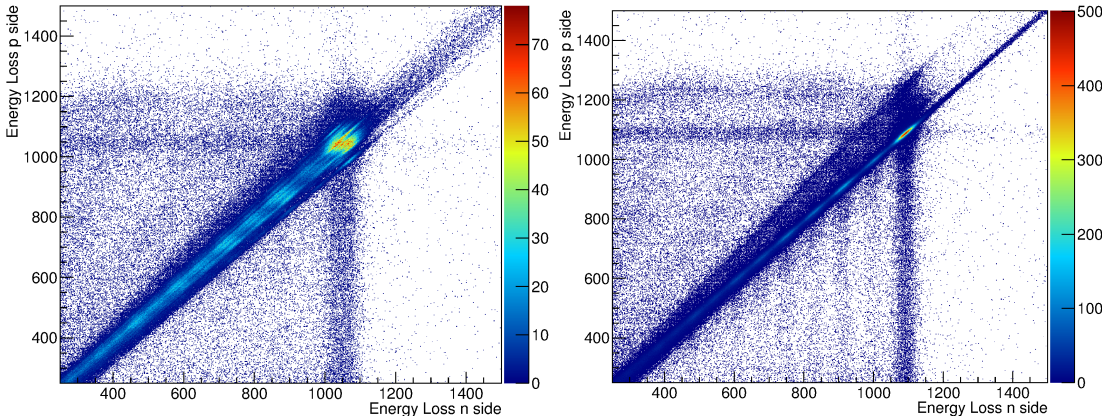

Figure 3.32: Energy loss measured in the p and n side of the LYCCA Wall Module number 7. Left Panel: before strips alignment. Right Panel: after strips alignment. The same procedure has been applied to all the modules of the Wall DSSSD and the target DSSSD.

After the alignment of all the strips on both sides, the measured energy loss in both target and Wall DSSSDs was plotted against the theoretical values calculated with LISE [84]. Gains and offsets were therefore extracted to obtain the correct total energy loss.

3.5.2.3 CsI detectors calibrations

The total energy E in the LYCCA Wall is measured by CsI scintillators, as shown in Sec. 3.4.3. Each Wall module comprises 9 CsI detectors. The signal recorded by the 9 detectors were aligned to a fixed value by means of a gain-matching procedure. The effect of the alignment is clearly visible in Fig. 3.33.

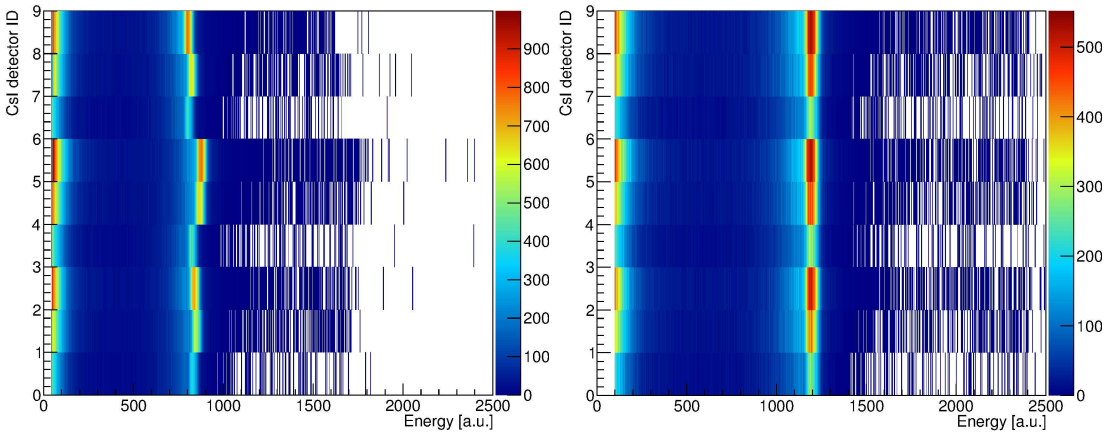

Figure 3.33: Total energy measured in the CsI scintillators of the LYCCA Wall Module number 7. Left Panel: before alignment. Right Panel: after alignment.

The aligned signals were then calibrated to obtain the correct energy measurement by plotting the raw values against the theoretical ones obtained with LISE.

3.5.2.4 Particle Identification

The main task of the LYCCA calorimeter is the identification of the outgoing ion. The proton number Z can be determined from the $E - \Delta E$ matrix, where the energy loss ΔE is measured by the Wall DSSSDs and the total energy is the sum of the energy values recorded by the DSSSDs and the CsI detectors of the LYCCA Wall. The energy loss depends from Z^2 according to the Bethe-Bloch relation (3.15), therefore every different isotopic specie will cover a well determined locus on the $E - \Delta E$ plane, as reported in Fig. 3.34.

The strongest blob corresponds to the ^{46}Ti nucleus. In principle, the possibility to measure event-by-event the ToF of the outgoing ions allows to distinguish

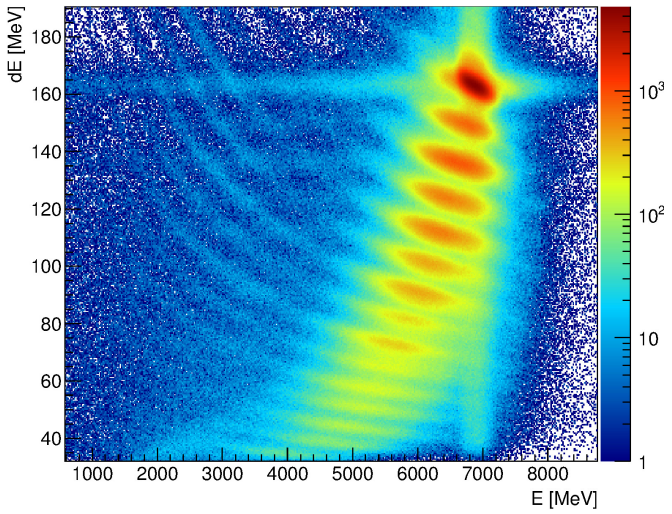

Figure 3.34: $E - \Delta E$ matrix reconstructed from the LYCCA Wall detectors for the ^{46}Ti beam runs.

the particles also according to their mass. However the achievable resolution is not sufficient to discriminate the different isotopes in this experiment. Moreover, the selection on the atomic number is sufficient for the present Coulomb excitation experiment, where the outgoing gate is used mainly to remove from the γ spectrum the unwanted background coming from different reactions. It is important to notice that no γ transitions in the energy region of interest are expected, therefore a condition on the mass of the outgoing particle would not improve the spectrum.

3.5.3 AGATA Analysis

The γ rays emitted in the reaction of interest are detected by the AGATA spectrometer, described in Sec. 3.4.4. In the present work the interaction position was determined by the Pulse Shape Analysis via the adaptive grid search algorithm [79], while the reconstruction of the γ ray path was performed with the Mars Gamma Tracking (MGT) [83] algorithm. A number of different calibrations and optimization are needed to fully exploit the capabilities of AGATA. These consist in standard energy and efficiency calibrations, optimization of the Doppler correction and reduction of the unwanted background, which will be described in

this section.

3.5.3.1 Energy calibrations

Calibration curves are needed to convert the amplitudes of the signal recorded in the different detectors into real energy values. These have been obtained with standard calibration sources ^{152}Eu and ^{60}Co, which allowed to extract gain and offsets for each individual crystal. It is important to underline that the segments need to be properly calibrated as well since the energy deposition information is essential in the tracking procedure and in the determination of the first interaction point. The difference between the measured and the literature values obtained with a ^{152}Eu source and the core signals is reported in Fig. 3.35

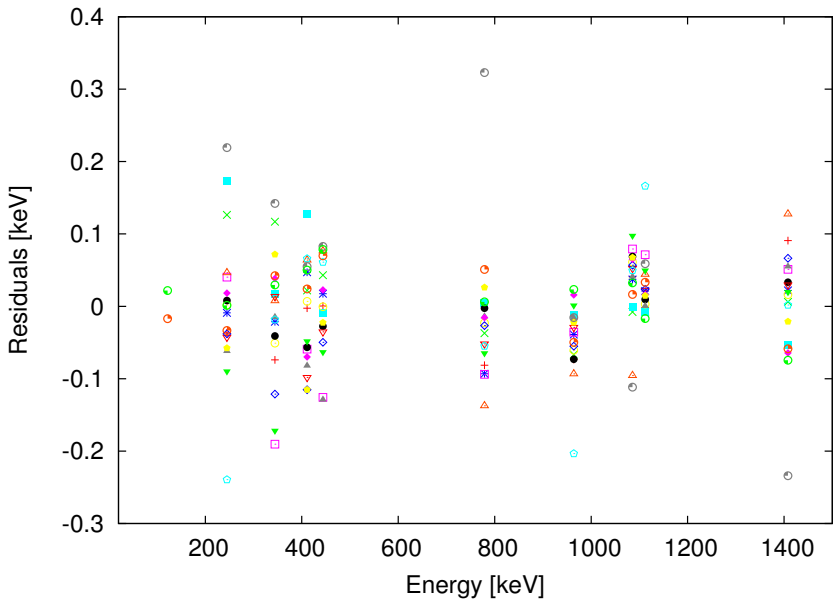

Figure 3.35: Difference between the measured energies and the literature values for ^{152}Eu. The core signals of each AGATA crystal have been used.

3.5.3.2 Efficiency calibrations

The determination of the efficiency of the apparatus is an essential step in this work, especially for the Coulomb excitation cross section measurement, where

the real number of γ rays emitted is needed. This task is particularly delicate for AGATA where different ways of reconstructing the γ-ray energy are available. In the present analysis the core common and the tracked methods have been used. In the core common mode the signals of the central contact of each detector are used while in the tracked mode the reconstructed energy given by the tracking algorithms [83, 82] is exploited. Each different method will give different performances in terms of peak-to-total and efficiency. In a recent work, the performances of the AGATA spectrometer in the PreSPEC campaign at GSI have been studied in detail with standard calibration sources and the efficiency for all both methods has been obtained [86]. The efficiency curves are reported in Fig. 3.36.

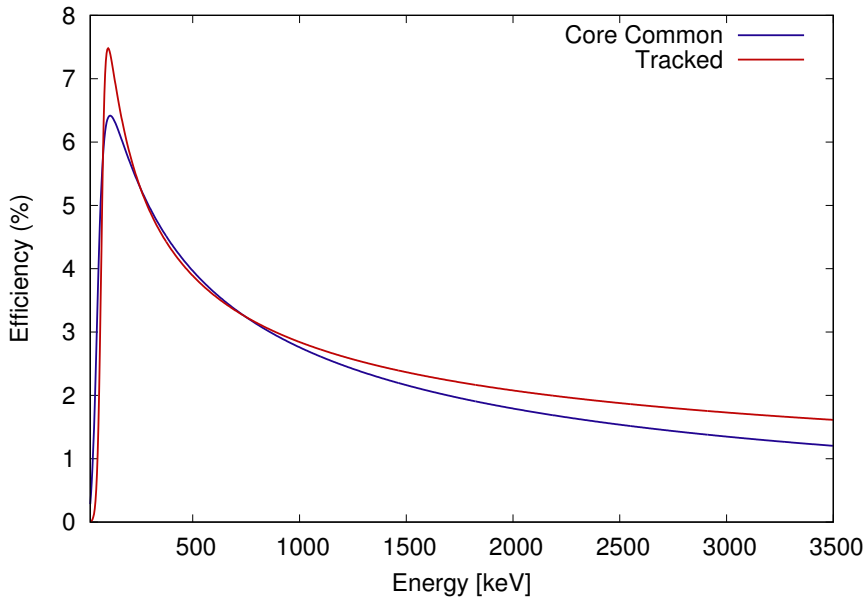

Figure 3.36: Absolute efficiency curves for the AGATA spectrometer for the Common Core (blue), Tracked (red) and Add Back (green) methods, as reported in [86].

Since the absolute efficiency is a key quantity in the cross section measurement, the most reliable and precise estimate must be used. The tracking efficiency to reconstruct the γ event strongly depends on the γ-ray energy and on its angular distribution. Moreover, it varies with the multiplicity and does not scale linearly

with respect to the number of detectors. This makes extremely complicated to get a reliable value for in beam data starting from source measurements. The Core common method efficiency can instead be treated in a more straightforward way. On the other hand the Core common efficiency is lower than the tracking one at energies higher than ∼500 keV, as can be seen in Fig. 3.36. This is due to γ rays which Compton scatter from one crystal to another. The tracking algorithm manage to reconstruct the majority of these events while in the Core common spectrum they end up in the background. This effect can be clearly seen in Fig. 3.37 where the γ-γ matrices obtained with the tracking (a) and the core common (b) methods are reported. The diagonal lines in panel (b) correspond to γ rays which Compton scatter between the two crystals. Those lines are not visible in panel (a) where the events are reconstructed by the tracking.

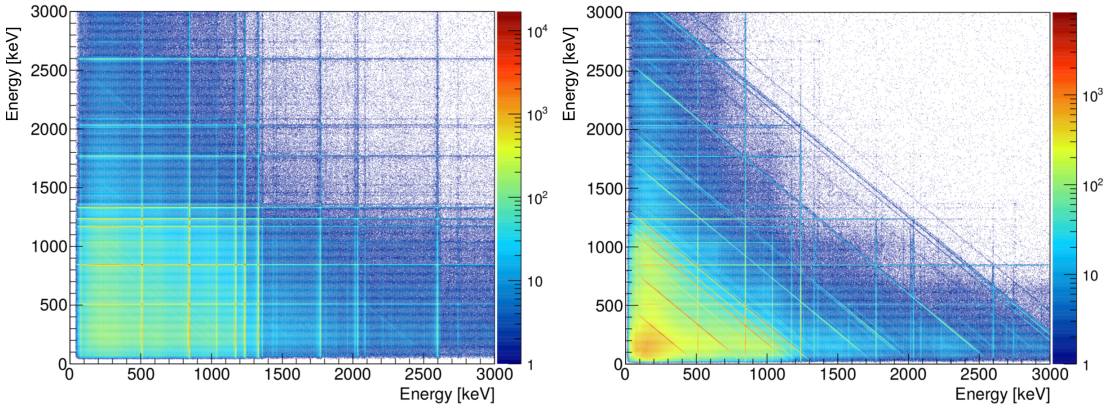

Figure 3.37: γ-γ matrices obtained with ^{56}Co and ^{60}Co sources and a) MGT tracking algorithm, b) Core common method.

For these reasons the Core common method has been used in the Cross section measurement while the tracking algorithm has been employed in the triple stack lifetime measurement, where the knowledge of the absolute efficiency plays a minor role. On the other hand, the efficiency of the setup in beam is affected by the absorption of γ rays in the scattering chamber, by the focusing of the γ rays in the forward direction by the Doppler Boost and by the average multiplicity of the event. We will describe the ways in which these effects are taken into account in the following paragraphs.

Absorption in the scattering chamber In the measurement from Lalovic *et al.* [86] the side parts of the scattering chamber were dismounted. This affects the absolute efficiency due to the absorption of γ rays in the aluminum material of the chamber. To have a reliable reference measurement, source runs were performed right before the in beam data taking. The ^{152}Eu source is a typical choice for relative efficiency curves estimates. In addition, the ^{56}Co source emits γ rays up to $\sim$3 MeV, allowing the extension of the curve to higher energy. We combine the data sets relative to these two sources to obtain the relative efficiency curve to be used in our experiment. The resulting curve for the core method is reported in Fig. 3.38, together with the experimental data points and the curve from [86].

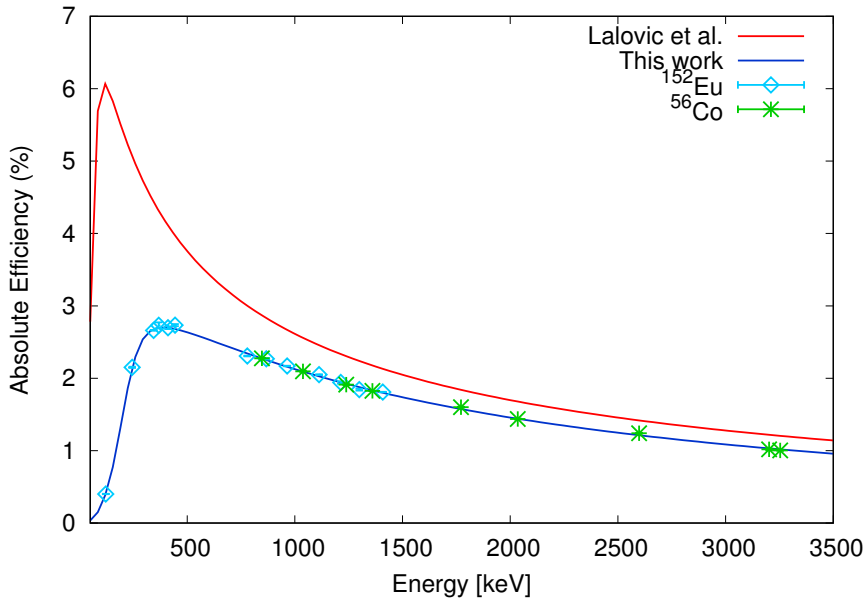

Figure 3.38: Absolute efficiency curves for the AGATA spectrometer for the Common Core method obtained for the present experiment (blue) and reported in [86] (red). The experimental data points are reported as well.

The effect of the absorption of γ rays in the scattering chamber is clear. It affects mainly the low energy part of the spectrum as expected, but it has a non-negligible impact also at the energies of interest for the present experiment. The ^{56}Co source allows, in addition, to get an absolute efficiency estimate as well. ^{56}Co β-decays to excited states in ^{56}Fe. In particular the $4^+ \rightarrow 2^+ \rightarrow 0^+$ cascade

is clearly visible through the observation of the $4^+ \rightarrow 2^+$ 1238-keV and $2^+ \rightarrow 0^+$ 846-keV lines in coincidence. The efficiency at 846 keV can therefore be obtained by comparing the number of counts in the singles spectrum in the 1238-keV peak to the one in the 846-keV peak in the $\gamma - \gamma$ projection gated on the 1238-keV line. The obtained result is 2.3(1) %. For its own nature the ^{56}Co source is not point-like neither transparent; the measured γ-ray efficiency can therefore be slightly biased by the self absorption of the photons inside the source material itself. Moreover, the angular correlation between the two γ rays plays a role as well. These effects have been taken into account in the error estimate. To overcome this issues and to cross-check the result, the absolute efficiency has been estimated with the ^{152}Eu source as well. By knowing the activity of the source at the time instant t, the efficiency at a given energy E is given by

$$\epsilon(E) = \frac{\text{Area Peak (E)}}{\text{Time of measurement} \times A(t) \times P_\gamma}$$

where P_γ is the probability of emission of the γ ray. For the 1408-keV transition a value of 1.84(2)% has been obtained, to be compared with the 1.8(1)% estimate given by the relative efficiency curve scaled for the 2.3(1)% value at 846 keV with the ^{56}Co source. The agreement is very good and the slight discrepancy can be attributed to the self-absorption of the ^{56}Co source. We take as the best estimate the one obtained with the ^{152}Eu.

In principle, γ rays could be absorbed by the 0.25 mm, 0.5 g/cm^2 ^{197}Au Coulex target as well. The half-lives of the states of interest are in the range 5-10 ps. Considering $\beta = 0.524$c and $T_{1/2} = 5$ ps, almost 20% of the ions will decay inside the target. The absorption coefficient of the gold target material is $\mu = 0.069\text{cm}^2/\text{g}$. The amount of γ rays lost due to the absorption in the target can therefore be estimated from the relation $I = I_0 \exp(-\mu d)$ where I and I_0 are the observed and emitted number of photons and d is the material thickness. The correction factor to be applied to the absolute efficiency can be written as:

$$F = 0.2 \cdot (1 - \exp(-\mu d))$$

Assuming that the decay occurs, on average, in the center of the target and

taking into account the angular dependence of the efficiency and the effective target thickness at different angles, the obtained value is $F = 0.46\%$. The effect is therefore negligible.

Doppler Boost At relativistic energies most of the photons are emitted along the nucleus direction of motion. This modifies the apparent luminosity of the emitting ion following the relation:

$$L' = L \cdot \left(\frac{\sqrt{1-\beta^2}}{1-\beta\cos(\theta)} \right)^2 \tag{3.22}$$

where β is the ion velocity and θ is the angle of emission of the photon. In the present work we have $\beta = 0.524$ c and all AGATA detectors were placed in the forward direction, covering a angular range of 15-65 deg. This implies a sizeable increase in the efficiency with respect to the source measurement which is only partially counterbalanced by the Doppler shift of the center-of-mass photon energy to higher values in the lab frame. To take into account this effect we started from the efficiency curve reported in in Fig. 3.38, then we converted the center-of-mass energy to the lab frame energy for each detector and finally we calculated the increase in luminosity given by the Lorentz boost. In Fig. 3.39 the Core efficiency curves before and after the Doppler boost correction are reported.

The increase in efficiency is clear and amounts to a factor ~ 1.7 in the energy range of interest.

γ-ray multiplicity correction Another effect which might modify the absolute γ efficiency is the average γ-ray multiplicity of each event, since the higher is the number of emitted background photons, the higher is the probability of pile up with the γ rays coming from the Coulex reaction. The energies of the two photons would therefore sum up and the total number of counts in the peak decreases. In Coulomb excitation only one γ ray is emitted; however random and prompt unwanted coincidences, given mostly by Bremsstrahlung radiation, result in background and increased multiplicity. In Fig. 3.40 we report the number of cores firing when one γ at the expected Coulex peak energy is emitted in the ^{46}Ti beam runs. To remove the contribution from unwanted random and prompt

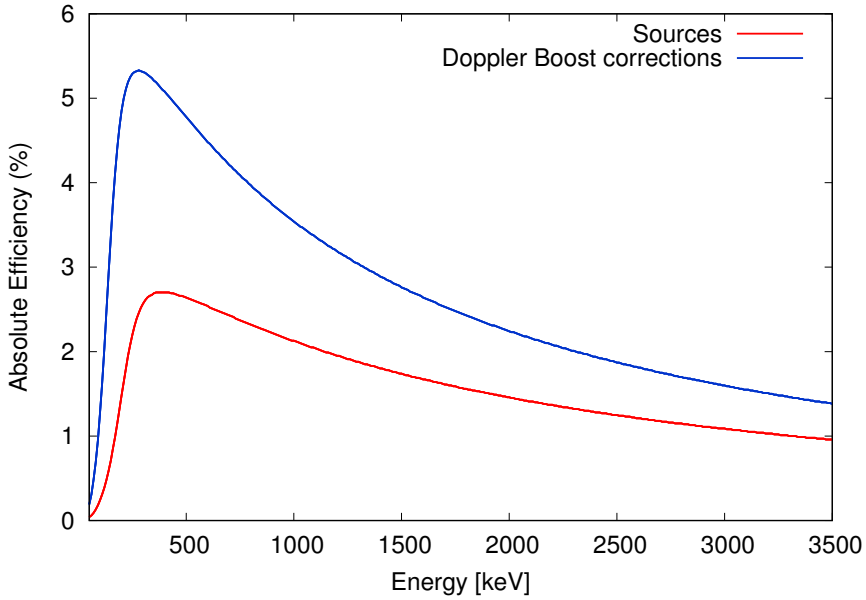

Figure 3.39: Effect of the Doppler Boost correction for $\beta = 0.524$ c on the efficiency curve of the AGATA spectrometer.

coincidences we subtracted to the total multiplicity spectrum (red), the average background multiplicity (blue), obtained from a portion of the spectrum where no γ rays were observed. The resulting spectrum (black) represents the number of detectors firing when a γ ray coming from the Coulex reaction is detected. This background subtraction procedure takes into account the different multiplicity of the background and Coulex event: the portion of the spectrum at the energy of interest contains obviously both kind of events; however the correction efficiency we are looking for has to be applied to the Coulex events, which are the one actually creating the γ peak. By considering the variation in the multiplicity at the Coulex peak energy with respect to the one of the background we are effectively measuring the average multiplicity of the Coulex events.

The fraction of events at a given multiplicity is reported in Tab. 3.4 for ^{46}Ti and ^{46}Cr runs.

The absolute AGATA efficiency can therefore be corrected for the γ-multiplicity

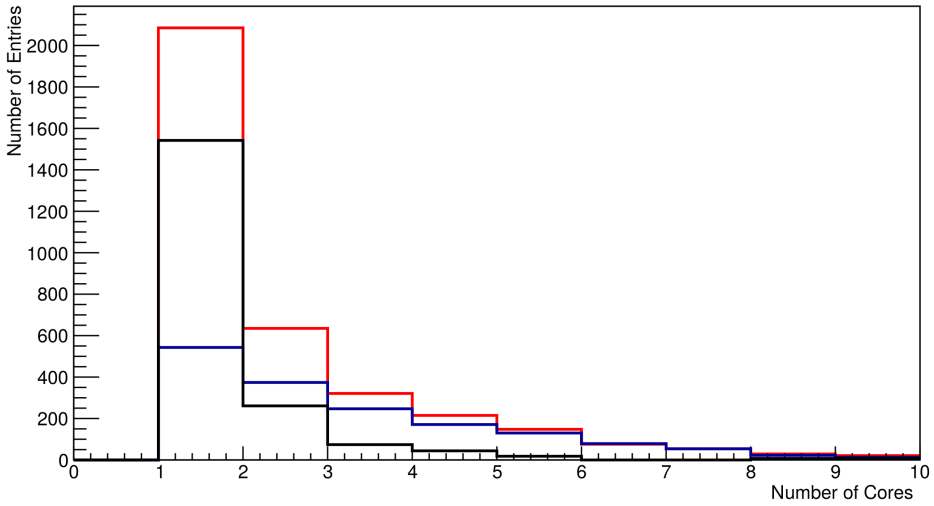

Figure 3.40: Red: average core multiplicity in coincidence with one 892-keV γ Blue: average background core multiplicity. Black: average core multiplicity in coincidence with one γ coming from Coulex reaction. The ^{46}Ti beam runs were used.

effect according to:

$$\epsilon_{corr,^{46}Ti} = \epsilon\left(0.795 + 0.135 \cdot \tfrac{21}{22} + 0.04 \cdot \tfrac{20}{22} + 0.02 \cdot \tfrac{19}{22} + 0.01 \cdot \tfrac{18}{22}\right) = 0.985 \cdot \epsilon$$

$$\epsilon_{corr,^{46}Cr} = \epsilon\left(0.91 + 0.09 \cdot \tfrac{21}{22}\right) = 0.996 \cdot \epsilon$$

The multiplicity correction described so far holds if the multiplicity of the source used for the efficiency calibration is 1. The absolute efficiency value has been obtained from the 1408-keV peak of the ^{152}Eu source. ^{152}Eu β decays to ^{152}Sm and the 1408-keV transition is in coincidence only with the 121-keV one. The emission multiplicity is therefore 2; on the other hand the effect on the efficiency is given by the number of γ rays detected by AGATA. Taking into account the absolute efficiency at 121 and 1408 keV, the probability to detect both γ rays is lower than 0.01%. Moreover, the transitions with energy higher than 1408 keV in the ^{152}Eu source are extremely weak and their Compton continuum below the 1408-keV peak is negligible. The detected multiplicity at the 1408-keV

Core multiplicity	Fraction (%)	
	^{46}Ti	^{46}Cr
1	79.5	91
2	13.5	9
3	4	0
4	2	0
5	1	0

Table 3.4: Fraction of events with a given Core multiplicity.

transition can therefore safely be considered as 1.

The overall effect of the γ-ray multiplicity is therefore a reduction of the absolute efficiency of the order of 2% as expected for a low-multiplicity reaction such as a Coulex one.

Correction for the effective number of working detectors During the in beam data taking, some detectors manifested a bad behavior and were therefore switched off. This can be due to many different reasons: loss of synchronization, too high noise, failure of preamplifiers, FET or electronic chain. This obviously affects the overall average efficiency since implies a different number of detectors available for a certain amount of time. The live time of each detector can be estimated by plotting the ID number of the firing crystal versus the timestamp, as reported in Fig. 3.41 for the ^{46}Ti runs.

On the other hand, the beam intensity may change during the data taking. One detector which did not manifest bad behavior was therefore chosen as beam monitor to determine the fraction of statistics collected in a specific time interval. In a such a way it is therefore possible to estimate the amount of loss in the data due to the switching off of a given detector. Finally, the effect of the Doppler Boost on the change in the efficiency was taken into account, since the loss of a forward detector will have a more important impact with respect to the one of detectors at larger angles. The correction values for the γ-ray efficiency obtained for ^{46}Ti and ^{46}Cr runs are reported in Tab. 3.5.

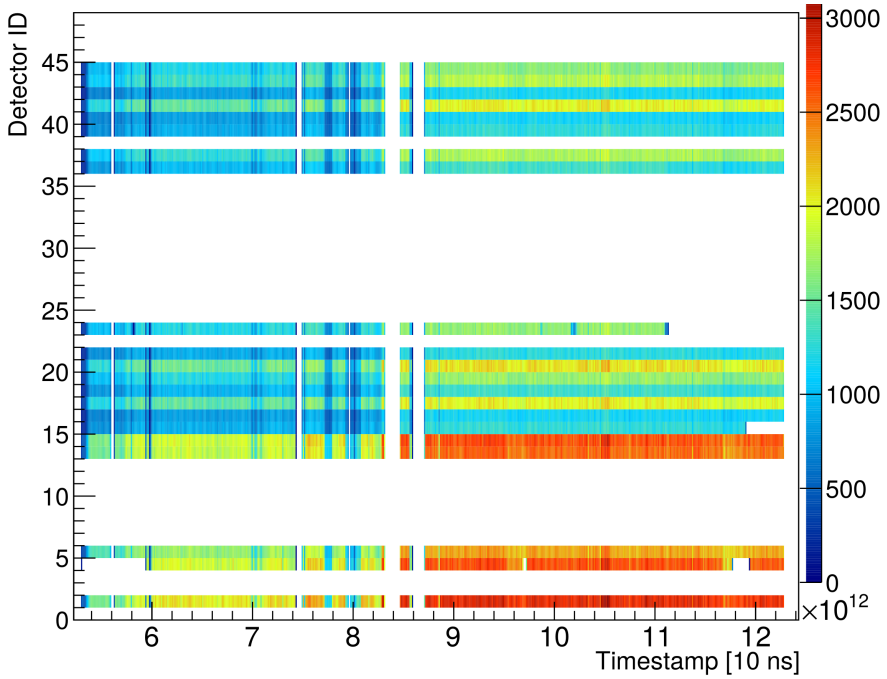

Figure 3.41: ID detector number versus the timestamp of the event. Detectors 4, 15, 23 manifest bad behavior in fixed time intervals.

^{46}Ti	^{46}Cr
0.929	0.964

Table 3.5: Correction factors for the γ-ray efficiency due to the effective number of working detectors for the different settings.

Angular distributions The angular distribution of the electromagnetic transition of interest plays an important role in the cross section determination, since it focuses the emitted γ rays in a certain solid angle, giving an anisotropic pattern. Since the angular coverage of AGATA is limited to 15-65 deg, this may result in an increasing or decreasing of the efficiency, according to the multipolarity of the transition. It is expected that in Coulomb excitation reactions at intermediate and high energies an almost complete prolate alignment of magnetic substates occurs [87]. In such a situation the quantization axis is conveniently chosen on the same direction of the beam axis. The angular distribution of a transition can

be expressed as:

$$W(\theta) = \sum_{keven} a_k P_k(\cos(\theta)) \tag{3.23}$$

where the coefficients a_k can be determined following the Winther and Alder approach [63]. For a detailed derivation see Ref. [88]. The transitions of interest in the present work are of purely quadrupolar character. The angular distribution depends from the energy of the reaction and the chosen cut on the maximum scattering angle. The calculated distributions for the present experiment are reported in Fig. 3.42, where the pattern expected for an isotropic behavior is reported as well.

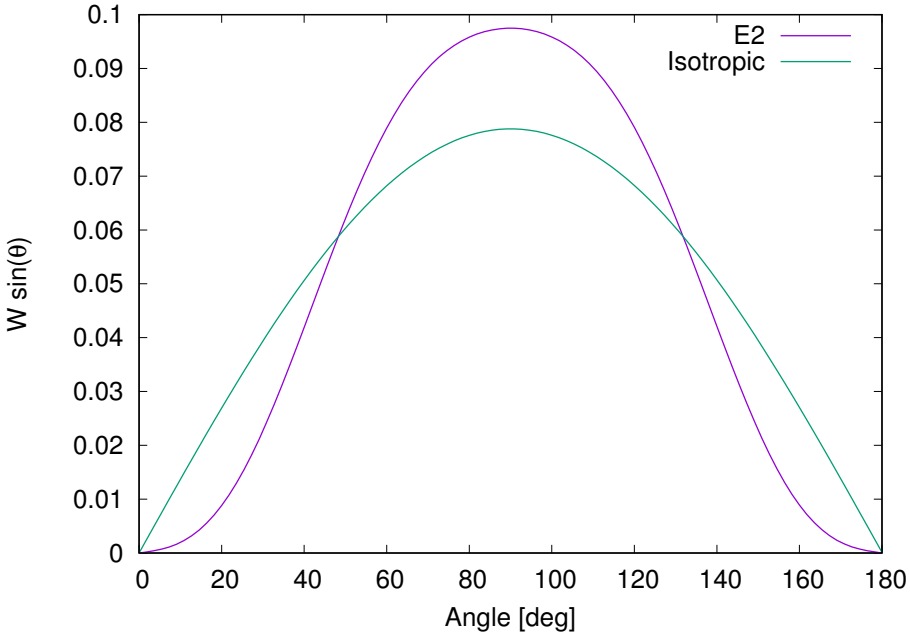

Figure 3.42: Calculated angular distribution for the present experiment. The isotropic distribution is indicated as well.

As already seen, at relativistic energies such as the ones of the present experiment, the γ rays are focused in the forward direction by the Doppler Boost effect. This effect obviously modifies the angular distributions reported in Fig. 3.42, shifting the curve towards forward angles. The overall effect is depicted in

Fig. 3.43, where the Doppler boosted quadrupole and isotropic distribution are reported.

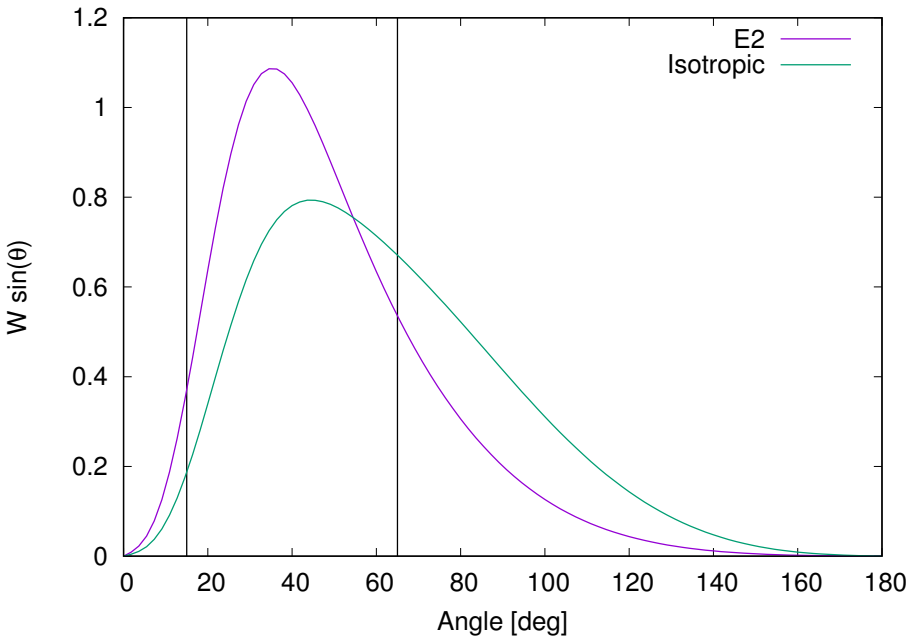

Figure 3.43: Calculated Doppler boosted angular distributions for the present experiment. The quadrupolar and isotropic distribution are considered. The vertical black lines correspond to the angular coverage of AGATA.

The impact on the γ-ray efficiency depends on the angular coverage of the detection apparatus. The range covered by AGATA is reported in Fig. 3.43. It is clear that the effect of the angular distributions on the γ-ray efficiencies is an overall increasing. Quantitatively, the efficiency is increased by 17%.

3.5.3.3 Doppler Correction Optimization

Z target position determination The Doppler shift is given by the Eq. (2.6) and depends from the velocity β and the angle θ between the γ ray and the emitting ion. It is therefore essential to achieve a proper determination of the ion and γ trajectory. The ion direction is reconstructed from the interaction positions in the target and Wall DSSSD detectors, while the γ-ray vector is determined from the target DSSSD and the AGATA PSA hit position. The Z position of the target

is, in principle, fixed from the geometry of the setup but the real point of de-excitation of the nucleus may be different due to the lifetime of the state we want to study and to the angle of scattering with the target. In order to determine the optimal average target position we adopted an iterative procedure. We modify the Z value by steps of 0.5 mm. For each Z value we found the velocity β of the ion which allowed to achieve the best energy resolution for the $2^+ \rightarrow 0^+$ transition in ^{46}Ti. We chose as best Z value the one where the measured centroid energy corresponded to the known literature value. This gave a target offset of -3.5 mm with respect to the nominal value, i.e. the center of AGATA. This position was then used for all the Coulomb excitation measurements, while corrections due to the geometry of the target where applied in the Triple Stack analysis.

LYCCA Target DSSSD (x,y) positions optimization To properly determine the hit position, the X and Y coordinates of the target DSSSD must be optimized as well. These values are fixed by the geometry of the setup but the position of the interaction of the ion with the real target may differ from the one measured by the DSSSD since the target silicon detector is placed ∼6 cm upstream with respect to the reaction target. Therefore, if the incoming trajectory of the nuclei is not perfectly straight, the measured positions are slightly different from the real ones. To correct this effect we implemented scanner routines where we vary the X and Y target DSSSD positions and the γ-ray spectrum is corrected for the different values of the angle between the photon and the particle given by those particular X and Y coordinates. We then fit the strong $2^+ \rightarrow 0^+$ transition in ^{46}Ti to find the offset value which allows to obtain the correct centroid energy and to minimize the FWHM. This effect is strictly related to the angle with the Z coordinate of the incoming beam, which in turn is given by the FRS setting and is different for each secondary beam. The scanning procedure must be therefore performed for each FRS setting. The matrices relative to both X and Y position for the ^{46}Ti runs are reported in Fig. 3.44.

LYCCA Time of Flight optimization The ion velocity β used in the Doppler Correction is obtained from the Time of Flight of the nucleus from the LYCCA ToF Start and Stop scintillators. However, the Target DSSSD and the reaction

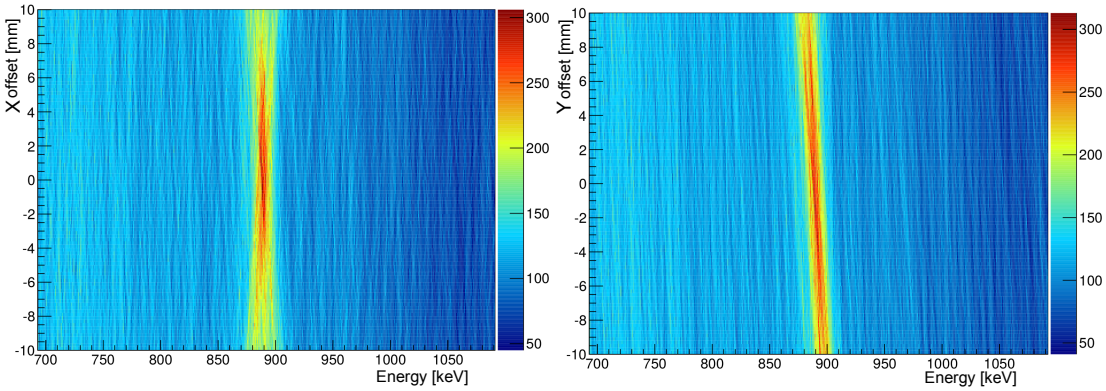

Figure 3.44: Scanner matrices for the $2^+ \rightarrow 0^+$ transition in ^{46}Ti. On the X axis the γ-ray energy Doppler corrected with a $\cos(\theta)$ derived from the X and Y offset shown in the Y axis is reported. Left panel: X scanner. Right panel: Y scanner.

target are situated between the two plastic scintillator. Therefore the ion looses part of its kinetic energy in the target material and in the reaction and its velocity β decreases. The effect is small but it must be taken into account in the optimization of the Doppler correction. In the present analysis we applied an effective correction to the measured ToF by adding a fixed value. To determine the optimal offset, a scanner was implemented where the γ-ray spectrum was Doppler corrected with the velocity β obtained from the measured ToF modified by the offset. Then the $2^+ \rightarrow 0^+$ transition in ^{46}Ti was fitted with an automatic routine. The offset value which allowed to obtained the sharpest peak was chosen as the optimal one. The scanning matrix and the FWHM relative to each different offset value are reported in Fig. 3.45.

The optimal ToF offset is given by the minimum of the parabolic function which fits the FWHM distribution reported on the left panel of Fig. 3.45.

3.5.3.4 Background reduction

The most important source of background in the present experiment is given by Bremsstrahlung radiation, caused by the slowing down of the beam nuclei in the target. The reduction of the contribution coming from these X rays is fundamental to improve the peak to total and to clean the γ-ray spectrum. This can be achieved in this work by putting conditions on the γ-particle time as we

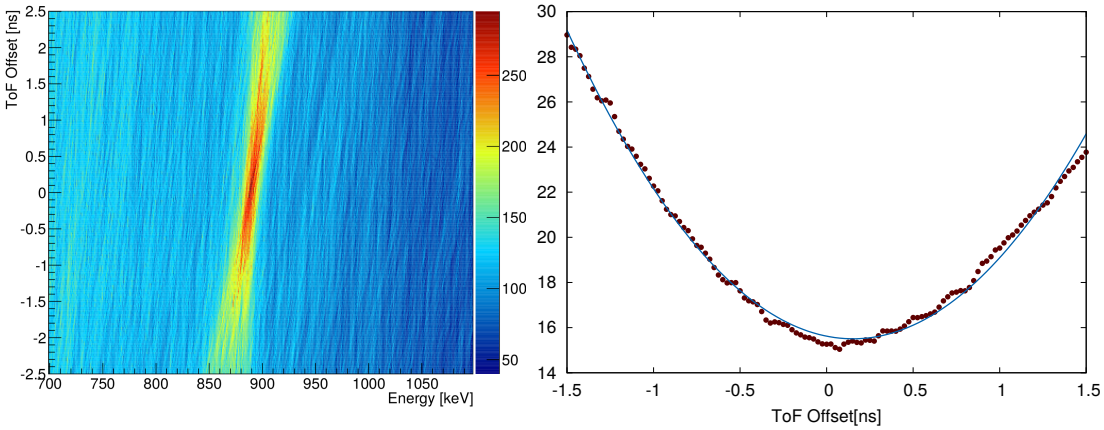

Figure 3.45: Left panel: Scanner matrix for the $2^+ \rightarrow 0^+$ transition in ^{46}Ti. On the X axis the γ-ray energy Doppler corrected with a β derived from the ToF offset shown in the Y axis is reported. Right panel: FWHM for the same transition as a function of the ToF offset.

describe in the next section.

Time condition The experimental setup gives the possibility to measure the time interval between the signal recorded in the FRS scintillator in S4 and the detection of the γ ray in AGATA. This allows to correlate a given photon with the relative ion. Since different isotopes will have slightly different velocities β, it is possible to remove γ rays coming from other reaction channels and uncorrelated unwanted background by imposing a time condition. In Fig. 3.46 the γ-ray time distribution is plotted against the photon energy.

By putting a narrow gate on the second peak of the time distribution reported in Fig. 3.46 it is possible to remove the background induced at higher energy by unwanted particles which hit AGATA.

3.6 Results

In this Chapter the results of the experiment will be presented. The steps towards the Coulomb excitation cross section determination for ^{46}Cr and ^{46}Ti will be explained in the first section, while the results from the triple stack measurement of

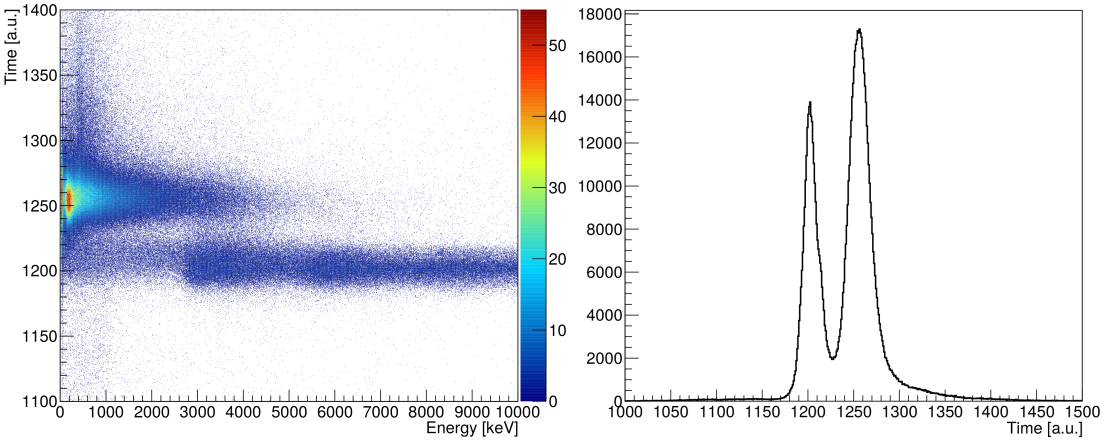

Figure 3.46: Left panel: Energy vs Time matrix for the ^{46}Ti run. The time value represents the interval between the Sc41 ion hit and the AGATA γ signals. Right panel: Time projection of the matrix shown in the left panel.

^{46}V and ^{46}Ti will be given in the second section. The amount of data taking time for each sub-experiment was different due to sizeable differences in the secondary beam intensities achievable. A summary of the performed measurements is given in Tab. 3.6.

Sub Experiment	^{46}Ti Coulex	^{46}Cr Coulex	^{46}Ti Lifetime	^{46}V Lifetime
Data Taking [h]	19	65	8	41
Primary Beam Intensity [s^{-}1]	5×10^{8}	2×10^{9}	1.4×10^{9}	2.5×10^{9}
Focal Plane S4 rate [s^{-}1]	1.4×10^{4}	1.2×10^{3}	4.1×10^{4}	2.5×10^{4}

Table 3.6: Data taking time and beam intensities for all the sub-experiments presented in this work.

3.6.1 Coulomb excitation cross section

In relativistic Coulomb excitation experiments the cross section is given by:

$$\sigma_{Coulex} = \frac{N_\gamma}{N_{beam} N_{target}} \tag{3.24}$$

where N_{target} is the number of target atoms per unit area, N_{beam} is the number of ions of interest impinging on the target and N_γ is the efficiency-corrected number of gamma rays in the peak. The derivation of each of these quantities is described in the following paragraphs.

Number of scattering centers in the target

N_{target} can be expressed as:

$$N_{target} = \frac{\rho N_A}{A}$$

where ρ is the density of the target in g/cm^2, N_A is the Avogadro number (N_A = 6.023 $\times 10^{23}$ particles/mole) and A is the atomic mass of the target in g/mole. In this experiment a 0.25 mm target of ^{197}Au was used in the Coulex runs, which implies $N_{target} = 1.48 \times 10^{21}$ particles/cm^2.

Number of incoming ions

N_{beam} is given by the Particle Identification plot of FRS with proper gates applied. It represents the number of ions of interest which hit the target, independently from the eventual type of reaction or the gammas produced. To ensure the minimum possible bias, a set of different triggers, summarized in Tab. 3.7, was used.

1	Clock	6	FRS + Hector
2	Lycca	7	FRS + AGATA
3	AGATA	8	FRS+Hector+Lycca
4	Hector	9	FRS+AGATA+LYCCA
5	FRS trigger box	10	FRS Downscaled

Table 3.7: Triggers used in the present experiment.

A priority encoder was implemented in order to assign the highest priority to the trigger with the highest number. Therefore, if an event satisfies two different triggers, it is labeled with the highest-priority one. This allows to properly estimate the number of incoming ions by requiring a trigger 10 condition on the FRS ID plot. A downscaling factor of 256 was applied to overcome any possible issue due to high beam intensity. The total amount of incoming ions can be therefore extracted by multiplying the number of ions detected by FRS and labeled with trigger 10 by the downscaling factor 256. As shown in Sec. 3.5.1, the position of the ions in the second and fourth focal planes of FRS was determined from the scintillators to overcome the loss in statistics induced by the TPCs at high counting rates. This results in a presence of two different blobs in the PID due to the bad behavior of the left PMT in the SC21 scintillator, as explained in Sec. 3.5.1. To determine the total number of incoming ions, one cut for each blob has therefore been used in the present analysis. The presence of two identical structures shifted in A/q requires however the use of stringent cuts, to avoid the contamination coming from the blobs corresponding to other isotopes in the other structure. The FRS particle identification plots for the ^{46}Ti and ^{46}Cr nuclei are reported in Fig. 3.47. The applied gates are shown as well.

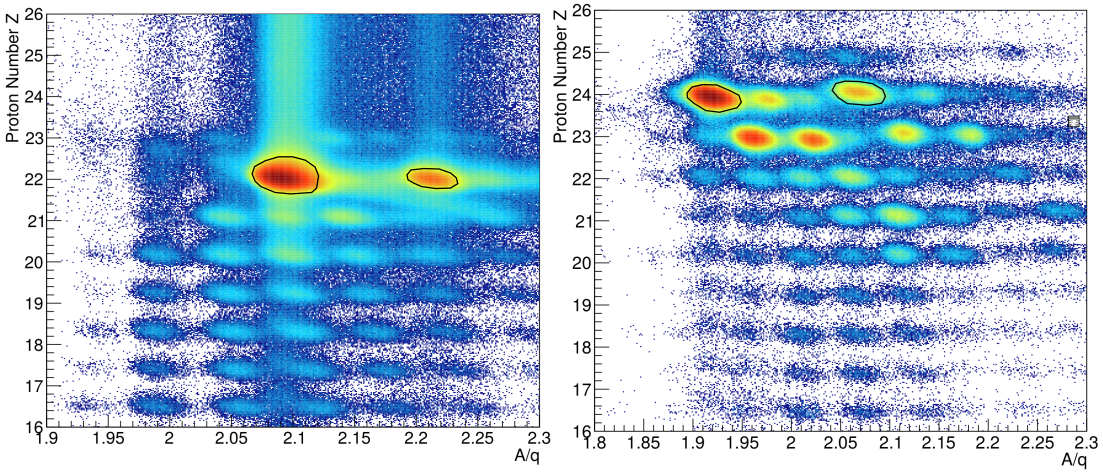

Figure 3.47: FRS particle identification plots for ^{46}Ti (left) and ^{46}Cr (right) used in the present analysis. The black curves denote the adopted incoming gates. Strict cuts were chosen in order to avoid contamination from unwanted incoming ions.

The purity of the gates can be tested by projecting the PID on the Z or A/q axis and by considering the leakage of the neighboring ions in the chosen cuts. We report in Fig. 3.48 as an example the case of ^{46}Ti.

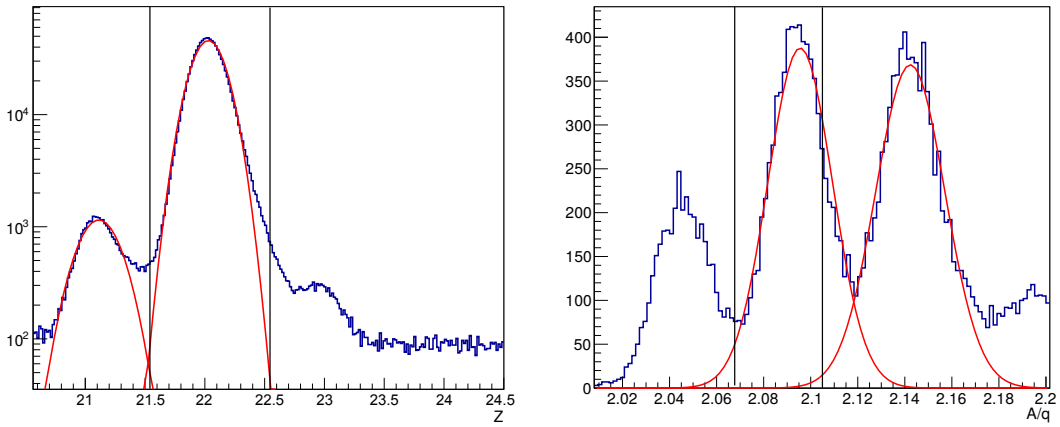

Figure 3.48: Z (left) and A/q (right) projections of the FRS PID plot for ^{46}Ti settings. The applied cuts are reported as well. The reported A/q spectrum corresponds to Sc isotopes. See text for details.

The leakage in the proton number Z due to different isotopes is negligible, as can be seen by the left panel of Fig. 3.48. The contribution of the continuous uncorrelated background below the peak of interest, visible above Z=24.5 and below Z=21, is less than 0.6%. Most of this background comes from incomplete information on the ion, such as lack of signal from one MUSIC, or pile up. Since more than 80% of the transmitted ions correspond to ^{46}Ti, the contribution of the background is lower than 0.2% and it is therefore negligible.

The leakage estimate in A/q is harder to obtain, since the large majority of the events are characterized by the same value. Moreover, as already seen, the use of scintillators worsen the resolution and causes the presence of two blobs. In order to get a reliable estimate we therefore focus the analysis on the scandium isotopes, which are transported in comparable quantities. The projection and the gates applied are reported in Fig. 3.48 (right). The leakage of the unwanted isotopes in the gate of the one of interest is of the order of 3% if the two ions are transmitted in comparable quantities as it is the case for scandium isotopes. On the other hand, the quantity of ^{46}Ti ions is more than two order of magnitude

larger than the one of the neighboring titanium isotopes. The effect of the leakage in the A/q gates is therefore negligible. These effects are even less significant for the ^{46}Cr runs, where the lower beam rate allowed to obtain cleaner spectra, as it is clear from Fig. 3.47.

The number of detected and downscale-corrected incoming ions for the nuclei of interest are given in Tab. 3.8.

Nucleus	^{46}Ti	^{46}Cr
Detected Ions	8.572(8)E5	7.754(8)E4
Total Ions	2.194(2)E8	1.985(2)E7

Table 3.8: Total number of ^{46}Ti and ^{46}Cr nuclei in the present experiment.

Number of detected γ rays

N_γ is the number of γ rays in the peak. To select only γ rays coming from Coulomb excitation reaction, the incoming gate shown in Fig. 3.47 has been combined with an outgoing gate on the atomic number Z of the ion detected by LYCCA. The main purpose of the outgoing gate is to clean the spectrum removing unwanted background and discarding gammas coming from other reaction channels. The chosen gates were therefore large enough to avoid any loss of good events. The outgoing PID is shown in Fig. 3.49 together with the applied gates.

To further reduce the background, coming primarily from Bremsstrahlung radiation, a narrow condition of 45 ns on the particle-γ time was put. As discussed in Sec. 3.5.3 the present setup allows a precise event-by-event Doppler correction, which results in a high resolution of the peak. The gamma spectra associated with the ^{46}Ti and ^{46}Cr nuclei after the application of incoming, outgoing and timing gates are reported in Fig. 3.50.

The number of counts in the γ-ray peak shown in Fig. 3.50 was corrected for the efficiency of the AGATA array, which has been discussed in Sec. 3.5.3.2. Taking into account all the correction already described, the adopted efficiency value in the present analysis is 4.16% and 4.34% for ^{46}Ti and ^{46}Cr, respectively, at the energy of interest.

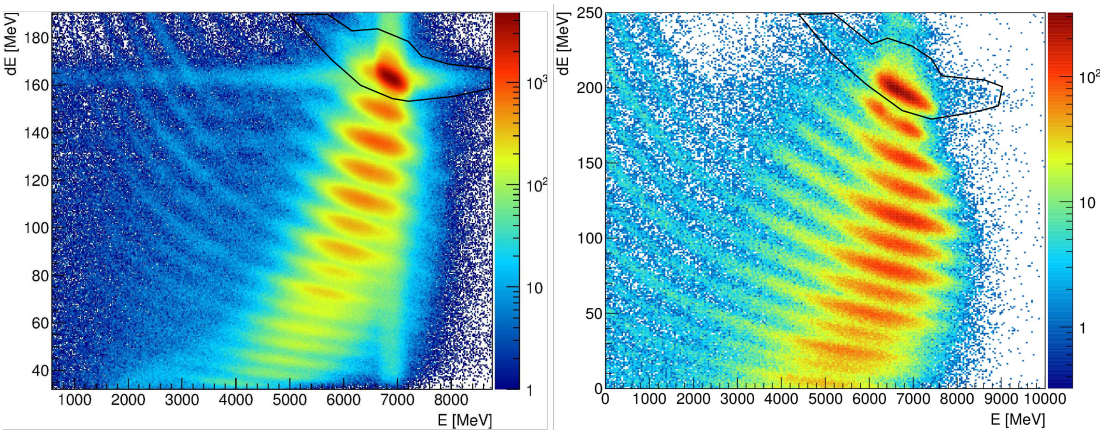

Figure 3.49: LYCCA outgoing atomic number identification plots for ^{46}Ti (left) and ^{46}Cr (right) used in the present analysis. The black curves denote the adopted outgoing gates.

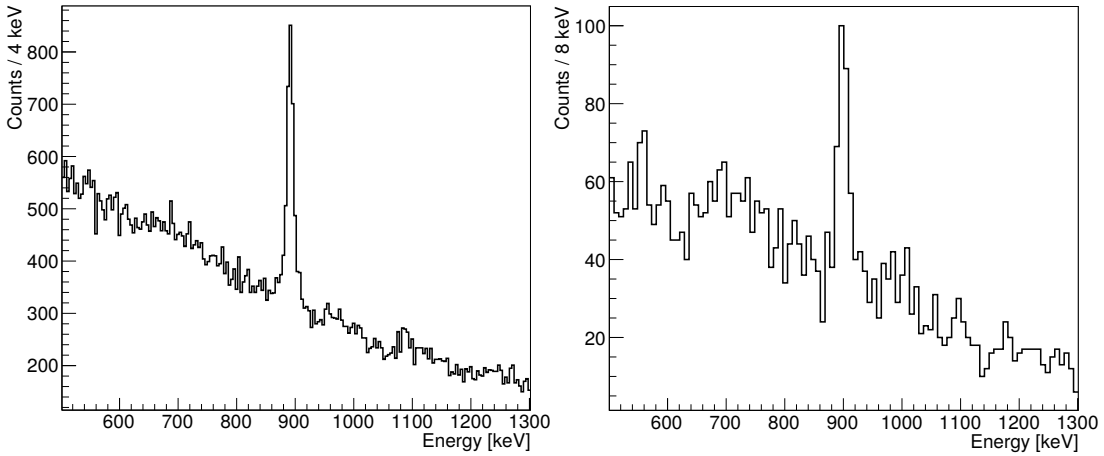

Figure 3.50: γ-ray spectra for the nuclei of interest ^{46}Ti and ^{46}Cr. Incoming, outgoing and time gates are applied. The event-by-event LYCCA β has been used.

Two other important effects must be considered to properly obtain the Coulomb excitation cross section: i) the dead time of the acquisition, which causes a loss in the detected events due to the processing time of each signals by the DAQ and ii) the scattering angle cut, which is essential in order to neglect the contribution of the nuclear interaction to the excitation of the nuclei of interest. These effects

will be discussed in the next paragraphs.

3.6.1.1 Dead Time estimate

Two different acquisition systems were used in the present experiment: the Multi-Branch System (MBS) [89], which treated the signals coming from FRS and LYCCA, and the "Nouvelle Acquisition temps Rel Version 1.2 Avec Linux" (NARVAL) [90], which processed the AGATA data. The two DAQs were then synchronized by a common clock and the physical event was reconstructed by a merger and an event builder. A detailed description of the data acquisition system in the PreSPEC-AGATA campaign can be found in [91]. The dead times of the two DAQs are independent and therefore must be treated separately.

To estimate the MBS dead time a 10-kHz pulser signal was sent into a scaler during all the beam runs. Two outputs were available: the "free" output was continuously increased every 100 microsecond, while the "vetoed" output was scaled only when the MBS DAQ was not busy. By comparing the increasing in the two outputs between two chosen events it is therefore possible to extract the average MBS dead time between those events. The 10-kHz and 10-kHz-vetoed scalers were read out with every trigger condition. The obtained value is 4.0% for the ^{46}Ti setting.

The MBS dead time reduces the number of detected incoming ions with respect to the number of nuclei which actually hit the target. However, coincidences with both FRS and LYCCA are required to obtain the γ-ray spectra shown in Fig. 3.50. These events are marked with Trigger 9. The MBS dead time affects therefore the number of counts in the γ peak as well. In other words, AGATA information not in coincidence with MBS data can not be used in the cross section measurement. Since the cross section is proportional to the ratio between the number of γ rays and the number of incoming ions, the effect of MBS dead time cancels out.

On the other hand, AGATA dead time affects only the number of γ rays in the peak reducing the amount of Trigger 9 events but does not influence the number of incoming ions, since Trigger 10 events are independent from NARVAL DAQ. To generate Trigger number 9, copies of AGATA detectors core preamplifier signals

are sent to CFDs modules. The OR of these signals is then sent to a Trigger Logic module in the MBS DAQ, which evaluates coincidences between these signals and the FRS/LYCCA ones to assign the correct Trigger number (Tab. 3.7). For any Trigger a gate to the AGAVA (AGAta VME Adaptateur) GTS is sent. The coincidences between the AGAVA GTS and the individual AGATA detectors GTS are evaluated by the Trigger Processor which marks every Trigger request with a validated or rejected flag and sends the information back to the AGAVA GTS. If AGATA DAQ is busy when the Trigger 9 is requested, the flag is set to rejected, otherwise to validated. The AGATA dead time can therefore be estimated from the ratio between rejected and requested Trigger 9 events. The values obtained for the two settings are reported in Tab. 3.9

Setting	^{46}Ti	^{46}Cr
AGATA dead time (%)	0.8	0.3

Table 3.9: Average dead time for the ^{46}Ti and ^{46}Cr settings.

3.6.1.2 Scattering Angle reconstruction

As already pointed out, the relativistic regime induced by the high beam energies typical of in-flight radioactive beams causes interference between the electromagnetic and the nuclear interactions. To extract the Coulomb excitation cross section it is therefore essential to disentangle the two contributions and to discard events in which the nuclear force plays a role in the projectile excitation. This can be achieved by restricting our analysis only to peripheral events in which the impact parameter of the incoming ions is sufficiently large that the short-range nuclear interaction contribution is negligible. A lower limit to the impact parameter b to ensure a "Safe Coulex" regime is given by the relation:

$$b_{min} = r_0 \left(A_P^{1/3} + A_T^{1/3} \right) + 5\text{fm} \tag{3.25}$$

where r_0 is 1.2 fm and A_T and A_P are the projectile and target masses, respectively. The safe impact parameters adopted in this analysis are reported in Tab. 3.10.

Setting	^{46}Ti	^{46}Cr
Impact Parameter (fm)	16.75	16.75

Table 3.10: Safe impact parameters adopted in the present analysis for ^{46}Ti and ^{46}Cr ion beams.

Since the impact parameter is not a direct observable, the Safe Coulex condition is put on the scattering angle θ_{max} of the ions trajectory before and after the reaction target. The relation between b_{min} and θ_{max} is:

$$b_{min} = \frac{a_0}{\gamma} \cot\left(\frac{\theta^{CM}_{max}}{2}\right) \tag{3.26}$$

where $a_0 = k\frac{Z_1 Z_2 e^2}{mv^2}$. To reconstruct the scattering angle of the ions, the (x,y) positions before and after the target, as well as the interaction point on the target itself, are needed. This information is obtained, in the present analysis, from the LYCCA ToF Start scintillator, the target DSSSD and the LYCCA Wall DSSSD. In order to check and properly optimize the alignment of the different detectors, the "unreacted" beam runs were exploited. In these measurements, the secondary target was removed and the ions proceeded therefore on a straight trajectory. The amount of material along the ion path due to the various FRS and LYCCA detectors may slightly deviate the beam nuclei. The probability of deflection is however symmetric around the straight trajectory and the effect will therefore cancel out. The correlation between the angles on the X(Y)Z plane, defined as $\arctan(dx(y)/dz)$ before and after the target is reported in Fig. 3.51.

The correlation between incoming and outgoing angles is evident in both X and Y directions. The reconstructed scattering angles for the ^{46}Ti and ^{46}Cr beam runs are shown in Fig. 3.52. The vertical lines show the Safe Coulex cuts applied, which correspond to the safe impact parameter reported in Tab. 3.10. The γ-ray spectra after the application of the scattering angle cut is reported in Fig. 3.53.

3.6.1.3 Background considerations

The background of the γ spectrum must be well understood in order to properly extract the number of counts in the peak. During the data taking, a ^{60}Co source

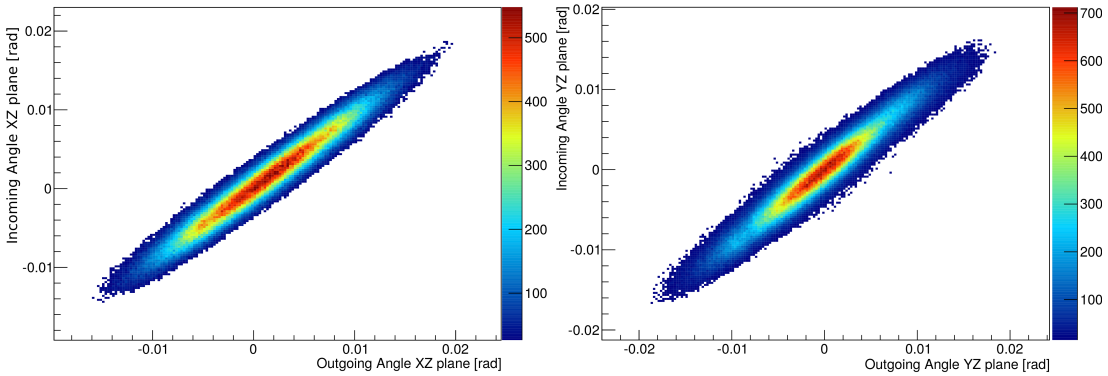

Figure 3.51: Correlation between incoming and outgoing angles on the XZ and YZ planes in the ^{46}Ti unreacted beam runs.

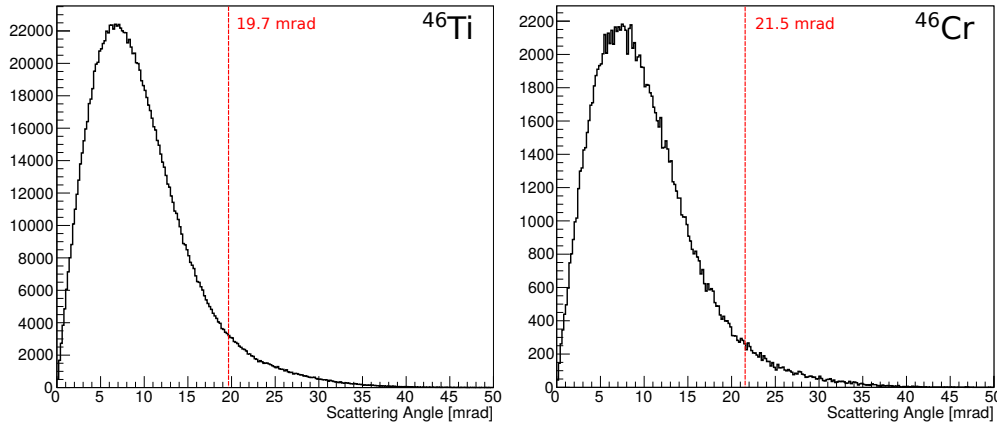

Figure 3.52: Scattering angle distribution for ^{46}Ti (left) and ^{46}Cr (right) secondary beams.

was placed outside the reaction chamber to monitor the stability of the setup. This causes anisotropic background since the solid angle covered by the different detectors with respect to the source position was different. Moreover, once the Doppler correction is applied, the 1173- and 1332-keV peaks are spread over a wide range of energy, which comprises the one of interest for the Coulex peak. This effect has been estimated by considering a spectrum of γ rays delayed with respect to the prompt coincidence with the incoming ions. This spectrum, properly normalized, has been then subtracted to the prompt one, canceling the effect of the ^{60}Co source on the background. The number of counts in the resulting

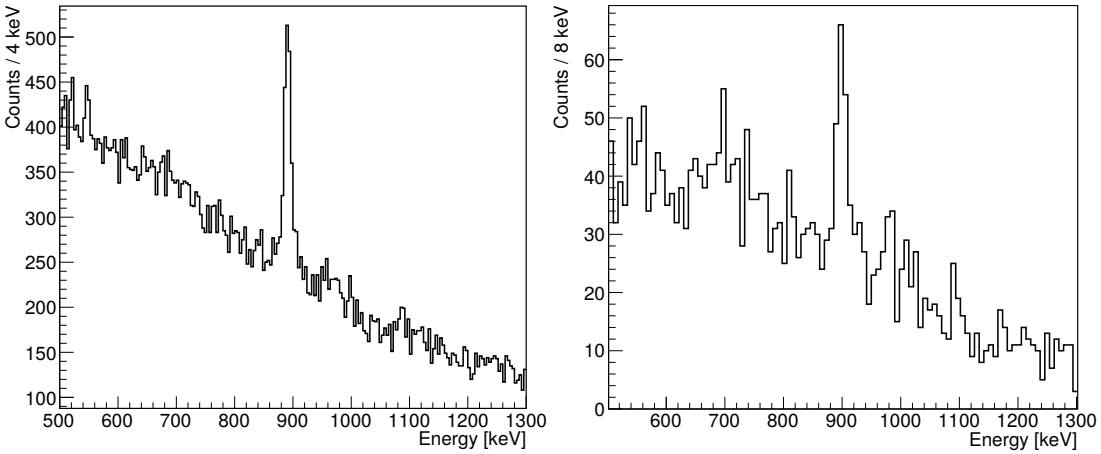

Figure 3.53: γ-ray spectra for the nuclei of interest ^{46}Ti and ^{46}Cr. Incoming, outgoing, time and scattering angle cuts are applied. The event-by-event LYCCA β has been used.

peak has then been obtained from the integral of the peak with a background subtraction.

3.6.1.4 Error Analysis

The uncertainties on the cross section and B(E2) have been estimated by using the standard error propagation.

Statistical Errors The only statistical error to be considered is the one due to the number of counts in the γ peak. This value has been obtained from the integral of the peak and takes therefore into account the errors on the background as well as the error on the peak.

Systematic errors The dominant sources of systematic errors are the uncertainties on the γ-ray efficiency as well as on the scattering angle cut applied. The error on the efficiency is related to several terms:

- **Efficiency curve**: the error due to the parameters of the relative efficiency curve is 0.6 % while the uncertainty on the activity of the source used to obtain the absolute efficiency is assumed to be 1%.

- **Doppler Boost**: the main source of uncertainty on the boost of the γ-ray efficiency due to the relativistic regime is a consequence of the error on the ion velocity β. This amounts to a relative 0.7%, which is reflected in a relative error of 0.2% on the efficiency.

- **Scattering Angle**: the error on the scattering angle determination has been estimated from the beam runs performed without the secondary target. In these runs the ions proceed along a straight line and the error on the reconstructed scattering angle has been measured from a gaussian fit. The obtained value is σ_θ=1.8 mrad, which corresponds to $\sim 0.1°$. The effect of this error on the cross section has been estimated by comparing the number of counts in the γ peak for scattering angle cuts in the range $20 \pm 2\sigma_\theta$ at steps of 0.2 mrad weighted by the gaussian distribution of the scattering angle values, with the value experimentally measured at 20 mrad. The two values differ by 0.4% and the effect is therefore negligible.

The errors adopted are summarized in Tab. 3.11.

Quantity	Magnitude	Effect on the Cross Section
Statistical Errors		
Number of γ in the peak	^{46}Ti: 8 % ^{46}Cr: 18 %	^{46}Ti: 8 % ^{46}Cr: 18 %
Systematic Errors		
ϵ calibration Parameters	0.6%	0.6%
Source Activity	1%	1%
Ion velocity	0.7%	0.2%
Scattering Angle	1.8 mrad (10%)	0.4%

Table 3.11: Summary of the statistical and systematic uncertainties for the present Coulex experiment.

3.6.1.5 Cross section and B(E2) results

The relevant numbers for the Cross section determination are listed in Tab. 3.12 together with the obtained results.

Setting	^{46}Ti	^{46}Cr
Incoming Ions	2.2E8	2.0E7
γ rays	1087(88)	117(21)
γ efficiency (%)	4.16	4.34
$\theta_{max}^{Safe}[mrad]$	19.7	21.5
$\sigma[mb]$	81.4±6.6	78.1±14.0

Table 3.12: Relevant quantities for the Cross section determination in ^{46}Ti and ^{46}Cr.

To extract the B(E2) values from the measured Cross sections we exploited the DWEIKO (Distorted Wave EIKOnal Approximation) code, which allows the calculations of elastic scattering differential cross sections, probabilities, and cross sections for inelastic scattering in nuclear collisions at intermediate and high energies in the framework of the Distorted Wave Born Approximation (DWBA), exploiting eikonal wavefunctions and solving coupled-channels equations [92]. The resulting B(E2) values for ^{46}Ti and ^{46}Cr are reported in Tab. 3.13 together with the known literature values [59, 62].

Setting	^{46}Ti	^{46}Cr
B(E2) - This work [e^{2}fm^4]	945 ± 77	921 ±165
B(E2) - Literature [e^{2}fm^4]	965 ± 9	930 ±200

Table 3.13: B(E2) values obtained in this work for ^{46}Ti and ^{46}Cr.

To check the validity of the approach and the consistency of the results we estimated the cross sections and the B(E2) as a function of the scattering angle cut. The cross section increases at larger scattering angle cuts since, when smaller impact parameters are allowed, the nuclei pass closer to each other and the interaction is stronger. On the other hand the B(E2) values should be independent on θ_{max} until $\theta_{max} < \theta_{max}^{Safe}$. At larger angles the interference between nuclear and electromagnetic interactions affects the B(E2) value and a deviation from a constant trend is expected. The results are shown in Figs. 3.54 and 3.55. In both cases the DWEIKO calculations results starting from the literature values

are reported as well. The black lines represent the scattering angle cuts applied in the present analysis.

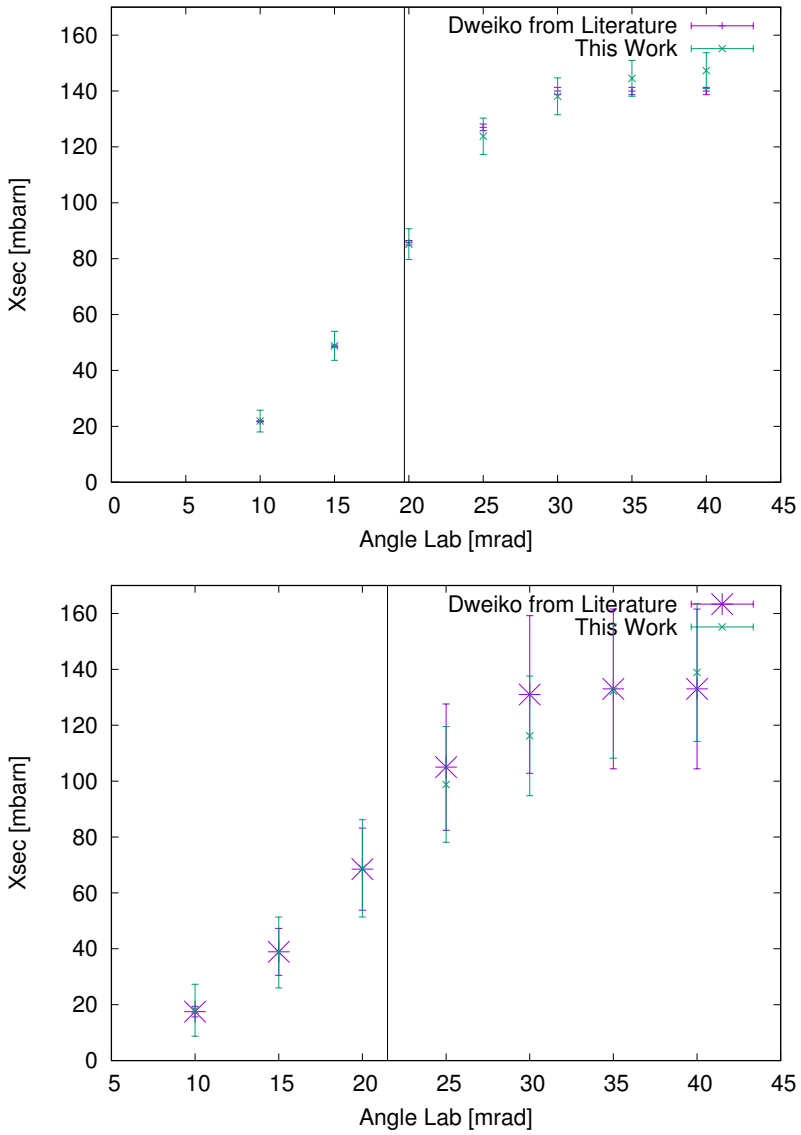

Figure 3.54: Measured cross section as a function of the cut on the scattering angle for ^{46}Ti (top) and ^{46}Cr (bottom) .

The results obtained in this work are in good agreement with the ones previously reported in literature. In particular Figs. 3.54 and 3.55 confirm the choice of the scattering angle cuts for both nuclei. It is clear how, for angles larger than

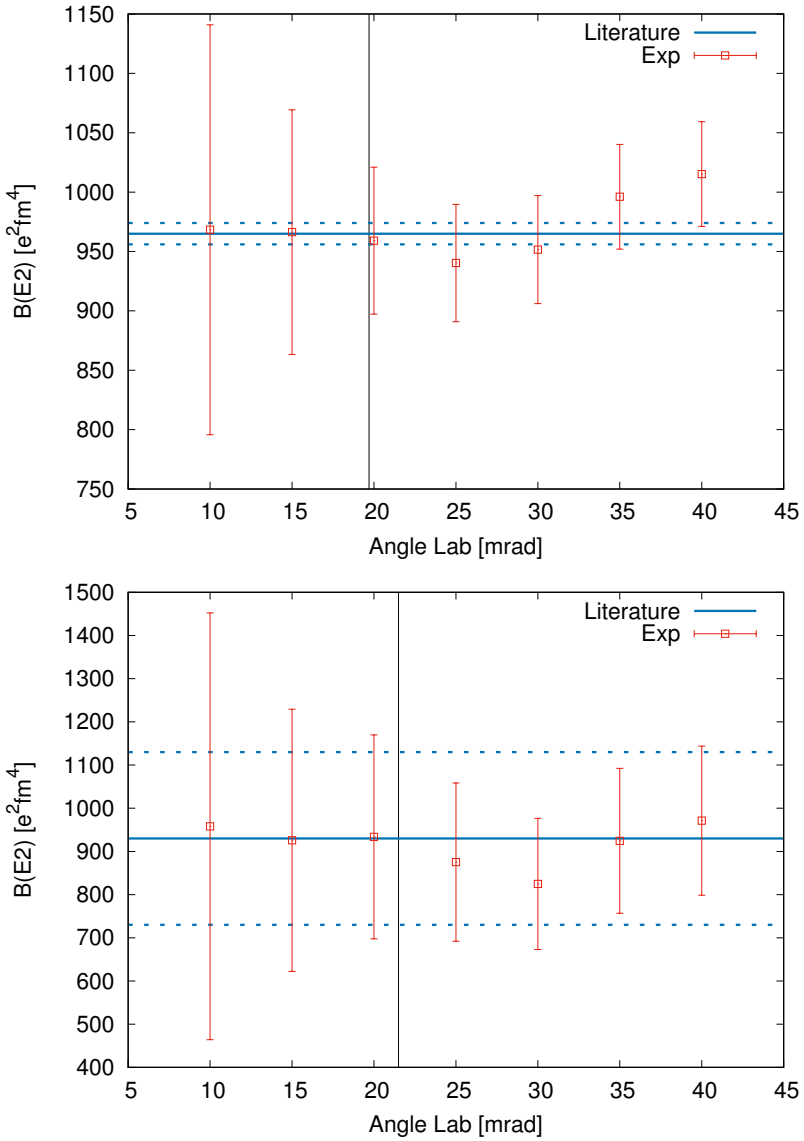

Figure 3.55: Measured B(E2) value as a function of the cut on the scattering angle for ^{46}Ti (top) and ^{46}Cr (bottom). The solid blue line represents the literature value, while the relative error is indicated by the dashed lines.

the one chosen as limit, the agreement between the measured and the literature value worsens. In this region the nuclear interaction comes into play and it gives rise to interference with the electromagnetic force.

In order to understand the effects into play, the obtained values have been

compared with shell model calculations. The KB3Gr interaction [93] has been used without any restriction on the excitations within the fp shell. The effective charges for protons and neutrons derived by Dufour and Zuker [94], $e_\pi = 1.31e$ and $e_\nu = 0.46e$, have been used. The resulting values are B(E2)=764 e^2fm^4 for ^{46}Cr and B(E2)=509 e^2fm^4 for ^{46}Ti. The values for both nuclei are clearly underestimated. It is important to notice that also the MED are badly reproduced in this mirror pair [1]. The origin of this discrepancy is not certain but seems to be due to the inadequacy of the fp valence space for calculations in these nuclei. The polarization effects of the valence nucleons on the inert core are taken into account by the effective proton and neutron charges e_π and e_ν. The underestimation of the ^{46}Ti B(E2) value, which is the one more precisely measured, suggests the need to use larger values of effective charges, which reflects a larger polarization of the core in these nuclei. In order to reproduce the experimental value, an increase of more than 30% in both effective charges is needed. The obtained value is B(E2)=925 e^2fm^4. The origin of this effect is not yet understood and further investigations are ongoing. To test the importance of excitations from the underlying core, shell model calculations with the ZBM2 interaction [95] have been performed as well. The $e_\pi = 1.31e$ and $e_\nu = 0.46e$ effective charges have been used. The adopted valence space was composed by the $s_{1/2}$, $d_{3/2}$, $f_{7/2}$ and $p_{3/2}$ orbits. The obtained B(E2) are 820 e^2fm^4 for ^{46}Ti and 789 e^2fm^4 for ^{46}Cr, which are closer to the experimental values with respect to the results given by the KB3Gr interaction, confirming the importance of excitations from the underlying sd shell in these nuclei.

Despite the large error bars in ^{46}Cr, it is interesting to notice that the B(E2) for the two nuclei are comparable in absolute value, a situation which is not reproduced by shell model calculations in the fp shell. This interestingly points towards the use of more similar effective charges for proton and neutrons in agreement with the values obtained by du Rietz *et al.* [96] for nuclei in the $f_{7/2}$ shell, $e_\pi = 1.15e$ and $e_\nu = 0.80e$. By using these values with the KB3Gr interaction in the fp valence space, we obtained B(E2)=823 e^2fm^4 for ^{46}Cr and B(E2)=708 e^2fm^4 for ^{46}Ti. The absolute values are still underestimated, confirming the role played by the core polarization; on the other hand the two values are more similar, as the experimental data suggest.

In conclusion, shell model calculations in the fp shell with the effective charges from ref. [94] underestimate the experimental values, suggesting that a core polarization mechanism is at play. This scenario is confirmed by calculations performed with a larger valence space, which includes excitations from the sd shell. Moreover, the close values of the B(E2) for the two mirror nuclei seems to point towards the need to use more similar effective charges for protons and neutrons in the calculations.

3.6.2 Lifetime measurements

The B(E2) value of the N=Z nucleus ^{46}V was measured from the lifetime of the 2^+ state, using the Recoil Distance Doppler Shift method and the triple gold stack device. Much of the work presented for the Coulex data could be exploited for the lifetime analysis. On the other hand, the different nature of the measurement allows to relax some conditions that are instead required in the Coulomb excitation experiment. In particular, in order to maximize the amount of statistics, no FRS incoming gate was applied in the analysis. This approach is justified from the fact that the lifetime of the state depends only on the lineshape of the γ-ray structure and not on the coincidences with the incoming or outgoing ions. The measurement is therefore independent from dead time and efficiency effects, which affect the overall statistics but not the relative distributions of counts in the triple peak structure. On the other hand, outgoing gates were applied in order to clean the spectra and reduce the background from unwanted reactions. Since the LYCCA Wall information is essential for the event-by-event Doppler correction, the Z condition on the E-dE matrix does not result in any loss of statistics.

The Recoil Distance Doppler Shift method is based on the different Doppler shift of a γ ray depending on the point where it is emitted. Three velocity values, relative to the ion β after each of the three targets, are therefore characteristic of the system. The event-by-event Doppler correction can be optimized only for one of the three peaks resulting in the shift and broadening of the other two peaks. The energy shifts due to this effect for the different velocities are simulated in Fig. 3.56 where the Doppler correction has been adjusted in order to reproduce the correct energy of the second peak.

The angular coverage of AGATA, combined with the angular dependence of the Doppler Shift shown in Fig. 3.56, results in a broad structure in the γ-ray spectrum, reported in Fig. 3.57, where the three peaks are not separated.
In order to separate the three peaks, a cut in the γ-ray angle is therefore needed. From Fig. 3.56 it is clear that the best separation is achieved at very small or very large angles. However this effect has to be combined with the efficiency of AGATA at different angles, in order to find the best compromise between the

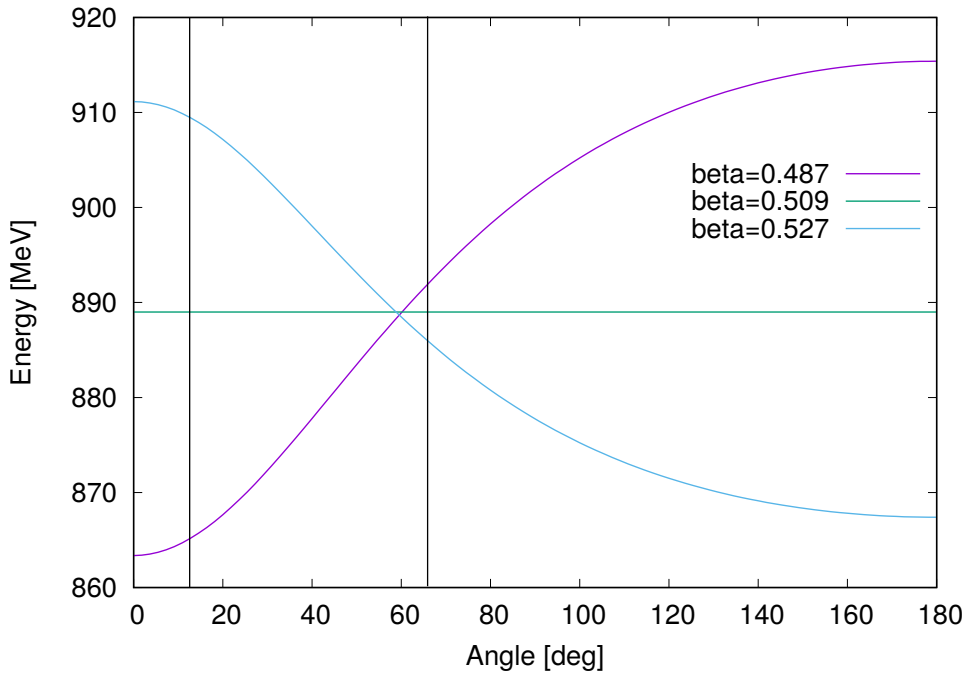

Figure 3.56: Simulated Doppler corrected energy as a function of γ-ray angle, for the $2^+ \rightarrow 0^+$ transition in ^{46}Ti emitted at the estimated velocity after each of the three foils. The Doppler correction was performed for the β value after the second target. The vertical lines denote the angular coverage of AGATA.

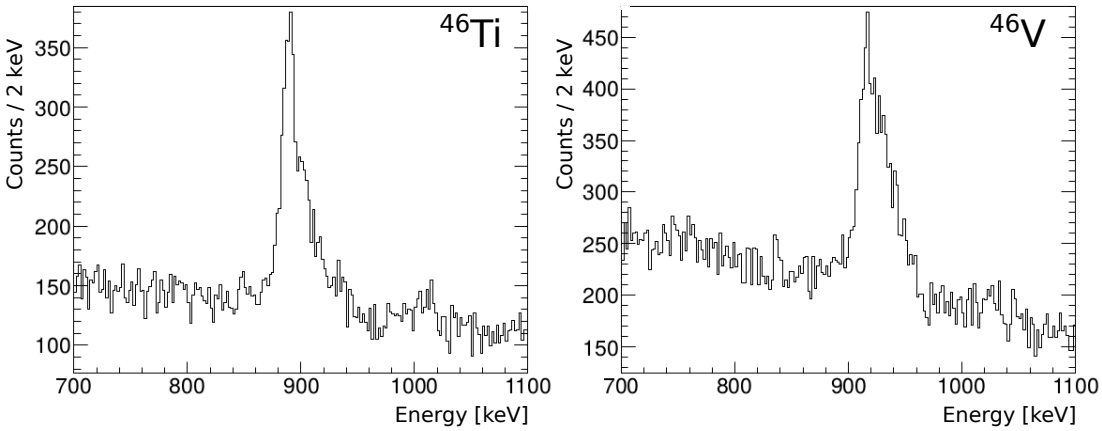

Figure 3.57: γ-ray spectra for ^{46}Ti (left) and ^{46}V (right). An event-by-event Doppler correction has been performed. No cuts were put on the γ-ray angle.

amount of statistics and the resolution of the peaks. The number of γ-ray counts as a function of the γ-ray detection angle is reported in Fig. 3.58.

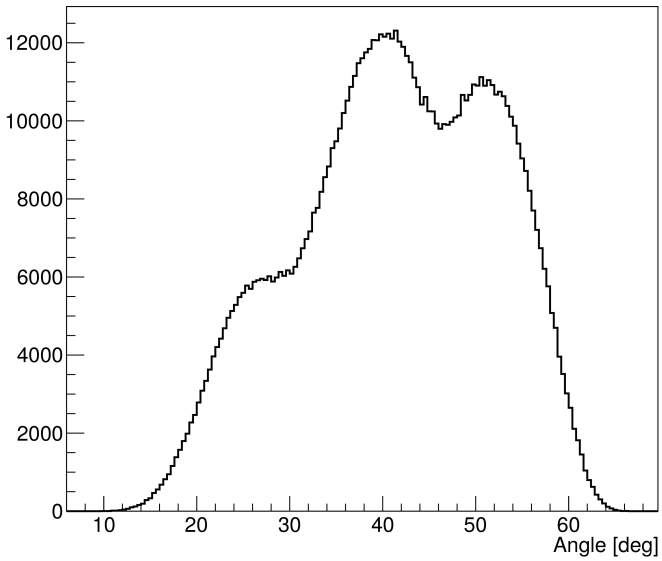

Figure 3.58: Distribution of γ-ray counts as a function of the detection angle.

The largest amount of statistics would be obtained from a cut around 40°; on the other hand, Fig. 3.56 shows that the separation of the peaks decreases rapidly moving towards 60°. Therefore, in the present analysis a cut of $30° \pm 5°$ was initially applied, which guarantees the best compromise between separation of the peaks and number of counts. The resulting spectra are shown in Fig. 3.59 where the triple peak structure is clearly visible.

The peak optimization was performed in a very similar way to the one described for the Coulex part in Sec. 3.5.3.3. The Z position of each target can be obtained from the value experimentally determined for the Coulex data and the mechanical geometry of the triple stack device. The experimental (x,y) offsets determined with the single gold target were adopted for ^{46}Ti. Then a ToF scanner with a γ-ray angular gate was implemented in order to optimize the velocity β of the ions. This procedure can be used to find the optimal value after each target. Initial β values from LISE++ simulations were used as starting values. On the contrary, for the ^{46}V secondary beam no Coulex data were taken and therefore a slightly different procedure had to be followed. The (x,y) target DSSSD off-

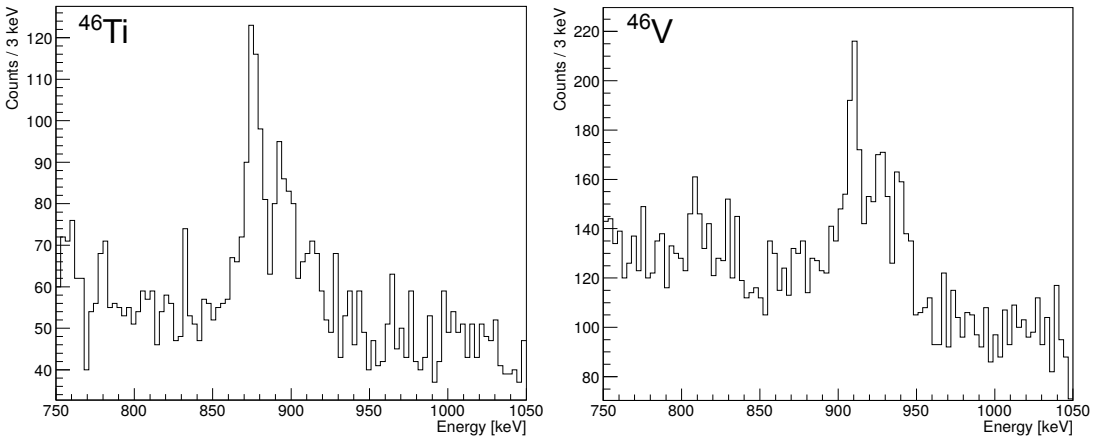

Figure 3.59: γ-ray spectra for ^{46}Ti (left) and ^{46}V (right). An event-by-event Doppler correction has been performed. A $30° \pm 5°$ cut was put on the γ-ray angle.

sets obtained from the ^{46}Ti Coulex data were used to optimize the ToF for the lowest energy peak. Then the (x,y) offset scanners were used to optimize the target position keeping β fixed. Despite the intrinsic limits of this procedure, a noticeable improvement in the energy resolution was achieved, which was crucial in the separation of the three peaks. Following this, the ToF value can be further optimize for each velocity β. In the present analysis the ToF value which allows to achieve the best separation between the peaks was used.

Lifetime estimate

The best lifetime estimate is obtained through detailed lineshape simulations. The development and optimization of the code is still ongoing. In order to extract a preliminary value, a different approach can be followed. Taking into account the Bateman equations for particle decays and the geometry of the triple target depicted in Fig. 3.4, the number of counts in each of the three peaks is given by:

$$I_1 = N_1\left(1 - e^{-\frac{d_1}{\beta_1 c\tau}}\right) \quad (3.27)$$

$$I_2 = N_2\left(1 - e^{-\frac{d_2}{\beta_2 c\tau}}\right) + N_1\left(e^{-\frac{d_1}{\beta_1 c\tau}} - e^{-\frac{d_1}{\beta_1 c\tau}-\frac{d_2}{\beta_2 c\tau}}\right) \quad (3.28)$$

$$I_3 = N_3 + N_2 e^{-\frac{d_2}{\beta_2 c\tau}} + N_1 e^{-\frac{d_1}{\beta_1 c\tau}-\frac{d_2}{\beta_2 c\tau}} \quad (3.29)$$

where β_1 and β_2 are the ion velocities after the first and the second target, respectively, d_i is the distance between the i-th and the $i+1$th gold foils, τ is the lifetime of the state and N_i is the number of ions excited in the i-th target. The N_i values depend on the target thickness and the cross section of the reaction, which in turns depends on the ion energy. In order to estimate the latter, we considered the ion kinetical energy before the triple stack, which is measured by FRS detectors, and calculated the energy loss of the nucleus at the center of each of the three targets. We performed DWEIKO calculations with the known B(E2) literature values as input for the three energies obtained, estimating in such a way the Coulomb excitation cross section. The relative number of excitations in each of the three foils can then be obtained by scaling these values for the target thickness. The distances d_i take into account the space between the targets as well as the foils thickness. The experimental number of counts in each peak has then been obtained by fitting the spectrum with three gaussian functions and a linear background, as shown in Fig. 3.60. Further effects have to be taken into account to properly estimate the area of the peaks. In particular, the γ rays emitted after the first target have to pass the following foils before being detected by AGATA. The effect of the absorption in the gold material is therefore different for the three peaks. A correction factor has thus been applied to the measured area of each peak, considering the effective thickness of the gold material at the adopted angle cut.

The lifetime of the state is correlated with the distribution of the number of counts in the different peaks. In particular, the ratio of the number of counts in the first peak with respect to the sum of the other two: $R = \frac{I_1}{I_2+I_3}$, turns out to be very sensitive to variations in lifetime. The experimental value was therefore compared with the theoretical one. The areas of the peaks and the resulting

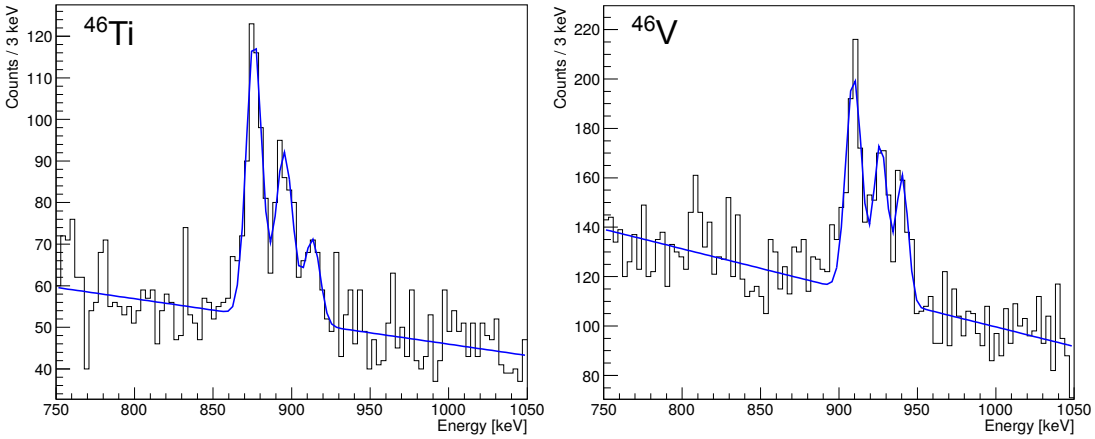

Figure 3.60: γ-ray spectra for ^{46}Ti (left) and ^{46}V (right) with a $30° \pm 5°$ cut on the γ-ray angle. The number of counts in each peak has been obtained by fitting the spectrum with a linear background and three gaussian functions.

values are reported in Tab. 3.14, where the associated error is only the statistical one, given by $\sqrt{n}$. A further correction due to the relativistic time dilation, which is proportional to $\gamma = \frac{1}{\sqrt{1-\beta^2}}$, has been applied to the measured lifetimes.

	^{46}Ti	^{46}V
I_1	276(17)	364(19)
I_2	184(14)	230(15)
I_3	83(9)	164(13)
$\frac{I_1}{I_2+I_3}$	0.98(9)	0.92(7)
$\tau_{exp}[ps]$	7.7(7)	7.1(5)
$\tau_{lit}[ps]$	7.63(7) [59]	6.8(8) [59]

Table 3.14: Number of counts in each peak and measured lifetime τ_{exp} with a cut of $30° \pm 5°$ on the γ-ray angle in ^{46}Ti and ^{46}V. The previously known values, τ_{lit}, are reported as well for comparison.

The preliminary values obtained with this method are compatible with the ones previously reported in literature. Even if the results are only preliminary and a further more detailed analysis is ongoing, the obtained values suggest a slightly shorter lifetime value for the 2^+, T=1 state in ^{46}V with respect to the

one in ^{46}Ti. This can be seen also in the lineshape structure shown in Fig. 3.59, where the sum of the number of counts in the second and third peaks with respect to the first one looks larger in ^{46}V than in ^{46}Ti.

In order to check the consistency of the result and to test the effect of the angle gate on the triple peak distribution, the γ spectrum with a cut at $39° \pm 5°$ was studied as well. As shown in Figs. 3.56 and 3.58, this gate should give a larger amount of statistics but a worse separation of the peaks, due to the decrease of the Doppler shift at larger angles. The corresponding spectra are reported in Fig. 3.61.

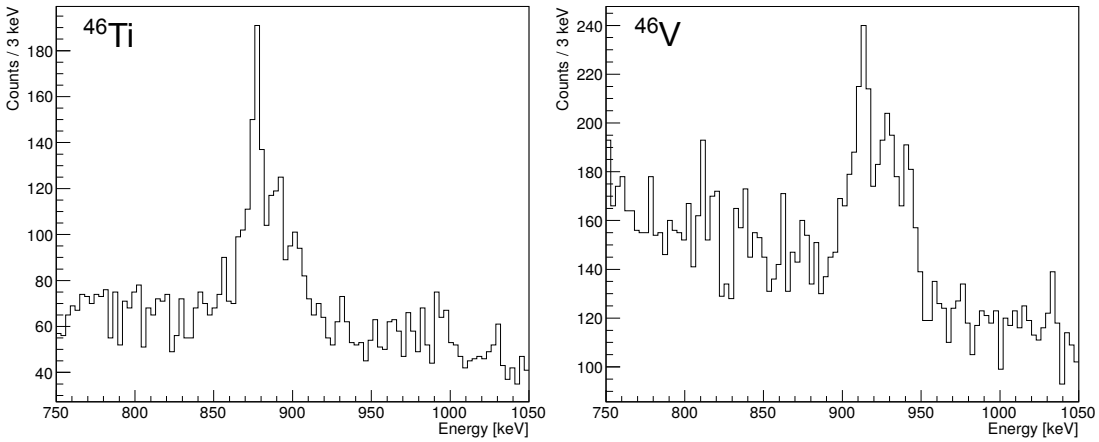

Figure 3.61: γ-ray spectra for ^{46}Ti (left) and ^{46}V (right). An event-by-event Doppler correction has been performed. A $39° \pm 5°$ cut was put on the γ-ray angle.

The separation of the peaks decreases, as expected, with respect to the spectrum with the $30° \pm 5°$ cut. On the other hand the triple structure is clearly visible and the three peaks can still be resolved. Moreover the number of counts slightly increases. It is evident how the relative area of the last two peaks with respect to the first one is larger in ^{46}V than in ^{46}Ti, further confirming the lower lifetime of the 2^+ state in this nucleus. Following the same approach described before, the number of counts in each peak has been measured and a preliminary lifetime value has been extracted; the results are reported in Tab. 3.15.

The values are compatible with the ones obtained with the $30° \pm 5°$ cut and with the literature values, within the error bars, thus further confirming the

	^{46}Ti	^{46}V
I_1	394(20)	430(21)
I_2	217(15)	288(17)
I_3	165(13)	170(13)
$\frac{I_1}{I_2+I_3}$	0.97(7)	0.94(6)
$\tau_{exp}[ps]$	7.6(6)	7.3(5)
$\tau_{lit}[ps]$	7.63(7) [59]	6.8(8) [59]

Table 3.15: Number of counts in each peak and measured lifetime τ_{exp} with a cut of $39° \pm 5°$ on the γ-ray angle in ^{46}Ti and ^{46}V. The previously known values, τ_{lit}, are reported as well for comparison.

consistency of the measurement and the principle technique of the triple foil device.

It is important to underline that the value presented here are still very preliminary and the complete analysis, based on detailed simulations, is ongoing. This includes several effects which are not taken into account in the analysis presented in this work. The gold material thickness amounts to more than 30% of the total distance between the entrance of the first target and the external surface of the last one. This implies that a large fraction of decays occurs inside one of the three foils, during the slowing down of the projectile. The resulting γ rays are emitted at an ion velocity β which does not correspond to any of the velocities after one of the targets. These events therefore end up in the valley between the different peaks, worsening their separation. This effect is not taken into account in the simple gaussian fit presented here, while it can be easily included in lineshape simulations. Event-by-event Montecarlo simulations are therefore needed and allow, in addition, to determine precisely the decay point and the γ angle, making possible an event-by-event determination of the absorption probability in the gold material. Moreover, the angular distribution of the emitted γ rays plays a role in the lineshape of the spectrum. In principle, if the alignment of the nucleus is constant along its path through the triple stack, the angular distribution should affect the three peaks in the same way and the effect should cancel out. However, the interaction of the ions with the gold material can cause a loss of alignment

between the first and the last foil, resulting in a variation of the efficiency between the three peaks. This effect can be simulated as well, including, obviously, the boost in efficiency caused by the Doppler focusing of γ rays in the forward direction, described in 3.5.3.2. The inclusion of all these effects in the lineshape simulations will allow a more precise and accurate estimate of the lifetime of ^{46}Ti and ^{46}V. Moreover, the possibility to treat the process event-by-event will allow to obtain the lineshape for the whole spectrum, without γ angle applied. As shown in Fig. 3.58 this would allow to recover a large amount of statistics, reducing noticeably the statistical error. This step is crucial for the scope of the experiment, since it is the precise measurement of the B(E2) in ^{46}V which allows to extract information on the possible isospin mixing along the A=46, T=1 triplet.

The preliminary result of the simulation for ^{46}Ti is reported in Fig. 3.62. The Doppler correction has been optimized for the third peak of the structure, and an angle cut of $30° \pm 5°$ has been applied in order to check visually the quality of the fit and the separation of the peaks. A half-life value of $T_{1/2} = \ln(2)\tau = 5.25$ ps has been assumed.

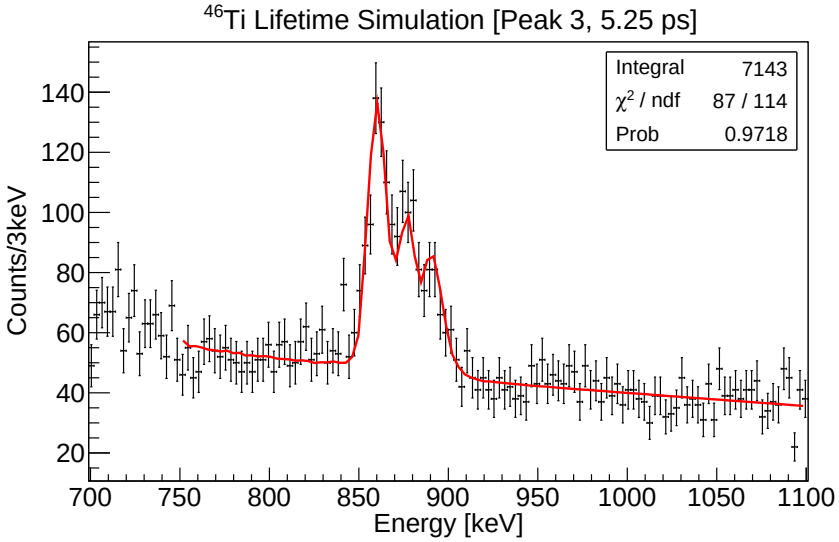

Figure 3.62: Triple peak structure for ^{46}Ti fitted with the simulated lineshape. An angle cut of $30° \pm 5°$ has been applied and a half-life value of $T_{1/2} = \ln(2)\tau = 5.25$ ps has been assumed [97].

In the fitting procedure the half-life of the state is varied and the corresponding χ^2 of the fit is obtained. Repeating the fit over a range of half-lives, it is therefore possible to estimate the value which allow to obtain the best agreement with the experimental distribution. This procedure is shown in Fig. 3.63.

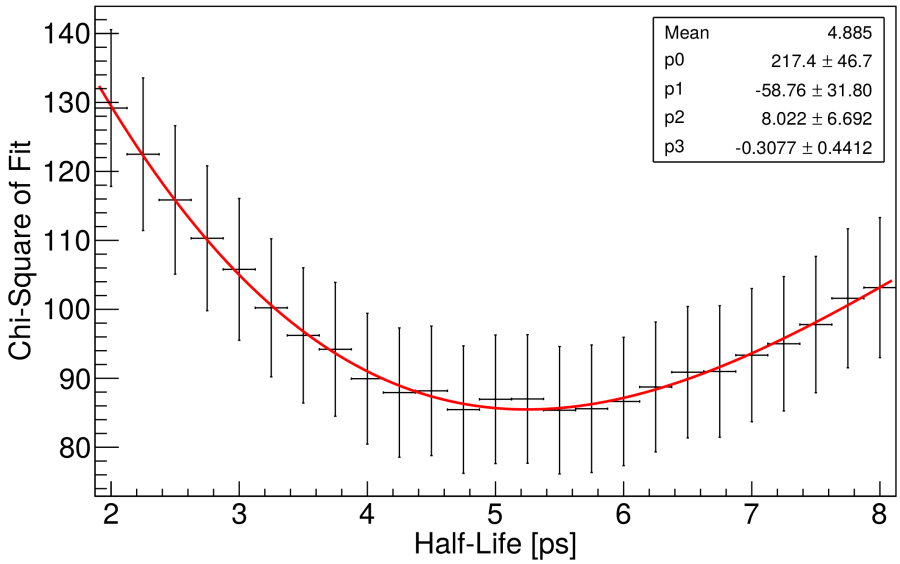

Figure 3.63: χ^2 of the simulation fit on the experimental data on ^{46}Ti as a function of the assumed half-life of the state [97].

The best agreement is given by $T_{1/2} = \ln(2)\tau = 5.2(6)$ ps, which is very close to the value used in Fig. 3.62. This compares very well with the literature value of 5.29(5) ps.

The same procedure has been followed for ^{46}V. An angular cut of $30° \pm 5°$ has been applied and the Doppler correction has been adjusted in order to have the third peak at the correct energy. The preliminary simulation of the experimental triple structure for a half-life value of $T_{1/2} = 4.75$ ps and the χ^2 value as a function of the assumed lifetime are reported in Fig. 3.64 and 3.65. The best fit of the simulations to the experimental data (i.e. the lowest χ^2 value) is obtained for $T_{1/2} = 4.8(6)$ ps, which is in excellent agreement with the literature value of 4.7(6) ps.

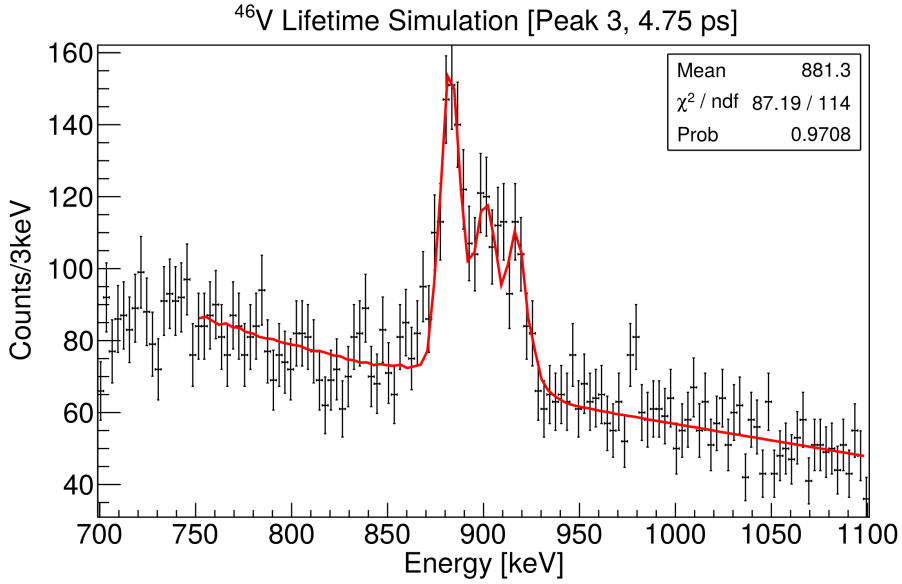

Figure 3.64: Triple peak structure for ^{46}V fitted with the simulated lineshape. An angle cut of $30° \pm 5°$ has been applied and a half-life value of $T_{1/2} = 4.75$ ps has been assumed [97].

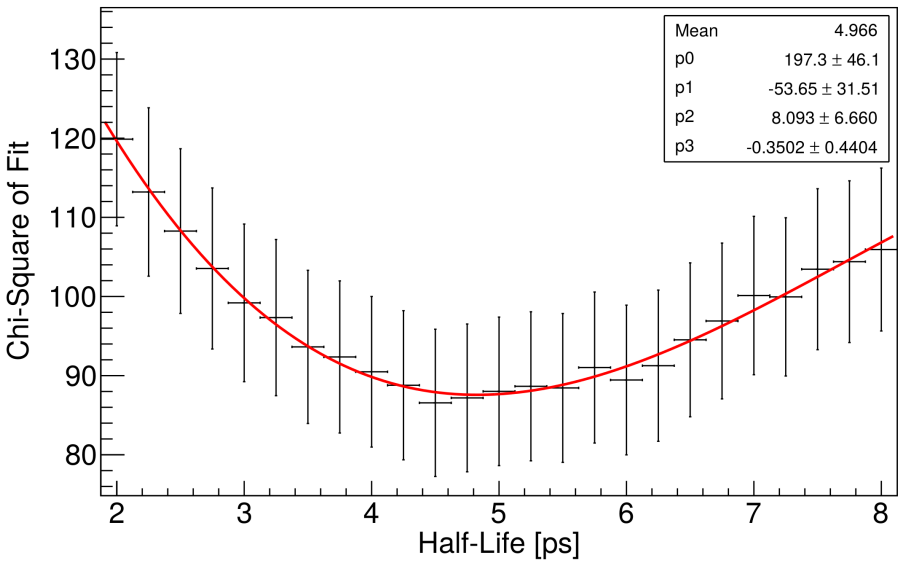

Figure 3.65: χ^2 of the simulation fit on the experimental data on ^{46}V as a function of the assumed half-life of the state [97].

The nuclear structure information is contained in the B(E2;$0^+ \rightarrow 2^+$) value, which is related to the half-life $T_{1/2}$ of the 2^+ state and to the transition energy E_γ by the formula:

$$B(E2; 0^+ \rightarrow 2^+) = \frac{5}{1.233 \cdot 10^9 \cdot E_\gamma^5 \cdot T_{1/2}/\ln(2)} \tag{3.30}$$

where E_γ is the transition energy in MeV and $T_{1/2}$ is the half-life of the state, expressed in s.

To summarize, the half-lives values measured in this work for ^{46}Ti and ^{46}V are reported in Tab. 3.16, together with the values previously known from literature and the extracted B(E2;$0^+ \rightarrow 2^+$) values.

	^{46}Ti	^{46}V
$T_{1/2,exp}[ps]$	5.2(6)	4.8(6)
$T_{1/2,lit}[ps]$	5.29(5) [59]	4.7(6) [59]
B(E2)[e^{2}fm^4]	981(113)	920(115)

Table 3.16: Half-lives and B(E2) values measured in this work for ^{46}Ti and ^{46}V. The $T_{1/2}$ literature values are reported as well.

In conclusion, the γ-ray spectra recorded in the triple stack measurements have been optimized for both ^{46}Ti and ^{46}V nuclei. The triple-peak structure is clearly visible after the application of a cut in the γ-ray angle of emission. Preliminary lifetimes values have been obtained from the comparison of the number of counts in the different peaks, and are in remarkably good agreement with the known literature values. Moreover, the agreement between the estimates obtained with different angle cuts prove the consistency of the method. Preliminary lineshape simulation results are in excellent agreement with the known data as well; further refinements of the code are under development, in order to get more precise and accurate lifetime values.

3.6.3 B(E2) in the T=1, A=46 triplet

In the previous sections, the analysis of the Coulomb excitation and the triple stack measurements and the relative preliminary results have been reported. This

allowed to obtain the B(E2) values for all the three members of the T=1, A=46 triplet. The quadrupole matrix elements are defined as $M_P(E2; 0^+ \rightarrow 2^+) = \sqrt{B(E2; 0^+ \rightarrow 2^+)}$. If the isospin symmetry holds, they should be linear with respect to the third component of the isospin quantum number, T_z, as described in detail in Sec. 1.3. The M_P values obtained in the present work are reported in the top panel of Fig. 3.66.

The ^{46}Ti value has been measured both in the Coulex and in the triple stack experiment; the agreement between the two independent measurements and with the literature value is excellent, giving confidence to the whole analysis. Since the ^{46}Ti value is very well known from previous experiments, it is possible to normalize the values measured in the present work for ^{46}Cr and ^{46}V to the titanium one, in order to minimize the dependence of the measurement from the experimental technique. The results are reported in the middle panel of Fig. 3.66. Moreover, in order to reduce the error bars and obtain the most precise B(E2) value, the weighted average with the previous measurements has been computed. The obtained values are shown in the bottom panel of Fig. 3.66.

The trend of the M_p values with respect to T_z is clearly linear and no hint of deviation is observed. This suggests the absence of isospin mixing between T=1 and T=0, $J^\pi = 2^+$ states in ^{46}V and the isospin symmetry seems to be therefore conserved along the T=1, A=46 triplet.

On the other hand the flat trend observed in the quadrupole matrix elements is unexpected. This situation is not reproduced by shell model calculations, as reported in Sec. 3.6.1.5. Keeping in mind Eq. 1.25, the matrix elements are given by the sum of isoscalar and isovector components, where the former is the same along the triplet and the latter depends on T_z. A flat trend suggests therefore a very small isovector component in the T=1, A=46 matrix elements with respect to the isoscalar one. The origin of this effect is not yet understood, and a detailed theoretical interpretation is ongoing. This will allow to investigate the balance between isoscalar and isovector components and to obtain information on the structure effect at play along the T=1, A=46 multiplet.

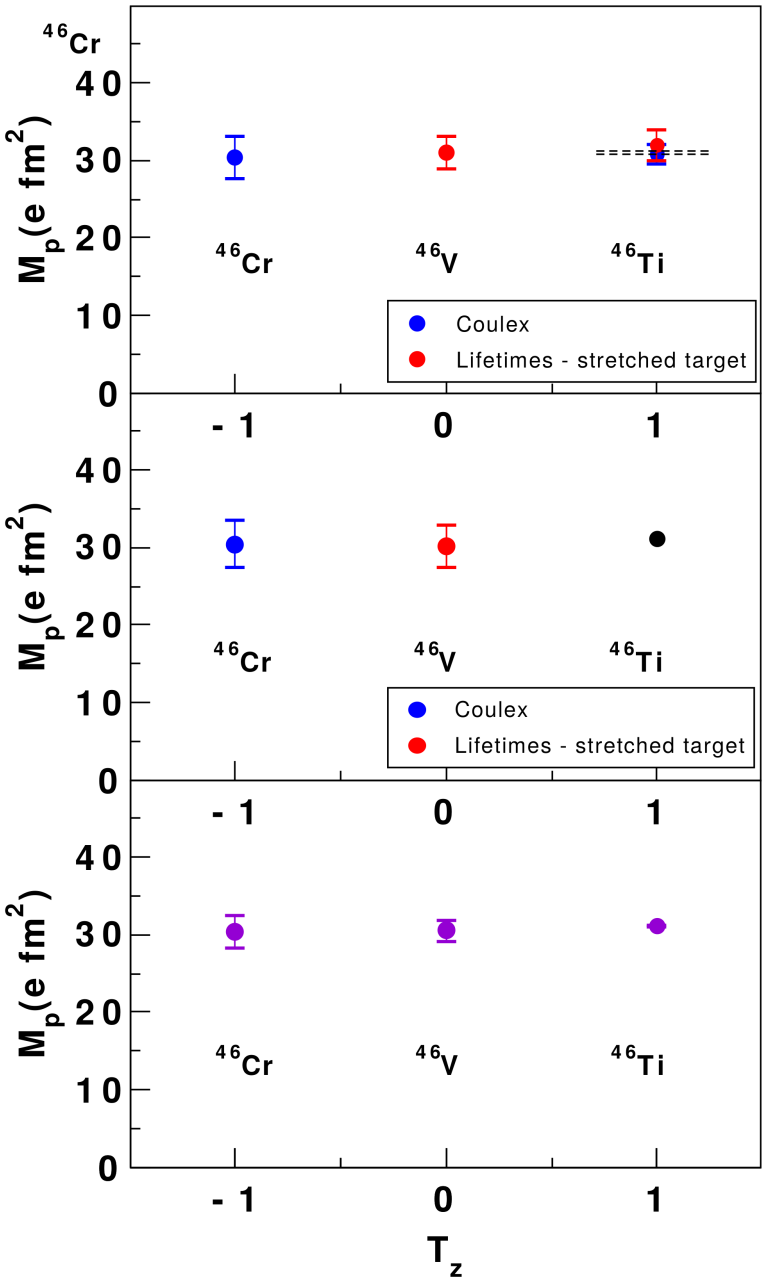

Figure 3.66: M_P value as a function of T_z along the T=1, A=46 triplet. Top panel: absolute values measured in the present work. Middle panel: M_p values normalized to the ^{46}Ti literature value. Bottom panel: weighted average with previously known values. Picture taken from [98].

.

Conclusions and Perspectives

In the present thesis, two experiments have been presented, both related to the study of the isospin symmetry breaking (ISB) and its consequences on the nuclear structure. In the first one, the mirror energy differences (MED) in the T=1/2 doublet ^{23}Mg-^{23}Na have been studied up to high spin. The MED should in principle be due only to the electromagnetic interaction, which naturally breaks the isospin symmetry and therefore introduces differences in the level schemes of mirror nuclei. Detailed studies in the $f_{7/2}$ shell have shown that, in addition to the Coulomb interaction, an isospin symmetry breaking term of nuclear origin has to be considered to account for the MED. The experimental information in other mass regions is however still scarce. The motivation of the measurement described here was thus to extend the systematics in the *sd* shell in order to get insightful information on the structure of these nuclei and on the ISB terms. High spin states were populated in the fusion evaporation reaction ^{16}O+^{12}C at the GANIL laboratory, France. The experimental setup consisted in the γ-ray spectrometer EXOGAM, the charged-particle detector DIAMANT and the neutron detector Neutron Wall. The previously identified levels were confirmed and four new transitions and two new states were identified. This allowed to extend the known MED up to $J = 15/2^+$. The experimental values have then been compared with shell model calculations, performed with the ANTOINE code. The same procedure adopted in the $f_{7/2}$ shell, based on the inclusion of a schematic ISB term has been firstly followed. Afterwards, in order to address discrepancies with the data, a new approach has been attempted *for the first time*. It is based on the use of the MCI interaction, which is derived from a realistic potential and naturally takes into account the "nuclear" ISB term, as well as the other terms of Coulomb origin. The effect of the proton and neutron radius variation has

been taken into account using different potential wells for the two fluids. The agreement with the experimental data is remarkably good, proving the quality of this approach. Moreover, a clear correlation between the difference of the proton and neutron radii needed to reproduce the experimental MED and the calculated difference in occupation numbers of the two fluids in the $s_{1/2}$ shell has been found. Quantitative refinements to the description of this correlation are ongoing. This is seen as a crucial step in the description of the MED, since it would allow the inclusion of all the known terms of the MED in a no-core interaction. The extension of the experimental studies towards high spin in the other mirror pairs of the *sd* shell, together with the wide systematic information available in the $f_{7/2}$ shell, will offer a valid benchmark to test and further refine the approach described here, giving the possibility to achieve a significative improvement in the understanding of the breaking of isospin symmetry in mirror nuclei.

The second experiment was performed at the GSI laboratory, Germany. The aim of the measurement was to determine the degree of isospin mixing in the T=1, J=2^+ state, in the N=Z ^{46}V nucleus, by testing the linearity of the quadrupole matrix elements along the isobaric triplet ^{46}Cr-^{46}V-^{46}Ti. If the isospin is a good quantum number, no mixing occurs, and the matrix elements, proportional to $\sqrt{B(E2)}$, would be linear with respect to T_z, the third component of the isospin. On the other hand the Coulomb interaction, as well as any other ISB force, can induce mixing between states with same spin and parity, J^π, and different isospin value, T. This can happen only in the N=Z member of the triplet, where T=1 and T=0 states can co-exist. In ^{46}V, two 2^+ states with similar energy and different T value are expected, making it an excellent candidate to study isospin mixing. The B(E2) values were studied in different ways: a standard relativistic Coulomb-excitation measurement was performed for ^{46}Cr due to the low secondary beam intensity available, while a new technique, based on the use of the Recoil Distance Doppler Shift method with a triple stack of gold foils, has been adopted for ^{46}V. In this framework, each of the three foils acts both as target and degrader. The well-known stable ^{46}Ti nucleus was studied with both techniques in order to have a good reference point. The secondary beams of interest were produced by the fragmentation of a ^{58}Ni beam on a beryllium target and were then separated with the FRagment Separator (FRS) spectrometer. The outgoing ions were

identified by the LYCCA calorimeter while the γ rays coming from the nuclear de-excitation were detected by the AGATA tracking array spectrometer. The measured B(E2) value in the Coulomb excitation experiment for ^{46}Ti are in excellent agreement with the ones previously known in literature, giving confidence to the ^{46}Cr measurement. Despite the large error bars due to the low statistics, the value obtained for the ^{46}Cr nucleus confirms the previously measured one. The B(E2) of ^{46}V has to be obtained from the lifetime of the state, measured with the triple stack device. Preliminary lifetime values have been obtained for both ^{46}Ti and ^{46}V nuclei and are in remarkable agreement with the literature values and independent from the γ angle cut applied. This proves the validity of the triple stack device for lifetime measurements. On the other hand, the best lifetime estimate can be obtained only from a full detailed simulation of the triple structure of the peak, which is ongoing. This procedure will allow to reduce the error bars and get a more precise and accurate value for the lifetime of ^{46}V. The preliminary values show a linear trend of the quadrupole matrix elements with respect to T_z. On the other hand, the measured values are constant along the triplet; this behavior is unexpected and so far not reproduced by shell model calculations. The theoretical interpretation of this effect is ongoing, and it will certainly shed light on the nuclear structure properties of these nuclei and on the interplay between the isoscalar and isovector components of the quadrupole matrix elements. Systematic studies of transition probabilities along T=1 triplets will allow, therefore, a better understanding of the origin of isosping mixing and of its evolution along the nuclide chart.

References

[1] M.A. Bentley and S.M. Lenzi. *Prog. Part. Nucl. Phys.*, 59:497–561, 2007.

[2] R. Machleidt and H. Muther. *Phys. Rev. C*, 63:034005, 2001.

[3] D. H. Wilkinson. *Isospin in nuclear physics*. North Holland Pub. Co., Amsterdam, 1969.

[4] E.P. Wigner. *Proceedings of the Robert A Welch Conference on Chemical Research, vol. 1.* Robert A Welch Foundation, Texas, 1957.

[5] W.E. Ormand and B.A. Brown. *Nuclear Phys. A.*, 491:1, 1989.

[6] J.A. Nolen and J.P. Schiffer. *Ann. Rev. Nucl. Sci.*, 471:19, 1969.

[7] G.A. Miller. *Chin. J. Phys.*, 471:1075, 1994.

[8] M.H. Shahnas. *Phys. Rev. C*, 50:2346, 1994.

[9] J. Duflo and A.P. Zuker. *Phys. Rev. C*, 66:051304(R), 2002.

[10] E. Caurier, G. Martinez-Pinedo, F. Nowacki, A.Poves, and A.P. Zuker. *Rev. Mod. Phys.*, 77.

[11] G. Martinez-Pinedo A.P. Zuker, S.M. Lenzi and A. Poves. *Phys. Rev. Lett.*, 89:142502, 2002.

[12] M.A.Bentley D.D. Warner and P. Van Isacker. *Nature Phys.*, 2:311, 2006.

[13] M.A. Bentley et al. *Phys. Rev. C*, 62:051303, 2000.

[14] S.M. Lenzi et al. *Phys. Rev. Lett.*, 87:122501, 2001.

[15] A.P. Zuker J. Bonnard S.M. Lenzi. *Phys. Rev. Lett.*, 116:212501, 2016.

[16] D.R. Inglis. *Phys. Rev.*, 82:181, 1951.

[17] M.A. Bentley et al. *Phys. Rev. C*, 92:024310, 2015.

[18] M.A. Bentley. *Private communication.*, 2017.

[19] E. K. Warburton and J. Weneser. *The role of isospin in electromagnetic transitions*. North Holland Pub. Co., Amsterdam, 1969.

[20] E. Farnea. *Spectroscopic Studies of Isospin Mixing in* ^{64}*Ge*. PhD thesis, University of Surrey, 2001.

[21] P. Van Isacker. Measuring isospin mixing from e1 and e2 transitions. Isospin symmetry, Saclay, 2011.

[22] S. Thummerer et al. *J. Phys. (London)*, G29:509, 2003.

[23] D. Evers et al. *Zeitschrift für Physik A Atoms and Nuclei*, 280:287–307, 1977.

[24] G.J. KeKelis et al. *Phys. Rev. Lett.*, 35:710, 1975.

[25] G.J. KeKelis et al. *Phys. Rev. C*, 15:664, 1977.

[26] H. T. Fortune and Kenneth Wells. *Phys. Rev. C*, 30:527, 1984.

[27] P. Tikkanen et al. *Phys. Rev. C*, 42:581, 1990.

[28] J. R. Powers H. T. Fortune and L. Bargeron. *Phys. Rev. C*, 51:1154, 1995.

[29] S. T. Thornton et al. *Phys. Rev. C*, 17:576, 1978.

[30] D. E. Gustafson et al. *Phys. Rev. C*, 13:691, 1976.

[31] J. Gomez del Campo et al. *Phys. Rev. C*, 12:1247, 1975.

[32] D.G. Jenkins et al. *Phys. Rev. C*, 87:064301, 2013.

[33] I. Y. Lee. *Nucl. Phys. A*, 520:641c, 1990.

[34] D.G. Jenkins et al. *Phys. Rev. Lett.*, 92:031101, 2004.

[35] F. Della Vedova. *Isospin Symmetry in the sd shell: The A=31 and A=35 Mirror Nuclei.* PhD thesis, University of Padova, 2004.

[36] W. Reisdorf et al. *Z. Phys. A*, 343:47–57, 1992.

[37] F. Azaiez et al. *Nuclear Physics A*, 654:1003–1008, 1999.

[38] J. Simpson et al. *Heavy Ions Physics*, 11:159–188, 2000.

[39] J. N. Scheurer et al. *Nucl. Instrum. Methods Phys. Res., Sect. A*, 385:501–510, 1997.

[40] J. Gál et al. *Nucl. Instrum. Methods Phys. Res., Sect. A*, 516:502–510, 2004.

[41] Ö. Skeppstedt et al. *Nucl. Instrum. Methods Phys. Res., Sect. A*, 421:531–541, 1999.

[42] http://pro.ganil-spiral2.eu/laboratory/detectors/exogam/exogam-detectors.

[43] T. K. Alexander et al. *Nucl. Instrum. Methods*, 13:244–246, 1961.

[44] J. Gál et al. *Nucl. Instrum. Methods Phys. Res., Sect. A*, 366:120–128, 1995.

[45] F. Ghazi Moradi. *Experimental Nuclear Structure Studies in the Vicinity of the N = Z Nucleus ^{100}Sn and in the Extremely Neutron Deficient ^{162}Ta Nucleus.* PhD thesis, KTH Stockholm, 2014.

[46] D. Wolski et al. *Nucl. Instrum. Methods Phys. Res., Sect. A*, 360:584–592, 1995.

[47] E. Caurier. 1989.

[48] B.A. Brown and B.H. Wildenthal. *Ann. Rev. Nucl. Part. Sci.*, 38:29, 1988.

[49] A. P. Zuker. *Monopole corrected interactions.*

[50] D. R. Entem and R. Machleidt. *Phys. Lett. B*, 93:524, 2002.

[51] J. Duflo and A. P. Zuker. *Phys. Rev. C*, 66:051304, 2002.

[52] H. Heylen et al. *Phys. Rev. C*, 94:054321, 2016.

[53] F. Nowacki A. Poves E. Caurier, G. Martinez-Pinedo and A. P. Zuker. *Rev. Mod. Phys.*, 77:427, 2005.

[54] A. P. Zuker et al. *Phys. Rev. C*, 92:024320, 2015.

[55] A.P. Zuker J. Bonnard. *arXiv:1606.03345*, 2016.

[56] F. Brandolini et al. *Phys. Rev. C*, 70:034302, 2004.

[57] S.M. Lenzi et al. *Phys. Rev. C*, 60:021303, 1999.

[58] P.E. Garrett et al. *Phys. Rev. C*, 75:014307, 2007.

[59] O. Möller et al. *Phys. Rev. C*, 67:011301, 2003.

[60] C. Dossat et al. *Nuclear Physics A, volume=792, pages=18-86, year=2007,*.

[61] S.C. Wu. *Nuclear Data Sheet*, 91:1, 2000.

[62] K. Yamada et al. *Eur. Phys. J. A*, 25:409, 2005.

[63] A. Winther and K. Alder. *Nucl Phys. A*, A319:518–532, 1979.

[64] S.A. Milne. *Investigation of Isospin Symmetry Breaking in the $f_{7/2}$ Region, Studied through One-nucleon Knockout and Lifetime Measurements.* PhD thesis, University of York, 2016.

[65] C. Domingo-Pardo et al. *Nucl. Instrum. Methods Phys. Res., Sect. A*, 694:297, 2012.

[66] W. Henning et al. *Nuclear Physics A*, 538:637–648, 1992.

[67] H. Geissel et al. *Nucl. Instrum. Methods Phys. Res., Sect. B*, 70:286–297, 1992.

[68] T. Baumann. *www.nscl.msu.edu*, 2001.

[69] R. Janik et al. *Nucl. Instrum. Methods Phys. Res., Sect. A*, 640:54–57, 2011.

[70] M. Pfützner et al. *Nucl. Instrum. Methods Phys. Res., Sect. B*, 86:213–218, 1994.

[71] P. Golubev et al. *Nucl. Instrum. Methods Phys. Res., Sect. A*, 723:55–66, 2013.

[72] R. Hoischen et al. *Nucl. Instrum. Methods Phys. Res., Sect. A*, 654:354–360, 2011.

[73] M. Reese et al. *GSI Scientific Report*, 2013-1:185, 2013.

[74] S. Akkoyun et al. *Nucl. Instrum. Methods Phys. Res., Sect. A*, 668:26–58, 2012.

[75] A. Wiens et al. *Nucl. Instrum. Methods Phys. Res., Sect. A*, 618:223–233, 2010.

[76] F. Recchia. *In-beam test and imaging capabilities of the AGATA prototype detector*. PhD thesis, University of Padova, 2008.

[77] B. Bruyneel et al. *Nucl. Instrum. Methods Phys. Res., Sect. A*, 569:764–773, 2006.

[78] B. Bruyneel et al. *Eur. Phys. J. A*, 52:70, 2016.

[79] R. Venturelli et al. *INFN-LNL Report*, pages 204–205, 2004.

[80] F. Recchia et al. *Nucl. Instrum. Methods Phys. Res., Sect. A*, 604:555–562, 2009.

[81] P.A. Söderström et al. *Nucl. Instrum. Methods Phys. Res., Sect. A*, 638:96–109, 2011.

[82] A. Lopez-Martens et al. *Nucl. Instrum. Methods Phys. Res., Sect. A*, 533:454–466, 2004.

[83] D. Bazzacco et al. *Nuclear Physics A*, 746:248–254, 2004.

[84] O. B. Tarasov et al. *Nucl. Instrum. Methods Phys. Res., Sect. B*, 266:19–20, 2008.

[85] O. Häusser et al. *Phys. Lett. B*, 73:127, 1978.

[86] N. Lalovic et al. *Nucl. Instrum. Methods Phys. Res., Sect. A*, 806:258–266, 2016.

[87] H. Olliver et al. *Phys. Rev. C*, 68:044312, 2003.

[88] H. Scheit. *Low-Lying Collective Excitations in Neutron-Rich Even-Even Sulfur and Argon Isotopes Studied via Intermediate-Energy Coulomb Excitation and Proton Scattering.* PhD thesis, Michigan State University, 1998.

[89] N.Kurz. *presentation EE, GSI*, Zagreb.

[90] X. Grave et al. *14th IEEE-NPSS*, 2005.

[91] D. Ralet et al. *Nucl. Instrum. Methods Phys. Res., Sect. A*, 786:32–39, 2015.

[92] T. Glasmacher C.A. Bertulani, C.M. Campbell. *Computer Physics Communication*, 152:317–340, 2003.

[93] E. Caurier and A. Poves. *Unpublished.*

[94] M. Dufour and A.P. Zuker. *Phys. Rev. C*, 54:1641–1660, 1996.

[95] G. Martinez-Pinedo F. Nowacki E. Caurier, K. Langanke and P. Vogel. *Phys. Lett. B*, 522:240, 2001.

[96] R. du Rietz et al. *Phys. Rev. Lett.*, 93:222501, 2004.

[97] S.A. Milne. *Private communication.*, 2017.

[98] M.A. Bentley. *Private communication.*, 2017.

List of Figures

1.1 Possible couplings of a pair of nucleons. 3
1.2 Ground state binding energies and CDE between $T = \frac{3}{2}$ states vs. proton number Z along the A=21, $T = \frac{3}{2}$ isospin quadruplet. Picture taken from [1]. 5
1.3 Average overlap of the wavefunctions of two like-particles in the $f_{\frac{7}{2}}$ shell as a function of the angular momentum J. Calculations from [12]. 8
1.4 MED in mirror nuclei of A=51, ^{51}Fe $-^{51}$ Mn [13]. 9
1.5 Forbidden and allowed isospin states for nuclei along the $N \sim Z$ line [18]. 14

2.1 Proposed rotational bands in ^{23}Na from Ref. [31]. 23
2.2 Fusion Evaporation reaction mechanism. Taken from [35]. 25
2.3 Predicted cross sections for the reaction ^{16}O + ^{12}C at 60 MeV (red numbers, in mb) for the different channels produced after particle evaporation, obtained with the HIVAP code [36]. Only the most intense channels are reported. The nuclei of interest are highlighted in green. 27
2.4 The segmented Clover germanium detector crystals. Taken from [42]. 30
2.5 The different elements of the Compton suppression shield for the segmented CLOVER Ge detectors (not to scale) [37, 42]. 30
2.6 Schematic view of the light charged particle detector DIAMANT. Taken from [45]. 32

2.7 Schematic view of the neutron detector Neutron Wall viewed from outside of the array downstream of the target position. Picture taken from [45]. 34
2.8 Trigger block and timing diagrams for Neutron Wall and TACs. . 36
2.9 Energy residuals for each detector obtained with the ^{152}Eu source. 39
2.10 Experimental data and relative efficiency curve of the EXOGAM array. The white circles correspond to the present experiment while the black squares come from a previous data set. The blue curve is the one used in the present analysis. The different shape at energies below 500 keV is due to the absorption of the reaction chamber and of DIAMANT, which were not present in the ^{35}Cl(n, γ) measurement. 41
2.11 EXOGAM spectra obtained with a ^{60}Co source. The sum of the crystals, the addback and the addback + Compton suppression spectra are reported. 44
2.12 2D histograms of the Doppler-corrected energy vs. the relative β value. 45
2.13 DIAMANT PID vs energy matrix. Protons, α and two proton gates are visible. 47
2.14 Energy resolution as a function of β_{CN} and E^*_α for the $\frac{9}{2}^+ \rightarrow \frac{5}{2}^+$, 2263 keV transition in ^{23}Na. 51
2.15 Difference between the measured and the known energy values as a function of β_{CN} and E^*_α for the $\frac{9}{2}^+ \rightarrow \frac{5}{2}^+$, 2263-keV transition in ^{23}Na. 52
2.16 Portion of the γ spectrum in coincidence with one α particle. The average Doppler and full kinematic corrections are compared. . . . 52
2.17 TOF spectrum of one NWall detector. The sharp peak of γ rays as well as the large neutron bump are visible. 53
2.18 TRF vs ZCO matrix of one Neutron Wall detector. The neutron and γ loci are clearly visible. 54

2.19 γ spectrum in coincidence with 1 α (upper panel) and 1 α and 1 α + 1 neutron (lower panel). The blue dots indicate peaks coming from ^{23}Na (αp) channel while the green squares highlight transitions from ^{23}Mg (αn) channel 55
2.20 Spectrum of γ rays detected in coincidence with one α particle and one proton, corresponding to ^{23}Na. The most intense transitions are marked with their energy. 57
2.21 Spectrum of γ rays detected in coincidence with one α particle and one neutron, corresponding to ^{23}Mg. The most intense transitions are marked with their energy. Contaminant peaks are marked with orange (^{24}Mg) and green (^{23}Na) circles. 58
2.22 Projection of particle gated $\gamma-\gamma$ matrices. A sum of gates on two of the most intense transitions, reported in the picture, has been applied. 59
2.23 Projection of particle gated $\gamma-\gamma$ matrices for ^{23}Na and ^{23}Mg gated on the $13/2^+ \rightarrow 9/2^+$ transition at 3531 and 3480 keV energy, respectively. 60
2.24 Projection of particle gated $\gamma-\gamma$ matrices for ^{23}Na and ^{23}Mg gated on 1153- OR 4564-keV and 1207- OR 4430-keV transitions, respectively. 61
2.25 Angular distribution for the following values of A_2 and A_4. $A_2 = -0.7; A_2 = 0.0$ (orange); $A_2 = 0.2; A_2 = -0.2$ (red); $A_2 = 0.1; A_2 = -0.1$ (green); $A_2 = -0.8; A_2 = 0.0$ (black); $A_2 = -0.5; A_2 = 0.0$ (dashed violet); $A_2 = 0.4; A_2 = -0.02$ (dashed blue). 63
2.26 R_{ADO} for ^{23}Na and ^{23}Mg measured in the present experiment. Typical values for L=2 stretched quadrupole transitions, obtained by the measured R_{ADO} for known E2 transitions in ^{24}Mg and ^{20}Ne, are highlighted by the blue area. 64
2.27 Level scheme of positive parity states in ^{23}Na obtained in this work. The width of the arrows indicates the relative intensity of the transitions. 68

2.28 Level scheme of positive parity states in ^{23}Mg obtained in this work. The width of the arrows indicates the relative intensity of the transitions. 69
2.29 Experimental (black) and calculated (red) level schemes for the mirror pair A=23. The USD interaction [48], without electromagnetic terms, has been used. 71
2.30 Experimental (left) and calculated (right) branching ratios for the mirror pair A=23. The USD interaction [48], without electromagnetic terms, has been used. 72
2.31 Contribution to the isospin non conserving term $V_B^{J=2}$ of the $d_{5/2}$ and $d_{3/2}$ orbits. The overall effect, obtained summing the two, is reported as well. 74
2.32 Contribution to the isospin non conserving term V_B of the the matrix elements relative to two nucleons coupled to $J = 0$ and $J = 2$ in the $d_{5/2}$ shell. 75
2.33 Contribution to the isospin non conserving term $V_B^{J=0}$ of the $s_{1/2}$, $d_{5/2}$ and $d_{3/2}$ orbits. The overall effect, obtained summing the two, is reported as well. 76
2.34 Fractional occupation numbers, defined as $\frac{n}{2j+1}$, for the $d_{5/2}$, $s_{1/2}$ and $d_{3/2}$ orbitals for the *yrast* states in the mirror nuclei of mass 23. Fluid 1 corresponds to neutrons for ^{23}Na and protons for ^{23}Mg. The opposite holds for Fluid 2. 76
2.35 Experimental and theoretical MED in mirror nuclei ^{23}Mg $-^{23}$ Na obtained with the USD interaction. The ISB part V_B, the radial contribution V_{Cm} and the multipole term V_{CM} are enlightened. . . 77
2.36 Experimental (black) and calculated (blue) level schemes for the nucleus ^{23}Na. The MCI interaction has been used. 81
2.37 Experimental and theoretical MED in mirror nuclei ^{23}Mg $-^{23}$ Na obtained with the MCI interaction. The radial term V_{Cm} and the MCI contribution are enlightened. 82
2.38 Calculated MED for the A=23 mirror pair as a function of the ζ parameter. 83

2.39 ζ and difference in the occupation number of the $s_{1/2}$ orbital for neutrons and protons for the known mirror nuclei in the *sd* shell. . 84

3.1 Adopted energies for the $J^\pi : 2^+ \rightarrow 0^+_{g.s.}$ transitions in the T=1 Isospin triplet ^{46}Cr $-^{46}$ V $-^{46}$ Ti [56, 57, 58, 59, 60, 61]. 89
3.2 Known M_p values for the $J^\pi : 2^+ \rightarrow 0^+_{g.s.}$ transitions in the T=1 Isospin triplet ^{46}Cr $-^{46}$ V $-^{46}$ Ti. 90
3.3 (a) Schematic view of the Stretched Gold Target (SGT) developed at the University of York. The three gold foils act both as targets and as degraders. (b) Simulated triple peak structure resulting from the use of the SGT device. The Doppler correction is optimized for the second peak. As a consequence, the first and third peaks show a larger broadening. Picture taken from [64]. 95
3.4 Stretched Gold Target used in the present experiment. Aluminum frames are placed around the gold foils [64]. 96
3.5 Schematic view of the experimental setup used in the PreSPEC-AGATA campaign at GSI [65]. 97
3.6 Schematic view of the FRS achromatic optics. a) and b) label the first two and second two dipoles of FRS, respectively. In the second focal plane S2, placed in position I in the figure, ions with the same A/q are dispersed due to the different initial momentum. This effect is counterbalanced in the last two dipoles, giving an overall achromatic transmission. Picture taken from [68]. 99
3.7 Schematic view of the FRS isotope selection. Picture taken from [67]. 100
3.8 Schematic view of the $B\rho - \Delta E - B\rho$ method within the FRS. The blue degrader varies the $B\rho$ depending on the proton number Z. Picture taken from [68]. 101
3.9 Thick copper slits placed along FRS beam line. 102
3.10 The energy loss of the ions in the shaped degrader counterbalances the momentum dispersion of ions with the same A/q. 102
3.11 Drawing of a Time Projection Chamber in the FRS [69]. 104

3.12 Schematic drawing of the LYCCA detectors used in the PreSPEC setup at GSI [71]. The ToF target scintillators was not available in the present experiment. 107
3.13 Picture of the ToF scintillator used in the PreSPEC-AGATA campaign [71]. 108
3.14 Picture of the target DSSSD detector used in the PreSPEC-AGATA campaign [71]. 109
3.15 Lycca Wall hit pattern observed in the present work. The convention used to label each module is reported. The white lines represent the spacing between the modules or broken strips. . . . 109
3.16 Schematic drawing of the full LYCCA Wall (sx) and of a single module (dx) [71]. 110
3.17 Schematic view of the final configuration of the AGATA γ ray spectrometer [74]. 111
3.18 (a) Labeling scheme for the standard AGATA crystal. (b) Scheme of the three different crystal shapes in a AGATA triple cluster. Dimensions are reported in mm. Taken from [64], adapted from [74]. 112
3.19 AGATA clusters configuration in the PreSPEC-AGATA campaign at GSI in 2014. 113
3.20 The AGATA γ-ray spectrometer in the PreSPEC-AGATA campaign at GSI in 2014. 114
3.21 Signal shape in the different segments of a detector for an interaction in the segment B4. The signals induced in the other segments can be used to deduce the position of the interaction. Figure taken from [76]. 115
3.22 Comparison between the simulated (red) and experimentally measured (blue) pulse shapes induced by a hit in the segment d5 [74]. The good agreement justifies the use of simulated basis as a reference. 116
3.23 Representation of a $E_\gamma = 1.33$ MeV, $M_\gamma = 30$ event detected in a full 4π Ge shell reconstructed with a cluster tracking algorithm. . 117
3.24 Calibrated hit pattern of the first TPC placed in S2. 118

3.25 Experimental energy loss for the different ^{58}Ni runs as a function of the velocity β for the first of the MUSIC detectors. The blue line represents the quadratic function $f(\beta)$ fitted to the data. . . . 120
3.26 Calibrated ToF spectrum for the ^{46}Ti experimental run obtained with the TDC modules. A sharp cut off due to the saturation of the TDC is visible at ∼207 ns. 121
3.27 Calibrated ToF spectrum for the ^{46}Ti experimental run obtained with the Multi-Hit TDC modules using a) the right PMTs and b) the left PMTs. A double structure is visible in the ToF_{LL} spectrum which is due to the bad behavior of the left PMT in S2. 121
3.28 Correlation between the X position in the fourth focal plane S4 measured by the TPCs and from the time difference between the two PMTs of the plastic scintillator. 123
3.29 Particle Identification plot relative to the ^{46}Ti setting. Left Panel: X position from TPCs in S2 and S4. Right Panel: X position from scintillators in S2 and S4. 124
3.30 Particle Identification plot relative to the ^{46}Cr setting. Left Panel: X position from TPCs in S2 and S4. Right Panel: X position from scintillators in S2 and S4. 124
3.31 Correlation between the PMT recorded time and the distance from the hit position to the PMT for PMT number 5 of the LYCCA ToF Start detector. Left Panel: before position correction. Right Panel: after position correction. 126
3.32 Energy loss measured in the p and n side of the LYCCA Wall Module number 7. Left Panel: before strips alignment. Right Panel: after strips alignment. The same procedure has been applied to all the modules of the Wall DSSSD and the target DSSSD. 127
3.33 Total energy measured in the CsI scintillators of the LYCCA Wall Module number 7. Left Panel: before alignment. Right Panel: after alignment. 128
3.34 $E - \Delta E$ matrix reconstructed from the LYCCA Wall detectors for the ^{46}Ti beam runs. 129

3.35 Difference between the measured energies and the literature values for ^{152}Eu. The core signals of each AGATA crystal have been used. 130
3.36 Absolute efficiency curves for the AGATA spectrometer for the Common Core (blue), Tracked (red) and Add Back (green) methods, as reported in [86]. 131
3.37 γ-γ matrices obtained with ^{56}Co and ^{60}Co sources and a) MGT tracking algorithm, b) Core common method. 132
3.38 Absolute efficiency curves for the AGATA spectrometer for the Common Core method obtained for the present experiment (blue) and reported in [86] (red). The experimental data points are reported as well. 133
3.39 Effect of the Doppler Boost correction for $\beta = 0.524$ c on the efficiency curve of the AGATA spectrometer. 136
3.40 Red: average core multiplicity in coincidence with one 892-keV γ Blue: average background core multiplicity. Black: average core multiplicity in coincidence with one γ coming from Coulex reaction. The ^{46}Ti beam runs were used. 137
3.41 ID detector number versus the timestamp of the event. Detectors 4, 15, 23 manifest bad behavior in fixed time intervals. 139
3.42 Calculated angular distribution for the present experiment. The isotropic distribution is indicated as well. 140
3.43 Calculated Doppler boosted angular distributions for the present experiment. The quadrupolar and isotropic distribution are considered. The vertical black lines correspond to the angular coverage of AGATA. 141
3.44 Scanner matrices for the $2^+ \rightarrow 0^+$ transition in ^{46}Ti. On the X axis the γ-ray energy Doppler corrected with a $\cos(\theta)$ derived from the X and Y offset shown in the Y axis is reported. Left panel: X scanner. Right panel: Y scanner. 143
3.45 Left panel: Scanner matrix for the $2^+ \rightarrow 0^+$ transition in ^{46}Ti. On the X axis the γ-ray energy Doppler corrected with a β derived from the ToF offset shown in the Y axis is reported. Right panel: FWHM for the same transition as a function of the ToF offset. . . 144

3.46 Left panel: Energy vs Time matrix for the ^{46}Ti run. The time value represents the interval between the Sc41 ion hit and the AGATA γ signals. Right panel: Time projection of the matrix shown in the left panel. 145
3.47 FRS particle identification plots for ^{46}Ti (left) and ^{46}Cr (right) used in the present analysis. The black curves denote the adopted incoming gates. Strict cuts were chosen in order to avoid contamination from unwanted incoming ions. 147
3.48 Z (left) and A/q (right) projections of the FRS PID plot for ^{46}Ti settings. The applied cuts are reported as well. The reported A/q spectrum corresponds to Sc isotopes. See text for details. 148
3.49 LYCCA outgoing atomic number identification plots for ^{46}Ti (left) and ^{46}Cr (right) used in the present analysis. The black curves denote the adopted outgoing gates. 150
3.50 γ-ray spectra for the nuclei of interest ^{46}Ti and ^{46}Cr. Incoming, outgoing and time gates are applied. The event-by-event LYCCA β has been used. 150
3.51 Correlation between incoming and outgoing angles on the XZ and YZ planes in the ^{46}Ti unreacted beam runs. 154
3.52 Scattering angle distribution for ^{46}Ti (left) and ^{46}Cr (right) secondary beams. 154
3.53 γ-ray spectra for the nuclei of interest ^{46}Ti and ^{46}Cr. Incoming, outgoing, time and scattering angle cuts are applied. The event-by-event LYCCA β has been used. 155
3.54 Measured cross section as a function of the cut on the scattering angle for ^{46}Ti (top) and ^{46}Cr (bottom) 158
3.55 Measured B(E2) value as a function of the cut on the scattering angle for ^{46}Ti (top) and ^{46}Cr (bottom). The solid blue line represents the literature value, while the relative error is indicated by the dashed lines. 159

3.56 Simulated Doppler corrected energy as a function of γ-ray angle, for the $2^+ \rightarrow 0^+$ transition in ^{46}Ti emitted at the estimated velocity after each of the three foils. The Doppler correction was performed for the β value after the second target. The vertical lines denote the angular coverage of AGATA. 163
3.57 γ-ray spectra for ^{46}Ti (left) and ^{46}V (right). An event-by-event Doppler correction has been performed. No cuts were put on the γ-ray angle. 163
3.58 Distribution of γ-ray counts as a function of the detection angle. 164
3.59 γ-ray spectra for ^{46}Ti (left) and ^{46}V (right). An event-by-event Doppler correction has been performed. A $30^\circ \pm 5^\circ$ cut was put on the γ-ray angle. 165
3.60 γ-ray spectra for ^{46}Ti (left) and ^{46}V (right) with a $30^\circ \pm 5^\circ$ cut on the γ-ray angle. The number of counts in each peak has been obtained by fitting the spectrum with a linear background and three gaussian functions. 167
3.61 γ-ray spectra for ^{46}Ti (left) and ^{46}V (right). An event-by-event Doppler correction has been performed. A $39^\circ \pm 5^\circ$ cut was put on the γ-ray angle. 168
3.62 Triple peak structure for ^{46}Ti fitted with the simulated lineshape. An angle cut of $30^\circ \pm 5^\circ$ has been applied and a half-life value of $T_{1/2} = \ln(2)\tau = 5.25$ ps has been assumed [97]. 170
3.63 χ^2 of the simulation fit on the experimental data on ^{46}Ti as a function of the assumed half-life of the state [97]. 171
3.64 Triple peak structure for ^{46}V fitted with the simulated lineshape. An angle cut of $30^\circ \pm 5^\circ$ has been applied and a half-life value of $T_{1/2} = 4.75$ ps has been assumed [97]. 172
3.65 χ^2 of the simulation fit on the experimental data on ^{46}V as a function of the assumed half-life of the state [97]. 172

3.66 M_P value as a function of T_z along the T=1, A=46 triplet. Top panel: absolute values measured in the present work. Middle panel: M_p values normalized to the ^{46}Ti literature value. Bottom panel: weighted average with previously known values. Picture taken from [98]. 175

List of Tables

1.1 $f_{7/2}$ Coulomb and isospin non conserving matrix elements deduced from experimental data in A=42. Taken from [1]. 13

2.1 Main properties of DIAMANT. 33
2.2 Parameters acquired in the present experiment. 38
2.3 Coefficients of the measured efficiency curve. 40
2.4 Absolute efficiency determined with the *sum peak method* for each EXOGAM Clover in the present setup. 42
2.5 Measured detection efficiencies for α and protons. 48
2.6 Optimized values for β_{CN} and E^*_α. 51
2.7 Angular distribution, multipolarity and intensity of the transitions between positive parity states in ^{23}Na. 65
2.8 Angular distribution, multipolarity and intensity of the transitions between positive parity states in ^{23}Mg. 66
2.9 Top: new levels and transitions identified in this work in ^{23}Mg. Bottom: mirror energy differences in the mirror pair ^{23}Mg-^{23}Na. . 67

3.1 Targets and degraders used in FRS for the different settings. . . . 103
3.2 Properties of the ^{58}Ni calibration runs performed prior to the experiment. The ToF and β values have been obtained by LISE simulations [84]. 118
3.3 Composition of the secondary beams for the settings used in the present experiment. 125
3.4 Fraction of events with a given Core multiplicity. 138

3.5 Correction factors for the γ-ray efficiency due to the effective number of working detectors for the different settings. 139
3.6 Data taking time and beam intensities for all the sub-experiments presented in this work. 145
3.7 Triggers used in the present experiment. 146
3.8 Total number of ^{46}Ti and ^{46}Cr nuclei in the present experiment. . 149
3.9 Average dead time for the ^{46}Ti and ^{46}Cr settings. 152
3.10 Safe impact parameters adopted in the present analysis for ^{46}Ti and ^{46}Cr ion beams. 153
3.11 Summary of the statistical and systematic uncertainties for the present Coulex experiment. 156
3.12 Relevant quantities for the Cross section determination in ^{46}Ti and ^{46}Cr. 157
3.13 B(E2) values obtained in this work for ^{46}Ti and ^{46}Cr. 157
3.14 Number of counts in each peak and measured lifetime τ_{exp} with a cut of $30° \pm 5°$ on the γ-ray angle in ^{46}Ti and ^{46}V. The previously known values, τ_{lit}, are reported as well for comparison. 167
3.15 Number of counts in each peak and measured lifetime τ_{exp} with a cut of $39° \pm 5°$ on the γ-ray angle in ^{46}Ti and ^{46}V. The previously known values, τ_{lit}, are reported as well for comparison. 169
3.16 Half-lives and B(E2) values measured in this work for ^{46}Ti and ^{46}V. The $T_{1/2}$ literature values are reported as well. 173

Ringraziamenti

Grazie a Silvia, che con una grande dolcezza ed uno spirito quasi materno mi guida ormai da tempo, con uno sguardo attento alle cose davvero importanti.

Grazie a Francesco, che con la sua presenza costante ed una disponibilità assoluta mi ha accompagnato in questi anni, credendo in me e aiutandomi a crescere, sotto tantissimi punti di vista.

Grazie a Santo, perché la"contrazione delle lunghezze" dei luoghi di origine ha superato la "dilatazione dei tempi" della differenza di età.

Grazie a Daniele, perché tra la condivisione di interessi ed idee ed una naturale empatia è un prezioso ed inconsapevole punto di riferimento.

Grazie a Franco, perché percorriamo sentieri simili, e stando due passi avanti a me, mi dimostra sempre che la strada è quella giusta.

Grazie a Javier, che spesso e volentieri mi ha fatto un regalo pregiato: un punto di vista originale.

Grazie a Denise, che ha colorato l'ultima parte del tragitto.

Grazie a Scott, costante compagno di viaggio nei tortuosi alti e bassi dell'analisi.

Grazie ad Alain, Daniel, Dino, Dmitry, Giacomo, Grzes, Kasia, Marco, Philipp, Roberto per avermi insegnato e fatto star bene molto più di quanto credano.

Grazie a Stefano, a cui sono bastate poche occasioni per toccare le corde giuste e dare il "la" ad una splendida melodia.

Grazie ad Ale, Sere, Stefy, per aver reso Via Marzolo una seconda famiglia.

Grazie a Padova, che per prima mi ha fatto scoprire quanto mondo c'è al di fuori delle mura di Verona; grazie a Verona, perché tra quelle mura sarà sempre casa.

Grazie agli amici e alle amiche di sempre, Andrea, Anna, Federica, Francesco, Francesco, Irene, Nicolò, Nicolò, Paolo, per essere entrati nel mio gioco, ed aver giocato la loro meravigliosa parte.

Grazie ai miei fratellini, di ieri e di oggi, per avermi fatto ammirare i fiori più belli, che non son quelli di serra. Siamo d'uno stesso sangue voi ed io.

Grazie a chi, tra una corsa fino al mare e un bicchiere di vino, una chiacchierata ed un concerto, ha incrociato la sua strada con la mia, facendomi diventare un pochino più grande.

Grazie a mio papà e a mia sorella, perché le cose giuste non hanno un gran bisogno di parole.

Grazie a Valentina, perché la cosa più preziosa è alla fine un albero di pesco.

Grazie alla mia mamma, che mi tiene sempre una mano sulla testa.